Models of the circumstellar medium of evolving, Galactic, massive runaway stars

Dissertation
zur
Erlangung des Doktorgrades (Dr. rer. nat.)
der
Mathematisch-Naturwissenschaftlichen Fakultät
der
Rheinischen Friedrich-Wilhelms-Universität Bonn

vorgelegt von
Dominique M.-A. Meyer
aus
Straßburg, Frankreich

Bonn 2014

À mes parents et à ma soeur,

Massive stars are uncommon objects but they are preponderant in the understanding of the cycle of matter in the interstellar medium (ISM) of galaxies (Langer, 2012). Throughout their life, they release strong winds replenishing the ISM with metals, momentum and kinetic energy. Thus, they crucially participate in the constitution of molecular clouds which fragment and give birth to the next generation of stars. The ejection of massive stars out of their parent cluster, e.g. by dynamical ejection during multiple-body encountering (Gvaramadze & Gualandris, 2011) or by supernovae occurring in binaries (Gvaramadze et al., 2011b), produces the about 10 to 25 per cent of them which are moving supersonically through the ISM (Huthoff & Kaper, 2002). They may generate bow shocks of swept-up gas, whose morphology and brightness can be used to constrain both their stellar wind and ambient medium properties (Kaper et al., 1997). When these stars die, the supernova blastwave expands inside their pre-shaped surroundings and interacts with the bow shock (Borkowski, Blondin & Sarazin, 1992). The shape of the produced supernova remnants is therefore a function of the intrinsic properties and of the past evolution of its progenitor, and depends on the local ISM properties.

Our models provide the first self-consistent grid of the evolution of the circumstellar medium of massive Galactic runaway stars from the main sequence phase up to the development of the supernova remnants in a series of two-dimensional, non-ideal hydrodynamical simulations. We stress that thermal conduction (Spitzer, 1962) is an important process governing the shape (see Comerón & Kaper, 1998, and references therein) and luminosity of the bow shocks driven by our runaway main sequence stars. The bow shocks around hot stars have an optical luminosity principally from forbidden lines, e.g. [O II] and [O III], originating from the shocked ISM material. All our bow shock models are brightest in the infrared. We identify the regions of maximum emission in Hα and in the infrared regime of both the bow shocks generated by hot and cool stars. We predict that in the Galactic plane, the most common and easily detectable of them are produced by high-mass stars moving with small space velocities. Finally, we explore how an external source of radiation affects the bow shock of a runaway red supergiant (Decin et al., 2012). We tailored our simulations to the optically-detected bow shock of IRC -10414 (Gvaramadze et al., 2014) and find that the ionization of its stellar wind makes its contact discontinuity more stable and enhances its [N II] optical line emission from the shocked wind. On the basis of these arguments, we constrain the mass loss and the local ISM properties of IRC -10414.

After the death of the star, the supernova shock wave interacts with the pre-shaped circumstellar medium (van Veelen et al., 2009). We find that the bow shocks produced by our high-mass, slowly-moving stars which accumulate more than about 1.5 $M_{\odot}$ throughout their progenitor's history imposes high deviations from sphericity on the supernova shock wave. The reverberation of the blastwave induced by the presence of a dense structure (Ferreira & de Jager, 2008) such as a bow shock produces a region of hot-phased ISM that grows, augmenting the volume of hot shocked gas whose emission by thermal Bremmstrahlung and X-ray photons in the soft energy band dominate their lightcurves. It produces a strong mixing of ejecta, wind and ISM gas in the remnants. The shock wave velocity differs from about an order of magnitude whether its is channeled into the trail of the bow shock or decelerated by the mass in the bow shock upstream from the center of the explosion, as observed in RCW86 (Vink, Kaastra & Bleeker, 1997). The remnants' morphologies are consistent with the bilateral character of observed barrel-like remnants such as G296.5+10.0 (Manchester, 1987). Moreover, the [O III]-bright jet-like features of channeled ejecta are similar to those found in the Crab nebula (Cox, Gull & Green, 1991).

Les étoiles massives sont des objets astrophysiques rares mais qui sont prépondérants dans la compréhension du cyle de la matière au sein du milieu interstellaire (ISM) des galaxies (Langer, 2012), puisque tout au long de leur vie, leurs vents le réapprovisionnent en métaux et moment cinétique. Ainsi, elles participent de manière cruciale à la consitution de nuages moléculaires qui vont ensuite se fragmenter et donner naissance à la prochaine génération d'étoiles. L'éjection d'étoiles massives hors des amas stellaires qui les ont vu naître est rendu possible lors de processus dynamiques à plusieurs corps (se reporter á l'étude de Gvaramadze & Gualandris, 2011) ou bien au sein de systèmes binaires lorsque leur compagnon explose en supernova (Gvaramadze et al., 2011b). Ceci produit les 10 a 25 pour cent d'étoiles massives se déplacant en mouvement supersoniques par rapport à l'ISM (Huthoff & Kaper, 2002). Elles sont susceptiles des générer des arcs-de-chocs de gas situés à la proue du milieu circumstellaire de l'étoile en mouvement et dont la morphologie et/ou la brillance de surface peut être utilisée pour contraindre à la fois les propriétés des vents stellaires mais aussi du milieu ambient (Kaper et al., 1997). Lorsque ces étoiles meurent, l'onde de choc de la supernova se propage à l'intérieur des structures circumstellaires et interragie avec l'arc-de-choc (voir Borkowski, Blondin & Sarazin, 1992). La forme du vestige de supernova qui se développe est fonction de l'évolution passée de son progéniteur et des propriétés locales de l'ISM.

Les modèles présentés dans ce travail constituent la première grille de simulations hydrodynamiques portant sur l'évolution du milieu circumstellaire des étoiles massives en mouvement supersoniques dans le plan galactique. L'évolution des étoiles est suivie depuis leur entrée sur la séquence principale jusqu'à leur explosion finale en supernova. La considération de la conduction thermique (Spitzer, 1962) est nécessaire dans l'établissement des arcs-de-chocs (Comerón & Kaper, 1998) et gourverne leur luminosité. Ceux menés par des étoiles chaudes ont une luminosité optique principalement due a des émissions en [O II] et [O III] provenant du ISM pénétrant l'arc-de-choc. Nos models predisent qu'ils sont d'avantage lumineux en infrarouge, et donc que cette bande du spectre électromagnétique est la plus apropriées pour les observer. Nous avons mis en évidence que les régions émettrices en Hα ainsi qu'en infrarouge des arcs-de-chocs autours des étoiles, à la fois durant leur phases chaudes et froides. Nos simulations prédisent que, dans le plan galactique, les arcs-de-chocs le plus facilement détectables sont ceux générés par des étoiles de forte masses se mouvant a des vitesses juste au-delà de la limite supersoniques. Finalement, nous avons exploré les effets d'une source externe de radiation (Decin et al., 2012) sur l'arc-de-choc de la supergéante rouge IRC -10414 (Gvaramadze et al., 2014) et avons trouvé que l'ionisation de son environnement provoque une stabilisation de l'interface entre le vent et l'ISM, et augmente l'intensité des émissions en [N II] du vent pénétrant l'arc-de-choc. De plus, nous avons contraint le taux de perte de masse, ainsi que la densité du milieu ambient de IRC -10414.

Après la mort de l'étoile, le front d'onde créé par l'explosion de supernova interagie avec le milieu circumstellaire (van Veelen et al., 2009). D'après nos estimations, les arcs-de-chocs produits par des étoiles de forte masses accumulant plus de $1.5\,\mathrm{M_\odot}$ de gas durant la vie de leur progéniteur impose au front d'onde de fortes déviations par rapport à la solution sphérique. La réflection de l'onde induite par la présence d'une structure dense (Ferreira & de Jager, 2008) tel un arc-de-choc, donne naissance à une région dans la phase chaude du ISM qui grandie et provoque une augmentation du volume de gas bordé par le front d'onde, dont les emissions X et par Bremstrhalung thermique domine leur courbe de lumière. Ceci produit un mélange de matériel conséquent dans le vestige de la supernova. La vitesse du front d'onde diffère d'un ordre de magnitude selon qu'il se propage vers l'arc qui le décélère ou bien qu'il soit canalisé dans son sillage tel que cela a été observé pour RCW86 (Vink, Kaastra & Bleeker, 1997). Les morphologies de nos modèles sont consistent avec le charactère bilateral de certains vestiges de supernova, particulièrement ceux de type barillet, tels que G296.5+10.0 (Manchester, 1987). De plus, l'extension d'éjecta émettant en [O III] dans la direction opposée à la direction du mouvement du progéniteur sont similaires a celui trouvé dans la nébuleuse du Crabe (Cox, Gull & Green, 1991).

Acknowledgements

First and foremost, I would like to thank Prof. Norbert Langer for having allowed me to carry on with my studies within his research group, in the wonderful field of stellar astrophysics. Without his guidance, advice and constant help, this dissertation would not have been possible. He has never refused to share his huge knowledge and to spend his precious time to follow, discuss and supervise my work. I am very grateful to him. Moreover, his connection with the ongoing German DFG priority program 1573 ISM-SPP "The physics of the interstellar medium" gave me the opportunity to attend various conferences and summer schools in Jülich, Freising, Göttingen, Bonn, Garching, Köln, Münich and Bad Honnef in Germany, but also further away in Europe, i.e. in Copenhagen in Denmark and in Leiden in the Netherlands. I have met there many other outstanding scientists who inspired my work.

My next thought immediately goes to Prof. Robert Izzard, who has been an patient advisor and widened my horizon to the fascinating but also complex field of binary stars. I deeply thank him for having patiently advised me on a topic which is far from his main expertise. Our numerous discussions largely participated to the achievement of this thesis. I also thank him for having given me the opportunity to tutor his exciting class on binary stars during two consecutive winter terms.

I more than deeply thank Her Royal Majesty Elizabeth Windsor the Second, Queen of the United Kingdom and of the Commonwealth realms, for preserving the tradition of allowing scientists from the whole world to openly publish their research in Monthly Notices of the Royal Astronomical Society.

I do not forget the main co-authors of my different research projects, particularly Dr. Jonathan Mackey from the University of Bonn and Dr. Vasilii V. Gvaramadze from Moscow State University for all their ideas and advices. I thank them for all the time they have spent over the last three years, working with all my curiosity, patience... and impatience. As far as I am concerned it was a daily enriching task to learn from their knowledge, skills... and all the rest. Last but not least, I thank Prof. Andrea Mignone from the University of Torino (Italy), because the progress made with his code PLUTO during his visit in Bonn was a critical step in this thesis.

The pioneers of bow shock modelling with thermal conduction are warmly thanked, i.e. Dr. Fernando Comerón from the Chilean branch of the European Southern Observatory and Prof. Lex Kaper from the Astronomical Institute Anton Pannekoek at University of Amsterdam (the Netherlands) for their comments and help. I thank Prof. Wolfgang Steffen Burg, Dr. Guillermo García-Segura, Prof. Alejandro Raga and Dr. Pablo Veázquez from Instituto de Astronomía at Universitad Nacional Autonomia de Mexico and from Ensenada for their support with the software SHAPE, their comments on thermal conduction, on the Parker solution and on the asymmetric nature of some supernova remnants, respectively. I thank the other experts in bow shocks modelling, namely Dr. Allard Jan van Marle from Instituut voor Sterrenkunde at University of Leuven (Belgium), Dr. Shazerene Mohamed from South African Observatory in Capetown and Dr. Niccolo Bucciantini from Osservatorio di Arcetri in Firenze (Italy) for helpful discussions in Leiden.

Contents

Introduction

1.1 General

Thinkers have always conjectured about how Nature functions, and scientists have tried to verify their theories. Astronomy has evidently suffered from the fact that the object of its study, i.e. the Universe and its evolution, its components and their governing mechanisms, can hardly be subject to reproducible experiments. To validate or reject their hypothese, ancient astronomers (Fig. 1.1) had first to think up ideas and then confronted them with well-accepted arguments, e.g. the religious dogma or theological principles ruling their society. Along with population migrations, technology progressed and complex devices were used to understand the behaviour of Nature. The norm used to discuss and approve or reject a postulate became more rationalised, based on mathematics and on the laws of physics. More recently, computer science allowed scientists to perform numerical simulations, i.e. synthetic experiments, that are becoming a widely used method to test theories.

Over the past decades, several facilities such as the WISE (infrared, Wright et al., 2010), SPITZER (infrared, Werner et al., 2004), HUBBLE (optical, Dalcanton, 2009), CHANDRA and XMM-NEWTON (X-rays, Santos-Lleo et al., 2009) ground and space based telescopes have opened high-resolution, multi-wavelength windows on the sky. They refine our knowledge regarding the governing processes of stellar evolution. Recently, the HERSCHEL (Pilbratt et al., 2010) and SOFIA (Gehrz et al., 2009, Fig. 1.2) high-resolution infrared facilities continued to provide us with information enriching our comprehension of stellar physics, for example via observations of the circumstellar medium of massive stars. Simultaneously, capabilities of supercomputers such as the JUROPA supercomputer in Jülich[1] (Fig. 1.3) are bringing us into an era in which high-performance numerical models will be directly comparable with observations of parsec-scale[2] structures, e.g. the stellar wind bow shocks generated by massive runaway stars such as the red-supergiant star Betelgeuse (Section 1.4.2).

The aim of this thesis is to produce dynamical models of the circumstellar medium of the most common massive runaway stars, i.e. the massive stars whose bulk velocity is supersonic with respect to their ambient medium. The resulting nebulae created by the translational motion of these stars with respect to their surroundings are called bow shocks (Section 1.4.2). The data from our simulations are used to predict the emission properties of these bow shocks. Exploring the most probable range of initial stellar masses and space velocities, we aim to converge on a picture correlating emission properties of

---

[1] http://www.fz-juelich.de/ias/jsc/EN/Expertise/Supercomputers/JUROPA/JUROPAnode.html
[2] 1 parsec $\approx$ 3.26 light-year $\approx$ 3.09 $\times$ 10^{18} cm
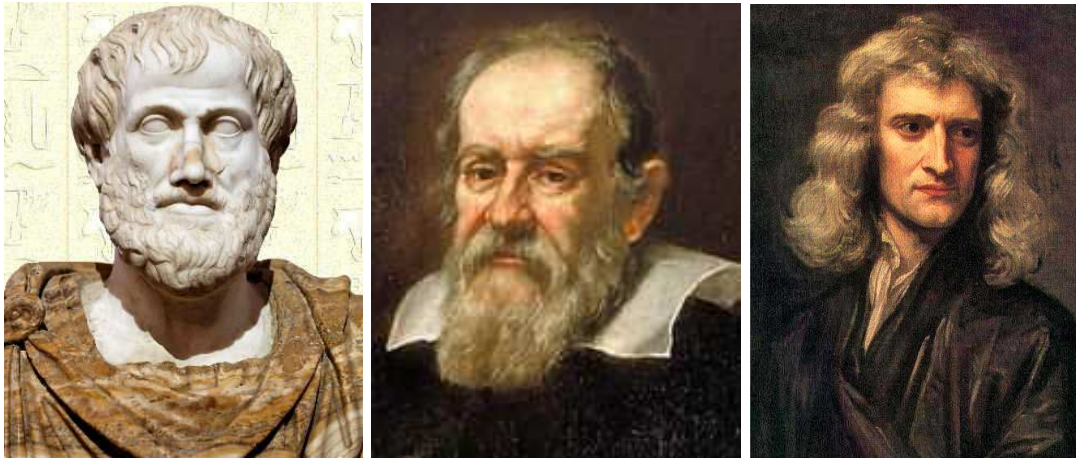
Figure 1.1: Ancient astronomers whose understanding of the Universe followed different approaches. Aristotle (384−322 B.C., left panel) based his non-experimental conception of the Universe on a series of a few elements rationally interacting with each other to explain the Universe's functioning. His philosophy is the foundation for all sciences up to the end of the Middle-Ages, both in the European and Arabic worlds. Galileo (1564−1641 A.D., middle panel) forgave the medieval European way of considering sciences, i.e. an Aristotelician-inspired alchemy, to develop a conception of the Universe based on mathematics, which he then experimentally verified within a given measurable error. This is the beginning of science as we still understand it. Newton (1642−1726 A.D., right panel) knew the transition between Aristotelician and rationalised conceptions of the world. Left panel is a bust of Aristotle (330 B.C.), Museo Nazionale Romano, Palazzo Altemps, Roma. Middle panel is the portrait of Galileo Galilei by Justus Sustermans (1636 A.D.), Pitti palazzo, Firenze. Right panel is the portrait of Isaac Newton by Godfrey Kneller (1689 A.D.), The Royal Mint Museum.

Figure 1.2: The SOFIA airborne infrared facility (Credit: NASA/DLR).

Figure 1.3: Cabinet of parallelised Intel dual-core processors, part of the JUROPA supercomputer at Jülich Super-computing center.

the circumstellar medium of runaway massive stars with their intrinsic physical characteristics, e.g. their stellar wind mass-loss rate. This procedure is applied to main-sequence and red supergiant stars moving through the Galactic plane (Chapter 2). Secondly, we explore the effects of photoionization by an external source of radiation on the stability of bow shocks produced by runaway red-supergiant stars (Chapter 3). Finally, we focus on the supernova phase of these stars, when the blastwave generated during the explosion interacts with the previously formed bow shocks (Chapter 4). We conclude in Chapter 5.

1.2 Massive stars and stellar evolution

In this section, we very briefly summarize the main steps of the evolution of stars[3], from their birth in a molecular cloud to the final phase of their transformation.

1.2.1 The birth of stars

Stars are born when a cold and dense molecular cloud contracts and collapses by gravitational instability (McKee & Ostriker, 2007). Once fragmented into dense cloudlets that allow nuclear fusion to take place, the former molecular region (Section 1.3) becomes a cradle of proto-stars whose masses follow a particular distribution, the canonical initial mass function (IMF, Salpeter, 1955; Kroupa, 2001). Depending on the composition and physical properties of their parent cloud, e.g. the angular momentum, the new-born stars evolve chemically and thermodynamically. The more massive the stars, the faster they evolve through several distinct evolutionary phases whose number increases and characteristic timescale decreases with increasing initial mass (Kippenhahn & Weigert, 1994; Maeder, 2009, and references therein). Stellar evolution theory aims to produce models to explain the fate of stars according

---

[3] See lecture notes on Stellar Physics by Prof. N. Langer, Bonn University at http://www.astro.uni-bonn.de/~nlanger/siu_web/teach_sse.html
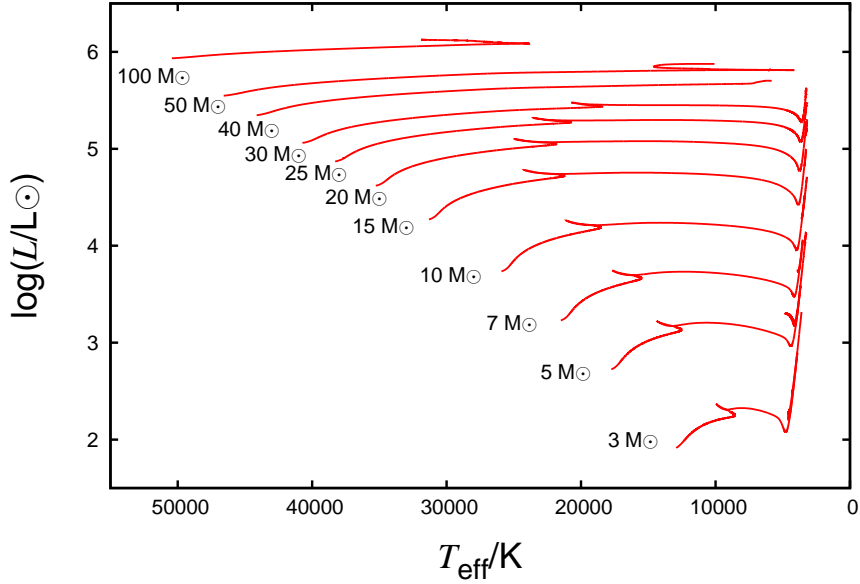
Figure 1.4: Hertzsprung-Russell diagram of stellar evolutionary tracks assuming no stellar rotation and an initial solar composition (Brott et al., 2011). It shows the stellar luminosity L (in $L_\odot$) as a function of their surface temperature, i.e. effective temperature T_{eff} (in K). The zero-age main sequence mass of these stellar models is the mass of the stars when they join the main-sequence phase by burning hydrogen. It is indicated near the beginning of the plotted evolutionary tracks and ranges from 3 to 100 $M_\odot$ and their evolution is followed at least until the helium burning phase (Brott et al., 2011).

to their initial properties. A usual representation of stellar evolution models is the surface temperature-luminosity plane, or Hertzsprung-Russell diagram (Fig. 1.4). It allows to classify the stars as a function of their spectroscopic properties, but also to compare theoretical calculations of stellar structures and evolution with observations.

1.2.2 Massive stars evolution

Massive stars have an initial mass larger than $8\,M_\odot$ and spend most of their lives as hot main sequence stars, releasing radiation and material in fast and low density winds into the interstellar medium (ISM). These stars are hotter than about 22000 K and have luminosities larger than about $10^{38}\,\mathrm{erg\,s^{-1}}$, whereas their mass loss is about $10^{-9}-10^{-6}\,M_\odot\,\mathrm{yr^{-1}}$ and their wind velocities are about $1000\,\mathrm{km\,s^{-1}}$. The exhaustion of hydrogen in their core triggers a transition to the red supergiant phase (Heger, Langer & Woosley, 2000). Their mass loss becomes huge, about $10^{-5}\,M_\odot\,\mathrm{yr^{-1}}$. Their envelope inflates while their wind velocity decreases to about $10\,\mathrm{km\,s^{-1}}$. These stars are cold and have effective temperatures of the order of 3000 K. Alternatively, if their initial mass is smaller than $20\,M_\odot$, they may further evolve to become a blue supergiant charaterized by stellar properties similar to a main-sequence star before to return to the red supergiant phase (Langer, 1991). Stars with initial masses between 20 and $30\,M_\odot$ directly evolve to the red supergiant phase before to explode as a core-collapse supernova. If their initial mass ranges between 30 and $50\,M_\odot$, they become a Wolf-Rayet star with a surface temperature of about 10^5 K, and with a very fast wind of about $5000\,\mathrm{km\,s^{-1}}$ and a large mass-loss rate of about $10^{-4}\,M_\odot\,\mathrm{yr^{-1}}$ (Schaller et al., 1992). Stars with initial mass larger than $50\,M_\odot$ evolve through the Luminous Blue Variable phase after their main sequence. This phase is still poorly understood. These hypergiant stars are very rare,

extraordinarily luminous and have outbursts produced by very violent mass-loss events. The fate of massive stars is the supernova explosion. Nevertheless, because their internal and emission properties are strongly influenced by rotation, which changes the course of stellar evolution, some massive stars die as gamma-ray bursts (Yoon & Langer, 2005), returning huge (10^{53} erg) amounts of energetic radiation into the ISM (Rigon et al., 2003). The final state of the evolution of massive stars is a neutron star or a black hole (Heger, 2012).

1.2.3 The death of stars

Massive star finish their life exploding as a supernova. According to their initial masses, several mechanisms have been proposed so far to explain the explosion and are listed below.

1. The electron capture supernova (Nomoto, 1984, 1987). Their progenitors are so-called super-asymptotic giant branch stars exhausting the carbon of their oxygen-neon-magnesium core. If this core reaches a mass of about $1.375\,M_\odot$, electrons are captured by the nuclei. Consequently, the electron pressure decreases and the core collapses. The neutron star emits neutrinos whose pressure is thought to be responsible for the acceleration of material out of the stellar envelope.

2. The iron core-collapse supernova (Janka et al., 2007). This happens when massive stars burn elements up to silicon, while their innermost part forms an iron core. To compensate for energy losses, the core of the progenitor starts contracting. This mechanism produces high temperatures that induce the disintegration of heavier elements. The core shrinks up to a density similar to that of an atom nucleus. Its collapse stops, reflecting the infalling material out of the stellar surface. This event is usually called "the bounce".

3. The pair instability supernova (Fraley, 1968; Heger et al., 2003). This concerns extremely massive stars in which electron-positron pairs are created from photons which previously prevented the core from collapsing. The subsequent burning of the oxygen triggers an explosion which totally disrupts these stars.

The interaction of the supernova ejecta with its circumstellar material produces emission whose evolution as a function of time, i.e. the supernova lightcurves, has a rich and varied taxonomy reflecting the complexity of the circumstellar medium at the pre-supernova phase (Lozinskaya, 1997).

1.3 The interstellar medium

The interstellar medium (ISM) is the matter constituting the galaxies and which does not reside in stars (Osterbrock & Bochkarev, 1989). It is physically described by its thermodynamics properties which classify the different kind of regions observed in the ISM into several phases, according to their temperature, density, composition and ionization state. A two-phase model was first introduced as the GHF model in Goldsmith, Habing & Field (1969) and was later extended to a more complete description by McKee & Ostriker (1977). Each of these phases possesses characteristic observational features as follows[4].

1. Clouds of molecular hydrogen (H_2) are observable in CO mm-wavelength molecular emission lines. They are cold, about $10-20\,K$, and very dense, with number densities up to $10^5\,cm^{-3}$.

---

[4] See lecture notes on Astrophysics by Prof. Richard W. Pogge, Ohio State University at http://www.astronomy.ohio-state.edu/~pogge/

Their volume occupies a small fraction of a Galaxy, and they are gravitationally bound. They contain about 30 per cent of the mass of the ISM. They are surrounded by a layer of atomic gas that shields their interior from UV radiation.

2. The cold neutral medium (CNM) is made of atomic hydrogen HI and remains in the form of filaments and sheets. It is observable in ultra-violet absorption lines and in the optical. Its temperature is about $70-100\,\mathrm{K}$ and its density exceeds $50\,\mathrm{cm}^{-3}$.

3. The warm neutral medium (WNM) of atomic hydrogen HI is observable in the 21cm line. It has a temperature of about $8000\,\mathrm{K}$ and densities of about $0.5\,\mathrm{cm}^{-3}$. It is located at the egde of HII regions and molecular clouds.

4. The warm ionized medium (WIM) of diffuse gas is observable in absorption lines in the far-ultraviolet. Its temperature is about $6000-12000\,\mathrm{K}$ and its density is less than about $0.1\,\mathrm{cm}^{-3}$. It contains more that 90 per cent of the ions (H^+) that are in the ISM of the Galaxy.

5. The hot ionized medium (HIM) is made of low-density gas that is collisionally heated by supernovae shock waves. It is generally hotter than $10^6\,\mathrm{K}$ and its density is less than $0.003\,\mathrm{cm}^{-3}$. It is observable in absorption lines in the far-ultraviolet, e.g. the O IV and N IV lines if its temperature is less than 10^5 K or in diffuse soft X-rays at higher temperatures.

The gas constituting the thermal phases can be locally inhomogeneous, turbulent, neutral and magnetized. However, the classical picture assumes kinetic, excitation, ionization and pressure equilibrium.

1. Kinetic equilibrium implies that the velocity distribution of the protons, electrons and ions composing the gas is Maxwellian, and that all species have the same temperature. In other words, the velocity distribution $f(\vec{v})$ of a volume element of gas dV is,

$$f(\vec{v})\,d^3V = \left(\frac{\tilde{\mu}}{2\pi k_\mathrm{B}T}\right)^{1/2} \exp\left(-\frac{\mu\vec{v}^2}{2k_\mathrm{B}T}\right) d^3V, \qquad (1.1)$$

where $\vec{v}$ is the particles vector velocity, where $\vec{v}^2 = \vec{v}\cdot\vec{v}$, $\tilde{\mu}$ is the reduced mass of the particles[5], k_B is the Boltzmann constant and T is the kinetic temperature of the gas[6]. The electron-electron scattering timescale is shorter than any other timescale in ionized regions such as the WIM or the HIM. This means the gas to thermalise fast, i.e. its constituting particles rapidly to converge to a state that has a Maxwellian velocity distribution.

2. Excitation equilibrium is a description of the atoms and molecules level populations in the gas assuming locally that Eq. (1.1) is satisfied. With n_i the population of the level i of a given species,

$$n_\mathrm{i} = \frac{n_\mathrm{i}g_\mathrm{i}}{f(T)} \exp\left(-\frac{E_\mathrm{i}}{k_\mathrm{B}T}\right), \qquad (1.2)$$

where g_i is a statistical weight of the corresponding level i and E_i its energy.

---

[5] The reduced mass $\tilde{\mu}$ of a set of particles of mass m_i is defined as as the inverse of the sum of the quantity m_i^{-1} over all particles.

[6] The kinetic temperature of a gas is defined as $\alpha k_\mathrm{B}T = E_\mathrm{kin}$, where α is the number of degrees of freedom of the particles constituting the gas and E_kin its average kinetic energy.

3. A gas is in ionization equilibrium as long as the photoionization and collisional ionisation rate of a species counterbalances the recombination of the corresponding ions with free electrons. The ISM gas is either ionized by the background radiation field or by photons from hot stars. In case of shocks, collisional heating can also liberate photons able to ionize the ISM. The ionization equilibrium for a species X follows from the following equation, balancing the rate of ionisations with the rate of recombinations,

$$\frac{n(X^{r+1})}{n(X^r)} = \frac{1}{n_e} \frac{\Gamma}{\alpha(T)},$$ (1.3)

where $n(X^{r+1})$ and $n(X^r)$ are the number densities of ionized and neutral gas with respect to the ionizable species X and n_e is the electron number density. In Eq. (1.3), $\alpha(T) = \sigma_{\text{recomb}}|\vec{v}_X - \vec{v}_e|$ is the recombination term, with $|\vec{v}_X - \vec{v}_e|$ the modulus of the resulting recombined ion velocity and c the speed of the light. The term $\Gamma = n_{\text{photons}}\sigma_{\text{ionize}}c$ is the radiation term, with σ_{ionize} and σ_{recomb} representing the mean cross-sections of the ionizing and recombining particles, respectively, and n_{photons} represents the photons number density of the medium.

4. Pressure equilibrium means that the force exerted per unit surface at each side of a discontinuity, such as at the edge of a molecular cloud, in the WIM are equal. The borders of the cloud do not evolve spatially because,

$$\left(\rho\vec{v}^2 + nk_B T + \frac{\vec{B}^2}{8\pi} + p_{\text{CR}} + p_{\text{rad}}\right)_{\text{in}} = \left(\rho\vec{v}^2 + nk_B T + \frac{\vec{B}^2}{8\pi} + p_{\text{CR}} + p_{\text{rad}}\right)_{\text{out}},$$ (1.4)

where the subscripts in and out refer to the inner and outer borders of the cloud, respectively. In Eq. (1.4) $\rho\vec{v}^2$ represents the hydrodynamical ram pressure, $nk_B T$ the thermal pressure of the gas, $\vec{B}^2/8\pi$ is the magnetic pressure of the gas with $\vec{B}$ the magnetic field of the medium, p_{CR} the pressure generated by cosmic rays and p_{rad} the pressure produced by the radiation field of the medium.

In the warm and neutral phases of the ISM, solid dust grains of size of about micrometers up to clusters of hundreds of grains are in the gas (Mathis, Rumpl & Nordsieck, 1977) and this is a source of extinction and of chemical reactions (Indebetouw et al., 2005). Cooling induced by the gas-grain coupling can become relevant and could be included in the gas equation of state (Hollenbach & McKee, 1989). As a function of the gas properties, heating (photoelectric heating from dust grains, photoheating or cosmic rays heating), cooling (collisionally excited line emission, hydrogen collisional ionization, Bremsstrahlung radiation, hydrogen recombination cooling, molecular cooling and non-thermal emission) mechanisms are at work. The sum of a region's main relevant radiative processes as a function of temperature is called its cooling curve (Fig. 1.5). The investigation of the structure of the ISM is an active field of research involving state-of-the-art numerical simulations and high resolution multi-wavelengths observations. This field is at the border between ISM, star formation and the circumstellar medium studies.

The ISM equilibria are perturbed by violent events such as material ejection or the release of photons. When these perturbations are of stellar origin, they rise to *ionized diffuse nebulae*, i.e. regions heated and ionized by ultraviolet photons from the photosphere of young OB star(s), *shells* of photoionized ejected stellar envelopes, i.e. heated and ionized circumstellar material expelled from evolved massive stars, or collisionally ionised by the shock wave *supernova remnants*, i.e. hot regions ionized by the passage of supernovae shock wave heating the gas. Supernova remnants can be either young structures ionized by ultra-violet synchrotron radiation emitted by relativistic compact objects or old structures emitting X-rays from collisionally heated dense regions.
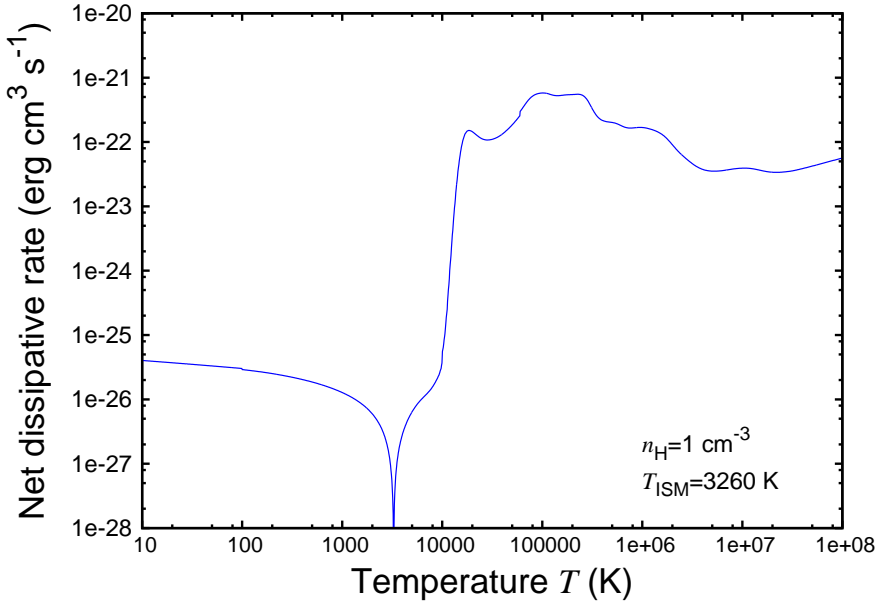
Figure 1.5: An interstellar cooling curve assuming solar metallicity and Galactic ultraviolet photoheating (Wiersma, Schaye & Smith, 2009). The figure shows the absolute value of the sum of the cooling and heating rates. It is presented for an ambient medium total gas number density $n_H = 1.0\,\mathrm{cm}^{-3}$ and its equilibrium temperature is about 3260 K. The curve shows heating for $T \leq 3260\,\mathrm{K}$ and cooling for $T > 3260\,\mathrm{K}$.

These nebulae have emission properties of both their driving stars and their surroundings. They often host inner structures which are governed by the interaction between stellar winds and ambient medium, e.g. wind bubbles which can be observed and interpreted to extract information about the stars and their surroundings properties. The study of these objects consist in understanding the consequences of stellar evolution on the the star's local ambient medium (Garcia-Segura, Mac Low & Langer, 1996; Garcia-Segura, Langer & Mac Low, 1996).

1.4 Models of the circumstellar medium of massive runaway stars

This section reviews previous works on the modelling of the local interstellar medium of massive stars. It particularly focuses on the models of bow shocks generated by massive runaway stars.

1.4.1 The circumstellar medium of massive stars at rest

Stellar wind bubbles

About a quarter of massive stars are found in the field (Gies, 1987) and are surrounded by gas in the warm neutral phase of the ISM. The highly exothermic reactions at work during their main-sequence phase liberate thermonuclear energy previously contained by strong interaction in the core nucleons' binding energy. This allows the stars to sustain their energy losses via electromagnetic radiation, and lose mass through stellar winds (Lamers & Cassinelli, 1999). The stellar wind−ISM interaction gives birth to circumstellar structures called stellar wind bubbles (Weaver et al., 1977). The volume in which the number of ionizing photons emitted by the star is balanced by recombinations in the ISM delimits a region of fully-ionized gas, i.e. a H II region, inside which photoionization compensates recombination.

Its outermost border is the so-called Strömgren sphere of radius,

$$R_{\mathrm{S}} = \left(\frac{3S_{\star}}{4\pi n^2 \alpha_{\mathrm{rr}}^{\mathrm{B}}} \right)^{1/3}, \tag{1.5}$$

where n is the ISM number density, $S_{\star}$ is the flux of ionizing photons and $\alpha_{\mathrm{rr}}^{\mathrm{B}}$ is the recombination rate of H^+ to all energy levels except the ground state.

The supersonic stellar winds collide with the ISM and a contact discontinuity forms. The reverberated and transmitted waves move from this interface and establish the outermost borders of both regions of subsonic shocked wind and ISM gas, i.e. the reverse and forward shocks. The shocked wind is called the hot bubble and has a low density, whereas the shocked ISM is called the shell and is cold and dense. The wind properties are nearly constant during the main-sequence phase of massive stars and, assuming the gas is adiabatic, the time evolution of the bubble radius, $R(t)$, can be analytically approximated as,

$$R(t) = 27 n^{-1/5} \left(\frac{L_{\mathrm{w}}}{10^{36} \ \mathrm{erg \ s^{-1}}} \right)^{1/5} \left(\frac{t}{10^6 \ \mathrm{yr}} \right)^{3/5} \ \mathrm{pc}, \tag{1.6}$$

where t is the time of expansion and where,

$$L_{\mathrm{w}} = \frac{1}{2} \dot{M} v_{\mathrm{w}}^2 \ \mathrm{erg \ s^{-1}}, \tag{1.7}$$

is the wind mechanical luminosity with $\dot{M}$ the stellar mass-loss rate and v_{w} the wind velocity (Weaver et al., 1977).

The temperature difference between the shell and the bubble implies that circumstellar structures surrounding hot stars are subject to heat transfer by electronic thermal conduction (Spitzer, 1962). Radiative cooling induced by the shocks increases the density in the post-shock region at the reverse shock, going along with a subtraction of internal energy from the hot bubble. Consequently, its internal energy locally drops and the continuous input of momentum from the wind triggers oscillations of the reverse shock that propagates in the hot region up to the contact discontinuity and make the whole hot region of perturbed shocked wind. Moreover, the contact discontinuity is intrinsically Rayleigh-Taylor unstable because the light wind material pushes the denser ISM gas. Realistic wind-ISM interaction, including non-ideal processes, is a problem that must be solved numerically (Appendix 6.1.1). If $R(t) < R_{\mathrm{S}}$, the wind bubble develops inside the H II region and only sweeps photoionized material, whereas the circumstellar structures are more complex if the shell is dense enough to trap the radiation field (Weaver et al., 1977; van Marle, 2006). This happens around evolved, hot, e.g. main-sequence and blue supergiant, stars. In this situation $R(t) > R_{\mathrm{S}}$ and cold, neutral, red supergiant gas is shocked by the wind from a more recent mass-loss event, e.g. a Wolf-Rayet phase. A review of the studies devoted to stellar wind bubbles can be found in Freyer, Hensler & Yorke (2003, 2006).

Circumstellar evolution

After the exhaustion of its hydrogen in the core, a massive star of initial mass larger than $8 \, \mathrm{M_\odot}$ evolves through the red supergiant phase. Its mass-loss rate increases by several orders of magnitude and a second shell of slow and dense red supergiant wind expands into the main-sequence wind bubble. When the new-born red supergiant shell reaches the former wind termination shock, a collision occurs inducing mixing in the stellar surroundings.

Some stars of initial mass between 30 and $50 \, \mathrm{M_\odot}$ can become a Wolf-Rayet star. Both their strong

mass loss and fast wind velocity create a third shell which collides with the red supergiant shell (see in van Marle, Langer & García-Segura, 2005, 2007). The shells fragment because of hydrodynamical instabilities (Vishniac, 1994) and tear apart into the ISM (top left-hand panel[7] of Fig. 1.6). The circumstellar medium of an initially $35\,M_\odot$ star is detailed up to the pre-supernova phase for a time sequence evolution starting with a main-sequence O star which evolves to the red supergiant phase before to become a Wolf-Rayet star in Garcia-Segura, Langer & Mac Low (1996). Similarly, the circumstellar medium of an initially $60\,M_\odot$ star undergoing a red supergiant and a luminous blue variable phase is investigated in Garcia-Segura, Langer & Mac Low (1996) to understand the surroundings of η Carina. The combined effects of heating and cooling by optically-thin radiative processes, thermal conduction and photoionization on the formation and evolution of wind bubbles are explored in Freyer, Hensler & Yorke (2003, 2006). These works dwell upon the emission signature of the bubbles, e.g. X-rays, and provide the state-of-the-art two-dimensional description of wind bubbles generated by massive stars. The formation of rings around fast-rotating massive stars undergoing a blue loop is shown in Chita et al. (2008) and Chita (2011). This naturally explains the mid-latitude rings observed around the supernova remnant SN1987A (bottom right panel of Fig. 1.6).

1.4.2 The circumstellar medium of runaway massive stars

Stellar wind bow shocks

The supersonic motion of a star with strong winds with respect to the local ISM distorts its wind bubble into an arc of shocked wind and swept-up circumstellar material called a bow-shock. This process is common in nature and happens as soon as a body has a supersonic motion with respect to its surroundings (it is the three-dimensional, supersonic equivalent of surface waves that develop in the case of a body in subsonic motion on a surface, see Fig. 1.7). It concerns both small scales, e.g. microfluidic experiments, and large scales, e.g. bow shocks around galaxies (Markevitch et al., 2002). A nearby example is the bow shock produced by our Sun through the local ISM (Suess, 1990). Stellar winds can generate bow shocks around planetary obstacles. These structures on a scale of about a fraction of an astronomical unit[8] have been detected around most of the planets of the Solar system. They provide an insight into the physics of collisionless shocks (Russell, 1985). Similarly, the scientific literature is rich with studies of exoplanetary bow shocks (Vidotto, Jardine & Helling, 2011).

Spectacular astrophysical examples of bow shocks include the high-mass x-ray binary VELA-X1 (see Kaper et al., 1997, panel (c) of Fig. 1.6), the O star α Cam (panel (d) of Fig. 1.6) and ζ Oph (Gull & Sofia, 1979, panel (e) of Fig. 1.6). Very high velocity runaway stars, accelerated when they cross the Galactic center, are called "stellar interlopers" and exhibit bullet-nosed bow shock trails (Sahai et al., 2009, panel (f) of Fig. 1.6).

About 4 to 10 per cent of all massive runaway stars have a detected bow shock (Blaauw, 1993; Huthoff & Kaper, 2002). The bow shocks are detected in several wavebands such as X-rays (see in López-Santiago et al., 2012), ultraviolet in the case of Betelgeuse (Le Bertre et al., 2012), and optical, e.g. [OIII] line emission (Gull & Sofia, 1979). The first infrared detections of stellar wind bow shocks is in van Buren & McCray (1988) and the most recent in Jorissen et al. (2011). The Extensive stellar BOw Shock Survey (E-BOSS, Peri et al., 2012) compiles historical with original infrared data into a catalogue of bow shocks. Benaglia et al. (2010) records non-thermal emission from the bow shocks of massive runaway stars using GHz data from the Very Large Array.

---

[7] I am grateful to Bill Snyder, Pittsburgh, United States of America. His observations are available at http://billsnyderastrophotography.com/

[8] 1 astronomical unit = 1 AU $\approx 1.5 \times 10^{13}$ cm
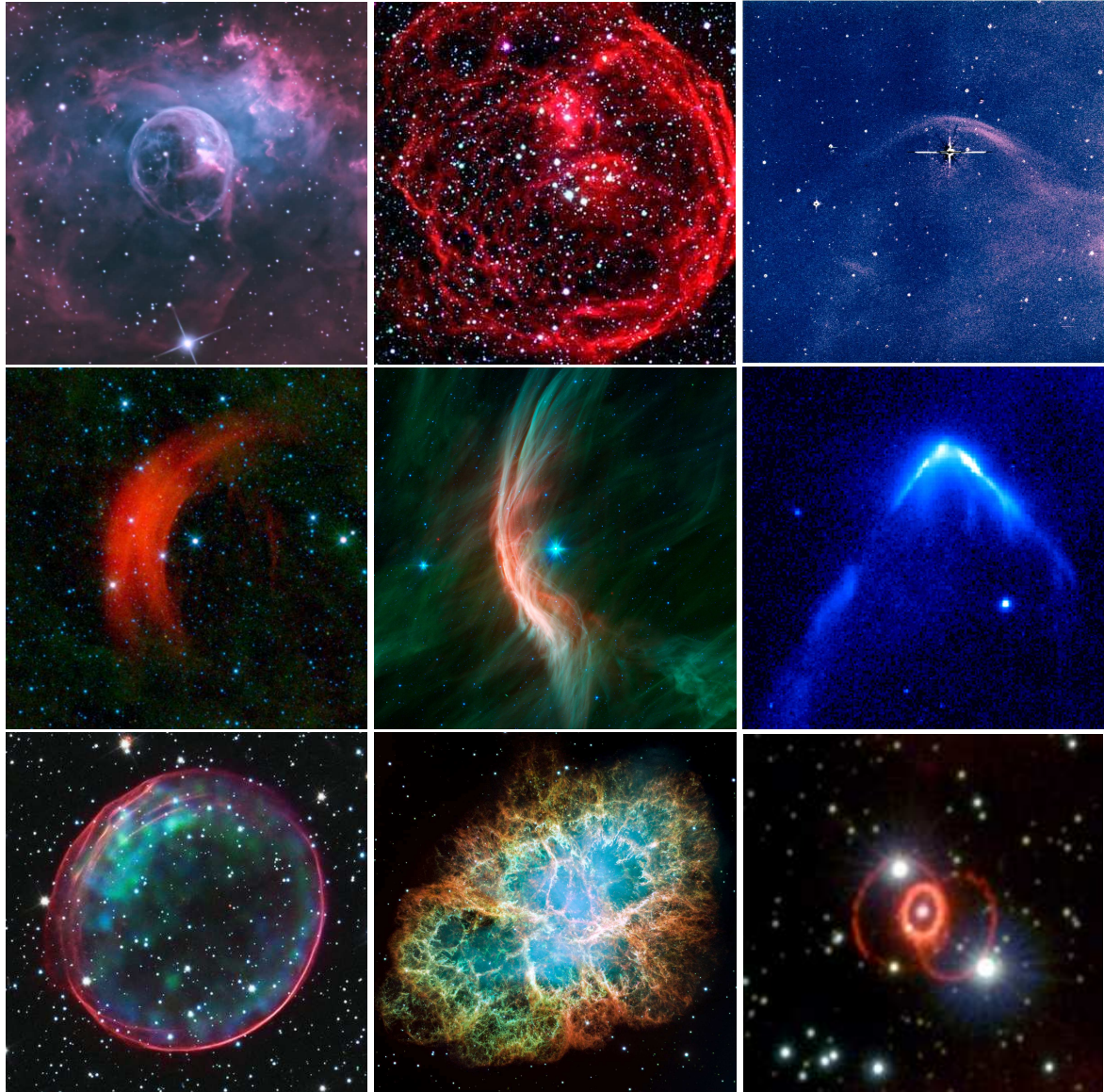
Figure 1.6: Examples of circumstellar nebulae. Top panels: HII region NGC7635 generated by the O star BD+602522 (left), superbubble blown by winds from hot massive stars and supernovae ejecta in the star cluster Henize 70 (middle), bow shock of the runaway binary system VELA-X1 composed of a neutron star and a blue supergiant star (right). Middle panels: bow shock around the O-type star α Camelopardalis (left), bow shock of the Earth's closest massive runaway star ζ Oph (middle), bow shock of a "stellar interloper" moving at very high velocity of about $1000\,\mathrm{km\,s^{-1}}$ through a hot medium (right). Bottom panels: supernova remnant SNR 0509-67.5 in the Large Magellanic Cloud (left), Crab Nebula supernova remnant around a neutron star (middle), ring structured supernova remnant SN1987A (right). Credits (from top to bottom and from left to right): Hα image, courtesy to Bill Snyders. FORS Team, 8.2-meter VLT, ESO. Danish Telescope/ESO. NASA/JPL-Caltech/WISE Team. NASA/JPL-Caltech/WISE Team. R. Sahai, NASA's Jet Propulsion Laboratory. NASA, ESA, and Hubble Heritage Team STScI/AURA. NASA, ESA, J. Hester and A. Loll, Arizona State University. Christopher Burrows, ESA/STScI and NASA.

Figure 1.7: Examples of surface bow waves. Top panel: uncatalogued swans in motion with respect to the surface of a lake. Bottom panel: the chemical carrier ship Xanthia (Norway) sailing with respect to the sea. These bodies move thanks to the work developed by their muscles/motors and this is transferred to their ambient medium through their feet/propeller, respectively. They do not lose momentum expelling material as the strong winds of massive runaway stars. The reverse shock of their circumplumage/circumhull medium roughly coincides with the swan's chest/ship's prow, respectively. The right-hand swan in the upper panel moves behind the left-hand wake-generating swan and therefore sails through a turbulent medium.

Bow shock detections mostly concern runaway hot stars, i.e. main sequence and blue supergiant stars (van Buren, Noriega-Crespo & Dgani, 1995; Peri et al., 2012). Some cool, post-main-sequence stars have nevertheless been classified as runaway. They are either red supergiants, e.g. the evolved massive stars Betelgeuse (Noriega-Crespo et al., 1997; Decin et al., 2012), μ Cep (Cox et al., 2012a) and IRC−10414 (Gvaramadze et al., 2014), or AGB stars (Cox et al., 2012a).

Bow shocks have been utilised to find new runaway stars (Gvaramadze, Kroupa, & Pflamm-Altenburg, 2010a) and to identify the stellar cluster from which they have been ejected, e.g. from the stellar cluster NGC6611 (Gvaramadze & Bomans, 2008). They noted several tens of bow shocks produced by OB stars running away from the cluster which support the hypothesis that young cluster can lose a significant fraction of their massive stars by ejection. A numerical study (Gvaramadze, Gualandris & Portegies Zwart, 2009) investigates the production of ejected massive stars during three-body encounters between a massive star and a hard massive binary. Bow shocks can constrain the properties of their central stars, e.g. to estimate ζ Oph's mass-loss rate (Gull & Sofia, 1979; Gvaramadze, Langer, & Mackey, 2012). Finally, bow shocks can be used to estimate the local ISM density of their driving star (Kaper et al., 1997; Gvaramadze et al., 2014).

Bow shocks generated by evolving stars

The general organisation of a bow shock is sketched in Fig.1 of Comerón & Kaper (1998), however the layers of shocked ISM can show turbulent patterns that are a function of the wind power and ISM properties. The contact discontinuity locates the balance between the wind and of the ISM pressures,

$$\rho_{\mathrm{w}} v_{\mathrm{w}}^2 = \rho_{\mathrm{ISM}} v_{\star}^2, \tag{1.8}$$

where ρ_{w}, v_{w}, $\rho_{\star}$ and $v_{\star}$ are the wind and ISM densities and velocities, respectively. The distance between the star and the contact discontinuity is called the stand-off distance $R(0)$ of the bow shock (see in Baranov, Krasnobaev & Kulikovskii, 1971; Wilkin, 1996),

$$R(0) = \sqrt{\frac{\dot{M} v_{\mathrm{w}}}{4\pi \rho_{\mathrm{ISM}} v_{\star}^2}}, \tag{1.9}$$

where $\dot{M}$ is the mass-loss rate of the runaway star and ρ_{ISM} its ambient medium density. An analytical approximation of the shape of an isothermal and infinitely thin bow shock is given in Wilkin (1996), and reads,

$$\frac{R(\theta)}{R(0)} = \mathrm{cosec}(\theta) \sqrt{3(1 - \theta)\mathrm{cotan}(\theta)}, \tag{1.10}$$

where $R(0)$ is the distance between the star and the bow shock at an angle of θ with respect to the direction of motion of the star. A general stability criterion against non-linear instabilities for stellar wind bow shocks shows that the stability depends on the respective values of the space velocity $v_{\star}$ and wind velocity v_{w} of the star. It is rather stable if $v_{\star}/v_{\mathrm{w}} < 1$, e.g. around a main-sequence or a blue supergiant star, and unstable if $v_{\star}/v_{\mathrm{w}} > 1$, e.g. around a red supergiant or an AGB star (see Dgani, van Buren & Noriega-Crespo, 1996a,b).

Models of the circumstellar medium of hot runaway stars were first presented in Comerón & Kaper (1998). They compare realistic wind-ISM interactions with (semi-)analytical models and conclude that the Wilkin thin-shell approximation has only partial validity. This work describes the variety of shapes which could be produced in bow shocks of OB stars and details how the action of the wind on the ISM, together with cooling in the shocked gas, shapes the circumstellar medium, determines the relative
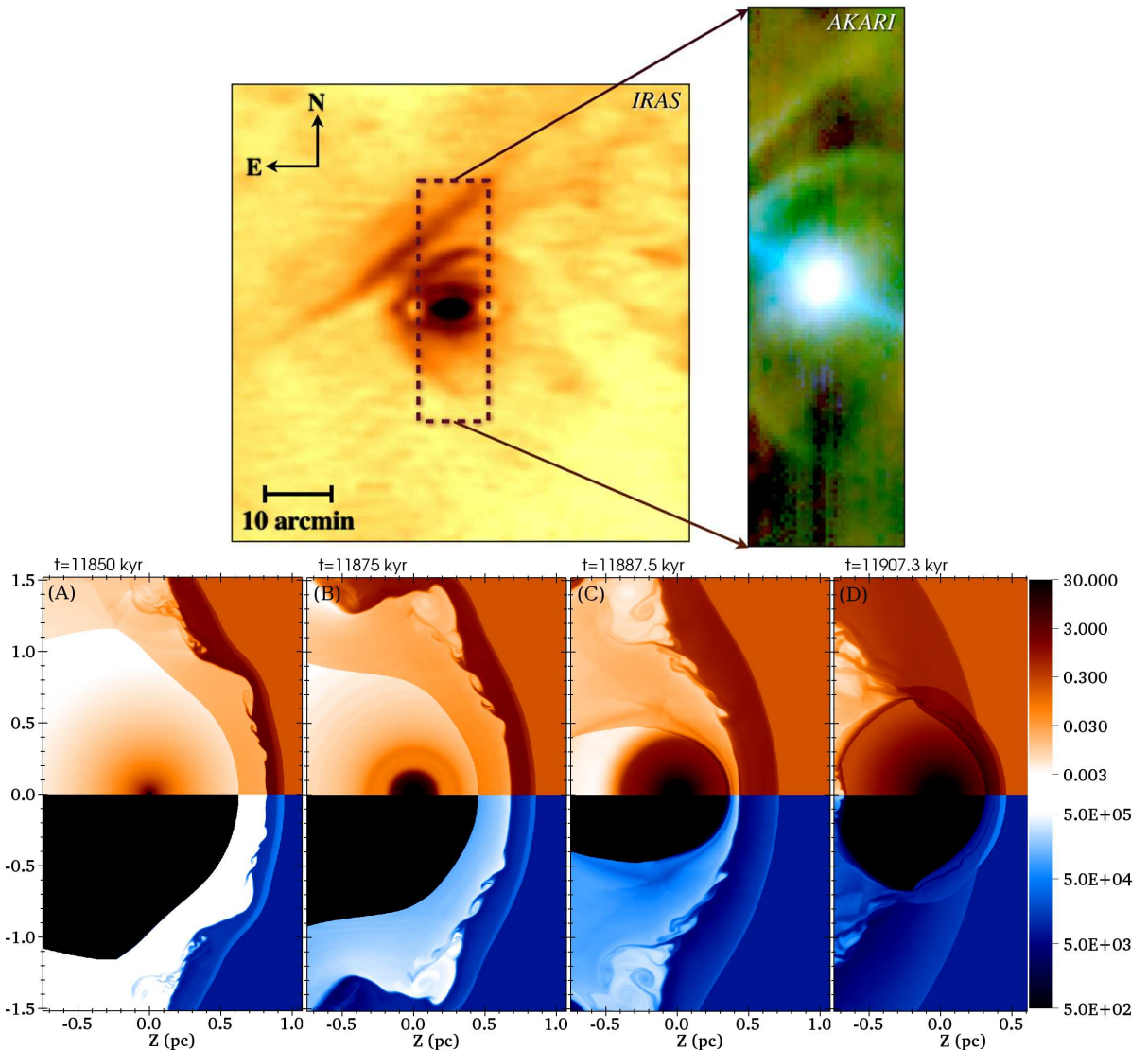
Figure 1.8: Infrared image of the bar-like feature surrounding the bow shock of the runaway red-supergiant star Betelgeuse. Upper panels; left: image extracted from IRAS archiv of Cao et al. (1997); right: composite colour image using AKARI data from Ueta et al. (2008). Lower panel; "double bow shock" model of Betelgeuse's bar (Mackey et al., 2012). The production of the bar-like circumstellar structure is explained by the collision between the former blue supergiant and the new-born red supergiant bow shocks happening when the star undergoes a blue loop. Credits: Mohamed, Mackey & Langer (2012). AKARI/MLHES team.
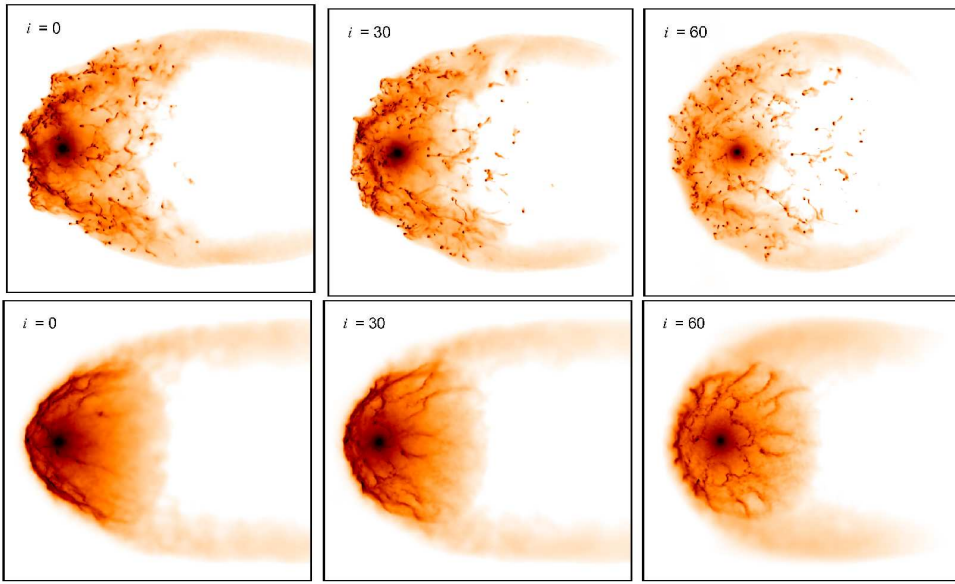
Figure 1.9: Density fields on a logarithmic scale in three-dimensional Lagrangian models of the bow shock generated by the red supergiant Betelgeuse (Mohamed, Mackey & Langer, 2012). Top and bottom panels show two model moving with velocity 32 and $72\,\mathrm{km\,s^{-1}}$, respectively. They are viewed at 0° (left), 30° (middle) and 60° inclination (right panels). This study concludes that the surprisingly smoothed and circular shape of the bow shock around Betelgeuse is an indication of its youngness, i.e. the bow shock produced during the last mass-loss event is not fully developed and has not yet reached a steady state.

thicknesses of the layers composing a bow shock, and determines its (in)stability. It shows the importance of heat conduction (Spitzer, 1962; Cowie & McKee, 1977) to the size of these bow shocks, and underlines that a rapid cooling can distort them. The shocked regions are thick if the shock is weak, but they cool rapidly and become denser and thinner in the regime involving either large space velocities or strong winds and/or high ambient medium densities. This leads to distorting instabilities such as the transverse acceleration instability (Blondin & Koerwer, 1998) and the non-linear thin shell instability (Dgani, van Buren & Noriega-Crespo, 1996a,b). Bow shocks around main sequence stars have been modelled in dense molecular clouds by Mac Low et al. (1991) and Arthur & Hoare (2006).

Hydrodynamical bow shock models of red supergiant are available in Brighenti & D'Ercole (1995a), Mohamed, Mackey & Langer (2012) and Decin et al. (2012). When a bow shock around a red supergiant star forms, the new-born shell swept up by the cool wind follows the former bow shock from the main sequence. A collision between the old and new shells of different densities precedes the creation of a second bow shock (Fig. 1.8 and Mackey et al., 2012). The typical structure of a bow shock around a runaway red supergiant has been detailed in Mohamed, Mackey & Langer (2012, see Fig. 1.9[9]). Bow shocks around cool stars develop Rayleigh-Taylor and Kelvin-Helmholtz instabilities, so the measure of their stand-off distance is more difficult (Decin et al., 2012). The dynamics of ISM dust grains penetrating into the bow shocks of red supergiant stars is numerically investigated in van Marle et al. (2011a), see Fig. 1.10[10]. The effect of the space velocity and of the ISM density on the morphology of Betelgeuse's bow shock is explored in Mohamed, Mackey & Langer (2012), however this study considers a single mass-loss rate and does not allow us to appreciate how the wind properties modify the bow shock shape or luminosity. In addition, van Marle, Decin & Meliani (2014) provides the first attempt to model

---

[9] Used with kind permission of Dr. S. Mohamed.
[10] Used with kind permission of Dr. A.-J. van Marle.
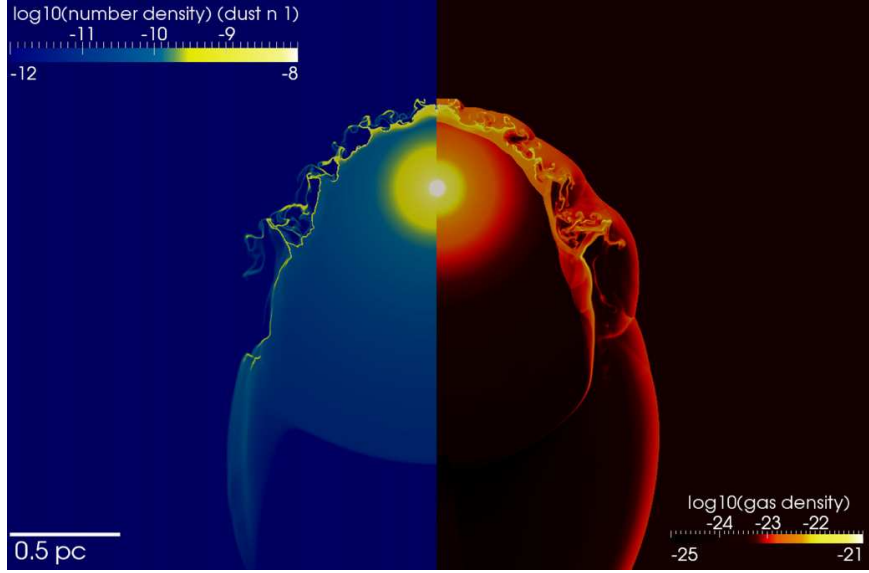
Figure 1.10: Bow shock model generated by a runaway red supergiant (van Marle et al., 2011a). The stellar wind and ISM properties are tailored to the runaway star Betelgeuse. This model is part of a series of simulations investigating the distribution and dynamics of dust grains in the bow shock generated by runaway cool stars. The model assumes that small dust grains of radius $0.005\,\mu$m accumulate at the contact discontinuity and follow the local Rayleigh-Taylor instabilities generated by the wind/ISM density difference. Left-hand panel is the dust number density and right-hand panel is the gas number density.

the effects of an ISM magnetic field on the stability of Betelgeuse's bow shock.

1.4.3 The circumstellar medium of exploding massive stars

Supernova blastwaves

When massive stars end their lives as supernovae, their surroundings are swept up by dense and fast ejecta. The description of the ejecta-ISM interaction is similar to the formalism used to describe wind bubbles. A contact discontinuity forms at the border between ejecta and ISM gas and its forward shock, i.e. the shock wave, and a reverse shock are created. A shell of mixed ejecta and circumstellar material forms and hits the ISM so the shock wave decelerates and emits light. Analytical solutions of the propagation of shock waves from supernovae exploding in a constant density medium and their associated lightcurves are provided in Woltjer (1972) and summed up in van Veelen (2010). The interaction is in four main phases:

1. *The ejecta dominated phase*, or free expansion phase that happens when the supernova front goes through the ISM. The shock wave expands at constant velocity, and is governed by the initial properties of the explosion. The circumstellar material beyond the shock wave is not relevant compared to the gas in the ejecta. This mechanism produces the early lightcurves of the supernova.

2. *The Sedov-Taylor phase*, or adiabatic expansion, begins when the mass of shocked ISM gas is larger than the amount of the ejecta. Up to the end of this phase the shocks decelerate by because of adiabatic cooling of the gas. The luminosity produced by the shocks is small compared to the explosion energy and so the radiative losses are negligible.
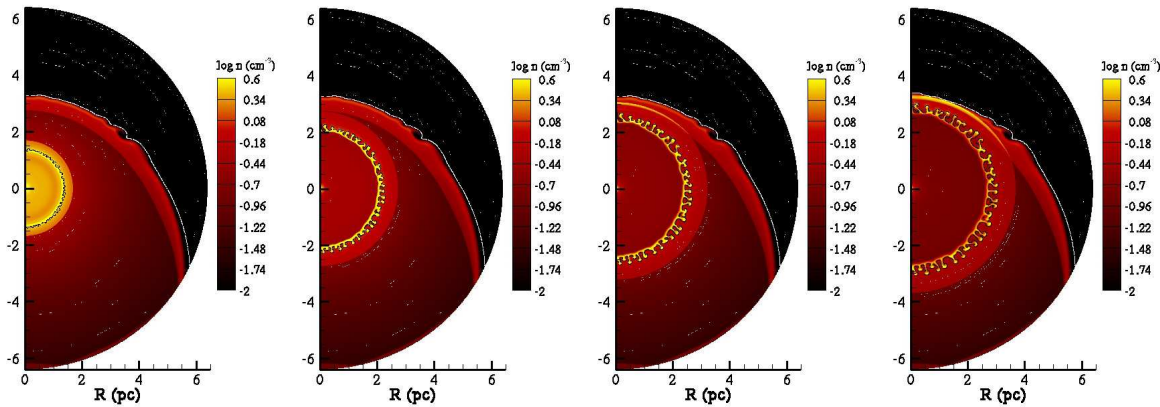
Figure 1.11: Number density in hydrodynamical model of Kepler's supernova remnant showed on a logarithmic scale (Chiotellis, Schure & Vink, 2012). The model explores whether the asymmetries observed in this remnant can be generated by the collision between the supernova shock wave and the bow shock generated by its progenitor.

3. *The radiative or pressure driven snow-plough phase* starts when the forward shock becomes radiative. The dynamics of the shocked circumstellar material are governed by the pressure of the expanding ejecta which decelerate. Radiative cooling from the shocked circumstellar gas in the post-shock region at the forward shock dominates the emission.

4. *The momentum driven snow-plough phase* begins when radiative cooling has converted the blastwave internal energy to radiation and the expansion of the remnant is ruled by the conservation of momentum. The interior of the supernova cools and loses internal pressure. This phase, also called dissipation, ends when the shock front velocity falls under the sound speed of the ISM, and the supernova remnants is no more distinguishable from the ISM.

This idealized picture assumes a constant and homogeneous medium, which is far from being a good approximation for massive stars whose winds strongly shape their surroundings. The interaction between supernovae and circumstellar structures can not be exactly treated with analytical methods and requires multi-dimensional hydrodynamics simulations. Moreover, the complexity of the processes at work in such events, e.g. thermal conduction, magneto-hydrodynamics effects and cooling by acceleration of cosmic rays, makes the corresponding numerical models computationally demanding.

Supernova remnants

The stars which explode as luminous supernovae release ejecta interacting with their pre-shaped environment (Borkowski, Blondin & Sarazin, 1992; Vink, Kaastra & Bleeker, 1996; van Veelen et al., 2009). After the supernova explosion, the forward shock of the blastwave interacts with the free-streaming stellar wind (Chevalier & Liang, 1989; Chevalier, 1982) and later on, when the blastwave ploughs through the unperturbed interstellar medium and replenishes it with momentum and kinetic energy, a supernova remnant is created and expands up to distances of about a hundred parsecs (Badenes, Maoz & Draine, 2010).

Surveys provide us with observations of Galactic supernova remnants, e.g. in X-ray (Pannuti et al., 2014), at Hα emission (James & Anderson, 2006) the infrared (Reach et al., 2006; Seok, Koo & Onaka, 2013), in gamma-rays (Abdo, Ackermann & Ajello, 2010), or the radio (Manchester, 1987) waveband.

Catalogues of remnants visible in the radio waveband in the northern and southern hemisphere are available in Kothes et al. (2006) and Whiteoak & Green (1996), respectively. These structures are observed, e.g. in the Galactic plane (middle bottom panel Fig. 1.6) and are listed in the exhaustive Cambridge catalogue of Galactic supernova remnants (Green, 2009) which reveals a rich diversity of shapes, e.g. shells, cylinders, rings and bipolar structures (see also Manchester, 1987; Gaensler, 1999).

The shape of supernova remnants is a function of both the geometry of the supernova explosion and of the local ISM distribution (Vink, 2012). They have a wide range of shapes that can be used to constrain their progenitors and/or ambient medium properties. The distribution of circumstellar matter depends on the progenitor properties (Bedogni & D'Ercole, 1988; Ciotti & D'Ercole, 1989; Dwarkadas, 2005, 2007) and the presence of ISM structures. Models of remnants developing in a pre-existing wind cavity are shown in Tenorio-Tagle et al. (1990, 1991), and demonstrate that mixing of material happens in the former wind bubble. Multi-dimensional models of the formation of knots by wind-wind collision in the surroundings Cassiopeia A are shown in Pérez-Rendón, García-Segura & Langer (2009) and the effects of this fragmented Wolf-Rayet shell on the rebrightening of young remnants is explored in van Veelen et al. (2009). Supernova remnants developing through an edge of a molecular cloud, give rise to champagne flows such as the one observed in the Cygnus loop nebula (see Tenorio-Tagle, Rozyczka & Yorke, 1985). On the other hand, if the supernova happens near a denser region, the reverse shock is reflected towards the center of the explosion and a hot region of shocked material forms (Ferreira & de Jager, 2008).

The bow shocks produced by moving massive stars provide a natural explanation for the generation of anisotropic circumstellar nebulae. Indeed, at a time of the order of about $10-100\,\mathrm{yr}$ after the explosion, the shock wave collides with the bow shock along the direction of motion of its progenitor, whereas it expands in a cavity of wind material in the opposite direction (Borkowski, Blondin & Sarazin, 1992). Rozyczka et al. (1993) model supernovae in oval bubbles generated by moving progenitors and show that elongated jet-like structures of size of about 10 pc arise when the shock wave expands into the cavity. One of the most famous and well-studied example is Kepler's remnant (Borkowski, Blondin & Sarazin, 1992; Velázquez et al., 2006; Chiotellis, Schure & Vink, 2012, Fig. 1.11[11]). Note that a model interpreting the cool jet-like [OIII] feature found in the Crab nebula (Blandford et al., 1983) as a shock wave channelled into the trail produced by its progenitor's motion is presented in Cox, Gull & Green (1991). A strong magnetization of the ISM can induce a collimation of the supernova ejecta engendering elongated remnants (Rozyczka & Tenorio-Tagle, 1995).

Interestingly, Brighenti & D'Ercole (1994) show that if a runaway progenitor evolves beyond the main-sequence phase, the supernova explosion happens out of the main-sequence wind bubble, and the subsequent remnant develops as an outflow upstream from the direction of motion of the progenitor. In this thesis, we will follow their approach, combining the techniques of bow shocks and core-collapse supernovae modelling (Fig. 1.12) to investigate the shape of old supernova remnants generated by runaway stars (see section 1.5 and chapter 4).

1.5 Method

In this thesis we adopt the approach of Garcia-Segura & Mac Low (1995a,b) in the spirit of the doctoral projects of van Marle (2006), van Veelen (2010) and Chita (2011). We run all the models presented in our thesis are 2D, cylindrically symmetric and produced using the grid code PLUTO (Mignone et al., 2007, 2012). The stellar wind is imposed onto a circle centered on the origin of the grid. The rest of the domain is filled with ISM gas with constant density and temperature. The evolution of the

---

[11] Used with kind permission of Dr. A. Chiotellis.
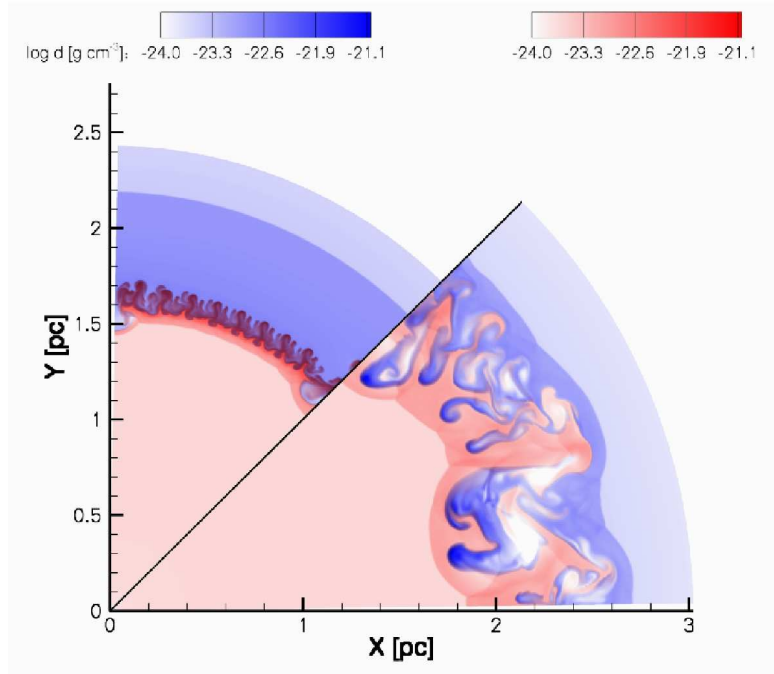
Figure 1.12: Hydrodynamical model of the supernova remnant of Cassiopeia A (van Veelen et al., 2009). This study investigates the formation of knots and foculi in this supernova remnant by the collision of the shock wave with the circumstellar medium that was pre-shaped by a massive star evolving up to the Wolf-Rayet phase. The supernova ejecta are in red and the circumstellar material in blue.

circumstellar medium is modelled in a co-moving frame of reference and centered on the runaway star (Brighenti & D'Ercole, 1995b,a; Comerón & Kaper, 1998). Because strong shocks around hot stars induce large temperature jumps ($\Delta T > 10^5$ K) the consideration of thermal conduction together with cooling by optically-thin gas radiation and photoheating is mandatory to properly model these objects.

1.5.1 Hydrodynamics

The code PLUTO is a parallelized, three-dimensional, MHD Eulerian code build for astrophysical purposes[12]. It offers modules for the explicit consideration of losses by optically-thin radiative cooling and for the treatment of thermal conduction. It integrates the hydrodynamical and MHD equations in the non-relativistic, relativistic regimes. In an inviscid, non-relativistic and non-magnetized fluid, the governing equations which describe the temporal evolution of the gas density ρ, velocity $\vec{v}$ and pressure p are the Euler equations. They consist of the continuity equation,

$$\frac{\partial \rho}{\partial t} + \vec{v} \cdot \vec{\nabla} \rho + \rho \vec{\nabla} \cdot \vec{v} = 0, \tag{1.11}$$

the momentum conservation equation,

$$\frac{\partial \vec{v}}{\partial t} + \vec{v} \cdot \vec{\nabla} \vec{v} + \frac{\vec{\nabla} p}{\rho} = \vec{0}, \tag{1.12}$$

---

[12] Available at http://plutocode.ph.unito.it/

and the energy equation,

$$\frac{\partial p}{\partial t} + \vec{v} \cdot \vec{\nabla} p + \rho c_s^2 \vec{\nabla} \cdot \vec{v} = \Sigma(T, \rho), \tag{1.13}$$

where the right-hand side of Eq. (1.13) is,

$$\Sigma(T, \rho) = (\gamma - 1) \left(\Phi(T, \rho) + \vec{\nabla} \cdot \vec{F_c} \right). \tag{1.14}$$

Note that the code PLUTO integrates the conservative form of Eq. 1.11−1.13, in which the pressure is replaced by a variable corresponding to the internal energy $\epsilon = p/(\gamma - 1)$ of the gas. Eq. 1.14 represents the terms corresponding to the losses Φ of internal energy by radiative cooling and the heat flux F_c (Section 1.5.2). We build the cooling function Φ such that,

$$\Phi(T, \rho) = n\Gamma(T) - n^2 \Lambda(T), \tag{1.15}$$

where Γ is the heating rate and Λ the cooling rate of the gas, respectively, and where n is the total number density of the gas. The gas temperature is given by,

$$T = \mu \frac{m_H}{k_B} \frac{p}{\rho}, \tag{1.16}$$

where k_B is the Boltzmann constant, m_H the proton mass and $\mu = \rho/(m_H n)$ the mean molecular weight of the gas. The sound speed of the an ideal gas is given by,

$$c_s = \sqrt{\frac{\partial p}{\partial \rho}} = \sqrt{\gamma \frac{p}{\rho}}, \tag{1.17}$$

with γ the ratio of calorific capacities closes the system of partial differential equations (1.11)−(1.13). The total energy of the gas is the sum of its thermal and kinetic energy components and

$$E = \frac{p}{(\gamma - 1)} + \frac{v^2}{2}, \tag{1.18}$$

is its specific form. Further details about our numerical methods are given in Section 2.

1.5.2 Heat conduction

Isotropic heat conduction (Cowie & McKee, 1977) is taken into account as the right-hand divergence term of Eq. (1.14). The heat flux vector is given by,

$$\vec{F_c} = \kappa \vec{\nabla} T, \tag{1.19}$$

which is oriented from the hottest to the coldest region and where the heat conduction coefficient,

$$\kappa = K T^{5/2}, \tag{1.20}$$

gives the rate of change of internal energy per unit time, volume, temperature and mass. The ratio $\kappa/T^{5/2}$ is,

$$K = \frac{1.84 \times 10^{-5}}{\ln(\Lambda)} \text{ erg s}^{-1} \text{ K}^{-1} \text{ cm}^{-1}, \tag{1.21}$$

where,

$$\ln(\Lambda) = 29.7 + \ln\left(\frac{T}{10^6 \sqrt{n}}\right), \qquad (1.22)$$

is the Coulomb logarithm (Spitzer, 1962). Details of the numerical treatment of heat conduction and the effects of thermal conduction on the circumstellar medium of hot stars are given in Chapter 2.

We model the supernova phase based on Whalen et al. (2008). The early supernova ejecta-bow-shock interaction requires both high temporal and spatial resolution. Because the associated 2D instabilities arising from the ejecta-wind interaction are not governing the ejecta-circumstellar shell interaction (van Veelen et al., 2009), we calculate this phase using a one-dimensional spherical coordinates system and map it into the 2D domain, shortly before the shell of swept-up ejecta reaches the reverse shock of the bow shock of the progenitor (our section 4).

1.6 Thesis content

The bow shock nebulae and supernova remnants resulting from the interaction between the strong winds of massive runaway stars and their surroundings are a unique window to probe the stellar and the local medium properties. The principal questions which motivate this thesis work are listed below.

1. What are the combined roles of the mass loss and space velocity on the luminosities and surface brightnesses of the bow shocks of evolving Galactic massive runaway star? Can we use synthetic observables from numerical simulations of stellar wind bow shocks as a tool to constrain the physical properties of massive runaway stars?

2. What is the influence of an external photon field on the circumstellar medium of a cool runaway star? What can we learn about the ISM properties of such a star?

3. How far can the pre-shaped circumstellar medium of massive runaway stars influence the morphology of their supernova remnants? Which runaway stars generate supernova remnants that strongly deviate from sphericity? What are the properties of these aspherical remnants?

The layout of this thesis is as follows:

Chapter 2. Models of the circumstellar medium of Galactic, evolving, runaway massive stars.

At least 5 per cent of massive stars are both moving supersonically through the interstellar medium (ISM) and are expected to have a stellar wind bow shock. Observations of their bow shocks can constrain stellar, circumstellar and ISM properties. We explore how the mass-loss and space velocity of runaway massive stars of several initial masses affect the morphology of their bow shocks. We run a grid of two-dimensional hydrodynamical simulations following the evolution of the circumstellar medium of these stars from the main sequence to the red supergiant phase. We consider an interstellar medium which has physical properties similar to that of the Galactic plane. We find that thermal conduction is an important process affecting the shape, structure and luminosity of the bow shocks around main sequence stars. Bow shocks around hot stars have an optical luminosity mainly from forbidden lines, e.g. [O III], which is larger than their Hα emission. The Hα emission of the bow shocks around hot stars originate from their contact discontinuity. The Hα emission of bow shocks around cool stars originates from their forward shock, and is very faint. The maximum Hα emission is generally upstream from the star in the supersonic regime and it is extended downstream from the star in the hypersonic regime. The

emission of optically-thin radiation mainly comes from the shocked ISM material. All bow shock models are brighter in the infrared, i.e. the infrared is the most appropriate waveband to search for bow shocks. Our study suggests that the infrared emission comes from the outermost layer of shocked ISM for bow shocks of hot stars and from the inner region of shocked wind for bow shocks around cool stars. Our bow shock luminosities of main sequence stars are governed by the wind momentum and exhibit a scaling behaviour with their volume. We predict that, in the Galactic plane, the brightest infrared bow shocks, i.e. the most easily detectable of them, are produced by high mass stars moving with small space velocities.

Chapter 3. On the stability of bow shocks around runaway red supergiant stars.

In this chapter, we explore the hypothesis that the smooth appearance of bow shocks around some red supergiants might be caused by the ionization of their winds by external sources of radiation. Our numerical simulations of the bow shock generated by $IRC -10414$ (the first-ever red supergiant with an optically detected bow shock) show that the ionization of the wind results in its acceleration by a factor of two, which reduces the difference between the wind and space velocities of the star and makes the contact discontinuity of the bow shock stable for a range of stellar space velocities and mass-loss rates. Our best fit model reproduces the overall shape and surface brightness of the observed bow shock and shows that the bow shock emission comes mainly from the shocked stellar wind. This naturally explains the enhanced nitrogen abundance in the line-emitting material, derived from the spectroscopy of the bow shock. We found that photoionized bow shocks are $\approx 10-100$ times brighter in optical line emission than their neutral counterparts, from which we conclude that the bow shock of $IRC -10414$ must be photoionized.

Chapter 4. Asymmetric supernova remnants from Galactic massive runaway stars.

After the death of a runaway massive star, its supernova shock wave interacts with the bow shocks produced by its defunct progenitor, and may lose its spherical symmetry before expanding into the local interstellar medium (ISM). We investigate whether the initial mass and space velocity of these progenitors can be associated with asymmetric supernova remnants. We run hydrodynamical models of supernovae exploding in the pre-shaped surroundings of moving Galactic core-collapse progenitors. We find that bow shocks that accumulate more than about $1.5\,M_\odot$ generate asymmetric remnants. The shock wave collides with these bow shocks before expanding freely into the ISM whereas it is channelled into the region of undisturbed wind material moving in the opposite direction. This applies to an initially $20\,M_\odot$ progenitor moving with velocity $20\,km\,s^{-1}$ and to our initially $40\,M_\odot$ progenitor. These remnants generate mixing of ISM gas, stellar wind and supernova ejecta that is particularly important upstream from the center of the explosion. Their lightcurves are dominated by emission from optically-thin cooling and by X-ray emission of the shocked ISM gas. We find that these remnants are most easily observed in the [OIII] spectral line emission or in the soft energy-band of X-ray that originate from the post-shock region at the shock wave. Finally, we discuss our results in the context of observed Galactic supernova remnants.

1.7 Concluding remark

Circumstellar medium modelling of runaway massive stars is far from being a completed field of research. The models presented here could be extended in the near future, e.g. to explore the effects of a non-aligned ISM background magnetic field on the structure of the bow shocks. This would require a three-dimensional approach. One could also perform simulations using adaptive mesh refinement (AMR) methods (van Marle & Keppens, 2010) coupled to a cooling network which self-consistently calculates the electron fraction (Smith & Rosen, 2003) in order to predict emission and absorption line ratios and build synthesis spectra. This would greatly help us to compare models with observations and to converge on a better understanding of the mechanisms responsible for circumstellar evolution and feedback from massive stars.

Models of the circumstellar medium of evolving, massive Galatic runaway stars

This chaper is published as a paper in Monthly Notices of the Royal Astronomical Society (Meyer et al., 2014b).

2.1 Introduction

Massive stars have strong winds and evolve through distinct stellar evolutionary phases which shape their surroundings. Releasing material and radiation, they give rise to ISM structures whose geometries strongly depend on the properties of their driving star, e.g. rotation (Langer, García-Segura & Mac Low, 1999; van Marle et al., 2008; Chita et al., 2008), motion (Brighenti & D'Ercole, 1995a,b), internal pulsation (see chapter 5 in van Veelen, 2010), duplicity (Stevens, Blondin & Pollock, 1992) or stellar evolution (e.g. the Napoleon's hat generated by the progenitor of the supernova SN1987A and overhanging its remnant, see Wang, Dyson & Kahn, 1993). At the end of their lives, most massive stars explode as a supernova or generate a gamma-ray burst event (Woosley, Heger & Weaver, 2002) and their ejecta interact with their circumstellar medium (Borkowski, Blondin & Sarazin, 1992; van Veelen et al., 2009; Chiotellis, Schure & Vink, 2012). Additionally, massive stars are important engines for chemically enriching the interstellar medium (ISM) of galaxies, e.g. via their metal-rich winds and supernova ejecta, and returning kinetic energy and momentum to the ISM (Vink, 2006).

Between 10 and 25 per cent of the O stars are runaway stars (Gies, 1987; Blaauw, 1993) and about 40 per cent of these, i.e. about between 4 and 10 per cent of all O stars (see Huthoff & Kaper, 2002), have identified bow shocks. The bow shocks can be detected at X-ray (López-Santiago et al., 2012), ultraviolet (Le Bertre et al., 2012), optical (Gull & Sofia, 1979), infrared (van Buren & McCray, 1988) and radio (Benaglia et al., 2010) wavelengths. The bow-shock-producing stars are mainly on the main sequence or blue supergiants (van Buren, Noriega-Crespo & Dgani, 1995; Peri et al., 2012). There are also known bow shocks around red supergiants, Betelgeuse (Noriega-Crespo et al., 1997; Decin et al., 2012), μ Cep (Cox et al., 2012b) and IRC$-$10414 (Gvaramadze et al., 2014) or asymptotic giant branch stars (Cox et al., 2012b; Jorissen et al., 2011). Bow shocks are used to find new runaway stars (Gvaramadze, Kroupa, & Pflamm-Altenburg, 2010a), to identify star clusters from which these stars have been ejected (Gvaramadze & Bomans, 2008) and to constrain the properties of their central stars, e.g. mass-loss rate (Gull & Sofia, 1979; Gvaramadze, Langer & Mackey, 2012), or the density of
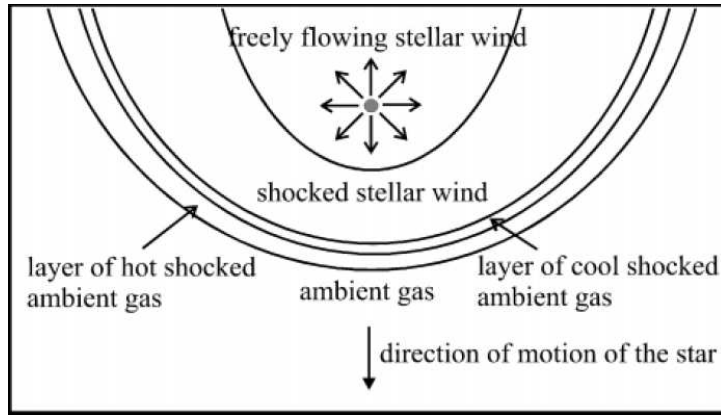
Figure 2.1: Typical structure of a bow shock generated by a hot runaway star. The figure is taken from Comerón & Kaper (1998).

the local ISM (Kaper et al., 1997; Gvaramadze et al., 2014).

The structure of such bow shocks is sketched in Fig. 2.1. However the layers of shocked ISM develop differently as a function of the wind power and ISM properties. The wind and ISM pressure balance at the contact discontinuity. It separates the regions of shocked material bordered by the forward and reverse shocks. The distance from the star to the contact discontinuity in the direction of the relative motion between wind and ISM defines the so-called stand-off distance of the bow shock (Baranov, Krasnobaev, & Kulikovskii, 1971). The shape of isothermal bow shocks, in which the shocked regions are thin, is analytically approximated in Wilkin (1996).

A numerical study by Comerón & Kaper (1998) compares wind-ISM interactions with (semi-)analytical models and concludes that the thin-shell approximation has partial validity. This work describes the variety of shapes which could be produced in bow shocks of OB stars. It details how the action of the wind on the ISM, together with the cooling in the shocked gas, shapes the circumstellar medium, determines the relative thickness of the layers composing a bow shock, and determines its (in)stability. It shows the importance of heat conduction (Spitzer, 1962; Cowie & McKee, 1977) to the size of these bow shocks, and that rapid cooling distorts them. The shocked regions are thick if the shock is weak, but they cool rapidly and become denser and thinner for the regime involving either high space velocities or strong winds and/or high ambient medium densities. This leads to distorting instabilities such as the transverse acceleration instability (Blondin & Koerwer, 1998) or the non-linear thin shell instability (Dgani, van Buren & Noriega-Crespo, 1996a,b). Mac Low et al. (1991) models bow shocks around main sequence stars in dense molecular clouds. The bow shock models in Comerón & Kaper (1998) are set in low-density ambient medium.

Models for bow shocks around evolved, cool runaway stars exist for several stellar evolutionary phases, such as red supergiants (Brighenti & D'Ercole, 1995a; Mohamed, Mackey & Langer, 2012; Decin et al., 2012) or even asymptotic giant branch (AGB) phases (Wareing, Zijlstra & O'Brien, 2007a; Villaver, Manchado & García-Segura, 2012). When a bow shock around a red supergiant forms, the new-born shell swept up by the cool wind succeeds the former bow shock from the main sequence. A collision between the old and new shells of different densities precedes the creation of a second bow shock (Mackey et al., 2012). Bow shocks around cool stars are more likely to generate vortices (Wareing, Zijlstra & O'Brien, 2007b) and their substructures are Rayleigh-Taylor and Kelvin-Helmholtz unstable (Decin et al., 2012). The dynamics of ISM dust grains penetrating into the bow shocks of red supergiants is numerically investigated in van Marle et al. (2011a). The effect of the

space velocity and the ISM density on the morphology of the bow shock of Betelgeuse is explored in Mohamed, Mackey & Langer (2012), however this study considers a single mass-loss rate and does not allow to appreciate how the wind properties modify the bow shock's shape or luminosity. In addition, van Marle, Decin & Meliani (2014) show the stabilizing effect of a weak ISM magnetic field on the bow shock of Betelgeuse.

In this study, we explore in a grid of 2D models the combined role of the star's mass-loss and its space velocity on the dynamics and morphology of bow shocks of various massive stars moving within the Galactic plane. We use representative initial masses and space velocities of massive stars (Eldridge, Langer, & Tout, 2011). Stellar evolution is followed from the main sequence to the red supergiant phase. The treatment of the dissipative processes and the discrimination between wind and ISM material allows us to calculate the bow shock luminosities and to discuss the origin of their emission. We also estimate the luminosity of the bow shocks to predict the best way to observe them. The project differs from previous studies (e.g. Comerón & Kaper, 1998; Mohamed, Mackey & Langer, 2012) in that we use more realistic cooling curves, we include stellar evolution in the models and because we focus on the emitting properties and observability of our bow shocks. We do not take into account the inhomogeneity and the magnetic field of the ISM.

This paper is organised as follows. We first begin our Section 2 by presenting our method, stellar evolution models, included physics and the numerical code. Models for the main sequence, the stellar phase transition and red supergiant phases are presented in Sections 3, 4 and 5, respectively. We describe the grid of 2D simulations of bow shocks around massive stars, discuss their morphology, compare their substructures to an analytical solution for infinitely thin bow shock and present their luminosities and Hα surface brightnesses. Section 6 discusses our results. We conclude in Section 7.

This paper is organised as follows. We first begin our Section 2 by presenting our method, stellar evolution models, included physics and the numerical code. Models for the main sequence and red supergiant phases are presented in Sections 3 and 4, respectively. We describe the grid of 2D simulations of bow shocks around massive stars, discuss their morphology, compare their substructures to an analytical solution for infinitely thin bow shock and present their luminosities and Hα surface brightnesses. Section 5 discusses our results. We conclude in Section 6.

2.2 Numerical scheme and initial parameters

2.2.1 Hydrodynamics, boundary conditions and numerical scheme

The governing equations are the Euler equations of classical hydrodynamics, including radiative cooling and heating for an optically-thin plasma and taking into account electronic thermal conduction, which are,

$$\frac{\partial \rho}{\partial t} + \vec{\nabla} \cdot (\rho \vec{v}) = 0, \tag{2.1}$$

$$\frac{\partial \rho \vec{v}}{\partial t} + \vec{\nabla} \cdot (\vec{v} \otimes \rho \vec{v}) + \vec{\nabla} p = \vec{0}, \tag{2.2}$$

and

$$\frac{\partial E}{\partial t} + \vec{\nabla} \cdot (E\vec{v}) + \vec{\nabla} \cdot (p\vec{v}) = \Phi(T, \rho) + \vec{\nabla} \cdot \vec{F}_{\text{c}}. \tag{2.3}$$

In the system of equations (2.1)−(2.3), $\vec{v}$ is the gas velocity in the frame of reference of the star, ρ is the gas mass density and p is its thermal pressure. The total number density n is defined by $\rho = \mu n m_{\text{H}}$, where μ is the mean molecular weight in units of the mass of hydrogen atom m_{H}. The total energy

density is the sum of its thermal and kinetic parts,

$$E = \frac{p}{(\gamma - 1)} + \frac{\rho v^2}{2}, \tag{2.4}$$

where γ is the ratio of specific heats for an ideal gas, i.e. $\gamma = 5/3$. The temperature inside a given layer of the bow shock is given by,

$$T = \mu \frac{m_\text{H}}{k_\text{B}} \frac{p}{\rho}, \tag{2.5}$$

where k_B is the Boltzmann constant. The quantity Φ in the energy equation (2.3) gathers the rates Λ for optically-thin radiative cooling and Γ for heating,

$$\Phi(T, \rho) = n_\text{H}^\alpha \Gamma(T) - n_\text{H}^2 \Lambda(T), \tag{2.6}$$

where the exponent α depends on the ionization of the medium (see Section 2.2.4), and n_H is the hydrogen number density. The heat flux is symbolised by the vector $\vec{F}_\text{c}$. The relation $c_\text{s} = \sqrt{\gamma p / \rho}$ closes the system of partial differential equations (2.1)−(2.3), where c_s is the adiabatic speed of sound.

We perform calculations on a 2D rectangular computational domain in a cylindrical frame of reference $(O; R, z)$ of origin O, imposing rotational symmetry about $R = 0$. We use an uniform grid divided into $N_\text{R} \times N_\text{z}$ cells, and we pay attention to the number of cells resolving the layers of the bow shocks (Comerón & Kaper, 1998). We choose the size of the computational domain such that the tail of the bow shocks only crosses the downstream boundary $z = z_\text{min}$. Following the methods of Comerón & Kaper (1998) and van Marle et al. (2006), a stellar wind is released into the domain by a half circle of radius 20 cells centred on the origin. We impose at every timestep a wind density $\rho_\text{w} \propto r^{-2}$ onto this circle, where r is the distance to O. We work in the frame of reference of the runaway star. Outflow boundary conditions are assigned at the $z = z_\text{min}$ and $R = R_\text{max}$ borders of the domain, whereas ISM material flows into the domain from the $z = z_\text{max}$ border. The choice of a 2D cylindrical coordinate system possessing an intrinsic axisymmetric geometry limits us to the modelling of symmetric bow shocks only.

We solve the equations with the magneto-hydrodynamics code PLUTO (Mignone et al., 2007, 2012). We use a finite volume method with the Harten-Lax-van Leer approximate Riemann solver for the fluid dynamics, controlled by the standard Courant-Friedrich-Levy (CFL) parameter initially set to $C_\text{cfl} = 0.1$. The equations are integrated with a second order, unsplit, time-marching algorithm. This Godunov-type scheme is second order accurate in space and in time. Optically-thin radiative losses are linearly interpolated from tabulated cooling curves and the corresponding rate of change is subtracted from the pressure. The parabolic term in the equation (2.3), corresponding to the heat conduction is treated with the Super-Time-Stepping algorithm (Alexiades, Amiez & Gremaud, 1996) in an operator-split, first order accurate in time algorithm.

We use PLUTO 4.0 where linear interpolation in cylindrical coordinates is correctly performed by taking into account the geometrical centroids rather than the cell centre (Mignone, 2014). We have found that this leads to better results compared to PLUTO 3.1, especially in close proximity to the axis. The diffusive solver chosen to carry out the simulations damps the dramatic numerical instabilities along the symmetry axis at the apex of the bow shocks (Vieser & Hensler, 2007; Kwak, Henley & Shelton, 2011) and is more robust for hypersonic flows. All the physical components of the model are included from the first timestep of the simulations.

2.2.2 Wind model

Stellar evolution models provide us with the wind parameters throughout the star's life from the main sequence to the red supergiant phase (see evolutionary tracks in Fig. 2.2). We obtain the wind inflow boundary conditions from a grid of evolutionary models for non-rotating massive stars with solar metallicity (Brott et al., 2011). Their initial masses are $M_\star = 10, 20$ and $40\,M_\odot$ (the masses of the stars quoted hereafter are the zero-age main sequence masses, unless otherwise stated), and they have been modelled with the Binary Evolution Code (BEC) (Heger, Langer & Woosley, 2000; Yoon & Langer, 2005) including mass-loss but ignoring overshooting. The mass-loss rate calculation includes the prescriptions for O-type stars by Vink, de Koter & Lamers (2000, 2001) and for cool stars derived by de Jager, Nieuwenhuijzen & van der Hucht (1988).

Fig. 2.3 shows the stellar wind properties of the different models at a radius of $r = 0.01\,\mathrm{pc}$ from the star. Mass-loss rate $\dot{M}$, wind density ρ_w and velocity v_w are linked by,

$$\rho_w = \frac{\dot{M}}{4\pi r^2 v_\mathrm{w}}. \tag{2.7}$$

The wind terminal velocity is calculated from the escape velocity v_esc using $v_\mathrm{w}^2 = \beta_w(T)v_\mathrm{esc}^2$ (Eldridge et al., 2006), with β_w a parameter given in their table 1.

The mass-loss rate of the star has a constant value of around $10^{-9.5}$, $10^{-7.3}$ and $10^{-6.2}\,M_\odot\,\mathrm{yr}^{-1}$ during the main sequence phase of the 10, 20 and $40\,M_\odot$ stars, respectively. After the transition to a red supergiant, the mass-loss increases to around $10^{-6.2}$ and around $10^{-5}\,M_\odot\,\mathrm{yr}^{-1}$ for the $10\,M_\odot$ and $20\,M_\odot$ stars, respectively. The evolutionary model of our $40\,M_\odot$ star ends at the beginning of the helium ignition, i.e. it does not have a red supergiant phase (Brott, private communication). Such a star may evolve through the red supergiant phase but this is not included in our model (see panel (f) of Fig. 2.3). The wind velocity decreases by two orders of magnitude from $\sim 1000\,\mathrm{km\,s}^{-1}$ during the main sequence phase to $\sim 10\,\mathrm{km\,s}^{-1}$ for the red supergiant phase. The effective temperature of the star decreases from $T_\mathrm{eff} \sim 10^4\,\mathrm{K}$ during the main sequence phase to $T_\mathrm{eff} \sim 2.5$–$4.5 \times 10^3\,\mathrm{K}$ when the star becomes a red supergiant. The thermal pressure of the wind is proportional to T_eff, according to the ideal gas equation of state. It scales as $r^{-2\gamma}$ and is negligible during all evolutionary phases compared to the ram pressure of the wind in the free expanding region.

We run two simulations for each $M_\star$ and for each considered space velocities $v_\star$: one for the main sequence and one for the red supergiant phase. Simulations are launched at 5 and 3 Myr of the main sequence phase for the 10 and $20\,M_\odot$ models, and at the zero-age main-sequence for the $40\,M_\odot$ star, given its short lifetime (see black circles in Figs 2.2 and 2.3). Red supergiant simulations are started before the main sequence to red supergiant transition such that a steady state has been reached when the red supergiant wind begins to expand (see black squares in Figs 2.2 and 2.3).

The wind material is traced using a scalar marker whose value Q obeys the linear advection equation,

$$\frac{\partial(\rho Q)}{\partial t} + \vec{\nabla} \cdot (\vec{v}\rho Q) = 0. \tag{2.8}$$

This tracer is passively advected with the fluid, allowing us to distinguish between the wind and ISM material. Its value is set to $Q(\vec{r}) = 1$ for the inflowing wind material and to $Q(\vec{r}) = 0$ for the ISM material, where $\vec{r}$ is the vector position of a given cell of the simulation domain.
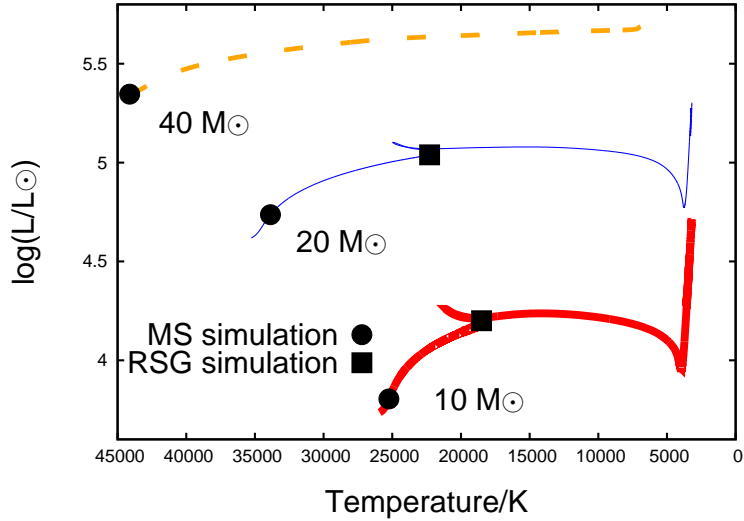
Figure 2.2: Stellar evolutionary tracks used in the simulations. Thick solid red line, thin solid blue line and dashed orange line are the evolutionary tracks for our 10, 20 and 40 $M_\odot$ models, respectively. Circles indicate the time of the beginning of the simulations for the main sequence phase and squares for the red supergiant phase.

2.2.3 Interstellar medium

We consider homogeneous and laminar ISM with $n_{\mathrm{H}} = 0.57 \, \mathrm{cm}^{-3}$, which is typical of the warm neutral medium in the Galactic plane (Wolfire et al., 2003) from where most of runaway massive stars are ejected. The initial ISM gas velocity is set to $v_{\mathrm{ISM}} = -v_\star$.

The photosphere of a main sequence star releases a large flux of hydrogen ionizing photons $S_\star$, that depends on $R_\star$ and T_{eff}, which allows us to estimate $S_\star = 10^{45}$ photon s^{-1} ($T_{\mathrm{eff}} \approx 2.52 \times 10^4$ K), $S_\star = 10^{48}$ photon s^{-1} ($T_{\mathrm{eff}} \approx 3.39 \times 10^4$ K) and $S_\star = 10^{49}$ photon s^{-1} ($T_{\mathrm{eff}} \approx 4.25 \times 10^4$ K) for the 10, 20 and 40 $M_\odot$ stars, respectively (Diaz-Miller, Franco & Shore, 1998). These fluxes produce a Strömgren sphere of radius,

$$R_{\mathrm{S}} = \left(\frac{3S_\star}{4\pi n^2 \alpha_{\mathrm{rr}}^{\mathrm{B}}} \right)^{1/3}, \tag{2.9}$$

where $\alpha_{\mathrm{rr}}^{\mathrm{B}}$ is the case B recombination rate of H$^+$, fitted from Hummer (1994). The Strömgren sphere is distorted by the bulk motion of the star in an egg-shaped H II region (Raga, 1986; Raga et al., 1997; Mackey, Langer & Gvaramadze, 2013). $R_{\mathrm{S}} \approx 4.3$, 43 and 94 pc for the 10, 20 and 40 $M_\odot$ main sequence stars, respectively. R_{S} is larger than the typical scale of a stellar bow shock (i.e. larger than the full size of the computational domain of $\sim$ pc). Because of this, we treated the plasma on the full simulation domain as photoionized with the corresponding dissipative processes (see panel (a) of Fig. 2.4), i.e., we neglect the possiblity that a dense circumstellar structure could trap the stellar radiation field (Weaver et al., 1977). We consider that both the wind and the ISM are fully ionized until the end of the main sequence, and we use an initial $T_{\mathrm{ISM}} \approx 8000$ K which is the equilibrium temperature of the photoionized cooling curve (see panel (a) of Fig. 2.4).

In the case of models without an ionizing radiation field, involving a phase transition or a red supergiant star, the plasma is assumed to be in collisional ionization equilibrium (CIE). We adopt $T_{\mathrm{ISM}} \approx 3300$ K, which corresponds to the equilibrium temperature of the CIE cooling curve for the adopted ISM density (see panel (b) of Fig. 2.4).
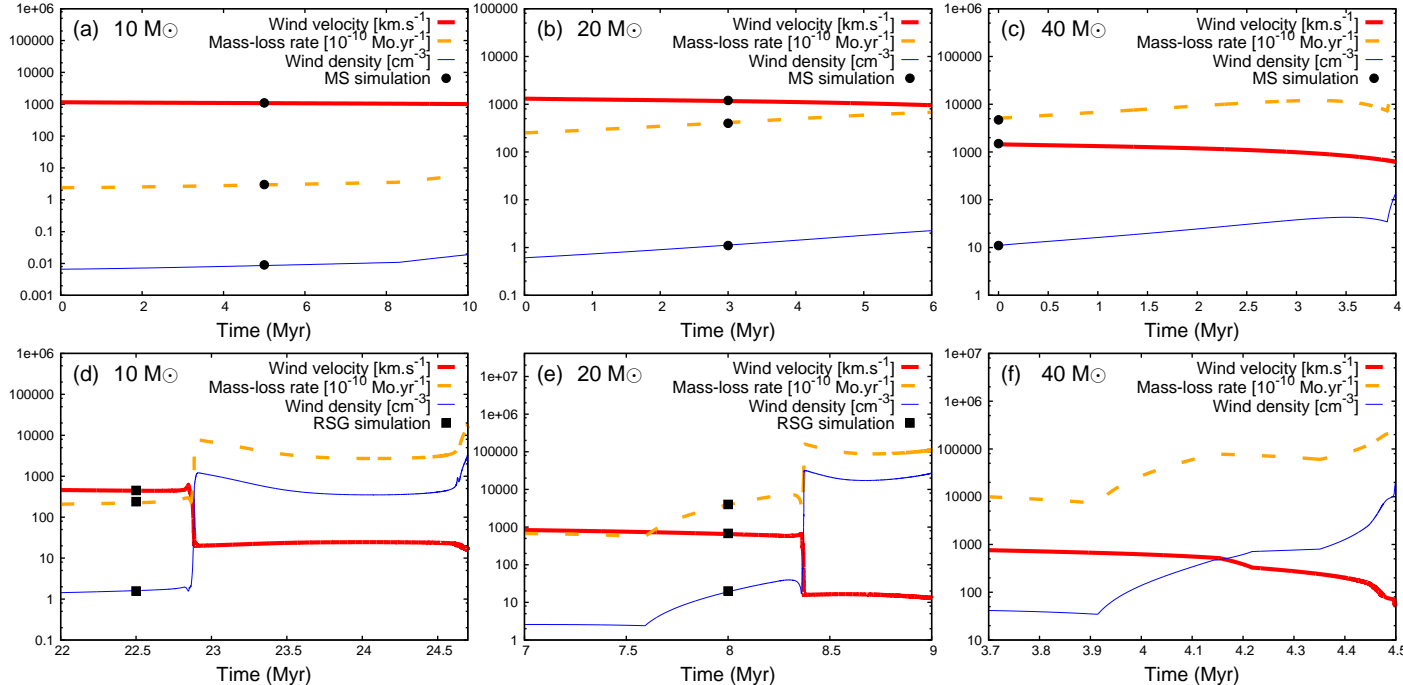
Figure 2.3: Physical parameters of the stellar winds used in our simulations. The top panels represent the wind velocity v_w (thick solid red line), the mass-loss rate $\dot{M}$ (dashed orange line) and the wind number density n_w (thin solid blue line) during the main sequence phase of the 10, 20 and 40 $M_\odot$ stars, whereas the bottom panels show these parameters during the red supergiant phase of the same stars. Wind number density is calculated at 0.01 pc from the star and are proportional to the mass-loss rate $\dot{M}$ (see Eq. 2.7). Black dots show the beginning of the simulations for the main sequence phase and black squares for the red supergiant phase (Table 2.1).

2.2.4 Radiative losses and heating

A cooling curve for photoionized material has been implemented, whereas another assuming CIE is used for the gas that is not exposed to ionizing radiation. In terms of Eq. (2.6), we set $\alpha = 2$ for photoionized gases and $\alpha = 1$ for the CIE medium. The cooling component Λ of Eq. (2.6) is,

$$\Lambda = \Lambda_{H+He} + \Lambda_Z + \Lambda_{RR} + \Lambda_{FL}, \tag{2.10}$$

where Λ_{H+He} and Λ_Z represent the cooling from hydrogen plus helium, and metals Z, respectively (see Wiersma, Schaye & Smith, 2009) for a medium with the solar helium abundance $\chi_{He} = n_{He}/n_H = 0.097$ (Asplund et al., 2009). $\Lambda_{H+He} + \Lambda_Z$ dominates the cooling at high T (see panel (a) of Fig. 2.4). A cooling term for hydrogen recombination Λ_{RR} is obtained by fitting the case B energy loss coefficient β_B (Hummer, 1994). The rate of change of E is also affected by collisionally excited forbidden lines from elements heavier than helium, e.g. oxygen and carbon (Raga, Mellema & Lundqvist, 1997). The corresponding cooling term Λ_{FL} is adapted from a fit of [O II] and [O III] lines (see Eq. A9 of Henney et al., 2009) with the abundance of $n_O/n_H = 4.89 \times 10^{-4}$ (Asplund et al., 2009).

The heating rate Γ_2 in Eq. (2.6) represents the effect of photons emitted by the hot stars ionizing the recombining H^+ ions and liberating energetic electrons. It is calculated as the energy of an ionizing photon after subtracting the reionization potential of an hydrogen atom, i.e.,, 5 eV for a typical main sequence star (Osterbrock & Bochkarev, 1989), weighted by α_{rr}^B.

At low temperatures ($T < 6 \times 10^4$ K), the cooling rate is the sum of all terms Λ_{H+He}, Λ_Z, Λ_{RR} and Λ_{FL}, whereas for higher temperatures ($T > 6 \times 10^4$ K) only the ones for hydrogen, helium and Z are used. The two parts of the curve are linearly interpolated in the range of $4.5 \times 10^4 < T < 6.0 \times 10^4$ K.

The CIE cooling curve (see panel (b) of Fig. 2.4) assumes solar abundances (Wiersma, Schaye & Smith, 2009) for hydrogen, helium and Z. The heating term Γ_1 represents the photoelectric heating of dust grains by the Galactic far-UV background. For $T \leq 1000$ K, we used equation C5 of Wolfire et al. (2003). We impose a low temperature ($T < 1000$ K) electron number density profile n_e using eq. C3 of Wolfire et al. (2003). For $T > 1000$ K we take the value of n_e interpolated from the CIE curve by Wiersma, Schaye & Smith (2009).

A transition between the main sequence and the red supergiant phases requires a transition between photoionized and CIE medium. At the beginning of the red supergiant phase, our model ceases to consider the dissipation and heating for photoionized medium and adopts the ones assuming CIE medium. The assumption of CIE specifies n_e/n_H as a function of T (Wiersma, Schaye & Smith, 2009). The mean mass per particle is calculated as,

$$\mu(T) = \frac{1 + 4\chi_{He}}{(1 + 4\chi_{He})[1 + x(T)]}, \tag{2.11}$$

where,

$$x(T) = \left(\frac{n_e}{n_H}\right)_T / \left(\frac{n_e}{n_H}\right)_{T_{max}}, \tag{2.12}$$

and T_{max} is the upper limit of the cooling curve temperature range (Wiersma, Schaye & Smith, 2009), and $x(T)$ is a quantity monotonically increasing with T, that gives the degree of ionization of the medium (see top inset in Fig. 2.5). We then have an expression for with low and high T limits of $\mu = 1.27$ and $\mu = 0.61$ for neutral and fully ionized medium, respectively (e.g. Lequeux, 2002). For simulations assuming CIE we then obtain through $\mu(T)$ a one-to-one correspondence between $T/\mu \propto p/\rho$ (known) and T (required) for each cell of the computational domain.
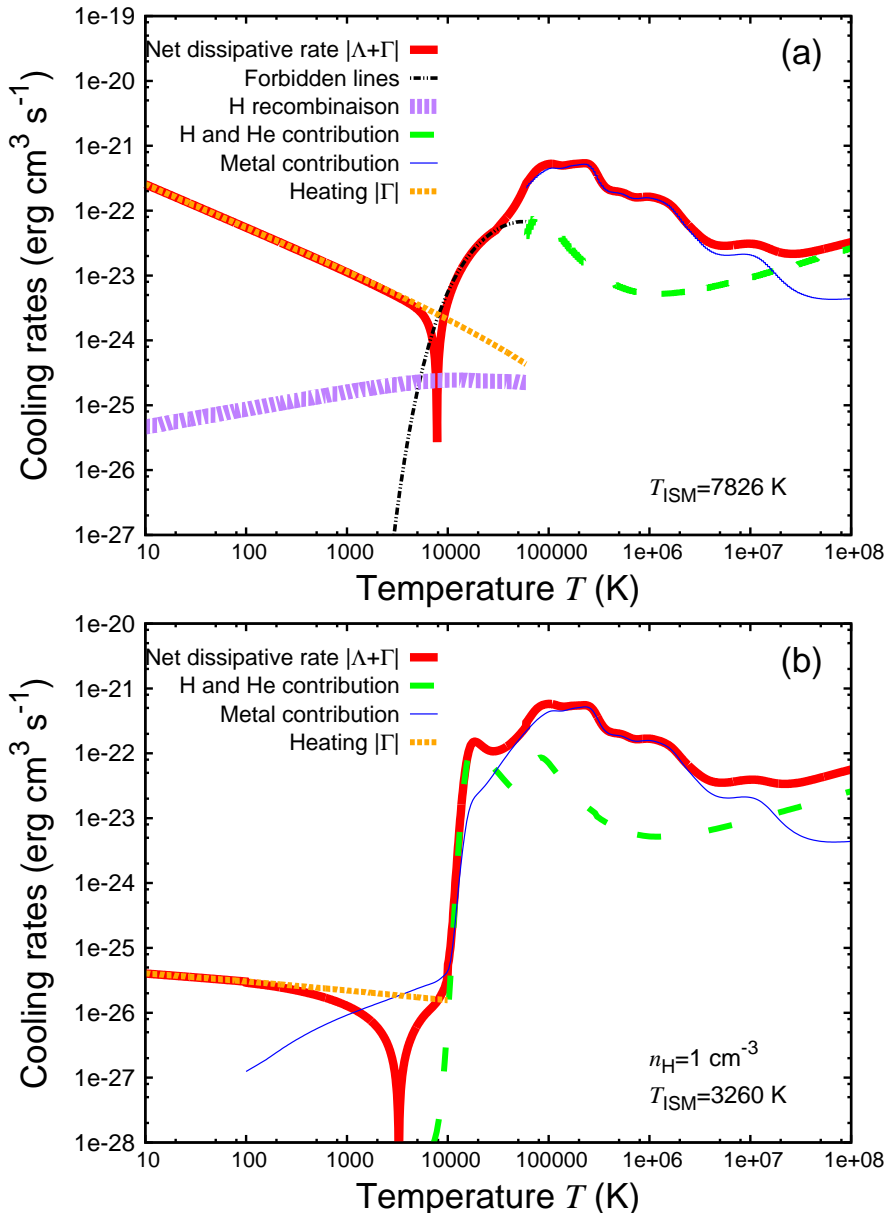
Figure 2.4: Cooling and heating rates as a function of temperature for photoionized (a) and collisional ionization equilibrium (b) medium. The solid thick red line is the curve representing the net rate of emitted energy, i.e. the absolute value of the sum of the luminosity due to cooling Λ and heating Γ. Dotted and thin lines correspond to the different processes the model takes into account: emission from forbidden lines (dotted dashed thin black), H recombination lines (dotted thick purple), hydrogen and helium (dashed green) and metals (solid thin blue) as well as the heating rate Γ (dotted orange). All luminosity from the different coolants and heating rate of processes are presented for $n_H = 1\,cm^{-3}$, within their range of interest. The x-axis represents temperature (in K) and the y-axis the emitted energy (in $erg\,s^{-1}\,cm^3$).
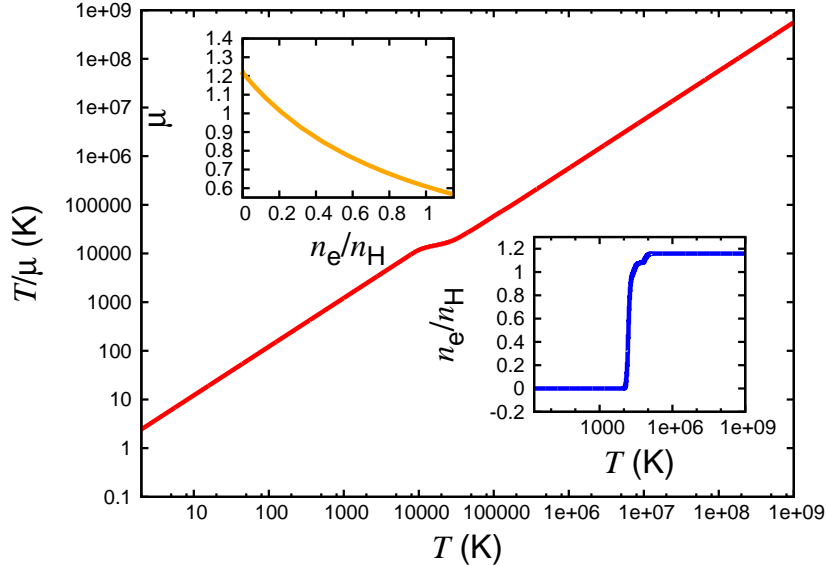
Figure 2.5: Temperature divided by the mean mass per particle T/μ (in K) as a function of temperature T (in K). Data are derived from the collisional ionization equilibrium cooling curves (Wiersma, Schaye & Smith, 2009). Top inset: μ as a function of electron fraction n_e/n_H. Bottom inset: n_e/n_H as a function of temperature T.

2.2.5 Thermal conduction

The circumstellar medium around runaway main sequence stars presents large temperature gradients across its shocks and discontinuities (e.g. $\Delta T \approx 10^7$ K at the reverse shock of the models for the 20 and 40 $M_\odot$ stars), which drive the heat flux (Spitzer, 1962; Cowie & McKee, 1977). Electrons move quickly enough to transfer energy to the adjacent low temperature gas. The consequent equilibration of the pressure smooths the density profiles at the discontinuity between the wind and ISM material (Weaver et al., 1977).

Heat conduction is included in our models over the whole computational domain. The models with partially neutral gas, e.g. during a phase transition or for models involving a red supergiant star, $\vec{F}_c$ is calculated at $T < 1000$ K with n_e from eq. C3 in Wolfire et al. (2003). Our study does not consider either the stellar or interstellar magnetic field, which make the heat conduction anisotropic (Orlando et al., 2008).

2.2.6 Relevant characteristic quantities of a stellar wind bow shock

A stellar wind bow shock generally has four distinct regions: the unperturbed ISM, the shocked ISM, the shocked wind material and the freely-expanding wind. The shocked materials are separated by a contact discontinuity, the expanding wind from the star is separated from shocked wind by the reverse shock and the structure's outermost border is marked by the forward shock (e.g. van Buren, 1993).

The stand-off distance of the bow shock is,

$$R(0) = \sqrt{\frac{\dot{M} v_w}{4\pi \rho_{ISM} v_\star^2}} \qquad (2.13)$$

(Baranov, Krasnobaev & Kulikovskii, 1971). The analytical approximation for the shape of an in-

finitely thin bow shock is,

$$R(\theta) = R(0)\text{cosec}(\theta\frac{\pi}{180})\sqrt{3(1 - \theta\frac{\pi}{180})\text{cotan}(\theta\frac{\pi}{180})}, \tag{2.14}$$

where θ is the angle from the direction of motion in degrees and $R(0)$ is given by Eq. (2.13).

The dynamical timescale of a layer constituting a stellar wind bow shock is equal to the time a fluid element spends in it before it is advected downstream,

$$t_{\text{dyn}} = \frac{\Delta z}{v}, \tag{2.15}$$

where Δz is the thickness of the layer along the Oz direction and v is a characteristic velocity of the gas in the considered region, i.e. the post-shock velocity $v \simeq v_{\text{w}}/4$ in the shocked wind or $v \simeq v_{\star}/4$ in the shocked ISM. The gas density and pressure govern the cooling timescale,

$$t_{\text{cool}} = \frac{E}{\dot{E}} = \frac{p}{(\gamma - 1)\Lambda(T)n_{\text{H}}^2}. \tag{2.16}$$

These two timescales determine whether a shock is adiabatic ($t_{\text{dyn}} \ll t_{\text{cool}}$) or radiative ($t_{\text{dyn}} \gg t_{\text{cool}}$).

2.2.7 Presentation of the simulations

The parameters used in our simulations are gathered together with information concerning the size of the computational domain in Table 2.1. The size of the computational domain is inspired by Comerón & Kaper (1998), i.e. we use a sufficient number of cells N_{R} to adequately resolve the substructures of each bow shock in the direction of the stellar motion. As $v_{\star}$ increases, the bow shock and the domain size decreases, so the spatial resolution $\Delta = R_{\text{max}}/N_{\text{R}}$ also decreases. The dimensions of the domain are chosen such that the tail of the bow shock only crosses the $z = z_{\text{min}}$ boundary, but never intercepts the outer radial border at $R = R_{\text{max}}$ to avoid numerical boundary effects.

We model bow shocks for a space velocity $20 \leq v_{\star} \leq 70 \, \text{km s}^{-1}$, since these include the most probable space velocities of runaway stars and ranges from supersonic to hypersonic (Eldridge, Langer & Tout, 2011). For the bow shocks of main sequence stars the label is MS, and the models for the red supergiant phase are labelled with the prefix RSG. In our nomenclature, the four digits following the prefix of a model indicate the zero age main sequence mass (first two digits) and the space velocity (next two digits).

The main sequence to red supergiant phase transition happens in a timescale of $\approx 10^4$ yr which is much shorter than both evolutionary phases themselves. Thus, we have not included into this paper a detailed consideration of the short-lived circumstellar structures which develop during this transition.

Simulations of bow shocks involving a main sequence star are started at a time t_{start} in the middle of their stellar evolutionary phase in order to model bow shocks with roughly constant wind properties. The distortion of the initially spherically expanding bubble into a steady bow shock takes up to $\approx 16 \, t_{\text{cross}}$, where $t_{\text{cross}} = R(0)/v_{\star}$ is the bow shock crossing-time. We stop the simulations at least $32 \, t_{\text{cross}}$ after the beginning of the integration, except for model MS4020 for which such a time is about half of the main sequence time.

Table 2.1: Nomenclature and grid parameters used in our hydrodynamical simulations. Parameters $\varDelta$, R_{max} and z_{min} are the resolution of the uniform grid (in pc cell^{-1}) and respectively the upper and lower limits of the domain along the x-axis and y-axis (in pc). N_{R} and N_{z} are the number of cells discretising the corresponding directions. The two last columns contain the starting time t_{start} of the simulations relative to the zero-age main-sequence and the crossing time t_{cross} of the gas because of the stellar motion for each associated bow shock (in Myr).

Model	$M_{\star}$ ($M_{\odot}$)	$v_{\star}$ (km s^{-1})	Δ (pc cell^{-1})	z_{min} (pc)	R_{max} (pc)	N_{R}	N_{z}	t_{start} (Myr)	t_{cross} (Myr)
MS1020	10	20	4.00×10^{-2}	-0.4	1.4	600	600	5.0	6.3×10^{-2}
MS1040	10	40	1.00×10^{-2}	-0.2	0.4	700	700	5.0	1.6×10^{-3}
MS1070	10	70	2.90×10^{-3}	-0.1	0.2	600	600	5.0	4.9×10^{-4}
RSG1020	10	20	6.36×10^{-3}	-2.00	2.0	315	644	22.62	1.5×10^{-2}
RSG1040	10	40	3.01×10^{-3}	-0.7	1.4	966	840	22.78	5.5×10^{-3}
RSG1070	10	70	8.36×10^{-4}	-0.3	0.6	854	908	22.86	2.1×10^{-3}
MS2020	20	20	4.00×10^{-1}	-4.0	10.0	500	500	3.0	7.0×10^{-2}
MS2040	20	40	1.00×10^{-1}	-2.5	4.0	600	600	3.0	1.7×10^{-2}
MS2070	20	70	2.00×10^{-2}	-0.75	1.5	700	700	3.0	5.4×10^{-3}
RSG2020	20	20	2.0×10^{-2}	-5.0	15.0	1000	700	8.0	6.8×10^{-2}
RSG2040	20	40	1.0×10^{-2}	-3.0	6.0	800	800	8.0	1.6×10^{-2}
RSG2070	20	70	5.0×10^{-3}	-2.0	1.0	400	400	8.0	4.4×10^{-3}
MS4020	40	20	1.50×10	-15.0	35.0	500	500	0.0	2.8×10^{-1}
MS4040	40	40	3.80×10^{-1}	-8.0	15.0	600	600	0.0	7.1×10^{-2}
MS4070	40	70	1.10×10^{-1}	-4.0	8.0	700	700	0.0	2.5×10^{-2}

2.3 The main sequence phase

2.3.1 Physical characteristics of the bow shocks

We show the gas density field in our bow shock models of the main sequence phase MS1020 ($10\,M_\odot$ initial stellar mass, $v_\star = 20\,\mathrm{km\,s^{-1}}$, upper panel), MS1040 ($10\,M_\odot$, $40\,\mathrm{km\,s^{-1}}$, middle panel) and MS1070 ($10\,M_\odot$, $70\,\mathrm{km\,s^{-1}}$, lower panel) in Fig. 2.6. Figs 2.7 and 2.8 are similar for the $20\,M_\odot$ and $40\,M_\odot$ initial mass stars. The figures correspond to a time $\approx t_{\mathrm{start}} + 32\,t_{\mathrm{cross}}$. The model MS4020 has a lifetime $< 32\,t_{\mathrm{cross}}$ (see panels (c) and (f) of Fig. 2.3), and is therefore shown at a time $\approx 16\,t_{\mathrm{cross}}$. In Figs 2.6 to 2.8 the overplotted solid black line is the material discontinuity, i.e. the border between the wind and ISM gas where the value of the material tracer $Q(\vec{r}) = 1/2$. The bow shock morphological characteristics such as the stand-off distance and the axis ratio $R(0)/R(90)$ measured from the simulations are summarised in Table 2.2.

The theory of Baranov, Krasnobaev & Kulikovskii (1971) predicts that $R(0) \propto v_\star^{-1}$ and $R(0) \propto \dot{M}^{1/2}$ because the stand-off distance depends on the balance between the wind ram pressure with the ISM ram pressure. The size of the bow shock decreases as a function of $v_\star$: $R(0)$ decreases by a factor of 2 if $v_\star$ doubles, e.g. $R(0) \approx 0.13$ in model MS1020 but $R(0) \approx 0.06$ in model MS1040 (see upper and middle panels of Fig. 2.6). The bow shocks also scale in size with $\dot{M}$, e.g. at fixed $v_\star$ its size for the $10\,M_\odot$ star is smaller by a factor of 10 compared to the size of the bow shock from the $20\,M_\odot$ star, which in turn is smaller by a factor of ≈ 3.5 compared to one from the $40\,M_\odot$ star (e.g. see middle panels of Figs. 2.6 to 2.8). If we look again at $\dot{M}$ in Fig. 2.3 (a−c), we find $\dot{M} \approx 10^{-9.5}$, $\approx 10^{-7.3}$ and $\approx 10^{-6}\,M_\odot\,\mathrm{yr^{-1}}$ for the 10, 20 and $40\,M_\odot$ star, respectively. We see that these sizes are in accordance with the theory and arise directly as a result of Eq. (2.13).

The relative thickness of the substructures varies with the wind and ISM properties because the gas velocity determines both the post-shock temperature, i.e. governs the cooling physics at the reverse shock and in the shell, and the compression of the shocked ISM. Our simulations with $v_\star = 20\,\mathrm{km\,s^{-1}}$ have weak forward shocks, i.e. compression at the forward shock is not important. The thickness of the layer of shocked ISM gas with respect to $R(0)$ is roughly independent of $M_\star$ for these models (see upper panels of Figs. 2.6, 2.7 and 2.8). The shocked ISM density increases for models with $v_\star \geq 40\,\mathrm{km\,s^{-1}}$ because the high post-shock temperature makes the cooling efficient. The variations of $\dot{M}$ at a given $v_\star$ modify the morphology of the bow shock because a stronger wind ram pressure enlarges the size of the bow shock and makes the shell thinner with regard to $R(0)$ (see models MS1020 and MS4020 in upper panels of Figs. 2.6 and 2.8).

Our simulations with $v_\star = 20\,\mathrm{km\,s^{-1}}$ all have a stable density field (see upper panels of Figs. 2.6 to 2.8). The simulations with $v_\star = 40\,\mathrm{km\,s^{-1}}$ are bow shocks with radiative forward shocks (i.e. with a dense and thin layer of shocked ISM). Our simulations for $M_\star \geq 20\,M_\odot$ and with $v_\star = 70\,\mathrm{km\,s^{-1}}$ show instabilities at both the contact and the material discontinuity, see middle panel of Fig. 2.7 and 2.8. Our models for the $40\,M_\odot$ star with $v_\star \geq 40\,\mathrm{km\,s^{-1}}$ are similar. Model MS4040 is slightly more unstable than model MS2070 whereas model MS4070 shows even stronger instability which develops at its forward shock and dramatically distorts its dense and thin shell, as shown in the bottom panel of Fig. 2.8. The large density gradient across the material discontinuity allows Rayleigh-Taylor instabilities to develop. The entire shell of cold ISM gas has distortions characteristic of the non-linear thin-shell instability (Vishniac, 1994; Garcia-Segura, Mac Low & Langer, 1996).
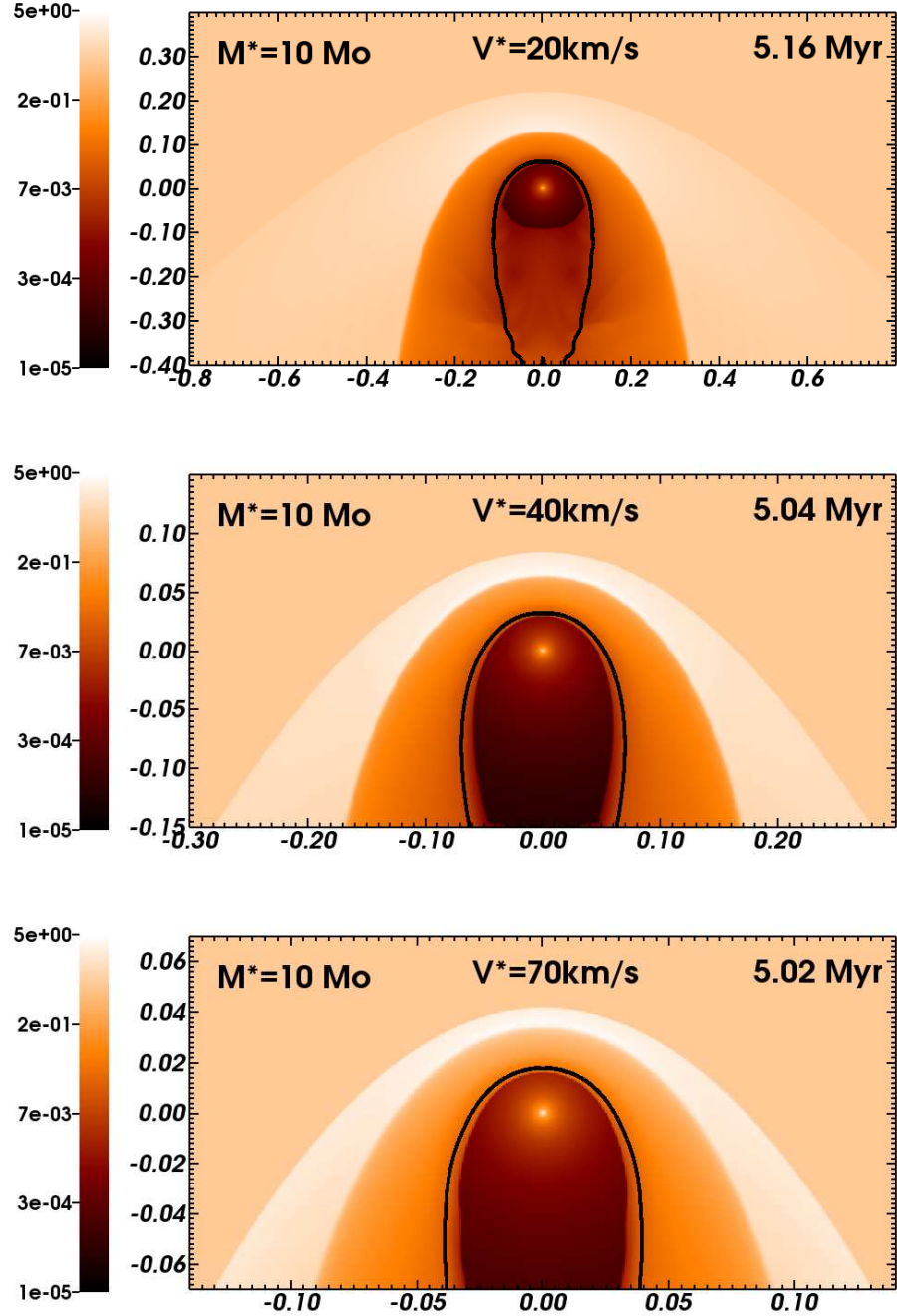
Figure 2.6: Grid of stellar wind bow shocks from the main sequence phase of the $10\,M_{\odot}$ initial mass star as a function of the space velocity with respect to the ISM, with $20\,\mathrm{km\,s^{-1}}$ (top panel), $40\,\mathrm{km\,s^{-1}}$ (middle panel) and $70\,\mathrm{km\,s^{-1}}$ (bottom panel). The nomenclature of the models follows Table 2.1. The gas number density is shown with a density range from 10^{-5} to $5.0\,\mathrm{cm^{-3}}$ in the logarithmic scale. The solid black contour traces the boundary between wind and ISM material $Q(\vec{r}) = 1/2$. The x-axis represents the radial direction and the y-axis the direction of stellar motion (in pc). Not all the computational domain is shown in the figures.
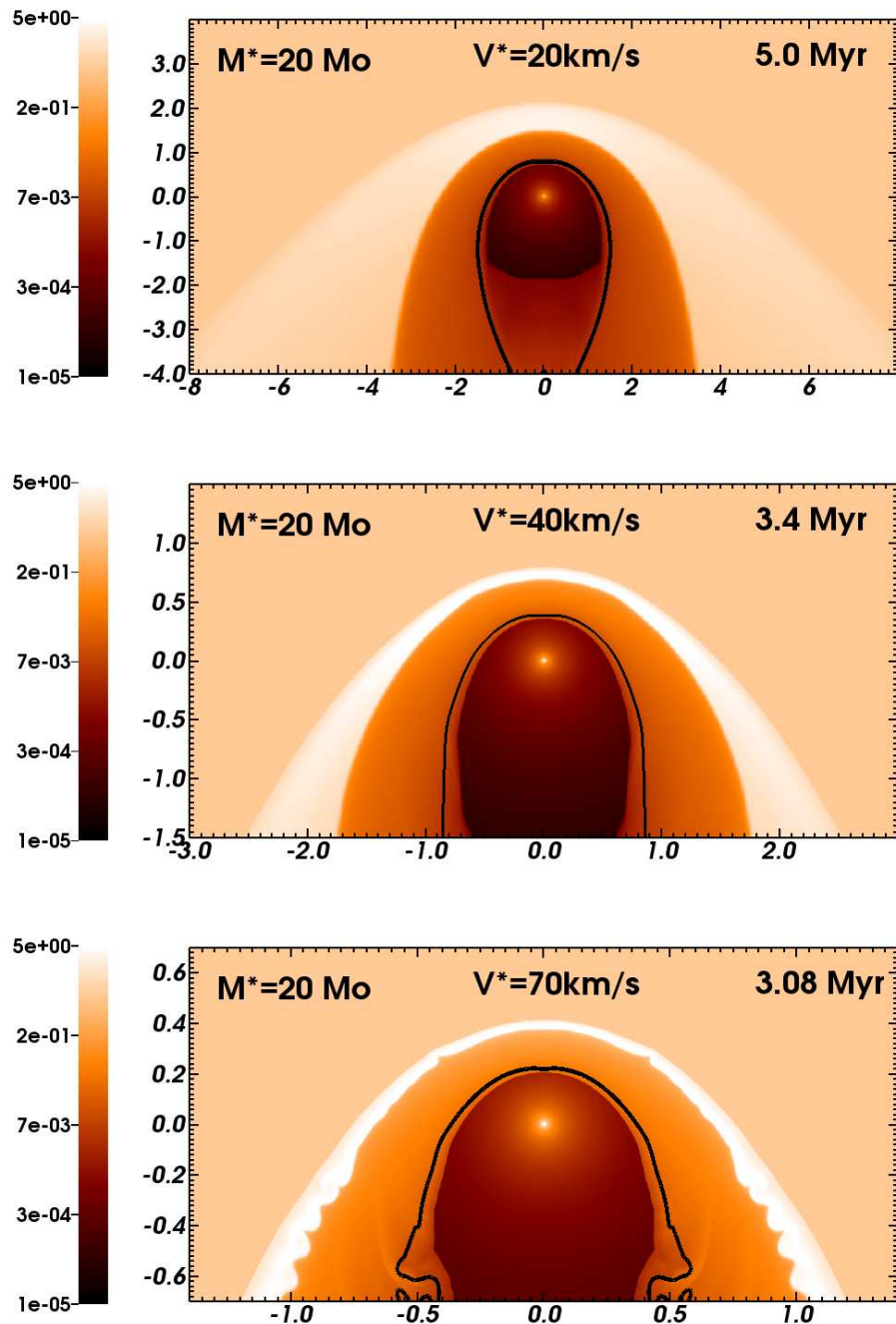
Figure 2.7: As Fig. 2.6, with an initial stellar mass of 20 M$_\odot$.
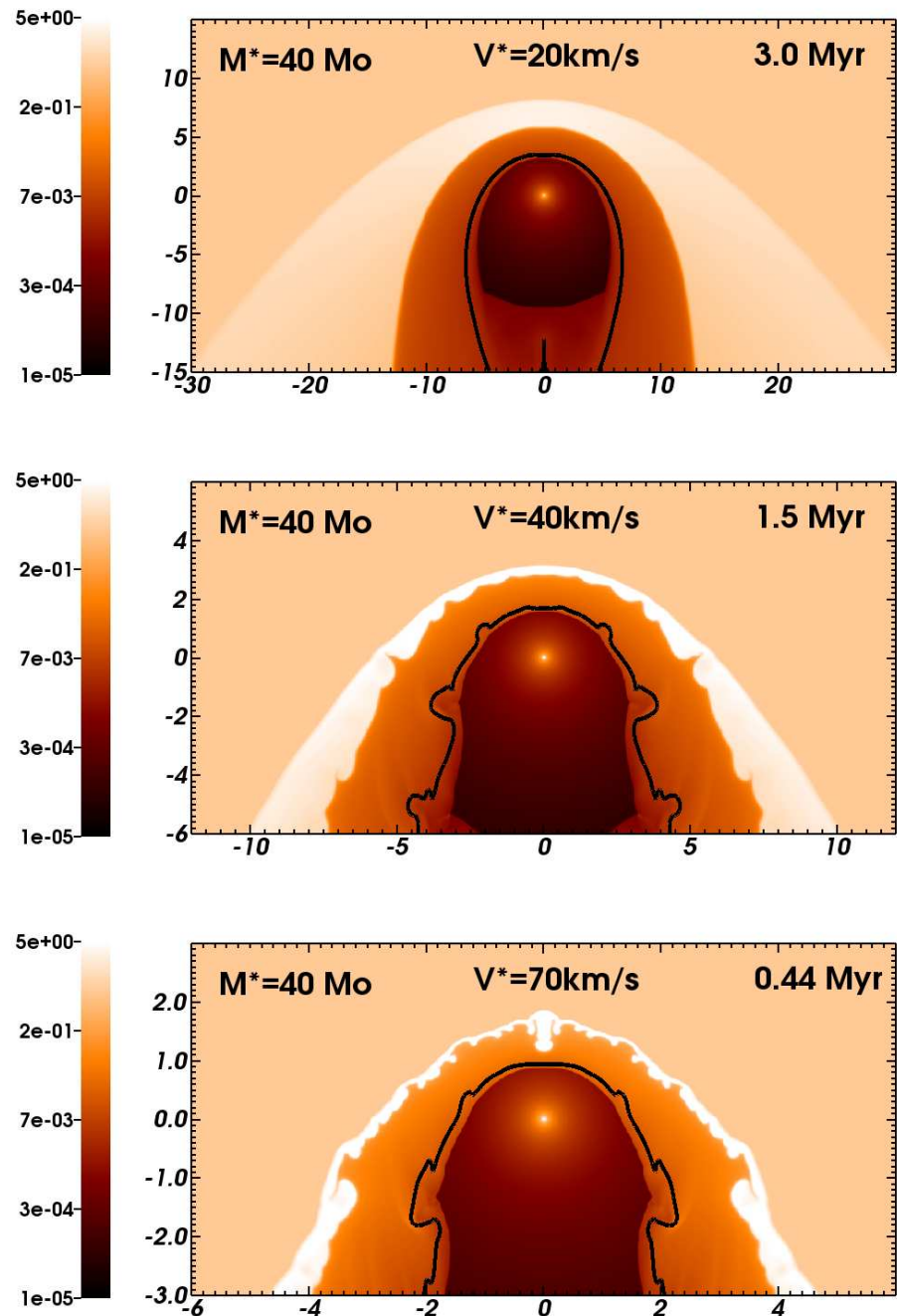
Figure 2.8: As Fig. 2.6, with an initial stellar mass of 40 M$_\odot$.
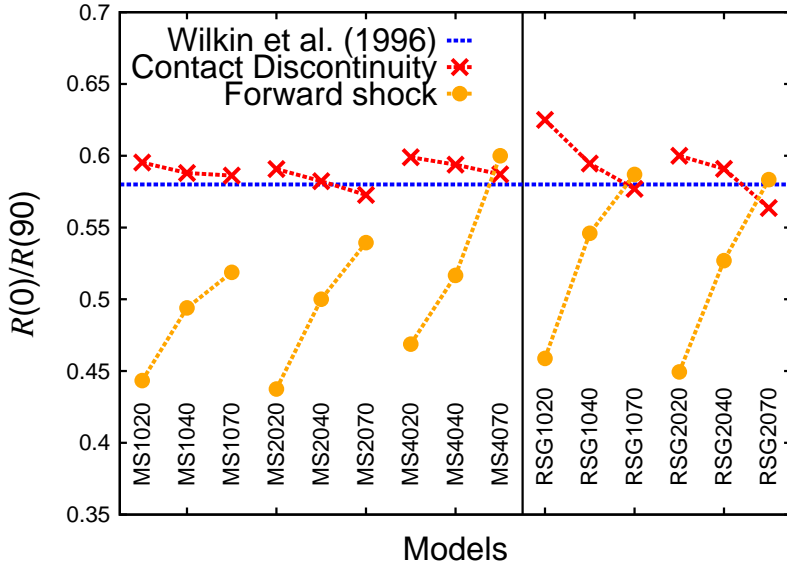
Figure 2.9: Comparison between the ratio $R(0)/R(90)$ for the main sequence and supergiant models with the theoretical value of $1/\sqrt{3} \approx 0.58$ predicted by Wilkin (1996, horizontal dotted blue line). We distinguish between the contact discontinuity (red crosses) and the forward shock (orange dots) of each model.

2.3.2 Comparison of the models with the analytical solution

In Fig. 2.9 we compare $R(0)/R(90)$ with the analytical solution for a bow shock with a thin shell (where $R(0)/R(90) \approx 1/\sqrt{3} \approx 0.58$; Wilkin, 1996). $R(0)/R(90)$ at the contact discontinuity decreases as a function of $v_\star$, e.g. models MS2020 and MS2070 have $R(0)/R(90) \approx 0.59$ and ≈ 0.56, respectively. $R(0)/R(90)$ at the forward shock increases with $v_\star$ and $\dot{M}$ (see Figs 2.6 to 2.8). The contact discontinuity is the appropriate measure to match the analytical solution (see Mohamed, Mackey & Langer, 2012). $R(0)/R(90)$ is within < 10 per cent of Wilkin solution but does not satisfy it at both discontinuities, except for MS4070 with $R(0)/R(90) \approx 0.59$ at the contact discontinuity and $R(0)/R(90) \approx 0.60$ at the forward shock. Model MS4070 is the most compressive bow shock and it has a thin unstable shell bounded by the contact discontinuity and forward shock. Fig. 2.10 shows good agreement between model MS4070 and Wilkin solution for angles $\theta > 90°$. Our model MS4020 is the most deviating simulation at the forward shock, because the brevizy of its main sequence phase prevents the bow shock from reaching a steady state.

2.3.3 Thermal conduction

Fig. 2.11 illustrates the effects of heat conduction on the shape of a bow shock. Panel (a) shows the density field of model MS2040, and panel (b) shows the same model but without thermal conduction. The dashed contour traces the border between wind and ISM gas. The streamlines show the penetration of ISM material into the hot bubble. The bow shock including thermal conduction is larger by a factor ≈ 1.4 in both the directions normal and parallel to the direction of motion of the star. Its shell is denser and splits into two layers of hot and cold shocked ISM, whereas the model without thermal conduction has a single and less compressed region of ISM material.

The position of the reverse shock is insensitive to thermal conduction because heat lost at the material discontinuity is counterbalanced by the large wind ram pressure (see panels (a) and (b) of Fig. 2.11). Fig. 2.12 illustrates that the shocked regions of a bow shock with heat conduction have smooth density
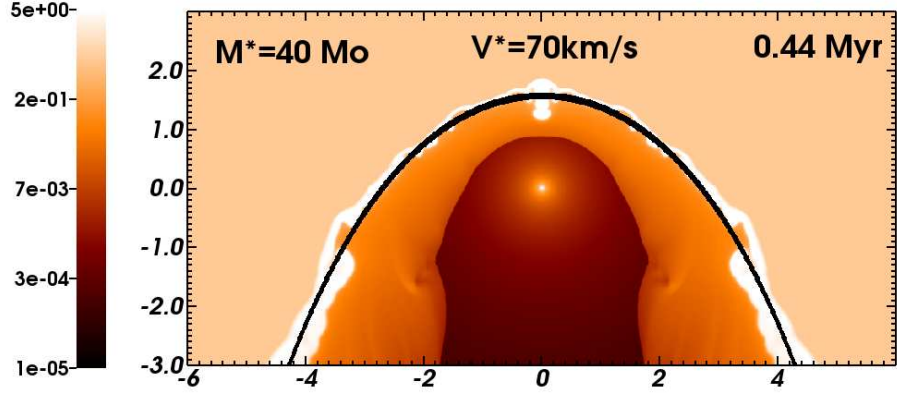
Figure 2.10: Comparison between the density field of model MS4070 presenting a thin shell and the corresponding analytical solution (Wilkin, 1996, solid black line). The gas number density is shown with a density range from 10^{-5} to $5.0\,\mathrm{cm}^{-3}$ in the logarithmic scale. The *x*-axis represents the radial direction and the *y*-axis the direction of stellar motion (in pc).

Table 2.2: Bow shock morphological properties at the contact discontinuity. The parameter $R(0)$ (in pc) is the stand-off distance of the bow shock at the contact discontinuity and $R(0)/R(90)$ is the ratio plotted in Fig. 2.9, with $R(90)$ the perpendicular radius of the shock.

Model	$R(0)$ (pc)	$R(0)/R(90)$
MS1020	0.13	0.595
MS1040	0.06	0.587
MS1070	0.03	0.586
RSG1020	0.30	0.625
RSG1040	0.22	0.594
RSG1070	0.15	0.576
MS2020	1.40	0.590
MS2040	0.69	0.582
MS2070	0.38	0.563
RSG2020	1.35	0.600
RSG2040	0.65	0.590
RSG2070	0.31	0.563
MS4020	5.60	0.598
MS4040	2.85	0.593
MS4070	1.72	0.587

profiles around the contact discontinuity (see panels (a) and (c) of Fig. 2.12). This is consistent with previous models of a steady star (see fig. 3 of Weaver et al., 1977) and of moving stars (see fig. 7 of Comerón & Kaper, 1998). Electrons carry internal energy from the hot shocked wind to the shocked ISM, e.g. the $10 \, M_\odot$ models have a temperature jump amplitude of $\Delta T \approx 10^7 \, \mathrm{K}$ across the contact discontinuity.

Our simulation of model MS1040 (see Fig. 2.6) provides us with the parameters of the hot bubble ($T \approx 10^7 \, \mathrm{K}$, $n \approx 0.02 \, \mathrm{cm}^{-3}$) and the shell ($T \approx 10^4 \, \mathrm{K}$, $n \approx 3.3 \, \mathrm{cm}^{-3}$). The shocked ISM gas has a velocity $v \approx 25 \, \mathrm{km \, s^{-1}}$ and $\mu = 0.61$. Using Eq. (2.15)−(2.16), we find that the hot gas in the inner ($t_{\mathrm{cool}} \approx 1.11 \times 10^2 \gg t_{\mathrm{dyn}} \approx 1.4 \times 10^{-3} \, \mathrm{Myr}$) and outer ($t_{\mathrm{cool}} \approx 2.94 \times 10^{-3} \gtrsim t_{\mathrm{dyn}} \approx 1.0 \times 10^{-3} \, \mathrm{Myr}$) layers of the bow shock are adiabatic and slightly radiative, respectively. The radiative character of the shell is more pronounced for models with $v_\star > 40 \, \mathrm{km \, s^{-1}}$. Note that the hot bubble never cools, i.e. t_{cool} refers here to the timescale of the losses of internal energy by optically-thin radiative processes, which are compensated by the conversion of kinetic energy to heat at the reverse shock. The thermal conduction timescale is,

$$t_{\mathrm{cond}} = \frac{7pl^2}{2(\gamma - 1)\kappa(T)T},\tag{2.17}$$

where $\kappa(T)$ is the heat conduction coefficient and l a characteristic length along which heat transfer happens (Orlando et al., 2008). Because $\kappa(T) \propto T^{5/2}$ (Cowie & McKee, 1977), $t_{\mathrm{cond}} \propto T^{-7/2}$, i.e. heat conduction is a fast process in a hot medium. Consequently, we have $t_{\mathrm{dyn}}/t_{\mathrm{cond}} \approx 1.46 \times 10^5 \gg 1$ and $t_{\mathrm{cool}}/t_{\mathrm{cond}} \approx 1.16 \times 10^{10} \gg 1$ in the hot bubble ($l = 0.035 \, \mathrm{pc}$) whereas we find $t_{\mathrm{dyn}}/t_{\mathrm{cond}} \approx 1.71 \times 10^{-5} \ll 1$ and $t_{\mathrm{cool}}/t_{\mathrm{cond}} \approx 5.03 \times 10^{-5} \ll 1$ in the shell ($l = 0.025 \, \mathrm{pc}$) of the model MS1040, which explains the differences between the models shown in Fig. 2.11. All of our simulations of the main sequence phase behave similarly because their hot shocked wind layers have similar temperatures. Heat transfer across the bubble is always faster than the dynamical timescale of the gas.

As a consequence, the pressure increases in the shocked ISM, pushing both the contact discontinuity inwards and the forward shock outwards. The region of shocked wind conserves its mass but loses much of its pressure. To balance the external pressure, its volume decreases and the gas becomes denser. Two concentric substructures of shocked ISM form: an inner one with high temperature and low density adjoining the material discontinuity, and an outer one with low temperature and high density. Previous investigations about the effects of heat conduction inside circumstellar nebulae around runaway hot stars are available in section 4.6 of Comerón & Kaper (1998).

2.3.4 Bow shock emissivity

Luminosities

The bow shock luminosities of all our models are plotted in panel (a) of Fig. 2.13. It shows the emitted light as a function of mass-loss $\dot{M}$ and space velocity $v_\star$ (i.e. by model). L_{gas} is the bow shock luminosity from optically-thin cooling of the gas and the part of this which originates from the wind material is designated as L_{wind}. The bow shock luminosities are calculated taking into account the cylindrical symmetry of the models by integrating the radiated energy in the $z \geq 0$ region (Mohamed, Mackey & Langer, 2012). The optically-thin gas radiation is therefore computed as,

$$L_{\mathrm{gas}} = 2\pi \iint_{\mathcal{D}} \Lambda n_{\mathrm{H}}^2 R dR dz,\tag{2.18}$$
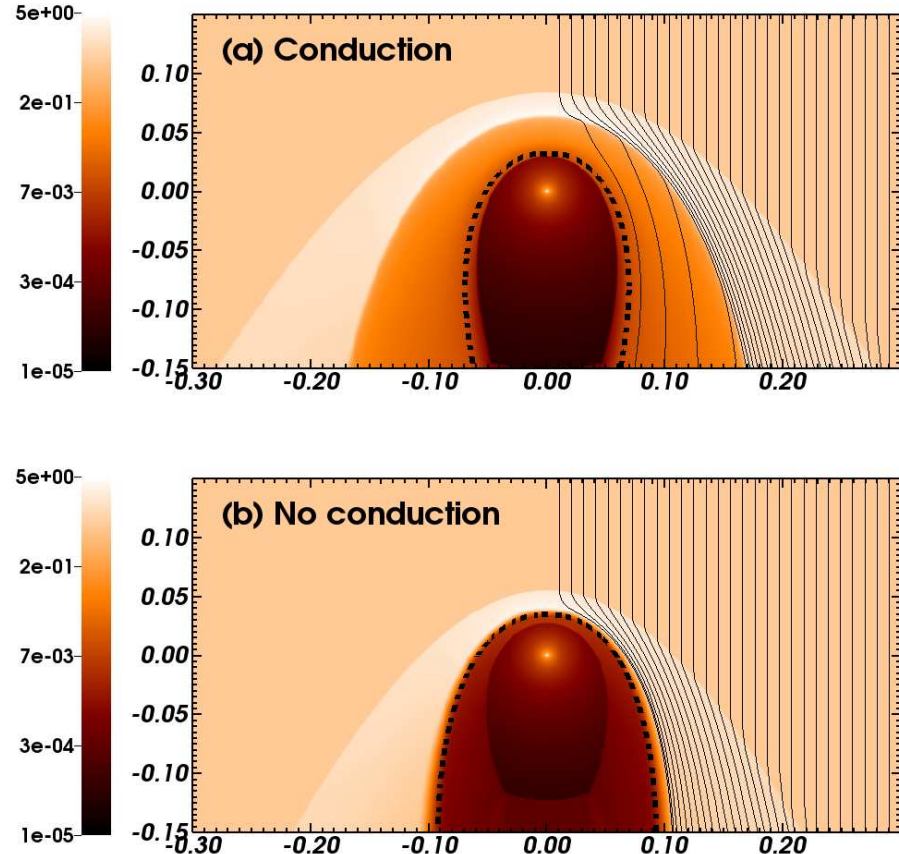
Figure 2.11: Changes in the location of ISM and wind material induced by thermal conduction in the hot bubble of a bow shock. Figures show gas number density (in cm^{-3}) for model MS1040 (a) and for the same setup run without heat conduction (b). For each figure the dotted thick line traces the material discontinuity, $Q(\vec{r}) = 1/2$. The right part of each figure overplots ISM flow streamlines. It highlights the penetration of ISM material into the hot layer of the bow shock because of heat conduction. Comparing the two figures illustrates its effects, increasing the density inside the region of shocked wind and enlarging the global size of the bow shock. The x-axis represents the radial direction and the y-axis the direction of stellar motion (in pc). Not all the computational domain is shown in the figures.
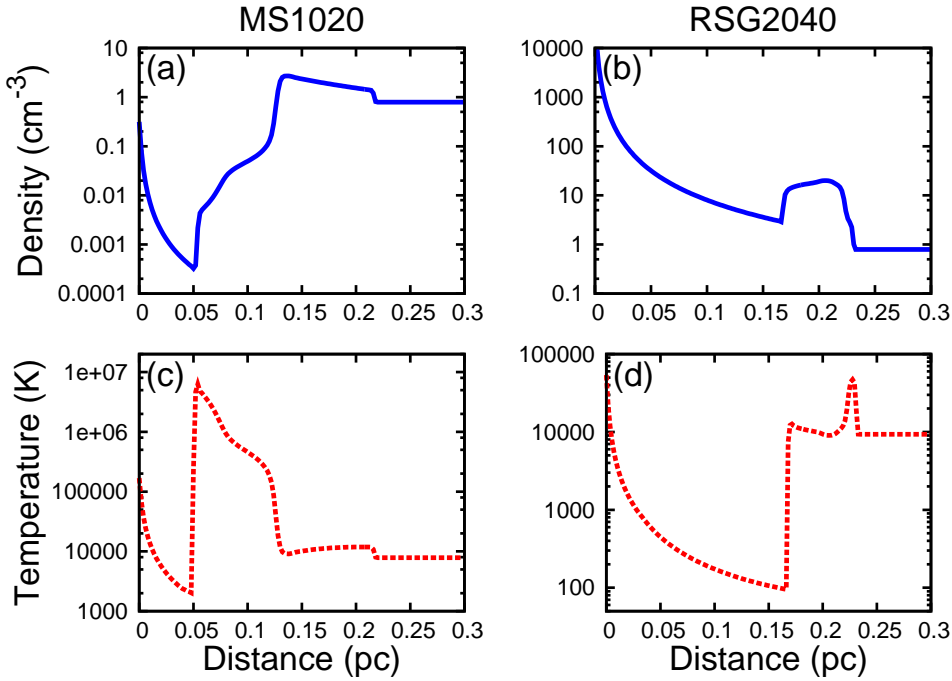
Figure 2.12: Total number density (solid blue lines, in cm^{-3}) and temperature (dotted red lines, in K) profiles for two typical bow shocks of a main sequence and a red supergiant star. The profiles are plotted for the model MS1020 in panels (a) and (c) and for the model RSG2040 in panels (b) and (d) as a function of the distance to the star along the direction of motion.

where $\mathcal{D}$ represents the considered volume. The heating terms are estimated with a similar method, as,

$$\Gamma = 2\pi \iint_{\mathcal{D}} \Gamma_{\alpha} n_H^{\alpha} R dR dz, \tag{2.19}$$

where $\Gamma_{\alpha=1}$ is the heating rate per unit volume for UV heating of grains, and $\Gamma_{\alpha=2}$ is the heating rate per unit volume square for photoionization heating. Inserting the quantities $Q(\vec{r})$ or $1-Q(\vec{r})$ in the integrant of Eq. (2.18) or (2.19), allows us to separate the contributions from wind and ISM material. The panels of Fig. 2.13 also specify the luminosity from Hα emission $L_{H\alpha}$ (calculated using the prescriptions by Osterbrock & Bochkarev (1989), our Appendix 6.2) and the infrared luminosity of reprocessed starlight by dust grains L_{IR} (calculated treating the dust as in Mackey et al. (2012), our Appendix 6.3). Nonetheless, L_{IR} does not contribute to the thermal physics of the plasma and is not included in the calculations of either L_{gas} or L_{wind}. The luminosities L_{gas}, L_{wind}, $L_{H\alpha}$, L_{IR}, the heating rates Γ, and the stellar luminosity $L_{\star}$, provided by the stellar evolution models (Brott et al., 2011), are detailed in Table 2.3.

The bow shock luminosity from optically-thin gas radiation L_{gas} decreases with $v_{\star}$ decreases by an order of magnitude between the models with $v_{\star} = 20$ to $70\,\mathrm{km\,s^{-1}}$, but increases by several orders of magnitude with $\dot{M}$, e.g. $L_{gas} \approx 1.4 \times 10^{31}$ and $\approx 3.9 \times 10^{35}\,\mathrm{erg\,s^{-1}}$ for the models MS1020 and MS4020, respectively. L_{gas} is influenced by i) $v_{\star}$ which governs the compression factor of the shell, and ii) by the size of the bow shocks which increases with $\dot{M}$ and decreases with $v_{\star}$. Moreover, we find that emission by optically-thin cooling is principally caused by optical forbidden lines such as [O II] and [O III] which is included in the cooling curve in the range $\approx 8000 \leq T \leq 6.0 \times 10^{4}$ K (see estimate of the luminosity L_{FL} produced by optical forbidden lines in Table 2.3).

The contribution of optically-thin emission from stellar wind material, L_{wind}, to the total luminosity of optically-thin gas radiation is negligible e.g. $L_{\text{wind}}/L_{\text{gas}} \approx 10^{-6}$ for model MS2020. The variations of L_{wind} roughly follows the variations of L_{gas}. The volume occupied by the shocked wind material is reduced by heat transfer (see black contours in Figs 2.6 to 2.8) and this prevents L_{wind} from becoming important relative to L_{gas}. It implies that most of the emission by radiative cooling comes from shocked ISM gas which cools as the gas is advected from the forward shock to the contact discontinuity.

$L_{\text{H}\alpha}$ is smaller than L_{gas} by about 1−3 orders of magnitude and larger than L_{wind} by 2−5 orders of magnitude, e.g. model MS2040 has $L_{\text{H}\alpha}/L_{\text{gas}} \approx 10^{-1}$ and $L_{\text{H}\alpha}/L_{\text{wind}} \approx 10^4$. The H$\alpha$ emission therefore mainly comes from ISM material. More precisely, we suggest that $L_{\text{H}\alpha}$ originates from the cold innermost shocked ISM since the Hα emissivity $\propto T^{-0.9}$ (our Appendix 6.2). The variations of $L_{\text{H}\alpha}$ follow the global variations of L_{gas}, i.e. the Hα emission is fainter at high $v_\star$, e.g. $L_{\text{H}\alpha} \approx 1.3 \times 10^{33}$ and $\approx 3.6 \times 10^{31} \, \text{erg s}^{-1}$ for models MS2020 and MS2070, respectively. The gap between L_{gas} and $L_{\text{H}\alpha}$ increases with $v_\star$ because the luminosities are calculated for $z > 0$ whereas the Hα maximum is displaced to $z < 0$ as $v_\star$ increases (see further discussion in Section 2.3.4).

L_{IR} is larger than L_{gas} by about 1−3 orders of magnitude in all our simulations, because infrared light is a reemission process that is not included in the calculation of L_{gas} (our Appendix 6.3). We find that $L_{\text{IR}} \gg L_{\text{H}\alpha}$, with a gap increasing with $v_\star$ at a considered $\dot{M}$, e.g. $L_{\text{IR}}/L_{\text{H}\alpha} \approx 10^2$ and $\approx 10^3$ for models MS2020 and MS2070, respectively. These large L_{IR} suggest that bow shocks around main sequence stars should be much more easily observed in the infrared than at optical wavelength. We draw further conclusions on the detectability of bow shocks generated by a runaway main sequence star in Section 2.6.2.

Synthetic emission maps

Figs 2.14, 2.15 and 2.16 show synthetic Hα emission maps of the bow shocks (left) together with dust surface mass density maps (right), from the slowest ($v_\star = 20 \, \text{km s}^{-1}$, top panels) to the fastest ($v_\star = 70 \, \text{km s}^{-1}$, bottom panels) models, respectively. These maps take into account the rotational symmetry of the coordinate system (our Appendix 6.2). The ISM background is ignored, i.e. we set its density to zero in the computation of the projected emissivity and dust density, so that the surface brightness and the surface mass density only refer to the bow shocks. The dust surface density is calculated by projecting the shocked ISM gas, i.e. we considered that the wind material of a star is dust free during the main sequence, weighted by a gas-to-dust ratio (our Appendix 6.3).

The region of maximum Hα surface brightness is located at the apex of the bow shocks in the simulations with $v_\star = 20 \, \text{km s}^{-1}$ and extends or displaces to its tail (i.e. $z < 0$) as $v_\star$ increases. As the ISM gas enters a bow shock generated by a main sequence star, its density increases and the material is heated by thermal conduction towards the contact discontinuity, so its Hα emissivity decreases (see panels (a) and (c) of Fig. 2.12). The competition between temperature increase and gas compression produces the maximum emission at the contact discontinuity which separates hot and cold shocked ISM gas. The reverse shock and the hot bubble are not seen because of both their low density and their high post-shock temperature. Simulations with $v_\star \geq 40 \, \text{km s}^{-1}$ have their peak emissivity in the tail of the bow shock because the gas does not have time to cool at the apex before it is advected downstream. Simulations with high $v_\star$ and strong $\dot{M}$ (e.g. model MS4070) have bow shocks shining in Hα all along their contact discontinuity, i.e. the behaviour of the Hα emissivity with respect to the large compression factor in the shell ($\propto n^2$) overwhelms that of the post-shock temperature ($\propto T^{-0.9}$).

The dust surface mass density increases towards the contact discontinuity (see left panels of Figs 2.14 to 2.16). Panel (a) of Fig. 2.17 shows that normalized cross-sections of both the Hα surface brightness and the dust surface mass density of model MS2040, taken along the direction of motion of the star in
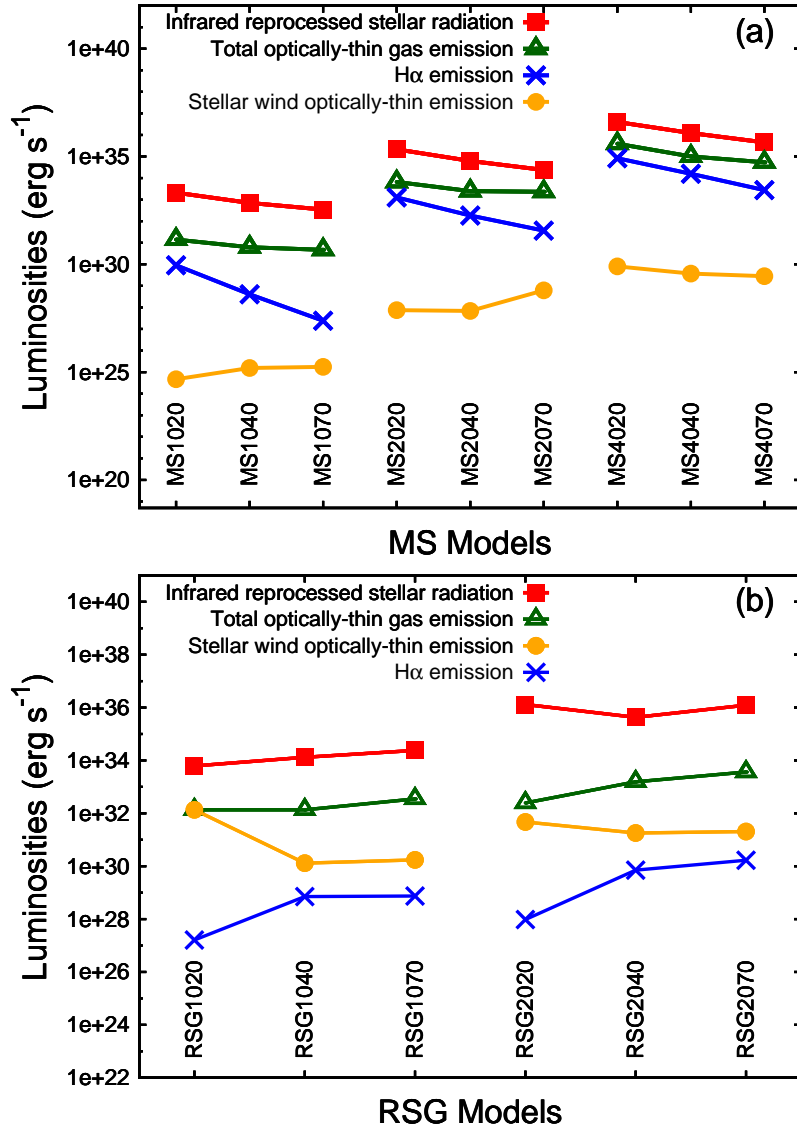
Figure 2.13: Bow shock luminosities and reprocessed stellar infrared radiation for main sequence (a) and red supergiant models (b). The total bow shock luminosity of optically-thin gas radiation (green triangles) is distinguished from the contribution due to the wind material only (orange dots). The luminosity of Hα emission (blue crosses) and the reprocessed infrared stellar radiation (red squares) are also plotted. The infrared radiation is not considered in the simulations and is therefore not included in the total optically-thin gas radiation. The simulation labels are written vertically under each triplet related to a given stellar model (see Table 2.1).

the $z \geq 0$ region of the bow shock, peak at the same distance from the star. We find a similar behaviour for all our bow shock models of hot stars. This suggests that both maximum Hα and infrared emission originate from the same region, i.e. from the cold region of shocked ISM material constituting the outermost part of a bow shock generated by a main sequence star.

The maximum Hα surface brightness of the brightest models (e.g. model MS2020) is larger than 6×10^{-17} erg s^{-1} cm^{-2} arcsec^{-2}, which is above the diffuse emission sensitivity limit of the SuperCOSMOS H-alpha Survey (SHS; Parker et al. 2005) of $1.1 - 2.8 \times 10^{-17}$ erg s^{-1} cm^{-2} arcsec^{-2} and could therefore be observed. The bow shocks around a central star less massive than $20 \, M_{\odot}$ are fainter and could be screened by the H II region generated by their driving star. This could explain why we do not see many stellar wind bow shocks around massive stars in Hα.

2.4 The stellar phase transition

In Fig. 2.18, we show the gas density field in our bow shock model of our initially $20 \, M_{\odot}$ star moving with velocity $v_{\star} = 40 \, \text{km s}^{-1}$ during the stellar phase transition from the main sequence phase (top panel) to the red supergiant phase (bottom panel). The figures correspond to times 3.400, 8.208, 8.430, 8.468 and 8.500 Myr, respectively.

The panel (a) of Fig. 2.18 shows the density field of the circumstellar medium during the main-sequence phase of our star (as in the middle panel of Fig. 2.7). When the main sequence phase ends, both the stellar mass-loss rate $\dot{M}$ and wind density n_{w} increase by more than an order of magnitude (see panel (e) of Fig. 2.3) so that the bow shock inflates and its stand-off distance doubles to reach about 1.7 pc (see panel (b) of Fig. 2.18). At about 8.350 Myr, the wind velocity decreases rapidly and a shell of dense and slow red supergiant wind develops inside the bow shock from the main sequence phase (see panel (c) of Fig. 2.18). A double-arced structure forms at its apsis, as shown in the study detailing a model of Betegeuse returning to the red supergiant phase after undergoing a blue loop (Mackey et al., 2012). Under the influence of the stellar motion, the colliding shells expand beyond the forward shock of the main sequence bow shock and penetrate into the undisturbed ISM. The former bow shock recedes downwards from the direction of stellar motion because it is not supported by the ram pressure of the hot gas, whereas the new-born red supergiant bow shock adjusts itself to the changes in the wind parameters and a new contact discontinuity is established (see panel (d) of Fig. 2.18). After the phase transition, only the bow shock from the red supergiant phase remains in the domain (see panel (e) of Fig. 2.18).

As the star leaves the main sequence phase, the modifications of its wind properties affect the strengths of its termination and forward shocks. The decelerating wind slows the gas velocity by about 2 orders of magnitude in the post-shock region at the reverse shock. The hot bubble cools rapidly ($t_{\text{cool}} \ll t_{\text{dyn}} \ll t_{\text{cond}}$) while the region of shocked wind becomes thicker and denser (see panels (c)-(d) of Fig. 2.3). The transfer of thermal energy by heat conduction ceases because there is no longer a sharp temperature change $\Delta T \geq 10^7$ K across the contact discontinuity. Consequently, the position of the material discontinuity migrates from near the reverse shock to be coincident with the contact discontinuity (see the solid black line in panels (a) to (c) of Fig. 2.18). It sets up a dense and cold bow shock whose layer of shocked wind is thicker than the outer region of ISM gas (see panel (d) of Fig. 2.18).

The above described young bow shock of our initially $20 \, M_{\odot}$ star is typical of the circumstellar medium of a runaway star undergoing a transition from a hot to a cold evolutionary phase. The phase transition timescale is longer for small $v_{\star}$ and shorter for high $v_{\star}$. The bow shocks generated by lower mass stars, e.g. our initially $10 \, M_{\odot}$ star may be more difficult to observe because of their smaller and fainter shells. The wind parameters of our initially $10 \, M_{\odot}$ star change more abruptly ($\sim 10^4$ yr, see panels (a) and (d) of Fig. 2.3), i.e. the preliminary increase of $\dot{M}$ and n_{w} is quicker and the subsequent
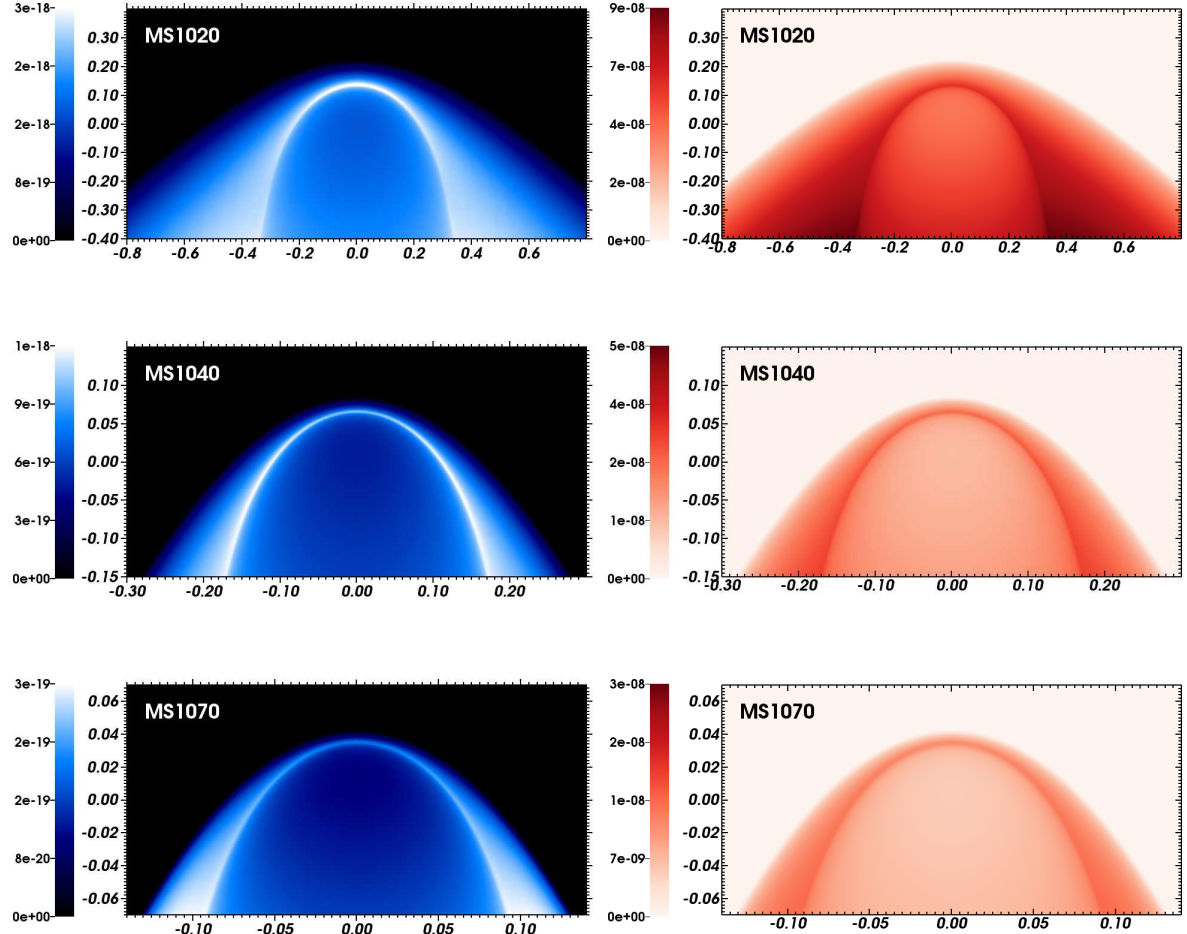
Figure 2.14: The figures show the Hα surface brightness (left, in $\mathrm{erg\,s^{-1}\,cm^{-2}\,arcsec^{-2}}$) and the dust surface mass density (right, in $\mathrm{g\,cm^{-2}}$) for the bow shocks from the main sequence phase of our $10\,\mathrm{M_\odot}$ initial mass star. Quantities are calculated excluding the undisturbed ISM and plotted in the linear scale, as a function of the considered space velocities. The *x*-axis represents the radial direction and the *y*-axis the direction of stellar motion (in pc). Not all of the computational domain is shown in the figures.
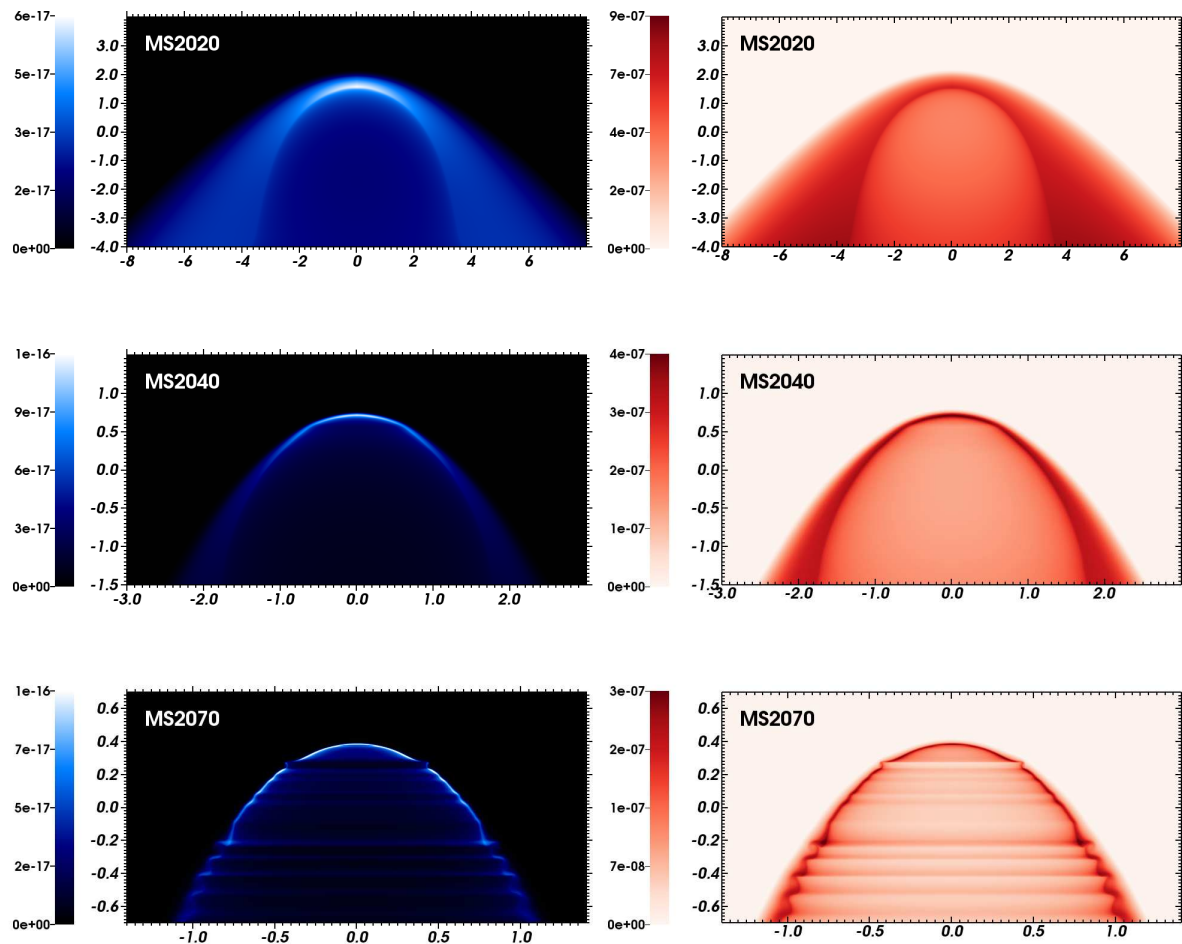
Figure 2.15: As Fig. 2.14, with an initial stellar mass of 20 M$_\odot$.
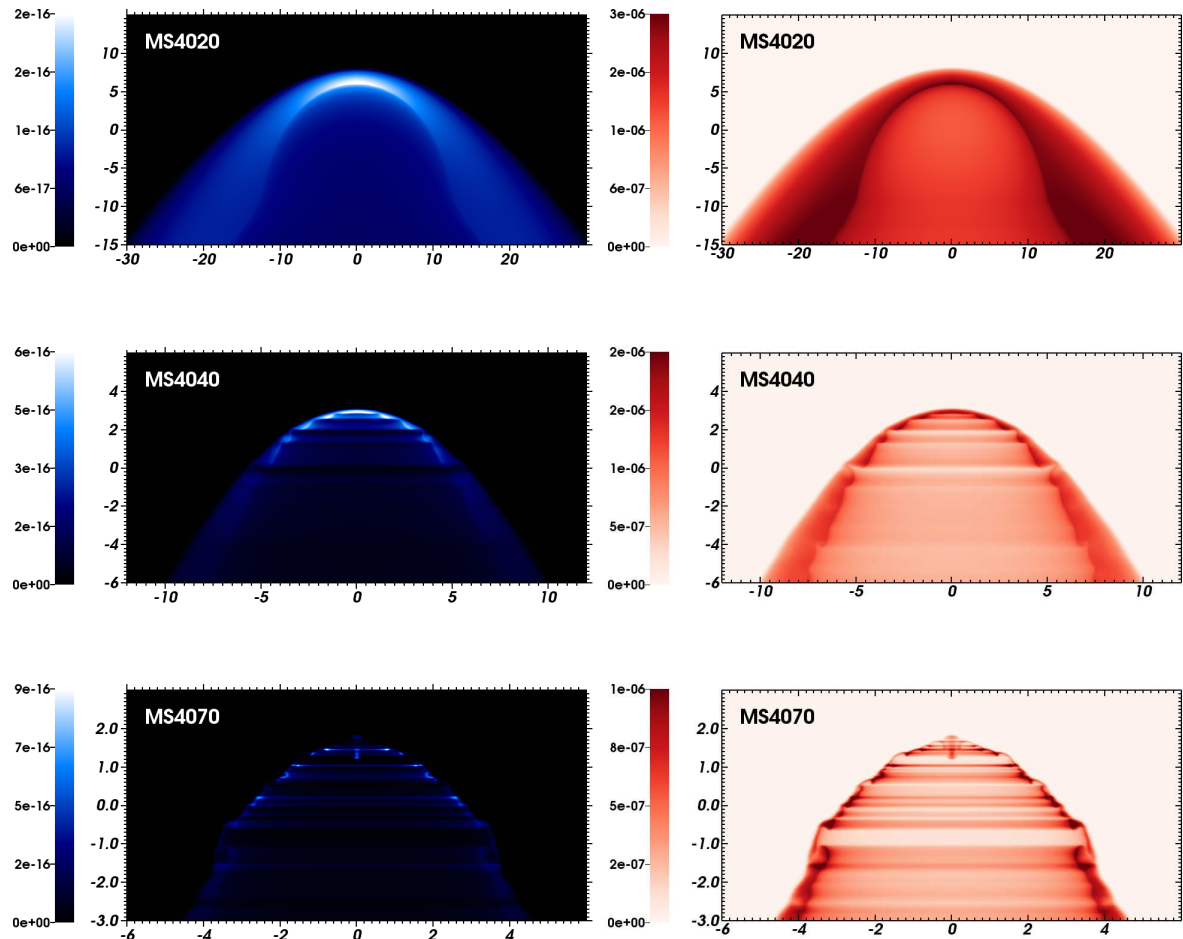
Figure 2.16: As Fig. 2.14, with an initial stellar mass of $40\,\mathrm{M_\odot}$.
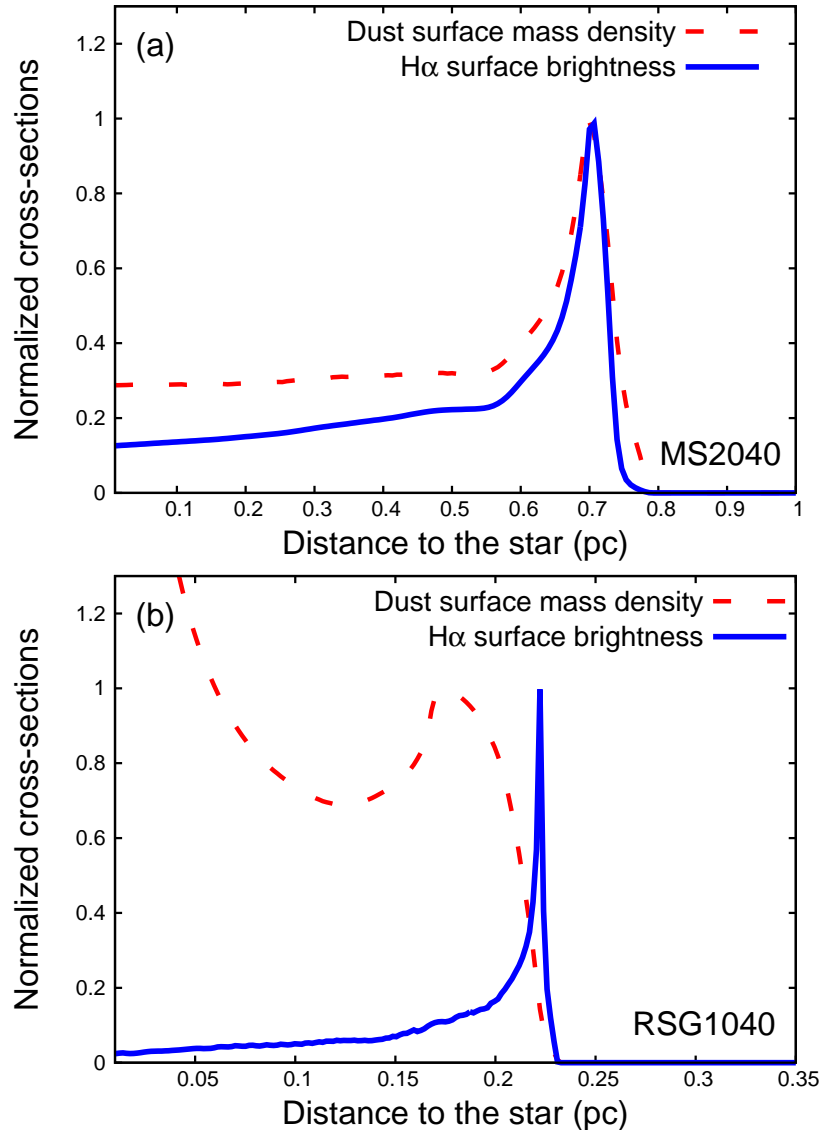
Figure 2.17: Normalized cross-sections taken along the direction of motion of the star, through the Hα surface brightness and the dust surface mass density of the bow shock models MS2040 (a) and RSG1040 (b).

inflation of their bow shock is much less pronounced. The slightly inflated bow shock from the main sequence phase has no time to reach a steady state before the transition happens (as in panel (b) in Fig. 2.18). Our slowly moving star with velocity $20\,\mathrm{km\,s^{-1}}$ (i.e. the model RSG2020) has a supergiant phase that is shorter than the advection time of the hot bow shock, i.e. the former bow shock has not progressed downstream when the star ends its life (Section 2.5).

Our stellar phase transitions last $10^4 - 10^5$ yr, i.e. they are much shorter than both the main sequence and the red supergiant phases (see Fig. 2.3). This makes the direct observation of interacting bow shocks of stars in the field a rare event. Changes in the ambient medium can also affect the properties of bow shocks and wind bubbles, e.g. the so-called Napoleon's hat which surrounds the remnant of the supernova SN1987A (Wampler et al., 1990; Wang & Wampler, 1992) and highlights the recent blue loop of its progenitor (Wang, Dyson & Kahn, 1993).

2.5 The red supergiant phase

2.5.1 Physical characteristics of the bow shocks

We show the gas density field in our bow shock models of the red supergiant phase RSG1020 ($10\,\mathrm{M_\odot}$ initial stellar mass, $v_\star = 20\,\mathrm{km\,s^{-1}}$, upper panel), RSG1040 ($10\,\mathrm{M_\odot}$, $40\,\mathrm{km\,s^{-1}}$, middle panel) and RSG1070 ($10\,\mathrm{M_\odot}$, $70\,\mathrm{km\,s^{-1}}$, lower panel) in Fig. 2.19. Fig. 2.20 is similar for the $20\,\mathrm{M_\odot}$ initial mass star. Figs 2.19 and 2.20 show the contour $Q(\vec{r}) = 1/2$ which traces the discontinuity between the wind and the ISM gas. $R(0)$ and $R(0)/R(90)$ are summarised for each panel in Table 2.2. The simulations were run until at least $40\,t_{\mathrm{cross}}$ after the stellar phase transition, i.e. after the abrupt increase of $\dot{M}$ accompanied by a steep decrease of v_{w} (see panels (d)−(f) of Fig. 2.3).

The size of the bow shocks is predicted to scale as $\dot{M}^{1/2}$, $v_{\mathrm{w}}^{1/2}$ and $v_\star^{-1}$ according to Eq. (2.13) and Baranov, Krasnobaev & Kulikovskii (1971). The scaling between simulations with $v_\star = 40\,\mathrm{km\,s^{-1}}$ and $v_\star = 70\,\mathrm{km\,s^{-1}}$ follows the prediction well, but deviations occur in the $v_\star = 20\,\mathrm{km\,s^{-1}}$ simulations (see Table 2.2). The most deviating simulations either have a very weak shock preventing the forward shock from cooling and forming a thin shell (e.g. model RSG1020), or have not reached a steady state after the phase transition and consist of two interacting bow shocks (e.g. model RSG2020).

The thickness of the shocked layers depends on the cooling physics of the gas. Our simulations with $v_\star = 20\,\mathrm{km\,s^{-1}}$ have a roughly constant density across the material discontinuity. The reverse and forward shocks are weak without much heating and both layers can cool to about the same temperature. In models with $v_\star = 40\,\mathrm{km\,s^{-1}}$ the post-shock temperature at the forward shock is larger than for $v_\star = 20\,\mathrm{km\,s^{-1}}$ and rapid cooling to $T \approx 10^4\,\mathrm{K}$ leads to a stronger compression of the material (see panel (b) and (d) of Fig. 2.12). At $v_\star = 70\,\mathrm{km\,s^{-1}}$ the shocked ISM is a thin layer that has much lower density than the shocked wind (e.g. models RSG1070 and RSG2070). The forward shock is strong, therefore the hot shocked ISM has insufficient time to cool before it is advected downstream. As a consequence, these bow shocks tend to the thin shell limit and are more likely to develop instabilities (e.g. model RSG1070).

Our model RSG1020 with the weakest shocks is stable. Model RSG2020 has an expanding red supergiant wind that is replacing the previous main sequence shell. This simulation still has the remainder of the main sequence wind bow shock interacting with the bow shock from the red supergiant wind at the end of the star life. The contact discontinuity of the supergiant shell shows Rayleigh-Taylor fingers because of the density gradient between the old and new bow shocks. Our models with $v_\star \geq 40\,\mathrm{km\,s^{-1}}$ have $v_{\mathrm{w}} \ll v_\star$ and so their bow shocks develop instabilities which distort their dense and thin shells (Dgani, van Buren & Noriega-Crespo, 1996b). The density field of the model RSG2070 resembles an isothermal bow shock with a distortion of the forward shock typical of the non-linear
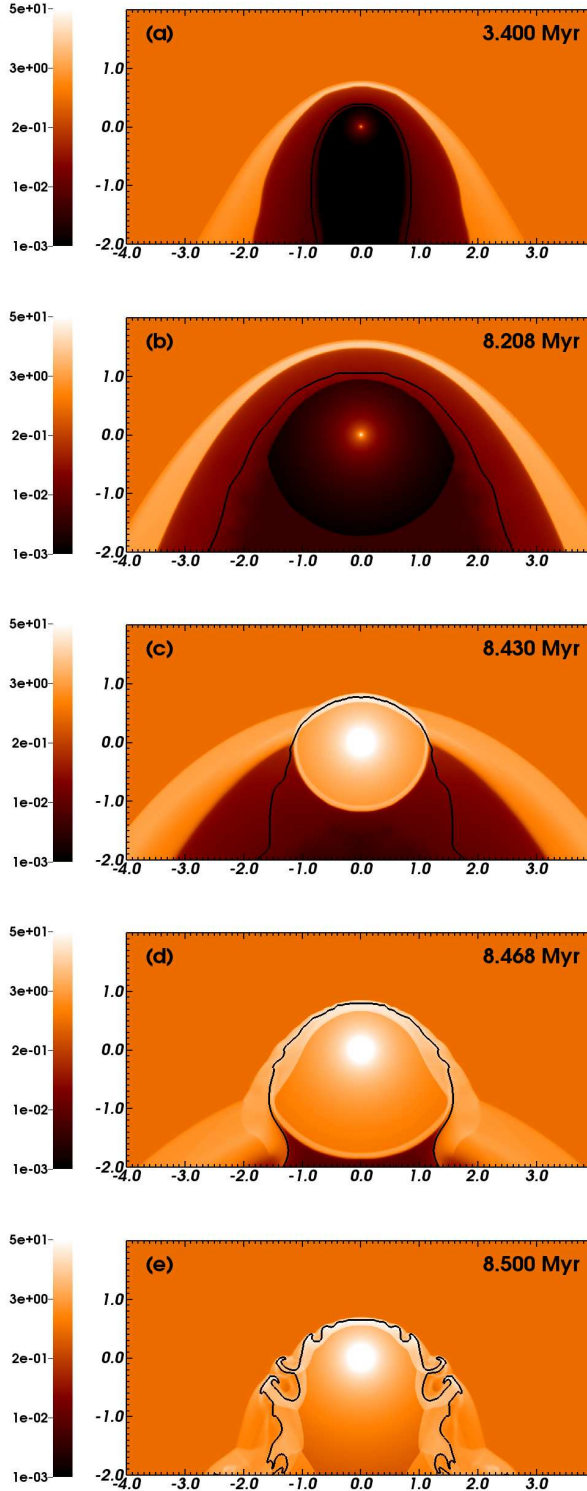
Figure 2.18: Time sequence of the stellar phase transition of the initially $20\,\mathrm{M_\odot}$ star moving with $40\,\mathrm{km\,s^{-1}}$. The figures show the transition from the main sequence phase (top panel) to the red supergiant phase (bottom panel) of the star. The gas number density is shown with a density range from 10^{-3} to $5.0\,\mathrm{cm^{-3}}$ in the logarithmic scale. The solid black contour traces the boundary between wind and ISM material $Q(r) = 1/2$. The x-axis represents the radial direction and the y-axis the direction of stellar motion (in pc).

thin shell and transverse acceleration instabilities (Blondin & Koerwer, 1998). This instability arises because $R(0)$ is much larger than the cooling length in the shocked ISM and shocked wind.

$R(0)/R(90)$ decreases at the contact discontinuity as a function of $v_\star$, e.g. $R(0)/R(90) \approx 0.63$ and ≈ 0.58 for models RSG2020 and RSG2070, respectively. $R(0)/R(90)$ at the forward shock increases with $v_\star$ and $\dot{M}$, e.g. model RSG2020 and RSG2070 have $R(0)/R(90) \approx 0.46$ and ≈ 0.59, respectively. These measures do not perfectly satisfy Wilkin solution, except for the models with $v_\star = 70\,\mathrm{km\,s^{-1}}$, although the ratios for the contact discontinuity are all within 10 per cent of the analytic solution. Only the $v_\star = 70\,\mathrm{km\,s^{-1}}$ simulations, with their thin bow shocks that come closest to the isothermal limit, have forward shocks that satisfy $R(0)/R(90) \approx 1/\sqrt{3}$ (see Fig. 2.20).

Because the temperature jumps are small across the interfaces and shocks in the bow shocks around the red supergiant stars, e.g. $\Delta T \approx 10^3$ K at the reverse shock and $\Delta T \approx 4 \times 10^4$ K at the forward shock of model RSG1040, thermal conduction is not important. The bow shocks around red supergiant stars therefore have coincident contact and material discontinuities (see black contours in Figs 2.21 and 2.22).

2.5.2 Bow shock emissivity

Luminosities

The luminosities L_{gas}, L_{wind}, $L_{\mathrm{H}\alpha}$ and L_{IR} of the bow shocks generated by our red supergiant models are plotted as a function of $\dot{M}$ and $v_\star$ in panel (b) of Fig. 2.13. As is the case for bow shocks produced by main sequence stars, L_{gas} is influenced by $v_\star$ and by the size of the bow shock. $L_{\mathrm{gas}} \propto n^2$ and slightly increases with $v_\star$ because the compression factor of the shell is larger for high $v_\star$. The variations in size drive the increase of L_{gas} as a function of $\dot{M}$ if $v_\star$ is fixed. In contrast to the bow shocks around main sequence stars, the increase of L_{gas} seen in panel (b) of Fig. 2.13 for a given model triplet shows that the luminosity is more influenced by the density than by the volume of the bow shocks.

L_{wind} is several orders of magnitude dimmer than L_{gas}, e.g. $L_{\mathrm{wind}}/L_{\mathrm{gas}} \approx 10^{-2}$ for model RSG1040, i.e. the wind contribution is negligible compared to the luminosity of the shocked ISM gas. The difference between L_{wind} and L_{gas} is less than in our main sequence models because the gas cooling behind the slow red supergiant reverse shock is efficient. Model RSG1020 behaves differently because even though it scales in volume with model RSG1040, its small $v_\star$ results in a weak forward shock which is cool so there is little cooling in the shocked ISM ($L_{\mathrm{wind}} \sim L_{\mathrm{gas}}$). The total bow shock luminosity of optically-thin radiation of model RSG2020 is increased by a contribution from the former main sequence bow shock around the forming red supergiant shell (see upper panel of Fig. 2.20).

The bow shock luminosity of Hα emission is negligible compared to the total bow shock luminosity, e.g. $L_{\mathrm{H}\alpha}/L_{\mathrm{gas}} \approx 10^{-3}$–$10^{-5}$, see lower panel of Fig. 2.13. $L_{\mathrm{H}\alpha}$ then increases with $v_\star$, e.g. $L_{\mathrm{H}\alpha} \approx 7.1 \times 10^{29}$ and $\approx 1.7 \times 10^{30}\,\mathrm{erg\,s^{-1}}$ for model RSG2040 and RSG2070, respectively. The Hα emission of the bow shocks for the 10 and $20\,\mathrm{M_\odot}$ stars differs by ≈ 1 order of magnitude. Models RSG1020 and RSG2020 have little Hα emission because their weak forward shocks prevent both the formation of a dense shell and do not ionize the gas significantly.

The infrared luminosity is such that $L_{\mathrm{IR}} \gg L_{\mathrm{gas}}$. This is because of the fact that L_{IR} provides an upper limit for the infrared light (our Appendix 6.3) and because the circumstellar medium around red supergiants is denser than that during the main sequence phase, i.e. there is a lot of dust from the stellar wind in these bow shocks that can reprocess the stellar radiation. L_{IR} increases by about two orders of magnitude between the 10 and $20\,\mathrm{M_\odot}$ models if $v_\star$ is considered fixed which is explained by their different wind and bow shock densities (see Figs 2.19 and 2.20). Model RSG2020 does not fit this trend because the huge mass of the bow shock of the previous evolutionary phase affects its luminosity $L_{\mathrm{IR}} \approx 1.3 \times 10^{36}\,\mathrm{erg\,s^{-1}}$. The enormous infrared luminosities of bow shocks around red supergiant
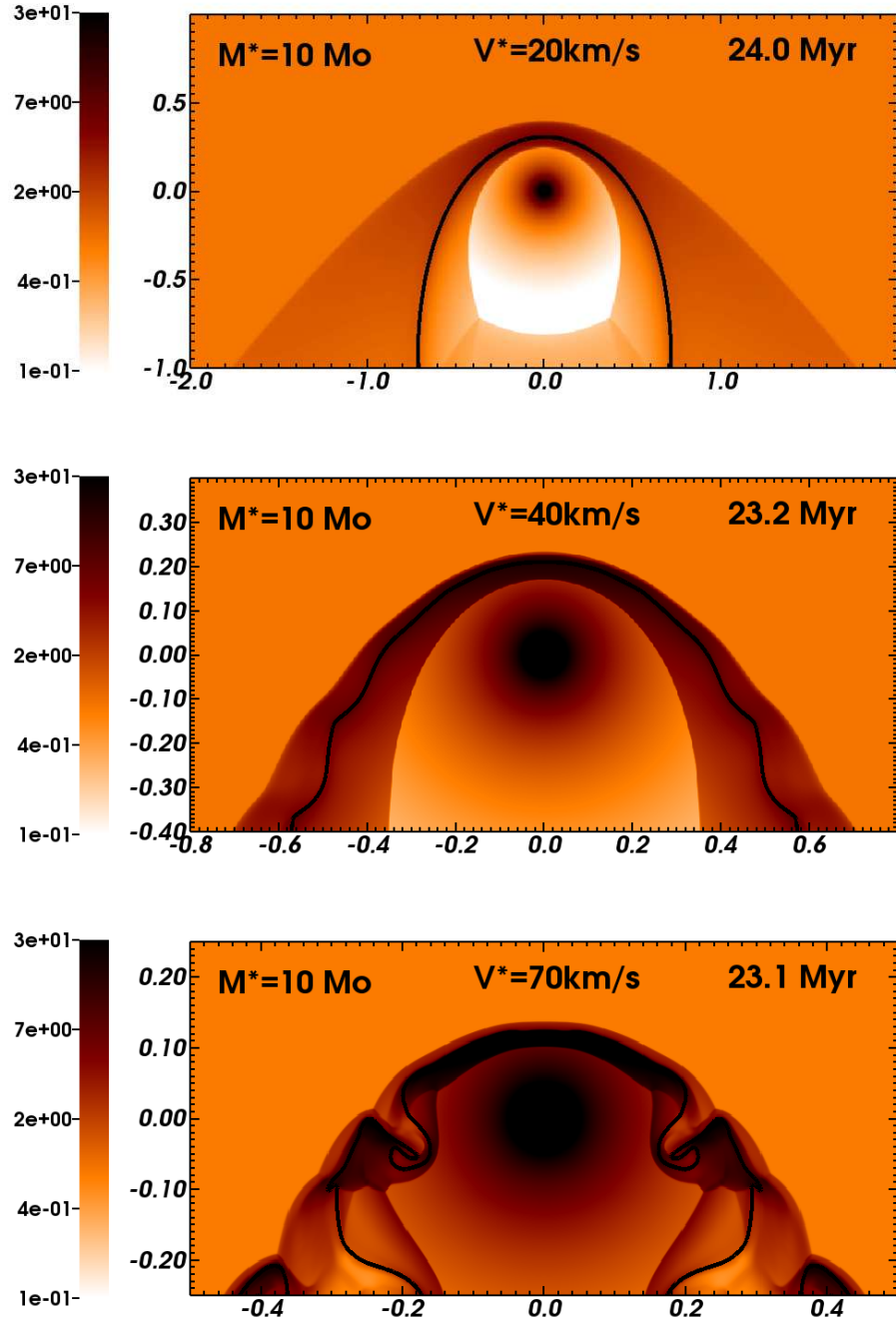
Figure 2.19: Grid of stellar wind bow shocks from the red supergiant phase of the $10\,M_\odot$ initial mass star according to the space velocity with respect to the ISM, with $20\,\mathrm{km\,s^{-1}}$ (top panel), $40\,\mathrm{km\,s^{-1}}$ (middle panel) and $70\,\mathrm{km\,s^{-1}}$ (bottom panel). Models nomenclature follows Table 2.1. Gas number density is shown with a density range from 0.1 to $30.0\,\mathrm{cm^{-3}}$ in the logarithmic scale. Note that the color scale is upset compared to Figs 2.6, 2.7 and 2.8. The solid black contours trace the boundary between wind and ISM, $Q(\vec{r}) = 1/2$. The *x*-axis represents the radial direction and the *y*-axis the direction of stellar motion (in pc). Not all the computational domain is shown in the figures.
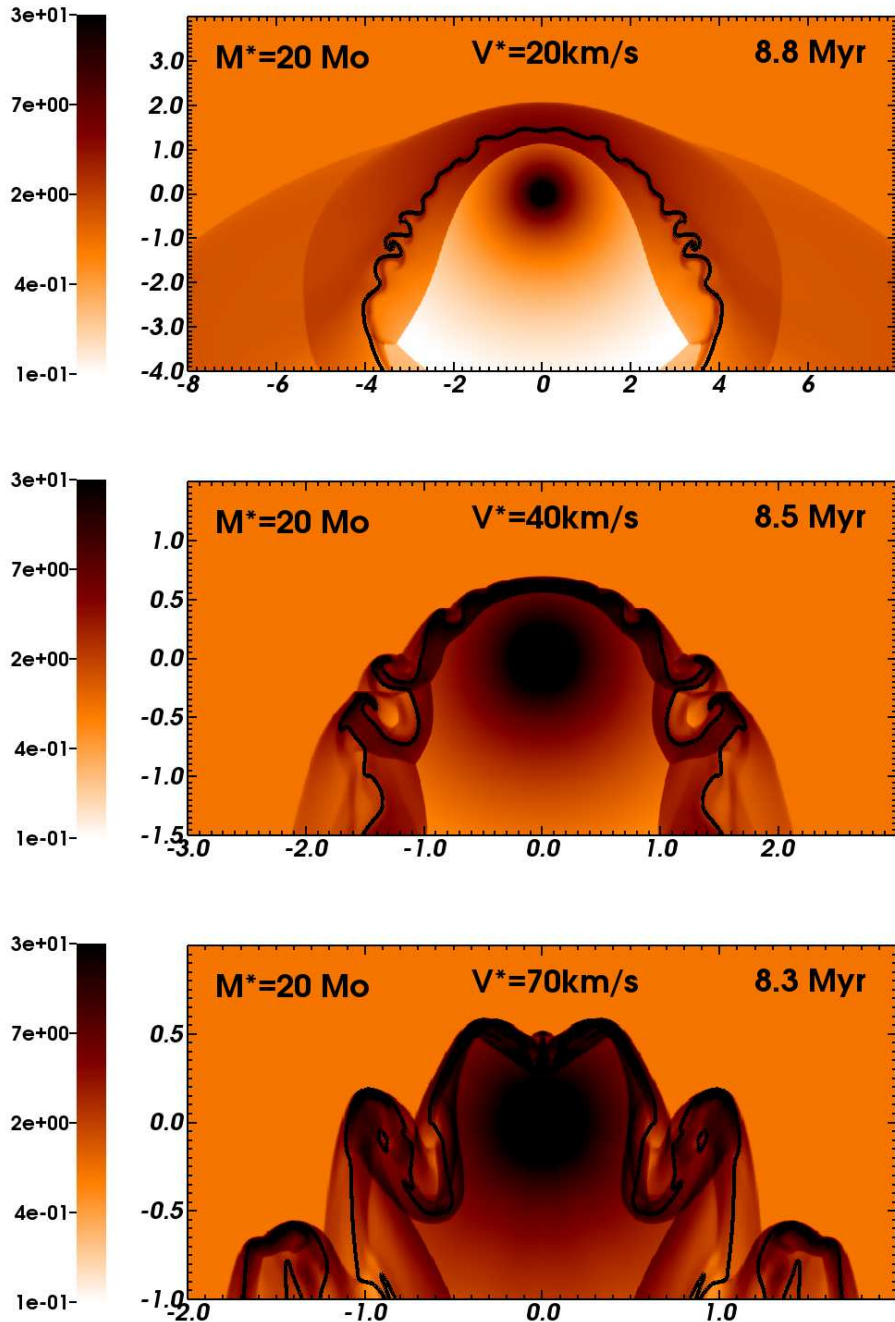
Figure 2.20: As Fig. 2.19, with an initial stellar mass of 20 M$_\odot$.

Table 2.3: Stellar and bow shock luminosities. $L_\star$ represents the stellar luminosity, $L_{\rm gas}$ is the bow shock luminosity from optically-thin cooling of the gas, and $L_{\rm wind}$ the part of $L_{\rm gas}$ originating from the wind material. $L_{{\rm H}\alpha}$ is the luminosity of Hα emission and $L_{\rm FL}$ is the luminosity generated for photoionized bow shocks by cooling from [O II] and [O III] forbidden lines emission is the range of $\approx 8000 \leq T \leq 6.0 \times 10^4$ K. $L_{\rm IR}$ is the infrared luminosity, calculated on the basis of reemission of starlight by the dust grains (our Appendix 6.3). Γ represents the radiative heating of the gas (see Eq. 2.19).

Model	$L_\star$ (erg s^{-1})	$L_{\rm gas}$ (erg s^{-1})	$L_{\rm wind}$ (erg s^{-1})	$L_{{\rm H}\alpha}$ (erg s^{-1})	$L_{\rm FL}$ (erg s^{-1})	$L_{\rm IR}$ (erg s^{-1})	Γ (erg s^{-1})
MS1020	2.42×10^{37}	1.39×10^{31}	4.66×10^{24}	9.00×10^{29}	1.26×10^{31}	2.10×10^{33}	5.32×10^{30}
MS1040	2.42×10^{37}	6.17×10^{30}	1.55×10^{25}	4.10×10^{28}	5.75×10^{30}	7.00×10^{32}	2.53×10^{29}
MS1070	2.42×10^{37}	4.70×10^{30}	1.76×10^{25}	2.40×10^{27}	3.53×10^{30}	3.50×10^{32}	1.21×10^{28}
RSG1020	7.66×10^{37}	1.16×10^{32}	1.35×10^{32}	1.60×10^{27}	–	6.20×10^{33}	2.27×10^{30}
RSG1040	7.32×10^{37}	1.35×10^{32}	1.30×10^{30}	7.10×10^{29}	–	1.30×10^{34}	3.62×10^{28}
RSG1070	7.32×10^{37}	3.50×10^{32}	1.73×10^{30}	7.50×10^{29}	–	2.40×10^{34}	2.30×10^{28}
MS2020	2.59×10^{38}	6.60×10^{33}	7.50×10^{27}	1.30×10^{33}	5.57×10^{33}	2.10×10^{35}	7.90×10^{33}
MS2040	2.16×10^{38}	2.48×10^{33}	6.83×10^{27}	1.90×10^{32}	2.17×10^{33}	6.20×10^{34}	1.00×10^{33}
MS2070	1.64×10^{38}	2.32×10^{33}	6.18×10^{28}	3.60×10^{31}	1.69×10^{33}	2.40×10^{34}	2.20×10^{32}
RSG2020	5.94×10^{38}	2.46×10^{32}	4.70×10^{31}	9.70×10^{27}	–	1.30×10^{36}	1.34×10^{31}
RSG2040	5.18×10^{38}	1.56×10^{33}	1.80×10^{31}	7.10×10^{29}	–	4.30×10^{35}	1.42×10^{31}
RSG2070	5.95×10^{38}	3.65×10^{33}	2.04×10^{31}	1.70×10^{30}	–	1.20×10^{36}	$9,98 \times 10^{30}$
MS4020	1.30×10^{39}	3.90×10^{35}	8.00×10^{29}	8.30×10^{34}	3.30×10^{35}	4.00×10^{36}	4.76×10^{35}
MS4040	1.03×10^{39}	1.00×10^{35}	3.70×10^{29}	1.60×10^{34}	8.74×10^{34}	1.20×10^{36}	9.10×10^{34}
MS4070	9.00×10^{38}	5.40×10^{34}	2.80×10^{29}	2.80×10^{33}	4.46×10^{34}	4.50×10^{35}	1.60×10^{34}

stars compared to their optically-thin gas radiation suggests that they should be more easily observed in the infrared than in the optical bands and partly explains why the bow shock around Betelgeuse was discovered in the infrared.

Synthetic emission maps

Figs 2.21 and 2.22 show the bow shock Hα surface brightness (left panels) and dust surface mass density (right panels) for our 10 and 20 M$_\odot$ models, respectively. Each figure shows $v_\star = 20\,\mathrm{km\,s^{-1}}$ (top), $v_\star = 40\,\mathrm{km\,s^{-1}}$ (middle) and $v_\star = 70\,\mathrm{km\,s^{-1}}$ (bottom). For red supergiant stars we assume that both the stellar wind and the ISM gas include dust (our Appendix 6.3).

In our models the Hα emission of bow shocks produced by red supergiant stars originates from the shocked ISM in the post-shock region at the forward shock. The region of maximum emission is at the apex of the structure for simulations with $v_\star = 20\,\mathrm{km\,s^{-1}}$ and is extended to the tail as $v_\star$ increases, e.g. for the model RSG1040. The surface brightness increases with $v_\star$ and $\dot{M}$ because the post-shock temperature at the forward shock increases when the shocks are stronger. However, these Hα emission is fainter by several orders of magnitude than our bow shock models for hot stars (see Figs 2.14 and 2.21). As a consequence, these bow shocks are not likely to be observed in Hα because their Hα surface brightnesses is below the detection sensitivity of the SHS (Parker et al., 2005).

Panel (b) of Fig. 2.17 plots the normalized cross-sections taken from the Hα surface brightness and the dust surface mass density of the bow shock model RSG1020. The Hα emission is maximum in the post-shock region at the forward shock, whereas the dust surface density peaks in the post-shock region at the reverse shock of the bow shock. All our models for bow shocks for red supergiants exhibit such comportment which suggests that Hα and infrared emission do not originate from the same region of the bow shock. Because the red supergiant wind is denser than the ISM, most of the infrared emission probably originates from the shocked wind.

2.6 Discussion

2.6.1 Comparison with previous works

Bow shocks around main sequence stars

We carried out tests with two numerical methods to integrate the parabolic term associated with heat conduction: the explicit method used in Comerón & Kaper (1998) and the Super-Time-Step (STS) method (Alexiades, Amiez & Gremaud, 1996). The results are consistent between the two methods, except that the explicit scheme is less diffusive but also extremely time consuming. We adopt the Super-Time-Step algorithm given that the spatial resolution of our models is better than in Comerón & Kaper (1998).

We tested this method using the code PLUTO with respect to the models in Comerón & Kaper (1998). Our simulations support their study in that all the bow shocks are reproduced reasonably well. Our simulations that aim to reproduce the highly unstable simulation cases C (bow shock with strong wind) and E (bow shock in high density ambient medium) in Comerón & Kaper (1998) are more dramatically affected by the development of overdensities at the apex of the structure which later govern the shape of the instabilities which distort the whole bow shocks. This is because of our higher spatial resolution. Our results vary depending on the chosen coordinate system and the interpolation scheme used at the symmetry axis. We conclude that instabilities growing at the apsis are artificially confined near $R = 0$ by the rotational symmetry imposed by the coordinate system.
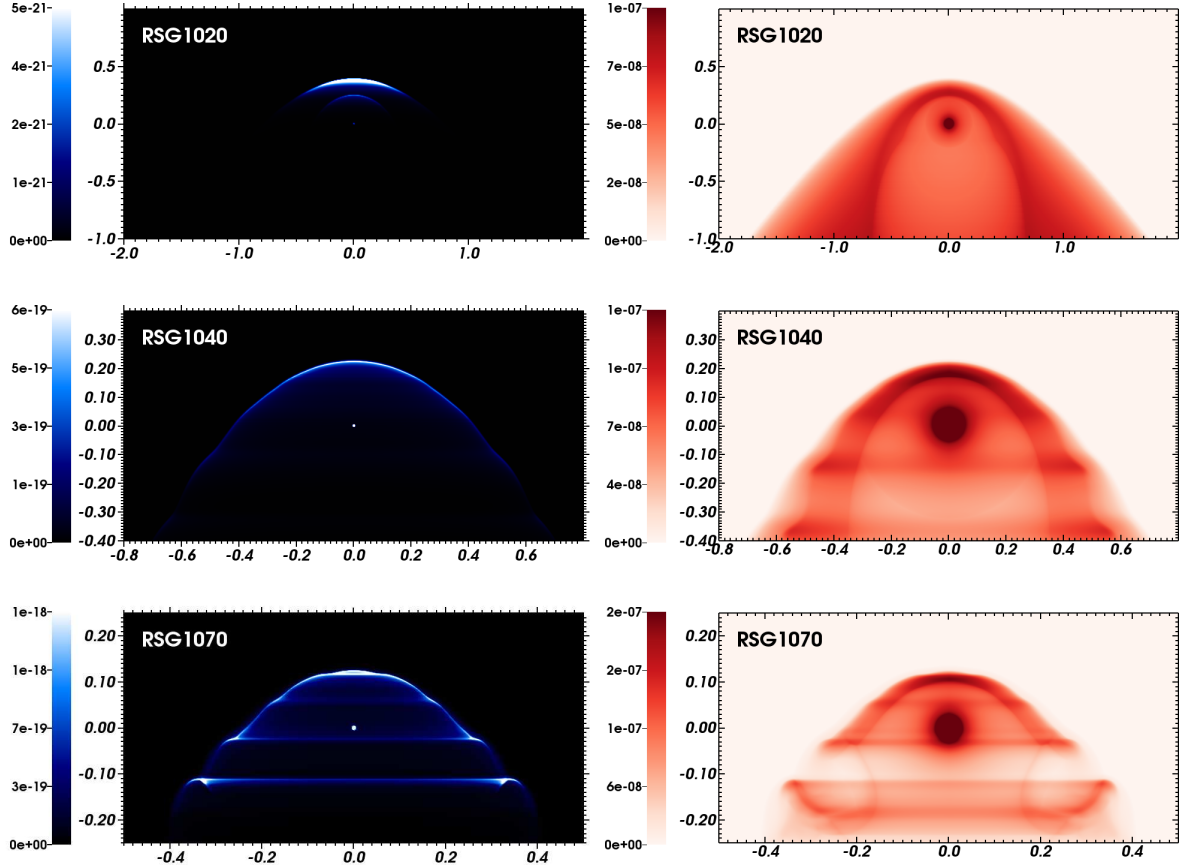
Figure 2.21: The figures show the Hα surface brightness (left, in erg s^{-1} cm^{-2} arcsec^{-2}) and the dust surface mass density (right, in g cm^{-2}) for the bow shocks from the red supergiant phase of our 10 M$_\odot$ initial mass star. Quantities are calculated excluding the undisturbed ISM and plotted in the linear scale, as a function of the considered space velocities. The x-axis represents the radial direction and the y-axis the direction of stellar motion (in pc). Not all of the computational domain is shown in the figures.
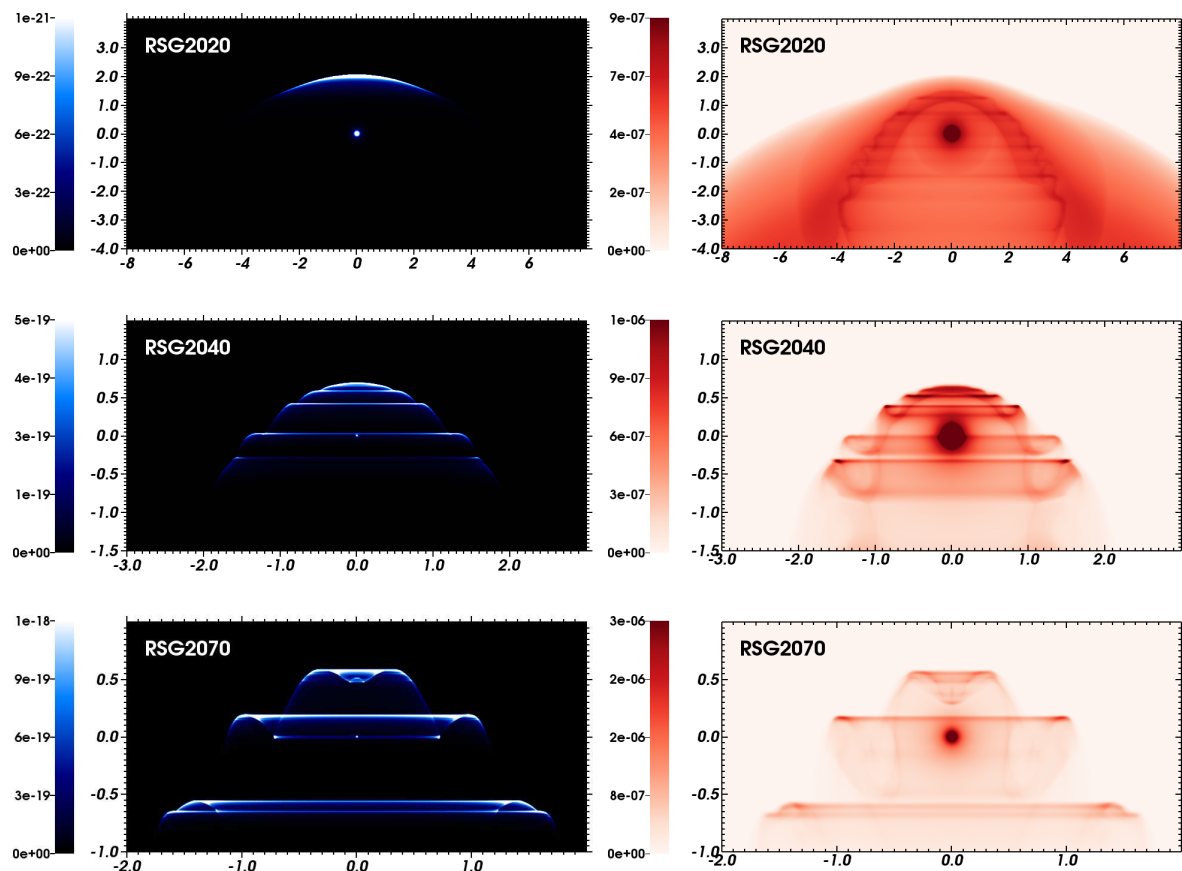
Figure 2.22: As Fig. 2.21, with an initial stellar mass of $20\,\mathrm{M_\odot}$.

Our models with $v_\star = 20\,\mathrm{km\,s^{-1}}$ produce weak bow shocks. Such bow shocks correspond to the Case A model in Comerón & Kaper (1998), which uses a similar wind velocity ($\sim 1000\,\mathrm{km\,s^{-1}}$), and a mass-loss rate of $10^{-7}\,\mathrm{M_\odot\,yr^{-1}}$ (i.e. 1.5 orders of magnitude larger, similar and one order of magnitude smaller than our 10, 20 and $40\,\mathrm{M_\odot}$ stars, respectively), a less dense ISM ($0.1\,\mathrm{cm^{-3}}$) and a much higher $v_\star$ ($\approx 100\,\mathrm{km\,s^{-1}}$). Our models include cooling by forbidden collisionally excited lines and assume the same $T_{\mathrm{ISM}} \approx 8000\,\mathrm{K}$ as their Case A. These models are similar because their weak forward shocks do not allow the gas to cool rapidly and they all have a region of shocked ISM thicker than the hot bubble along the direction of motion of the star, as signified by the absence of a sharp density peak in the region of shocked ISM in panel (a) of Fig. 2.12, compared to lower panel of fig. 7 in Comerón & Kaper (1998).

Our models MS4040 and MS4070 both have strong shocks and are similar to the Case C model in Comerón & Kaper (1998). Their case C uses a faster $v_{\mathrm{w}} \approx 3000\,\mathrm{km\,s^{-1}}$, a slightly larger $\dot{M} \sim 10^{-6}\,\mathrm{M_\odot\,yr^{-1}}$, a less dense ISM ($0.1\,\mathrm{cm^{-3}}$) and a higher $v_\star$ ($\approx 100\,\mathrm{km\,s^{-1}}$). The combination of fast $v_\star$ and fast v_{w} induces a strong compression factor at the forward shock where the gas cools rapidly and reduces the thickness of the shocked ISM into a thin, unstable shell. These models best fit analytical approximations of an infinitely thin bow shock (Comerón & Kaper, 1998).

We conclude that for overlapping parameters, i.e. for similar $\dot{M}$ and $v_\star$, our results agree well with existing models in terms of bow shock morphology and stability. We extend the parameter space for stars with weak winds, $\dot{M} \approx 10^{-9.5}$ in our $10\,\mathrm{M_\odot}$ model and use the typical particle density of the Galactic plane.

Bow shocks around red supergiant stars

We tested our numerical setup to reproduce the double bow shock around Betelgeuse (Mackey et al., 2012). Including heat conduction did not significantly change the results and we successfully reproduced the model using the same cooling curve as in Mackey et al. (2012). The simulations of red supergiant bow shocks of Mohamed, Mackey & Langer (2012) used a more precise time-dependent cooling network (Smith & Rosen, 2003) and, because of their Lagragian nature, these models are intrinsically better in terms of spatial resolution. To produce more detailed models which can predict principal emission line ratio is beyond the scope of this study but could be achieved using the native multi-ion non-equilibrium cooling module of the code PLUTO (Teşileanu, Mignone & Massaglia, 2008).

Model RSG2020 shows a weak bow shock with a dense and cold shell expanding into the former hot and smooth bow shock. Rayleigh-Taylor instabilities develop at the discontinuity between the two colliding bow shocks as in the model of Betelgeuse's multiple arched bow shock in Mackey et al. (2012).

Our simulations with $v_\star = 40\,\mathrm{km\,s^{-1}}$ show radiative forward shocks and unstable contact discontinuities. Model RSG1040 resembles the simulations of van Marle et al. (2011a) and Decin et al. (2012) which have a similar $\dot{M} \approx 3 \times 10^{-6}\,\mathrm{M_\odot\,yr^{-1}}$ but a smaller $v_\star \approx 28\,\mathrm{km\,s^{-1}}$ and denser ISM ($2\,\mathrm{cm^{-3}}$). We do not use the two-fluid approach of van Marle et al. (2011a) which allows the modelling of ISM dust grains and explains the differences in terms of stability of the contact discontinuity. Their simulation with type 1 grains is more unstable than our model RSG1040, probably because they use a denser ISM. Model RSG2040 has a thinner region of shocked ISM compared to the region of shocked wind which makes this model unstable. The instabilities of model RSG2040 are similar to the clumpy forward shock of models A-C in Mohamed, Mackey & Langer (2012) which have larger $\dot{M}$ and a denser medium.

Our simulations with $v_\star = 70\,\mathrm{km\,s^{-1}}$ show the largest compression. Model RSG2070 has a strongly turbulent shell with dramatic instabilities, consistent with the high $v_\star$ and high Mach number model in Blondin & Koerwer (1998). The data hold in RSG2070 illustrates the transverse acceleration instability where an isotropically expanding wind from the star meets the collinear ISM flow and pushes the developing eddies sidewards. Model RSG2070 is different from the model D with radiative cooling

of Mohamed, Mackey & Langer (2012) which has a similar $v_\star \approx 72.5\,\mathrm{km\,s^{-1}}$ but a weaker wind $\dot{M} \approx 3.1 \times 10^{-6}\,\mathrm{M_\odot\,yr^{-1}}$. Because of its particular initial conditions, i.e. a hotter and diluted ISM with $n \approx 0.3\,\mathrm{cm^{-3}}$ and $T_\mathrm{ISM} \approx 8000\,\mathrm{K}$, the gas does not cool efficiently at the forward shock and the post-shock regions of the bow shock remain isothermal, see right panel of fig. 10 of Mohamed, Mackey & Langer (2012).

With similar model parameters, our results agree well with the existing models and we conclude that heat conduction is not mandatory to model bow shocks from cool stars. Because we neglect the effects of dust dynamics on the bow shocks stability, our models differ slightly from existing models with $v_\star \approx 30-40\,\mathrm{km\,s^{-1}}$. However, this does not concern the overall shape of the bow shocks but rather the (in)stability of their contact discontinuities. We extended the parameter space by introducing models with $v_\star = 20\,\mathrm{km\,s^{-1}}$.

2.6.2 On the observability of bow shocks from massive runaway stars

Fig. 2.23 plots the luminosities of our bow shock models for main sequence (top panels) and red supergiant (bottom panels) stars as a function of $M_\star$ and $v_\star$. With respect to their optically-thin gas radiation, the brightest bow shocks produced by main-sequence stars are generated by the more massive stars moving with a slow space velocity, e.g. the $40\,\mathrm{M_\odot}$ main sequence star moving with $v_\star = 20\,\mathrm{km\,s^{-1}}$, and the brightest bow shocks produced by red supergiants are generated by the more massive star of our sample, moving at high space velocity i.e. a $20\,M_\odot$ red supergiant moving with $v_\star = 70\,\mathrm{km\,s^{-1}}$ (see panels (a) and (d) of Fig. 2.23). The same points arise from the luminosity of Hα emission (see panels (b) and (e) of Fig. 2.23). The infrared luminosity indicates that the brightest bow shocks generated by a main sequence star are produced by high mass, low velocity stars (see panel (c) in Fig. 2.23). Concerning the bow shocks generated by red supergiant stars, their infrared luminosities suggest that the brightest are produced by high-mass stars moving at either low or fast space velocities (see panel (f) in Fig. 2.23).

Because L_IR is larger than $L_{\mathrm{H}\alpha}$ or L_gas, the infrared waveband is the most appropriate to search for stellar-wind bow shocks around main sequence and red supergiant stars. According to our study, bow shocks produced by high mass main sequence stars moving with low space velocities should be the easiest ones to observe in the infrared. The most numerous runaway stars have a low space velocity (Eldridge, Langer & Tout, 2011) and consequently bow shocks produced by high-mass red supergiants moving with low space velocity are the most numerous ones, and the probability to detect one of them is larger. Many stellar wind bow shocks surrounding hot stars ejected from stellar cluster are detected by means of their $\leq 24\,\mu m$ infrared signature (see Gvaramadze, Kroupa & Pflamm-Altenburg, 2010a; Gvaramadze et al., 2011a). Because our study focuses on the most probable bow shocks forming around stars exiled from their parent cluster, we expect them to be most prominent in that waveband.

Fig. 2.24 plots the bow shock luminosities for our main sequence models as a function of $R(0)^3$. It shows a strong scaling relation between the luminosities and the volume of the bow shocks, i.e. the brightnesses of these bow shocks are governed by the wind momentum. The optical luminosities of our red supergiant models do not satisfy these fits because the gas is weakly ionized. This behaviour concerns the overall luminosities of the bow shocks, not their surface brightnesses. Nevertheless, this statement is only valid for the used ISM density, and some effects may make them dimmer, e.g. a lower density medium increasing their volume $\sim R(0)^3 \sim 1/\sqrt{n_\mathrm{ISM}^3}$.
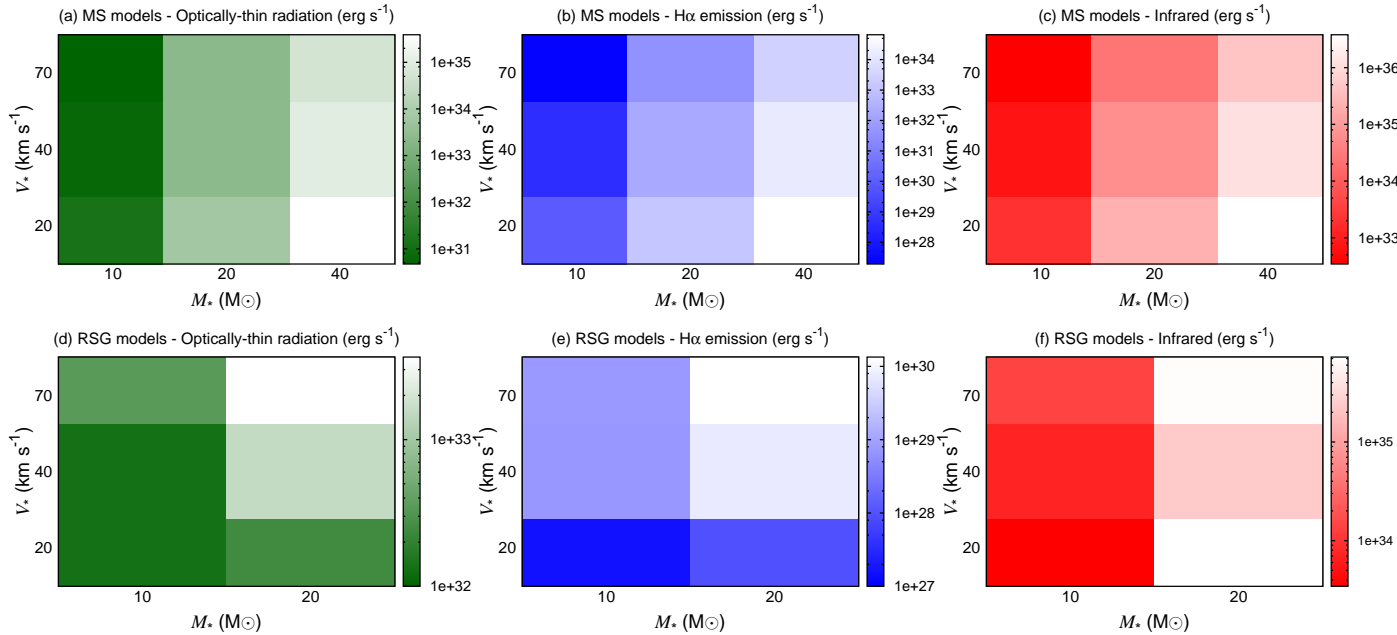
Figure 2.23: Bow shocks luminosities (in erg s⁻¹) in our main sequence (top panels) and red supergiant (bottom panels) models. We show the luminosity of optically-thin cooling (left green panels), Hα emission (middle blue panels) and reprocessed infrared starlight by dust grains (right red panels) of Table 2.3. On each plot the *x*-axis is the initial mass $M_\star$ (in M$_\odot$) and the *y*-axis is the space velocity $v_\star$ (in km s⁻¹) of our runaway stars.
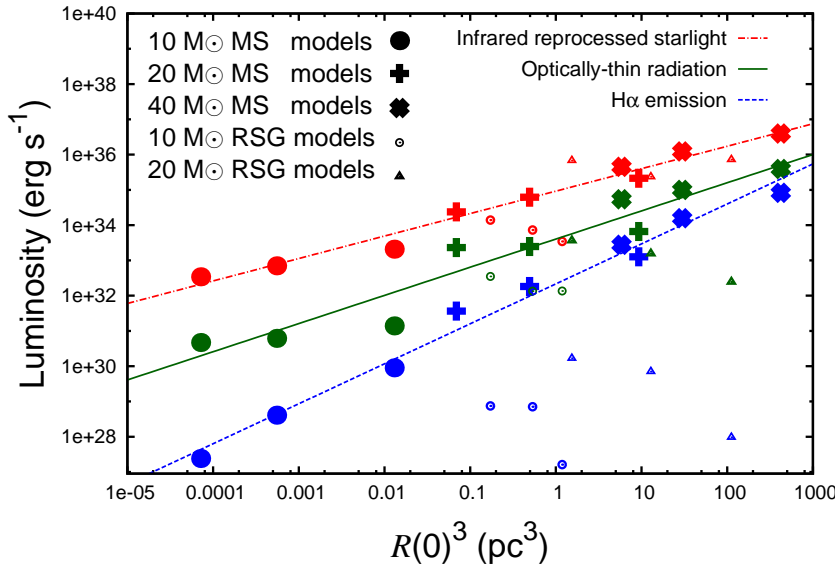
Figure 2.24: Bow shocks luminosities (in erg s^{-1}) as a function of $R(0)^3$ (in pc^3) for the main sequence (large symbols) and red supergiant models (small symbols). The overplotted thin lines are least square fits of the luminosity of optically-thin gas radiation (solid green line), the infrared luminosity of reprocessed starlight (dashed red line) and the luminosity of Hα emission (dotted blue line).

2.7 Conclusion

We present a grid of hydrodynamical models for bow shocks around evolving massive stars. The runaway stars initial masses range from 10 to 40 M$_\odot$ and their space velocities range from 20 to 70 km s^{-1}. Their evolution is followed from the main sequence to the red supergiant phase. Our simulations include thermal conduction and distinguish the treatment of the optically-thin cooling and heating as a function of the evolutionary phase of the star.

Our results are consistent with Comerón & Kaper (1998) because our bow shocks show a variety of shapes which usually do not fit a simple analytic approximation (Wilkin, 1996). We stress the importance of heat conduction to model the bow shocks around main sequence stars and find that this is not an important process to explain the morphology of bow shocks around red supergiant stars. We underline its effects on their morphology and structure, especially concerning the transport of ISM material to the hot region of the bow shocks generated by hot stars. The heat transfer enlarges the bow shocks and considerably reduces the volume of shocked wind so that optical emission mainly originates from shocked ISM material. We extend the analysis of our results by calculating the luminosities of the bow shocks and detail how they depend on the star's mass loss and space velocity.

Our bow shock models of hot stars indicate that the main coolants governing their luminosities are the optical forbidden lines such as [O II] and [O III]. The luminosity of optical forbidden lines is stronger than the luminosity of Hα emission, which only represents less than a tenth of the luminosity by optically-thin radiation. This agrees with the observations of Gull & Sofia (1979) who noticed that [O III] is the strongest optical emission line of the bow shock of ζ Oph. Our study also shows that those forbidden emission lines are fainter than the infrared emission of bow shocks produced by main sequence stars.

Our bow shocks models with hot stars are brightest in Hα in the cold shocked ISM material near the contact discontinuity. Because their dust surface mass density peaks at the same distance to the star as

their Hα emission, we suggest that their infrared emission is also maximum at the contact discontinuity. The Hα surface brightness is maximum upstream from the star for small space velocities and are extended downstream from the star for larger velocities. Our bow shocks models can have Hα surface brightnesses above the detection threshold of the SuperCOSMOS H-alpha Survey (Parker et al., 2005).

Our bow shocks generated by red supergiant stars have a large infrared luminosity. Their luminosity by optically-thin radiative cooling mainly originates from shocked ISM material, whereas our models indicate that their infrared luminosity principally comes from regions of shocked wind. The Hα emission of our bow shocks around cool stars originates from their forward shock. Its maximum is upstream from the star in the supersonic regime and is lengthened in the wake of the bow shock in the hypersonic regime. Their Hα emission is negligible compared to their luminosity of optically-thin radiation because their gas is weakly ionized. This supports the hypothesis that the optically-detected bow shock of IRC$-$10414 is photoionized by an external source because the collisionally excited [N II] line in the shocked wind is brighter than the Hα emission at the forward shock (Meyer et al., 2014a). In conclusion, these bow shocks are more likely to be observed in the infrared than in the optical or in Hα.

We also conclude that bow shocks produced by runaway main sequence and red supergiant stars should be easier to detect in the infrared. The brightest and most easily detectable bow shocks from main sequence stars are those of high mass stars ($\approx 40\,\mathrm{M}_{\odot}$) with small space velocity ($\approx 20\,\mathrm{km\,s^{-1}}$). With the ISM density of the Galactic plane, their luminosities are governed by their wind momentum and they scale monotonically with their volume. In the infrared, the most probable bow shocks to detect around red supergiant stars are produced by high mass ($\approx 20\,\mathrm{M}_{\odot}$) stars with small space velocity ($\approx 20\,\mathrm{km\,s^{-1}}$).

The hereby presented grid of models will be enlarged in a wider study, and forthcoming work will investigate the effects of an ISM background magnetic field. We also plan to focus on the latest stellar evolutionary stage in order to model the final explosion happening at the end of the massive star life, because the supernova ejecta interact with the shaped circumstellar medium.

Stability of bow shocks around runaway red supergiant stars

This chapter is a slightly augmented version of a Letter published as Meyer et al. (2014a).

3.1 Introduction

A significant fraction of runaway OB stars are moving supersonically through the local interstellar medium (ISM) (Huthoff & Kaper, 2002) and therefore generate bow shocks. The detection of these arc-like structures serves as an indication that their associated stars are massive enough to possess strong winds and could be used for i) identifying distant and/or highly reddened (runaway) OB stars (e.g., Gvaramadze, Kroupa & Pflamm-Altenburg, 2010b), ii) searching for parent clusters to these stars (e.g. Gvaramadze & Bomans, 2008) and iii) constraining mass-loss rates (Kobulnicky, Gilbert & Kiminki, 2010; Gvaramadze, Langer & Mackey, 2012) and the parameters of the local ISM (Kaper et al., 1997; Gvaramadze et al., 2014, hereafter Paper I).

Analytical (Dgani, van Buren & Noriega-Crespo, 1996b) and numerical studies (Comerón & Kaper, 1998; Blondin & Koerwer, 1998) of bow shocks show that they are subject to different kinds of instabilities, which along with density inhomogeneities and interstellar magnetic field can significantly affect their appearance. In particular, (Dgani, van Buren & Noriega-Crespo, 1996b) showed that isothermal bow shocks are unstable if the stellar space velocity, v_*, is larger than the wind velocity, v_w. This condition is usually fulfilled by cool runaway stars, e.g., red supergiants, whose wind velocities of ≈ 20 km s^{-1} are comparable to or less than their typical space velocities of several tens of km s^{-1}. Numerical simulations of bow shocks produced by red supergiants (Brighenti & D'Ercole, 1995a; Mohamed, Mackey & Langer, 2012; Cox et al., 2012a; Decin et al., 2012) confirmed that they are indeed generally unstable to a significant degree. This result is in conflict with the observed smoothness of bow shocks associated with two of the three known bow-shock-producing red supergiants, namely Betelgeuse (Noriega-Crespo et al., 1997) and IRC -10414 (Paper I). On the other hand, a bow shock around the third of these red supergiants, μ Cep, shows clear signatures of instabilities (Cox et al., 2012a) in good agreement with the theoretical and numerical predictions. There should therefore exist some factors which stabilize bow shocks around red supergiants. Decin et al. (2012) began to explore this subject by considering a bow shock from a red supergiant with a neutral wind but moving in an ionized ISM (photoheated to 8000 K), finding that this reduced the strength of instabilities compared to
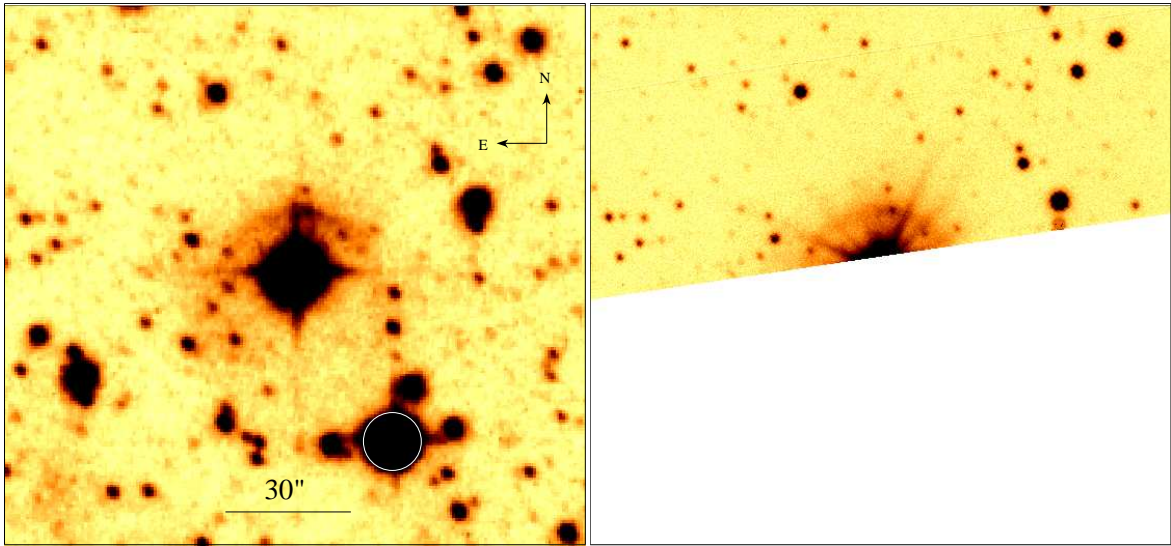
Figure 3.1: Left: Hα+[N II] image of IRC$-$10414 and its bow shock from the SHS. The WC5 star WR 114, located at $\approx$45 arcsec southwest of IRC$-$10414, is marked by a white circle. Right: Hα+[N II] image of the bow shock obtained with the 2.3-m Aristarchos telescope. The orientation and the scale of the images are the same. See the text for details. At a distance of 2 kpc, 30 arcsec correspond to $\approx$0.29 pc.

a bow shock in a neutral ISM.

In this Chapter, we use numerical simulations of the bow shock of IRC$-$10414 to investigate the hypothesis that bow shocks generated by red supergiants could be stable if the stellar wind and the ambient ISM are heated and ionized by an external source of radiation. The relevant data on the bow shock are reviewed in Section 3.2. The numerical models of the bow shock are presented in Section 3.3 and discussed in Section 3.4. We summarize in Section 3.5.

3.2 The bow shock of IRC$-$10414

The bow shock around IRC$-$10414 is the first-ever optically detected bow shock generated by red supergiants (the data on the bow shock and IRC$-$10414 quoted below are from Paper I unless otherwise stated). The left-hand panel of Fig. 3.1 presents the discovery Hα+[N II] $\lambda\lambda$6548, 6584 image of the bow shock from the SuperCOSMOS H-alpha Survey (SHS; Parker et al., 2005), showing a smooth arc-like nebula at $\approx$15 arcsec from the star. At a distance to IRC$-$10414 of 2 kpc (Maeda et al., 2008), the stand-off distance of the bow shock is $R_{SO} \approx$0.14 pc. For an inclination angle of the bow shock to the plane of the sky of $\approx$20°, the projection effect on the observed R_{SO} is negligible (see Gvaramadze et al., 2011b). The right-hand panel of Fig. 3.1 shows a follow-up image of the bow shock obtained with the 2.3-m Aristarchos f/8 telescope at Helmos Observatory, Greece on 2013 August 9 with 1800 s exposure, through a 40 Å bandwidth filter centred on the Hα+[N II] lines. To avoid saturation, IRC$-$10414 was placed outside the CCD detector. Although the resolution of this image is about three times higher than that of the SHS one, the bow shock still does not show any signatures of instabilities.

Using equation (1) and the flux calibration factor of 16.1 counts pixel^{-1} R^{-1} from Table 1 in Frew et al. (2013), we derived from the SHS image the surface brightness of the bow shock near the apex of $\Sigma_{obs} \approx$77 R (1R=5.66$\times$10^{-18} erg cm^{-2} s^{-1} arcsec^{-2} at Hα).

Optical spectroscopy of the bow shock (carried out with the Southern African Large Telescope)
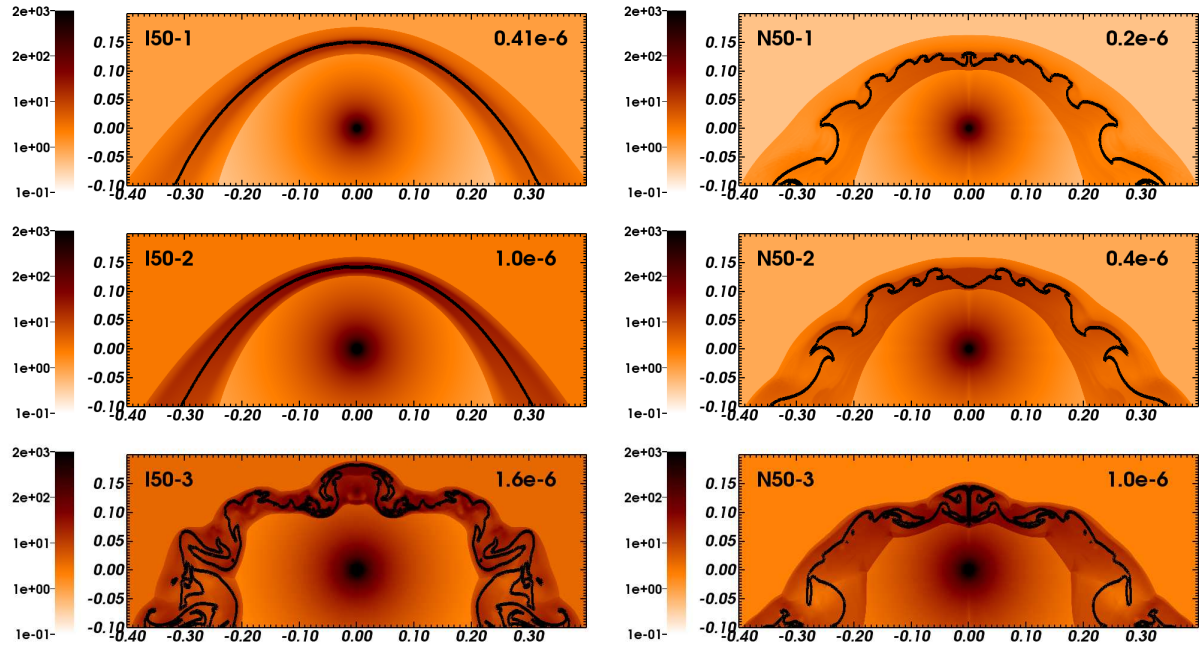
Figure 3.2: Grid of models of the bow shock of of IRC−10414 generated by a red supergiant moving at 50 km s^{-1}. The panels show the gas number density plotted on the logarithmic scale in units of cm^{-3}. On each panel the left-hand key refers to the nomenclature detailed in Table 3.1 and the right-hand key indicates $\dot{M}$ in units of M$_\odot$ yr^{-1}. The solid line traces the position of the contact discontinuity. Models are shown at least 0.1 Myr after the beginning of the simulations. The *x*-axis corresponds to the radial direction and the symmetry axis is aligned with the space velocity of the star (both axes are in units of pc). Note that not all of the computational domain is shown.

Table 3.1: Input parameters of the grid models and the surface brightness of the model bow shocks. Columns show, respectively, model identifier, space velocity in $\mathrm{km\,s^{-1}}$, mass-loss rate in $10^{-6}\,\mathrm{M_\odot\,yr^{-1}}$, ambient ISM number density in $\mathrm{cm^{-3}}$, and maximum surface brightness of the models, before and after correction for the interstellar extinction towards IRC-10414, in Rayleighs.

Model	v_*	$\dot{M}$	n_0	Σ_{max}	$\Sigma_{\mathrm{max}}^{\mathrm{cor}}$
I50-1	50	0.41	1.21	133.2	5.3
I50-2	50	1.01	3.30	1176.7	47.1
I50-3	50	1.62	5.00	8436.8	337.5
I70-1	70	0.41	0.73	155.4	6.2
I70-2	70	1.01	1.51	865.9	34.6
I90-1	90	0.41	0.41	144.3	5.8
N50-1	50	0.20	0.48	3.1	0.1
N50-2	50	0.41	0.91	8.0	0.3
N50-3	50	1.01	2.60	33.3	1.3
N70-1	70	0.41	0.35	3.1	0.1
N90-1	90	0.41	0.26	9.5	0.4

showed that the line-emitting material is enriched in nitrogen, which implies that the emission at least partially originates from the shocked stellar wind (cf. Section 3.4). It also allowed us to constrain the number density of the ambient ISM to be $n_0 \leq 5$ $\mathrm{cm^{-3}}$ $(v_*/70\,\mathrm{km\,s^{-1}})^{-2}$, which in its turn imposes a limitation on the mass-loss rate, $\dot{M}$, of IRC-10414. The space velocity of IRC-10414 $v_* \approx 70 \pm 20$ $\mathrm{km\,s^{-1}}$ is several times higher than the stellar wind velocity $v_\mathrm{w} = 21 \pm 2$ $\mathrm{km\,s^{-1}}$, derived from maser observations of a region within a few hundreds of AU from the star. Thus, if the bow shock of IRC-10414 is a thin shell (a natural assumption for bow shocks produced by cool stars), then, according to Dgani, van Buren & Noriega-Crespo (1996a), it should be unstable and ragged, which clearly contradicts our observations.

Previous numerical simulations of bow shocks generated by red supergiants proceeded from the common assumption that the stellar wind is neutral. This assumption, however, would be invalidated if the wind is ionized by an external source of radiation, like a nearby hot massive star or a star cluster. Good examples of such situation are ionized nebulae around the red supergiants NML Cyg and W26, which are the result of ionization of the stellar wind by the nearby association Cyg OB2 (Morris & Jura, 1983) and star cluster Westerlund 1 (Wright et al. 2013), respectively. As discussed in Paper I, the ionization of the wind might exert a stabilizing influence on red supergiant bow shocks. Proceeding from this, we proposed that the smooth shape of the bow shock around IRC-10414 is because the wind of this star and the ambient ISM are ionized by the nearby WC5 star WR 114 (see Fig. 3.1) and/or by the massive star cluster NGC 6611. In this connection, we note that the spectrum of the bow shock shows very strong [N II] $\lambda\lambda$6548, 6583 emission lines (see fig. 3 in Paper I), which means that the stellar wind is ionized to a significant degree (cf. Section 3.4). Since the wind material cannot be collisionally ionized because the reverse shock is too weak, it is natural to assume that the wind is photoionized by an external source. The above considerations motivated us to carry out numerical simulations presented in this Chapter.

3.3 Numerical simulations

We performed 2D numerical simulations using the PLUTO code (Mignone et al., 2007, 2012). The simulations were carried out in cylindrical coordinates on a uniform grid of size of $[0, 0.4] \times [-0.1, 0.3]$
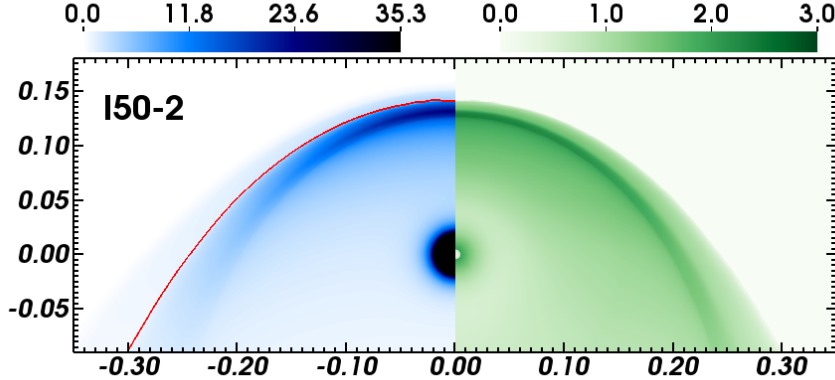
Figure 3.3: Left: Surface brightness for the ionized model I50-2 plotted on a linear scale in units of R. The solid (red) line traces the position of the contact discontinuity. Right: [NII]/Hα line ratio for the same model.

pc and spatial resolution of 2.25×10^{-4} pc cell^{-1}. A stellar wind was injected into the computational domain via an half circle of radius of 20 cells ($\approx$900 AU) centred at the origin, and its interaction with the ISM was modelled in the reference frame of the star. Wind material is distinguished from the ISM using a passive tracer advected together with the fluid. The ISM composition is assumed to be solar (Asplund et al., 2009).

Optically-thin radiative cooling and heating were taken into account. For a fully ionized medium, the cooling curve is the sum of contributions from H, He and metals (Wiersma, Schaye & Smith, 2009), collisionally excited forbidden lines (Henney et al., 2009) and H recombination together with heating from the reionization of recombining H atoms (Osterbrock & Bochkarev, 1989; Hummer, 1994). The equilibrium temperature of this curve is $\approx$8000 K. For models with the neutral medium, the cooling curve is the sum of contributions from H, He and metals (Cowie & McKee, 1977) and the dust heating by the Galactic far-ultraviolet background (Wolfire et al., 2003). The equilibrium temperature of this curve is $\approx$3300 K for n_0=1 cm^{-3}. All models include electronic thermal conduction (Cowie & McKee, 1977).

We have run a grid of 11 models, in which both the stellar wind and the ISM were considered to be either fully ionized or neutral, labelled 'I' and 'N', respectively. Three space velocities were considered, $v_* = 50, 70$ and 90 km s^{-1}, and $v_w = 21$ km s^{-1} was set in all models. For $\dot{M}$ we adopted a range of values based on various mass-loss prescriptions proposed for red supergiants (see Paper I), ranging from $\approx 0.4 \times 10^{-6}$ to 1.6×10^{-6} M$_\odot$ yr^{-1}. For each model, n_0 was adjusted in such a way that R_{SO} of a model bow shock is equal to the observed one, when a steady state was reached. All models are run for at least 0.1 Myr, which corresponds to more than 16 grid crossing times. The parameters of the models are summarized in Table 3.1.

For the sake of comparison with observations, we calculated the Hα+[NII] surface brightness of the model bow shocks using the prescriptions by Dopita (1973) and Osterbrock & Bochkarev (1989). To reproduce the observed [N]/Hα line ratio of 2.4±0.1 (measured in the spectrum of the bow shock at an angle of 25° from the apex; see Paper I), we assumed that the red supergiant wind is enriched in nitrogen by a factor of 6 (cf. Brott et al., 2011). The maximum value of the brightness, Σ_{max}, for each model is given in the column 5 of Table 3.1, while the column 6 gives Σ_{max} corrected for the interstellar extinction towards IRC$-$10414, which in the R-band is $\approx$3.5 mag (Paper I).
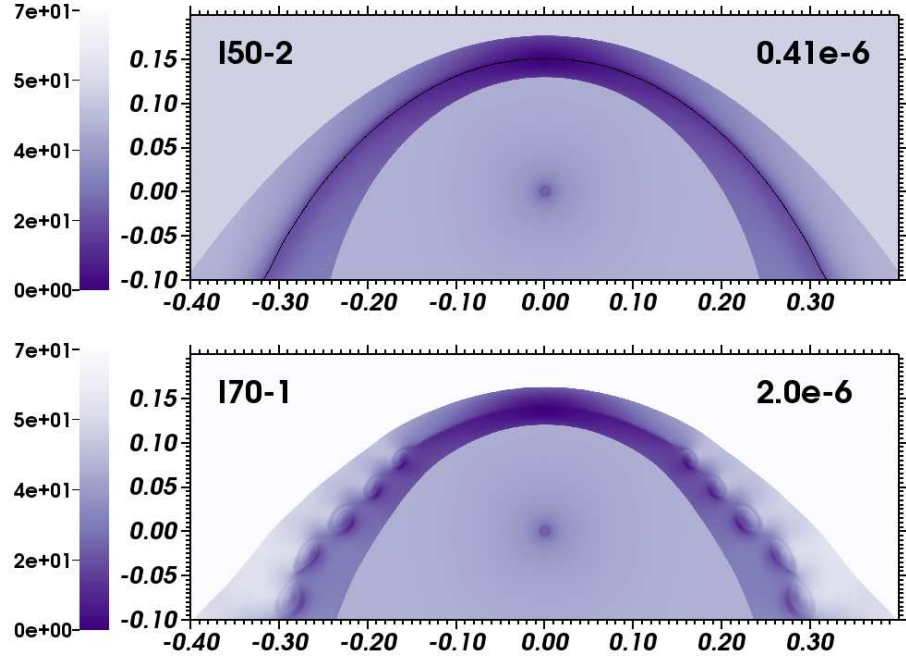
Figure 3.4: Unstability of the contact discontinuity of the bow shock models I50−2 and I70−1. The panels show the absolute value of the velocity plotted on the linear scale in units of cm s^{-1}. On each panel the left-hand key refers to the nomenclature detailed in Table 3.1 and the right-hand key indicates $\dot{M}$ in units of M$_\odot$ yr^{-1}. Models are shown at least 0.1 Myr after the beginning of the simulations. The x-axis corresponds to the radial direction and the symmetry axis is aligned with the space velocity of the star (both axes are in units of pc). Note that not all of the computational domain is shown.

3.4 Results and discussion

Fig. 3.2 plots the gas number density of the ionized (left-hand panels) and neutral bow shocks generated by red supergiants moving with a velocity of 50 km s^{-1}. The solid (black) line traces the position of the contact discontinuity. One can see that the ionized bow shocks are stable as long as $\dot{M} \leq 1 \times 10^{-6}$ M$_\odot$ yr^{-1}. For higher $\dot{M}$ and/or v_*, the ionized bow shocks became unstable (e.g. model I50-3 in Fig. 3.2), which prevent them from reaching a steady state. Of three neutral models shown in Fig. 3.2 two ones have smooth forward and reverse shocks, while the contact discontinuity in all of them is very ragged. For $\dot{M} \geq 10^{-6}$ M$_\odot$ yr^{-1} and/or $v_* > 50$ km s^{-1}, the contact discontinuity becomes even more unstable and the overall shape of the neutral bow shocks becomes highly distorted (e.g. model N50-3 in Fig. 3.2). The unstable character of a model can be appreciated looking at the absolute value of the velocity at the contact discontinuity (see Fig. 3.4). We therefore expect that one of the models I50-1, I50-2, N50-1 and N50-2 could represent the bow shock around IRC −10414.

To substantiate this expectation, we compare $\Sigma_{\rm obs}$ with the model predictions. An inspection of Table 3.1 shows that the higher $\dot{M}$ the higher $\Sigma_{\rm max}$ of the models. Three of the ionized models have $\Sigma_{\rm max}^{\rm cor}$ comparable to or larger than $\Sigma_{\rm obs}$. Of these models only I50-2 is stable (see Fig. 3.2). $\Sigma_{\rm max}^{\rm cor}$ of the remaining three ionized models slightly exceeds the sensitivity limit to diffuse emission of the SHS of 2−5 R (Parker et al., 2005) and therefore, in principle, these bow shocks could be detected with this survey. On the contrary, all the neutral models are so dim that their $\Sigma_{\rm max}^{\rm cor}$ is below the sensitivity limit of the SHS. Thus, we conclude that I50-2 is the best fit model of the bow shock of IRC −10414.
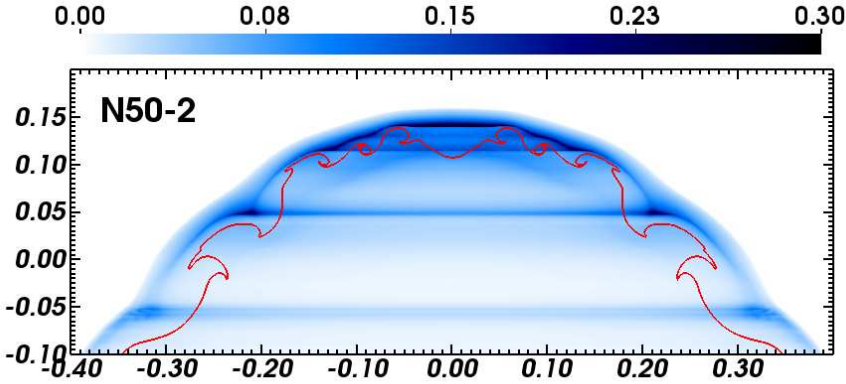
Figure 3.5: Surface brightness for the neutral model N50-3 plotted on a linear scale in units of R. The solid (red) line traces the position of the contact discontinuity

Interestingly, $\dot{M}$ adopted in this model is a factor of $5-10$ smaller than that predicted by most of the mass-loss prescriptions proposed for red supergiants (see Paper I) and a factor of two higher than what follows from the recipe by Verhoelst et al. (2009).

The left-hand panel of Fig. 3.3 presents a map of the surface brightness in the Hα+[NII] lines for our preferred model I50-2. It shows that the emission comes mainly from the shocked wind, which naturally explains why the brightness of the ionized models increases with $\dot{M}$ (see Table 3.1) and why the line-emitting material in the bow shock of IRC -10414 is enriched in nitrogen. The right-hand panel of Fig. 3.3 plots the [N II]/Hα line ratio for the emission originating from the shocked wind for the same model. This ratio has a value of 2.3 for an angle of 25° from the apex of the bow shock, which is in a good agreement with the observed value of 2.4±0.1.

Fig. 3.5 plots the surface brightness for the neutral model N50-2. Unlike the ionized models, the Hα+[NII] emission in the neutral ones originates from the collisionally ionized ISM, i.e. just behind the forward shock. Correspondingly, the model N50-2 has a rather smooth appearance, but its Σ_{max}^{cor} is below the sensitivity limit of the SHS. This further supports our claim that the bow shock of IRC -10414 is ionized by an external source.

Using Fig. 3.3, we measured a ratio $R_{SO}/R(\theta)$, where $R(\theta)$ is the distance between the star and the bow shock at an angle θ from the apex. For $\theta \approx 75°$ (the half-opening angle of the observed bow shock), we found $R_{SO}/R(\theta) = 1.36$, which is in a reasonable agreement with both the observed ratio of 1.33 and the theoretical one of 1.44, derived from the thin-shell bow shock model by (Wilkin, 1996).

It should be noted that the ionized models have higher ISM densities than the neutral ones with the same $v_\star$ and $\dot{M}$ (see Table 3.1). Since R_{SO} is fixed in all models, this difference implies that the wind velocity is higher in the ionized models. Indeed, the instantaneous heating of the wind material up to ≈ 8000 K results in increase of its thermal pressure, which in its turn leads to the wind acceleration (see Oort & Spitzer (1955) for more details). Fig. 3.6 shows the wind velocity profiles along the y-axis for the models I50-1 and N50-2. In I50-1 the wind is accelerated by a factor of two and its velocity becomes comparable to v_*, while in N50-2 the wind velocity remains constant[1], i.e. a factor of ≈ 2.5 less than v_*. Correspondingly, the shear produced by the relative motion of the shocked wind and shocked ISM is stronger in the N50-2 model, which makes it more prone to the development of the Kelvin-Helmholtz instability at the contact discontinuity. The same is true for the models with higher

---

[1] A slight acceleration of the wind in this model is because of a boundary effect.
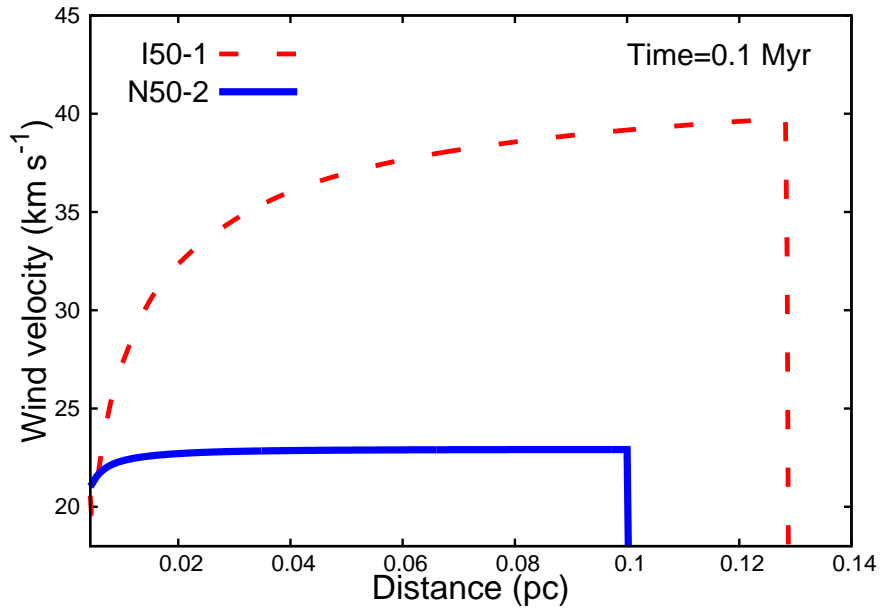
Figure 3.6: Wind velocity profiles along the y-axis for the models I50-1 and N50-2. Heating of the wind by photoionization results in its acceleration by a factor of two (see the text for details).

v_* because the growth time of the instability is inversionally proportional to the magnitude of the shear, which in its turn increases with v_*.

3.5 Summary

In this Chapter, we presented a grid of models of bow shocks produced by red supergiants, in which both the stellar wind and the ISM were considered to be either fully ionized or neutral. We investigated whether the smooth appearance of the bow shock around the red supergiant IRC$-$10414 might be caused by the ionization of the stellar wind by an external source of radiation. We found that although both kinds of models can have a smooth appearance in the Hα+[N II] lines, only the ionized ones can simultaneously reproduce the overall shape and the brightness of this bow shock. Our simulations showed that the ionization of the stellar wind results in its acceleration by a factor of two, which reduces the shear at the contact discontinuity and makes the bow shock stable for a range of stellar space velocities and mass-loss rates. Our best fit model of the bow shock suggests that the space velocity and mass-loss rate of IRC$-$10414 are ≈ 50 km s^{-1} and $\approx 10^{-6}$ M$_\odot$ yr^{-1}, respectively, and that the number density of the local ISM is ≈ 3.3 cm^{-3}. We found also that in the ionized models the Hα+[N II] emission originates mostly from the shocked red supergiant wind, which naturally explains why the line-emitting material in the bow shock of IRC$-$10414 is enriched in nitrogen. Our results suggest that the ionization of the stellar wind might be responsible for the smooth appearance of bow shocks generated by other red supergiants, or asymptotic giant branch stars.

Asymmetric supernova remnants generated by Galactic, massive runaway stars

This chaper is to be submitted as a paper to Monthly Notices of the Royal Astronomical Society (Meyer et al.).

4.1 Introduction

Massive stars are rare but crucial to understand the cycle of matter in the interstellar medium (ISM) of galaxies (Langer, 2012). Significantly influenced by their rotation (Langer, García-Segura & Mac Low, 1999; van Marle et al., 2008; Chita et al., 2008), bulk motion (Brighenti & D'Ercole, 1995a,b) or by the presence of a companion (Stevens, Blondin & Pollock, 1992), their strong winds shape their surroundings and chemically augment their ambient medium (Vink, 2006). Some of these stars explode as luminous supernovae which release ejecta interacting with their pre-shaped environment (see in Borkowski, Blondin & Sarazin, 1992; Vink, Kaastra & Bleeker, 1996, 1997; van Veelen et al., 2009). This event gives birth to supernova remnants replenishing the ISM with momentum and kinetic energy up to about 120 pc from the center of the explosion (Badenes, Maoz & Draine, 2010).

Supernovae have been noticed in ancient Asia with the naked eye, e.g. the guest-star recorded in AD185 by chinese astronomers (Green & Stephenson, 2003), whereas the first supernova remnant has been identified spectroscopically almost two millennia later (Baade, 1938). Nowadays, surveys provide us with observations of Galactic supernova remnants, e.g. in X-ray (Pannuti et al., 2014), the infrared (Reach et al., 2006) or in gamma-rays (Abdo, Ackermann & Ajello, 2010). Catalogues of remnants visible in the radio waveband in the northern and southern hemisphere are available in Kothes et al. (2006) and Whiteoak & Green (1996), respectively. An exhaustive catalogue of the known Galactic supernova remnants was compiled by Green (2009). These abundant observations reveal a diversity of complex morphologies such as shells, annuli, cylinders, rings and bipolar structures (cf. Gaensler, 1999).

The shape of young supernova remnants depends (i) on the geometry of the supernova explosion and (ii) on the (an)isotropy of their ambient medium (Vink, 2012). They therefore exhibit a wide range of morphologies that can be used to constrain their progenitors and/or ambient medium properties. The distribution of circumstellar matter depends on the progenitor properties (Bedogni & D'Ercole, 1988; Ciotti & D'Ercole, 1989; Dwarkadas, 2005, 2007) and the presence of ISM structures, e.g. bor-

ders of neighbouring diffuse nebulae or filaments that affect the propagation of the supernova ejecta. Models of remnants developing in a pre-existing wind cavity are shown in Tenorio-Tagle et al. (1990, 1991), and demonstrate that mixing of material happens in the former wind bubble. Multi-dimensional models of the formation of knots by wind-wind collision around Cassiopeia A are shown in the study of Pérez-Rendón, García-Segura & Langer (2009) and the effects of this fragmented Wolf-Rayet shell on the rebrightening of young remnants is explored in van Veelen et al. (2009). Supernova remnants developing through an edge of a dense region, e.g. a molecular cloud, give rise to champagne flows such as the one observed in the Cygnus loop nebula (Tenorio-Tagle, Rozyczka & Yorke, 1985). If the supernova happens near a denser region, the reverse shock is reflected towards the center of the explosion and a hot region of shocked material forms (Ferreira & de Jager, 2008). A strong magnetization of the ISM can induce a collimation of the supernova ejecta engendering elongated remnants (Rozyczka & Tenorio-Tagle, 1995).

Particularly, the bow shocks produced by runaway massive stars are an ideal site for the generation of an anisotropic circumstellar distribution. This is likely to happen in the Galactic plane, where most of the massive stars which are both in the field and classified as runaway are found (Gies, 1987; Blaauw, 1993; Huthoff & Kaper, 2002). A few of them are identified as evolved massive stars and three of them are red supergiants with detected bow shocks, i.e. Betelgeuse (Noriega-Crespo et al., 1997; Decin et al., 2012), μ Cep (Cox et al., 2012b) and IRC−10414 (Gvaramadze et al., 2013). Consequently, and because these stars will explode as core-collapse supernova, their circumstellar medium is of prime interest in the study of aspherical supernova remnants.

The circumstellar medium of Galactic runaway red supergiant stars is studied in Brighenti & D'Ercole (1995a,b) as an attempt to explain non-spherical supernova remnants. The works by van Marle et al. (2011b) and Decin et al. (2012) tailor models to Betelgeuse's bow shock and estimate in the context of recent observations (Cox et al., 2012b) how the drag force on dust grains modifies the evolution of its contact discontinuity. The effects of the mass loss and space velocity on the shape and luminosity of bow shocks around red supergiant star is investigated in Meyer et al. (2014b, hereafter Paper I). The repercussions of a weak ISM magnetic field on the damping of instabilities in the bow shocks of Betelgeuse is presented in van Marle, Decin & Meliani (2014). The stabilizing role of photoionization by an external source of radiation on the bow shock of IRC−10414 is shown in Meyer et al. (2014a). The above cited models can be understood as investigations of the circumstellar medium of Galactic runaway core-collapse progenitors near their pre-supernova phase.

After the supernova explosion, the forward shock of the blastwave interacts with the free-streaming stellar wind (Chevalier & Liang, 1989; Chevalier, 1982). Supernovae showing evidence of interaction with circumstellar structures are commonly denoted as Type IIn and their corresponding lightcurves provide information on the progenitor and properties of its close surroundings (Schlegel, 1990; Filippenko, 1997; van Marle et al., 2010). About 10−100 yr after the explosion, the shock wave collides with the bow shock along the direction of motion of its progenitor, whereas it expands in a cavity of wind material in the opposite direction (Borkowski, Blondin & Sarazin, 1992).

In this spirit, Rozyczka et al. (1993) model supernovae in oval bubbles generated by moving progenitors. They neglect the progenitor stellar evolution but demonstrate that elongated jet-like structures of size of about 10 pc form when the shock wave expands into the wind bubble. A model interpreting the cool jet-like [OIII] λ 5007 feature found in the Crab nebula (Blandford et al., 1983) as a shock wave channelled into the trail produced by its progenitor's motion is presented in Cox, Gull & Green (1991). Brighenti & D'Ercole (1994) show that if the runaway progenitor evolves beyond the main-sequence phase, the supernova explosion happens out of the main-sequence wind bubble, and the subsequent remnant develops as an outflow upstream from the direction of motion of the progenitor.

In this work, we aim to determine the degree of anisotropy of supernova remnants generated by

runaway core-collapse progenitors moving through the Galactic plane. We model the circumstellar medium from near the pre-supernova phase of a representative sample of the most common runaway massive stars (Eldridge, Langer & Tout, 2011). We calculate one-dimensional hydrodynamic models of the supernova ejecta interacting with the stellar wind and use them as initial conditions for two-dimensional simulations of the supernova remnants. Finally, we discuss the emitting properties of the most aspherical of these remnants.

This project is different from previous studies (Brighenti & D'Ercole, 1994) because (i) we use self-consistent stellar evolution models, (ii) we consider both optically-thin cooling and heating along with thermal conduction, (iii) we trace the mixing between ISM, stellar wind and supernovae ejecta inside the remnants and (iv) our grid of models explores a broader space of parameters than works tailored to a particular supernova remnant, e.g. Kepler's supernova remnant (Borkowski, Blondin & Sarazin, 1992; Velázquez et al., 2006; Vigh et al., 2011; Chiotellis, Schure & Vink, 2012; Toledo-Roy et al., 2014). We neglect the magnetization, inhomogenity and turbulence of the ISM and ignore the cooling in the shock wave induced by the production of Galactic cosmic rays (Orlando et al., 2012; Schure & Bell, 2013). We assume that the supernova explosions do not have any intrinsic anisotropy. Furthermore, we assume than no pulsar wind nebula remains inside the supernova remnants and modifies the reflection of the reverse shock towards the center of the explosion (Bucciantini et al., 2003).

This paper is structured as follows. We begin Section 4.2 by discussing our numerical methods and initial parameters. The modelling of the circumstellar medium of our progenitors is shown in Section 4.3. We describe the calculations of supernova remnants developing inside and beyond their progenitors' bow shock in Sections 4.4 and 4.5, respectively. Section 4.6 discusses and compares our models of aspherical remnants with observations. We conclude in Section 4.7.

4.2 Method and initial parameters

In this section, we review the utilised numerical methods to model the circumstellar medium of our progenitors and we present the procedure to set up supernova blastwaves.

4.2.1 Modelling the circumstellar medium

We perfom two-dimensional simulations using the code PLUTO (Mignone et al., 2007, 2012) to model the circumstellar medium of moving core-collapse supernova progenitors. We solve the equations of hydrodynamics in a cylindrical computational domain $(O; R, z)$ of origin O, which is coincident with the location of the runaway star and has rotational symmetry about $R = 0$. A uniform grid of $N_R \times N_z$ grid cells is mapped onto a domain of size $[0, R_{max}] \times [z_{min}, z_{max}]$, respectively. We define $\hat{R}$ and $\hat{z}$ as the unit vectors of the axis OR and Oz, respectively. The grid spatial resolution is $\Delta = R_{max}/N_R$. Following the method of Comerón & Kaper (1998), we release the stellar wind on a circle of radius 20 grid cells centered on the origin and compute the wind-ISM interaction in the frame of reference of the moving progenitor.

We model the circumstellar medium of initially 10, 20 and $40 \, M_\odot$ stars moving with space velocity ranging from $v_\star = 20$ to $70 \, \mathrm{km \, s^{-1}}$. The (time-dependent) stellar wind properties are taken from stellar evolution models (Brott et al., 2011). We consider a homogeneous ISM with a hydrogen number density $n_H = 0.57 \, \mathrm{cm^{-3}}$ (Wolfire et al., 2003), i.e. we assume that the stars are exiled from their parent cluster and move in the low-density ISM. We set the ISM temperature to $T_{ISM} \approx 8000 \, \mathrm{K}$ and include gain/losses by optically-thin radiative cooling assuming that the gas has solar metallicity (sections 2.3 and 2.4 of Paper I). All our bow shock models include electronic thermal conduction (Spitzer, 1962; Cowie & McKee, 1977).

Table 4.1: Wind properties at the end of the used stellar evolution models, at t_{psn}. $M_\star$ ($M_\odot$) is the initial mass of each star, $\dot{M}$ ($M_\odot$ yr^{-1}) their mass loss and v_{wind} (km s^{-1}) their wind velocity at a distance of 0.01 pc from the star, respectively.

$M_\star$ ($M_\odot$)	$\dot{M}$ ($M_\odot$ yr^{-1})	v_{wind} (km s^{-1})
20	$10^{-6.11}$	16
40	$10^{-4.79}$	11
70	$10^{-4.48}$	50

We start our models at $t_{start} \approx t_{psn} - 32\, t_{cross}$, where t_{psn} is the time at the end of the stellar evolution model. The duration $32\, t_{cross}$ is a time interval sufficient to simulate a bow shock without any trace of the switch-on effects arising during its development, where $t_{cross} = R(0)/v_\star$ is the crossing-time and $R(0)$ is the stand-off distance of the bow shock (Baranov, Krasnobaev, & Kulikovskii, 1971). The calculation of each bow shock model is followed until the end of the stellar evolution model, at t_{end}. Note that our initially 10 and 20 $M_\odot$ progenitors explode as a red supergiant (Paper I). We run these models with the same underlying assumptions as in Paper I, especially considering that no stellar radiation field is trapped into the bow shock (Weaver et al., 1977). Moreover, we assume that the evolutionary model of our initially 40 $M_\odot$ progenitor, that does not go all the way up to the pre-supernova phase, is sufficient to model a first order approximation of the mass distribution at the time of the supernova explosion. Our stellar evolution models are described in section 2.2 of Paper I and the wind properties at t_{psn} are shown in Table 4.1.

Our models of the circumstellar medium from near the pre-supernova phase are named with the prefix PSN followed by the initial mass of the progenitor $M_\star$ (first two digits, in $M_\odot$) and its space velocity $v_\star$ (two last digits, in km s^{-1}). We adopt grid dimensions such that it includes the wake of the bow shocks produced during about $v_\star 10 t_{cross}$ (our Table 4.2) in order to properly model the expansion of the shock wave through the tail of the bow shock up to times of the order of 10^4 yr. The stellar wind is distinguished from the ISM material using a scalar $Q_1(r)$ passively advected with the gas, where r is the position vector of a grid cell. Its value is set to $Q_1(r) = 1$ for the wind material and to $Q_1(r) = 0$ for the ISM gas. Our cooling curves and numerical methods are extensively detailed in section 2 of Paper I. Results are presented in Section 4.3.

4.2.2 Setting up the supernova shock wave

We perform one-dimensional hydrodynamical simulations of the shock wave expanding into the stellar wind. The blastwave is characterized by its energy fixed to the typical value $E_{ej} = 10^{51}$ erg s^{-1} for type II supernovae and by the mass of the ejecta M_{ej}. The latter is estimated as,

$$M_{ej} = M_\star - \int_{t_0}^{t_{psn}} \dot{M}(t)dt - M_{co}, \qquad (4.1)$$

where t_0 and t_{psn} are the time at the beginning and the end of the used stellar evolution model, respectively. Note that we assume M_{ej} for our 40 $M_\odot$ progenitor, because we ignore its post-main-sequence evolution. The quantity $M_{co} = 2\,M_\odot$ in Eq. (4.1) is the assumed mass of the residual compact object left after the supernova (our Table 4.3).

We set up the supernova using the method detailed in Whalen et al. (2008) and in van Veelen et al. (2009). It assumes that the blastwave density profile $\rho(r)$ is a radial piece-wise function of the distance r to the center of the explosion in the region $[0, r_{max}]$, where r_{max} is the radius of the shock wave when

Table 4.2: Input parameters used in our simulations of the bow shocks generated by supernova progenitors. Parameters z_{min} and R_{max} are the limits of the domain along the x-axis and y-axis (in pc), respectively. N_R and N_z are the number of cells discretising the corresponding directions and Δ is the grid resolution (in pc cell^{-1}). The simulations start at a time t_{start} (in Myr) after the star's birth and are run until the end of the used stellar evolution models, at t_{psn} (in Myr).

Model	$M_\star$ ($M_\odot$)	$v_\star$ (km s^{-1})	z_{min} (pc)	R_{max} (pc)	N_R	N_z	Δ (pc cell^{-1})	t_{start} (Myr)	t_{psn} (Myr)
PSN1020	10	20	−6.0	7.0	1225	1400	5.71×10^{-3}	23.7	24.7
PSN1040	10	40	−2.1	2.0	1143	1600	1.75×10^{-3}	24.5	24.7
PSN1070	10	70	−0.9	0.8	950	1425	8.42×10^{-4}	24.6	24.7
PSN2020	20	20	−30.0	35.0	2333	2333	1.49×10^{-2}	6.63	9.05
PSN2040	20	40	−9.0	8.0	600	1200	1.33×10^{-2}	8.65	9.05
PSN2070	20	70	−4.5	4.0	1067	1600	3.75×10^{-3}	8.70	9.05
PSN4020	40	20	−90.0	100.0	1500	1575	6.0×10^{-2}	0.0	4.5
PSN4040	40	40	−36.0	30.0	1500	2100	2.0×10^{-2}	2.00	4.5
PSN4070	40	70	−30.0	20.0	1000	2000	2.0×10^{-2}	3.50	4.5

Table 4.3: Simulations parameters used in our simulations of supernovae interacting with the unperturbed stellar wind. Parameter M_{ej} is the mass of the ejecta (in $M_{\odot}$) and r_{max} is the size of the one-dimensional spherically symmetric domain (in pc). The simulations are started at $t = 0.04$ yr. The last column indicates the time at the end of our simulations, t_{sncsm} (in yr).

Model	M_{ej} ($M_{\odot}$)	r_{max} (pc)	t_{sncsm} (yr)
SNCSM 1020	7.7	0.30	40
SNCSM 1040	7.7	0.20	13.5
SNCSM 1070	7.7	0.13	15
SNCSM 2020	17.7	0.90	40
SNCSM 2040	17.7	0.50	25
SNCSM 2070	17.7	0.25	20
SNCSM 4020	16	3.00	400
SNCSM 4040	16	1.50	200
SNCSM 4070	16	0.90	180

we start the simulations. Under these assumption, the ejecta density profile is,

$$\rho(r) = \begin{cases} \rho_{core}(r) & \text{if } r \leq r_{core}, \\ \rho_{max}(r) & \text{if } r_{core} < r < r_{max}, \\ \rho_{csm}(r) & \text{if } r \geq r_{max}, \end{cases} \tag{4.2}$$

where,

$$\rho_{core}(r) = \frac{1}{4\pi n} \frac{(10E_{ej}^{n-5})^{-3/2}}{(3M_{ej}^{n-3})^{-5/2}} t_{max}^{-3}, \tag{4.3}$$

is constant up to the inner core of radius r_{core} and,

$$\rho_{max}(r) = \frac{1}{4\pi n} \frac{(10E_{ej}^{n-5})^{(n-3)/2}}{(3M_{ej}^{n-3})^{(n-5)/2}} \left(\frac{r}{t_{max}}\right)^{-n}, \tag{4.4}$$

is a steeply decreasing function of inner radius r_{core} and external radius r_{max} (Truelove & McKee, 1999). The power law index n of Eq. (4.3)–(4.4) is set to the usual value $n = 11$ for core-collapse supernovae (Chevalier, 1982). In relation (4.2), ρ_{cms} is the freely-expanding wind profile measured from the simulations along the symmetry axis Oz, in the direction of motion of the progenitor ($z \geq 0$). We use it as initial condition in the $[r_{max}, r_{sncsm}]$ of the domain, where $r_{sncsm} < R(0)$ is outer border of the domain.

The ejecta obey a homologous expansion, i.e. the velocity profile $v(r)$ is,

$$v(r) = \frac{r}{t}, \text{ if } t > 0, \tag{4.5}$$

where t is the time after the supernova explosion. The ejecta velocity at r_{core} is therefore,

$$v_{core} = \left(\frac{10(n-5)E_{ej}}{3(n-3)M_{ej}}\right)^{1/2}, \tag{4.6}$$

(Truelove & McKee, 1999). The choice of r_{max} is free, as long as a mass of stellar wind smaller than M_{ej} is enclosed in $[r_{max}, r_{sncsm}]$. We determined its r_{max} using the numerical procedure described

in Whalen et al. (2008). We start the simulation at $t_{\max} = r_{\max}/v_{\max}$, where $v_{\max}$ is set to $30000 \, \mathrm{km \, s^{-1}}$ (see van Veelen et al., 2009).

We choose an uniform grid of resolution $\Delta \leq 10^{-4} \, \mathrm{pc \, cell^{-1}}$ and follow the expansion of the shock wave until slightly before it reaches the reverse shock of the bow shocks produced by our progenitors. These models are labelled with the prefix SNCSM (our Table 4.3). Additionally, we use a second passive scalar $Q_2(r)$ to distinguish the ejecta from the stellar wind. We carry out these one-dimensional calculations using a uniform spherically symmetric grid. We use a finite volume method with the Harten-Lax-van Leer approximate Riemann solver, and integrate the Euler equations with a second order, unsplit, time-marching algorithm. Dissipative processes are computed using our cooling curve for fully ionized gas. Results are presented in Section 4.4.

4.2.3 Modelling the supernova remnants

In order to resolve both the early interaction between the blastwave interacting with the circumstellar medium and the old supernova remnant, we adopt a mapping strategy. We run two-dimensional hydrodynamical simulations of the shock waves interacting with the bow shocks using a squared computational domain of size about $4R(0)$ which is supplied with a uniform rectilinear grid. These models are labelled with the prefix YSNR. The above described one-dimensional simulations of the ejecta interacting with the stellar wind is mapped into a circle of radius $r_{\max} < R(0)$ centered on the origin O of the domain. We run these simulations starting at t_{sncsm} until the shock wave has passed through the forward shock of the bow shock and reaches a distance of about $2R(0)$ in the direction of motion of the progenitor, at t_{ysnr} (our Table 4.4).

The remnants at t_{ysnr} are mapped a second time onto a larger computational domain which includes both the entire pre-calculated circumstellar medium and the calculations of the young supernova remnants (our Tables 4.2 and 4.4). The regions of this domain which overlap neither the bow shock nor the remnant are filled with unperturbed ISM gas. We start the simulations at time t_{ysnr} and follow edge of the domain in the $-\hat{z}$ direction, at t_{osnr}. These simulations are labelled with the prefix OSNR (our Table 4.5). Results are presented in Section 4.5.

4.3 The pre-supernova phase

In Fig. 4.1 we show the gas density fields in our bow shock from near the pre-supernova phase in the models PSN1020 (initially $10 \, \mathrm{M_\odot}$ star, $v_\star = 20 \, \mathrm{km \, s^{-1}}$, Fig. 4.1a), PSN1040 (initially $10 \, \mathrm{M_\odot}$ star, $v_\star = 40 \, \mathrm{km \, s^{-1}}$, Fig. 4.1b) and PSN1070 (initially $10 \, \mathrm{M_\odot}$ star, $v_\star = 70 \, \mathrm{km \, s^{-1}}$, Fig. 4.1c). Figs 4.2 and 4.3 show the same, but for our 20 and $40 \, \mathrm{M_\odot}$ stars. The figures plot the density at a time t_{psn} and do not show all of the computational domain. In Figs 4.1, 4.2 and 4.3 the overplotted solid black line is the contact discontinuity, i.e. the border between the wind and ISM gas where the value of the passive scalar $Q_1(r) = 1/2$.

The bow shock of our 10 and $20 \, \mathrm{M_\odot}$ stars have morphologies consistent with previous studies (see in van Marle et al., 2011b; Mohamed, Mackey & Langer, 2012, Paper I). Their overall shape is rather stable if $v_\star \leq v_\mathrm{w}$ (Dgani, van Buren & Noriega-Crespo, 1996a) and the flow inside the bow shocks is laminar (Fig. 4.1a). The bow shocks are unstable and exhibit Rayleigh-Taylor and/or Kelvin-Helmholtz instabilities for $v_\star \geq v_\mathrm{w}$ because of the large density difference between the dense red supergiant wind and the ISM gas (Figs 4.1b,c and 4.2a,b). For high-mass stars moving with large space velocities, e.g. the models with $M_\star \geq 20 \, \mathrm{M_\odot}$ and $v_\star \geq 40 \, \mathrm{km \, s^{-1}}$, the shocked layers develop non-linear thin-shell instabilities (Vishniac, 1994; Garcia-Segura, Langer & Mac Low, 1996; Blondin & Koerwer, 1998) and induce strong mixing in the wakes of the bow shocks (Fig. 4.2c).

Table 4.4: Input parameters used in our simulations of the supernova blastwaves interacting with the bow shocks of our progenitors. As input we use the solution of the shock waves interacting with the stellar winds (our Table 4.3). The grid parameters are similar as in our Table 4.2. Our simulations start at t_{sncsm} (our Table 4.2) shortly before that the shock wave interacts with the bow shock and the models are run until t_{ysnr} (in yr) once the shock wave has gone through it.

Model	Input	z_{min} (pc)	R_{max} (pc)	N_R	N_z	Δ (pc cell^{-1})	t_{sncsm} (yr)	t_{ysnr} (yr)
YSNR1020	SNCSM1020	-2.0	2.0	1000	2000	2.0×10^{-3}	40	264
YSNR1040	SNCSM1040	-1.3	1.3	1000	2000	1.3×10^{-3}	13.5	150
YSNR1070	SNCSM1070	-0.7	0.7	1000	2000	4.0×10^{-4}	15	60
YSNR2020	SNCSM2020	-8.0	8.0	1000	2000	8.0×10^{-3}	40	2400
YSNR2040	SNCSM2040	-2.0	2.0	1000	2000	2.0×10^{-3}	20	450
YSNR2070	SNCSM2070	-1.0	1.0	1000	2000	1.0×10^{-3}	25	170
YSNR4020	SNCSM4020	-25	25	1000	2000	2.50×10^{-2}	400	4900
YSNR4040	SNCSM4040	-7.0	7.0	1500	3000	4.67×10^{-3}	200	1360
YSNR4070	SNCSM4070	-4.0	4.0	1500	3000	2.67×10^{-3}	180	830

Table 4.5: Input parameters used in our simulations of the supernova blastwaves interacting with the tails of the bow shocks generated by our progenitors. As input we use the solution of the shock waves interacting with the bow shocks (our Table 4.4). The grid parameters are similar as in our Table 4.2. Our simulations start at t_{ysnr} (our Table 4.4) and the models are run until t_{osnr} (in yr).

Model	Input	$z_{\min}$ (pc)	$R_{\max}$ (pc)	N_{R}	N_{z}	Δ (pc cell^{-1})	t_{ysnr} (yr)	t_{osnr} (yr)
OSNR1020	YSNR1020	-6.0	6.0	500	1000	1.2×10^{-2}	264	1500
OSNR1040	YSNR1040	-2.1	2.1	500	1000	4.2×10^{-3}	150	1300
OSNR1070	YSNR1070	-0.9	0.9	500	1000	4.0×10^{-4}	60	1300
OSNR2020	YSNR2020	-30.0	25.0	1000	2000	9.0×10^{-2}	2400	21100
OSNR2040	YSNR2040	-9.0	9.0	1000	2000	2.5×10^{-3}	450	15000
OSNR2070	YSNR2070	-4.5	4.5	1000	2000	9.0×10^{-3}	170	10000
OSNR4020	YSNR4020	-90.0	70.	1000	1714	7.0×10^{-2}	4900	49500
OSNR4040	YSNR4040	-35.0	25.0	1000	2200	2.5×10^{-2}	1360	14000
OSNR4070	YSNR4070	-30.0	15.0	700	2333	2.14×10^{-2}	830	10500

Table 4.6: Gas mass M in the region of the bow shocks that is upstream from the progenitor ($z \geq 0$) and stand-off distance at the contact discontinuity (in pc) measured in our simulations of the circumstellar medium from near the pre-supernova phase, at a time $t_{\rm psn}$.

Model	$M\,(M_\odot)$	$R(0)\,({\rm pc})$
PSN1020	0.06	0.42
PSN1040	0.03	0.25
PSN1070	0.01	0.17
PSN2020	3.87	1.35
PSN2040	1.10	0.64
PSN2070	0.75	0.55
PSN4020	116.00	5.00
PSN4040	9.40	2.70
PSN4070	1.65	1.55

The stellar motion displaces the position of the star from the center of the cavity of unshocked wind material (Brighenti & D'Ercole, 1995a,b), and this displacement is larger for velocities $v_\star \geq 20\,{\rm km\,s^{-1}}$ (Fig. 4.2a). The bow shocks which have the most pronounced tunnels of low-density gas are produced either by our initially $20\,M_\odot$ star moving with $20\,{\rm km\,s^{-1}}$ or by our initially $40\,M_\odot$ star (Fig. 4.2a and 4.3a-c). In the region downstream from the progenitor, the reverse shock, which forms the walls of the cavity, has a rather smoothed appearance for $v_\star \leq 20\,{\rm km\,s^{-1}}$ (Fig. 4.2a) but it is ragged for $v_\star \geq 40\,{\rm km\,s^{-1}}$ (Fig. 4.3c). Finally, note that the model PSN2020 has a double bow shock due to the final increase of the mass loss that ends the red supergiant phase. This structure is called a Napoleon's hat and it develops when the bow shock from a new mass-loss event goes through the one generated by the previous evolutionary phase (Wang, Dyson & Kahn, 1993; Mackey et al., 2012).

The stand-off distance $R(0)$ and the mass M trapped in the bow shocks upstream from the star ($z \geq 0$) are summarised in Table 4.6. The more massive bow shock are the biggest ones, e.g. our bow shock model PSN4020 has the largest stand-off distance $R(0) \approx 5\,{\rm pc}$ and has accumulated about $116\,M_\odot$ of shocked gas. They are generated by high-mass stars moving with small space velocities, i.e. $M_\star \geq 20\,M_\odot$ and $v_\star \leq 40\,{\rm km\,s^{-1}}$ (Figs 4.2a-4.3ab). In Fig. 4.4 we show the average density profiles in our simulations of our 10 (Fig. 4.4a), 20 (Fig. 4.4b) and $40\,M_\odot$ models (Fig. 4.4c), that we use as initial conditions for our one-dimensional simulations of the supernova shock waves interacting with their surroundings, see Eq. (4.2)−(4.3). Fig. 4.4 illustrates that the most massive bow shocks have the largest $R(0)$, i.e. they are the most voluminous and are reached by the shock wave about $R(0)/v(r) \approx 10^3\,{\rm yr}$ after the explosion (Section 4.4).

4.4 The young supernova remnant

This section presents our simulations of the supernova blastwaves interacting with their circumstellar medium until the shock wave reaches the outer layer of its surrounding bow shock. Spherical remnants are distinguished from asymmetric remnants as a function of their progenitors' properties.

4.4.1 The ejecta-stellar-wind interaction

In Fig. 4.5 we show a typical interaction between a supernova shock wave and the surrounding stellar wind, before the shock wave collides with the bow shock. We plot the gas number density (solid blue
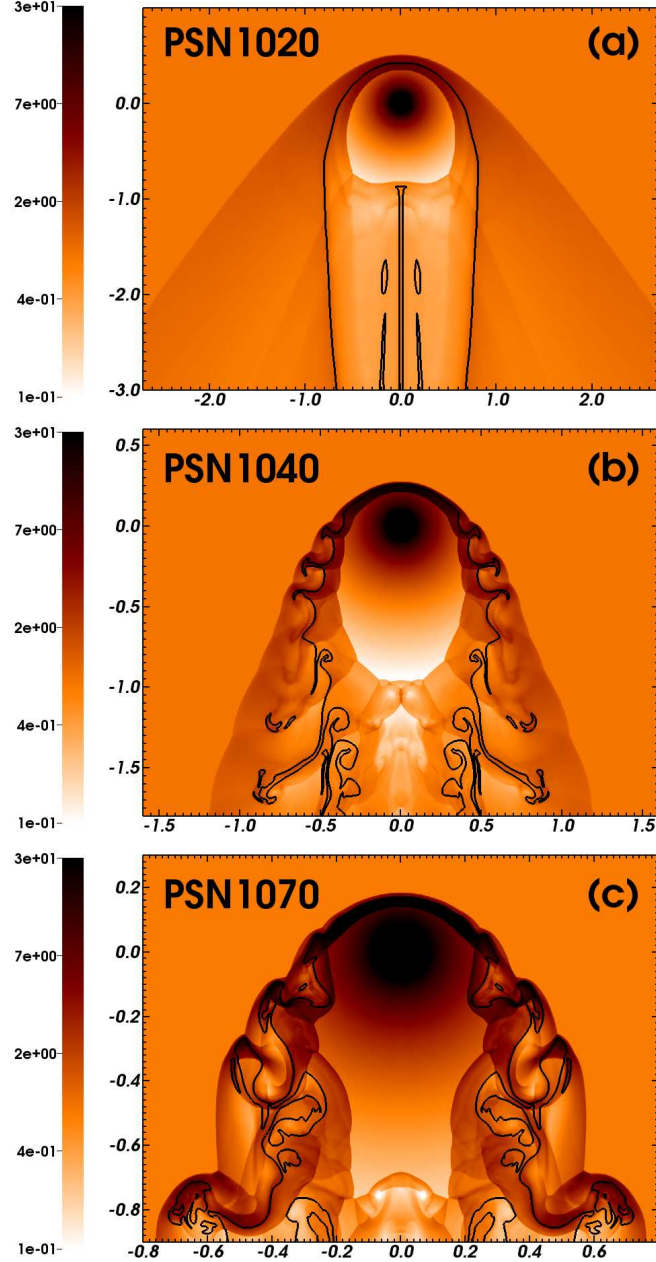
Figure 4.1: Grid of stellar wind bow shocks from the pre-supernova phase of our initially $10\,\mathrm{M_\odot}$ progenitor as a function of its space velocity with respect to the ISM, with velocity $v_\star = 20$ (a), 40 (b) and $70\,\mathrm{km\,s^{-1}}$ (c). The nomenclature of the models follows Table 4.2. The bow shocks are shown at t_psn. The gas number density is shown with a density range from 10^{-1} to $30.0\,\mathrm{cm^{-3}}$ in the logarithmic scale. The solid black contour traces the boundary between wind and ISM material $Q_1(r) = 1/2$. The x-axis represents the radial direction and the y-axis the direction of stellar motion (in pc). Only part of the computational domain is shown in the figures.
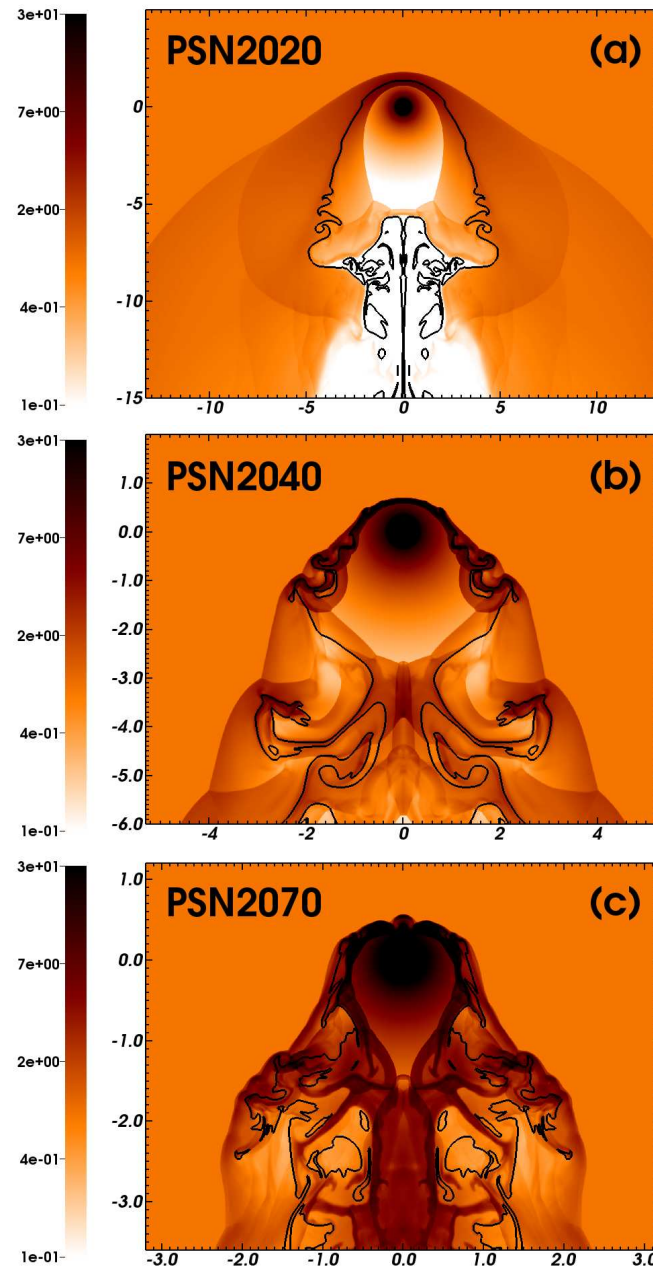
Figure 4.2: As Fig. 4.1, with our initially $20\,\mathrm{M}_\odot$ progenitor.
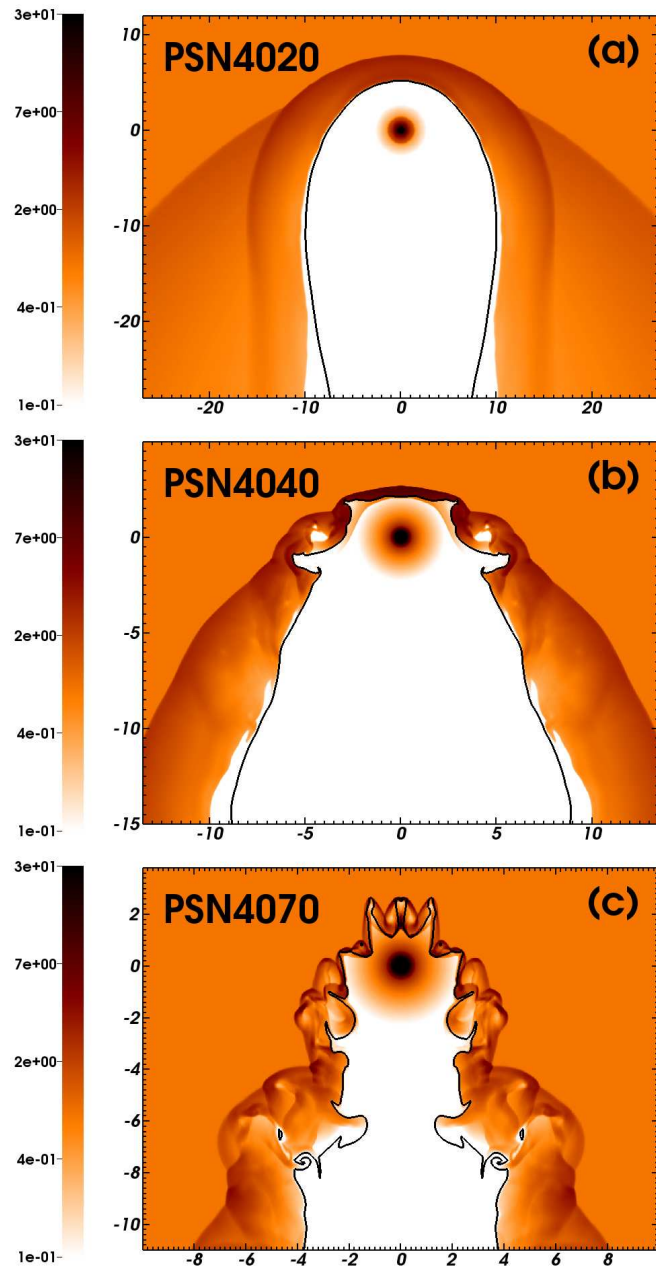
Figure 4.3: As Fig. 4.1, with our initially $40\,M_\odot$ progenitor.
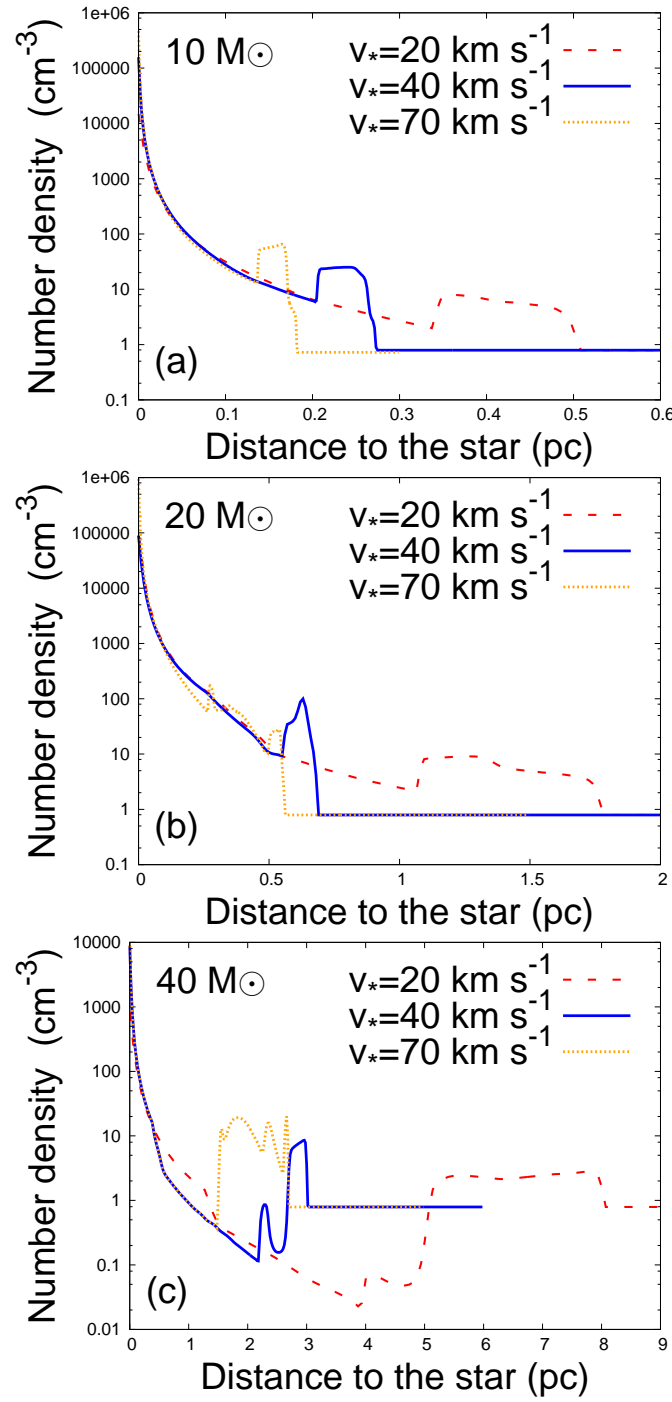
Figure 4.4: Gas number density profiles (in cm^{-3}) taken along the direction of motion of our initially 10 (a), 20 (b) and $40\,M_\odot$ (c) progenitors at t_{psn}.
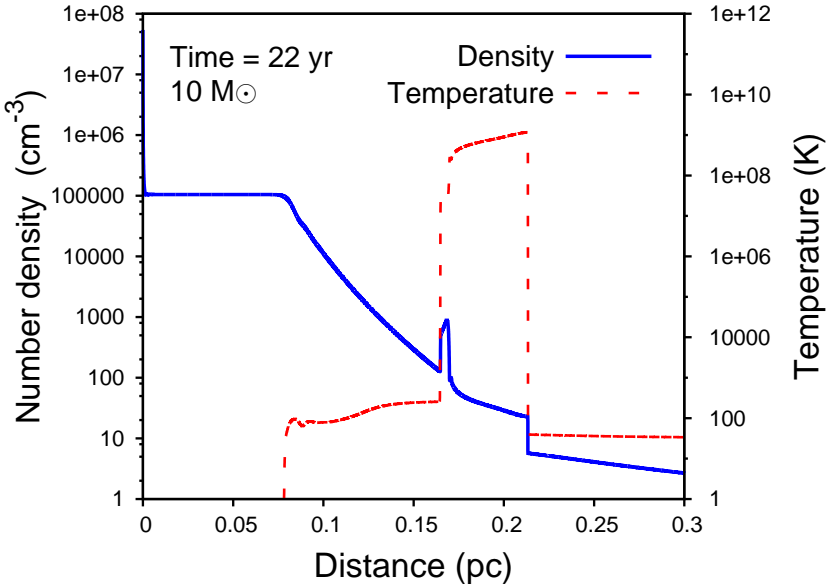
Figure 4.5: Total number density (solid blue line, in cm^{-3}) and temperature (dashed red line, in km s^{-1}) profiles of the supernova ejecta interacting with the circumstellar medium of our initially 10 M$_\odot$ progenitor. Profiles are shown at about 22 yr after the supernova.

line) and temperature (dashed red line) profiles in our model SNCSM1020 at a time about 22 yr after the supernova explosion. It assumes a release of M_{ej} = 7.7 $M_\odot$ of ejecta together with a kinetic energy of E_{ej} = 10^{51} erg (our Table 4.3). The structure is composed of 4 distinct regions: the expanding ejecta profile, itself made of two regions, the core and the envelope (Truelove & McKee, 1999), the shell of swept up shocked ejecta and shocked wind material, and finally the undisturbed circumstellar material (Chevalier, 1982).

The shell is bordered by two shocks, a reverse shock that is the interface between ejecta and shocked ejecta, and a forward shock constituting the border between shocked wind and undisturbed freely-expanding stellar wind (Chiotellis, Schure & Vink, 2012). The core of the ejecta (r < 0.08 pc) has a very low temperature because its thermal pressure is initially null (Whalen et al., 2008; van Veelen et al., 2009). The temperature slightly increases up to a few tens of degrees in the envelope of ejecta (0.08 $\leq$ r $\leq$ 0.16 pc) because (i) we use a homologous velocity profile which results in increasing the thermal pressure close to the high-velocity shock wave and (ii) the decreasing density $\rho_{max} \propto r^{-11}$ increases the temperature $T \propto p/\rho$. At radii $r \approx$ 0.16 pc is the hot ($T \approx 10^6$ K) and dense ($n \gg 10^3$ cm^{-3}) gas. This region between the shell and the shock wave is hot because it is shock-heated by the blastwave and it has not yet time to cool. All our models have a similar behaviour.

4.4.2 The shock wave interacting with the bow shock

The supernova interacting with the bow shock generated by the 10 M$_\odot$ star moving with $v_\star$ = 40 km s^{-1} is illustrated in Fig. 4.6. We show the density field in our simulation YSNR1040, composed of a shock wave interacting with its circumstellar medium (our model SNCSM1040). The density stratification is shown at times $t_{sncsm} \approx$ 152 yr (Fig. 4.6a), 154, 162, 168, 192 and $t_{ysnr} \approx$ 246 yr (Fig. 4.6f) after the explosion, respectively. Note that the part of the computational domain plotted in Fig. 4.6f is larger than in Figs 4.6a-e. Corresponding cross-sections measured in these density fields along the Oz axis are shown in Fig. 4.7.

At a time $t_{\mathrm{sncsm}} \approx 152\,\mathrm{yr}$ the solution SNCSM1040 is mapped on the model PSN1040 shortly before the supernova remnant shock wave reaches the reverse shock of the bow shock (Fig. 4.6a). From the origin to larger radius, the curve (a) of Fig. 4.7 plots the initial plateau of density $\rho_{\mathrm{core}}(r) \approx 10^5 \mathrm{cm}^{-3}$, the steep profile $\rho_{\mathrm{max}}(r) \propto r^{-n}$, the shell of swept-up ejecta at about $0.16\,\mathrm{pc}$ (cf. Fig. 4.5), the shock wave progressing in the freely-expanding wind, the red-supergiant bow shock from about 0.21 to about $0.27\,\mathrm{pc}$, and the unperturbed ISM.

In Fig. 4.6b the shock wave collides with the reverse shock of the bow shock and begins to interact with the dense ($n \approx 25\mathrm{cm}^{-3}$) shocked wind. The interaction starts at the stagnation point because this is the part of the bow shock with the smallest radius (Borkowski, Blondin & Sarazin, 1992). The blastwave decelerates and loses its spherical symmetry, the shock wave penetrates the reverse shock of the bow shock at a time $154\,\mathrm{yr}$ with velocity $v \approx 6700\,\mathrm{km\,s}^{-1}$ whereas it hits its forward shock $8\,\mathrm{yr}$ later with velocity $v \approx 4500\,\mathrm{km\,s}^{-1}$. At $162\,\mathrm{yr}$, the shell of shocked ejecta merges with the former post-shock region at the reverse shock of the bow shock, and its material is compressed to $n \approx 85\,\mathrm{cm}^{-3}$ (curve (c) of Fig. 4.7).

In Fig. 4.6c the shock wave has totally penetrated the bow shock, both a reflected and a transmitted shock wave form at both the ends of the bow shock. In Fig. 4.6d the transmitted shock at the former forward shock starts expanding into the undisturbed ISM. As sketched in fig. 3 of the study by Borkowski, Blondin & Sarazin (1992), a bump emerges beyond the bow shock and it reaches about $0.32\,\mathrm{pc}$ at a time $168\,\mathrm{yr}$ after the explosion (curve (d) of Fig. 4.7). It expands and enlarges laterally as the shock wave, that is no longer restrained by the material of the bow shock, penetrates the undisturbed ISM, accelerates and progressively recovers its spherical symmetry (Fig. 4.6e).

At a time $246\,\mathrm{yr}$, the shock wave has recovered its sphericity (Fig. 4.6f). Note that the shock wave is slightly constricted in the cavity of unshocked wind as it expands downstream from the direction of motion of the progenitor. This anisotropy is a function of the circumstellar density distribution at the pre-supernova phase and governs the long term evolution of the supernova remnant (Section 4.4.3). The curve (f) of Fig. 4.7 shows the density structure composed of the plateau whose density has diminished to $\rho_{\mathrm{core}} \approx 600\,\mathrm{cm}^{-3}$, the twice shocked ejecta, shocked ejecta, twice shocked stellar wind, twice shocked ISM, shocked ISM and finally the unperturbed ISM (c.f. Borkowski, Blondin & Sarazin, 1992). These regions are not clearly discernible because of the mixing at work provoked by the multiple reflections and refractions proliferating through the remnant (curve (f) of Fig. 4.7).

4.4.3 Spherical and aspherical supernova remnants

In Fig. 4.8 we represent the density profiles of our models of supernova remnants at a time t_{ysnr}, taken along the direction of motion of the progenitors. The models produced by our $10\,M_\odot$ progenitor conserve their symmetry after the shock waves collide with the bow shocks, e.g. our model YSNR1020 has a plateau of density $n \approx 10^2\,\mathrm{cm}^{-3}$ at $|z| \leq 1.7\,\mathrm{pc}$, whereas its density distribution in both directions beyond the shock wave is about the ISM ambient medium density. Here, the shock wave expansion is barely disturbed by the light bow shocks (our Table 4.6) and the remnants grow quasi-spherically (Fig. 4.6).

The remnant generated by our $20\,M_\odot$ star moving with $v_\star = 20\,\mathrm{km\,s}^{-1}$ is aspherical, in that it has a cavity of $n \approx 10^{-2}\,\mathrm{cm}^{-3}$ at $z < -8\,\mathrm{pc}$ (red curve in Fig. 4.8b). This is much less pronounced for models with a larger $v_\star$, i.e. our models YSNR2040 and YSNR2070, see blue and yellow curves in Fig. 4.8b. They have a rather spherical density distribution, and only a bulge of swept-up wind material in the direction $+\hat{z}$ distinguishes them from a spherically symmetric structure. A small accumulation of swept-up gas that could slightly brake the shock wave forms in the direction $-\hat{z}$, i.e., these models do form a pronounced wind cavity (Fig. 4.8bc).
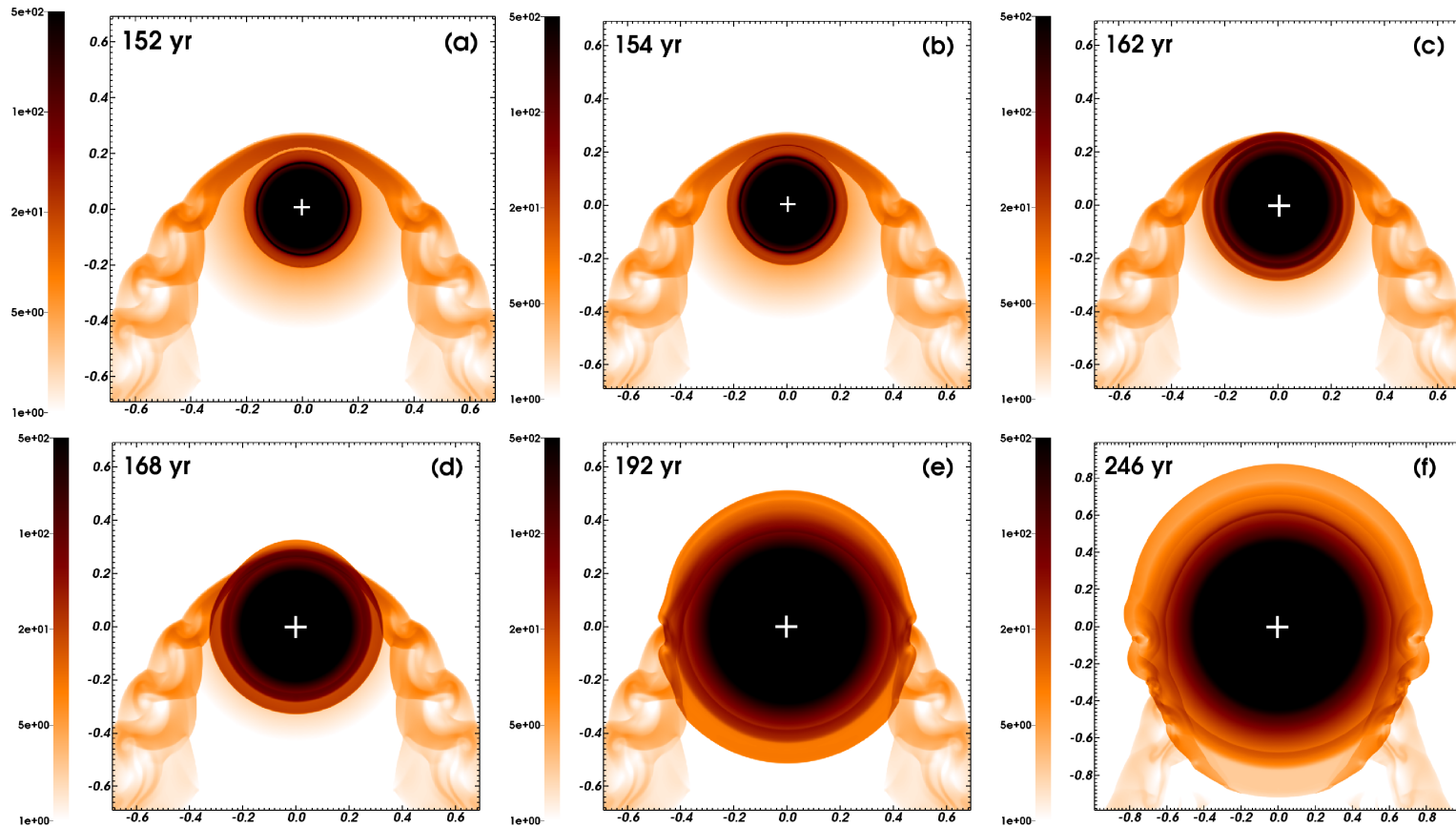
Figure 4.6: Time sequence of a supernova interacting with the bow shock generated by our initially $10\,\mathrm{M_\odot}$ progenitor moving with velocity $40\,\mathrm{km\,s^{-1}}$. The figures correspond to times t_sncsm (a) up to about t_ysnr (f). The gas number density is shown with a density range from 1.0 to $5 \times 10^2\,\mathrm{cm^{-3}}$ on a logarithmic scale. The white cross marks the center of the explosion. The x-axis represents the radial direction and the y-axis the direction of stellar motion (in pc). Only part of the computational domain is shown in the figures. Note that the panel (f) shows the supernova remnant at larger scale than in panels (a-e).
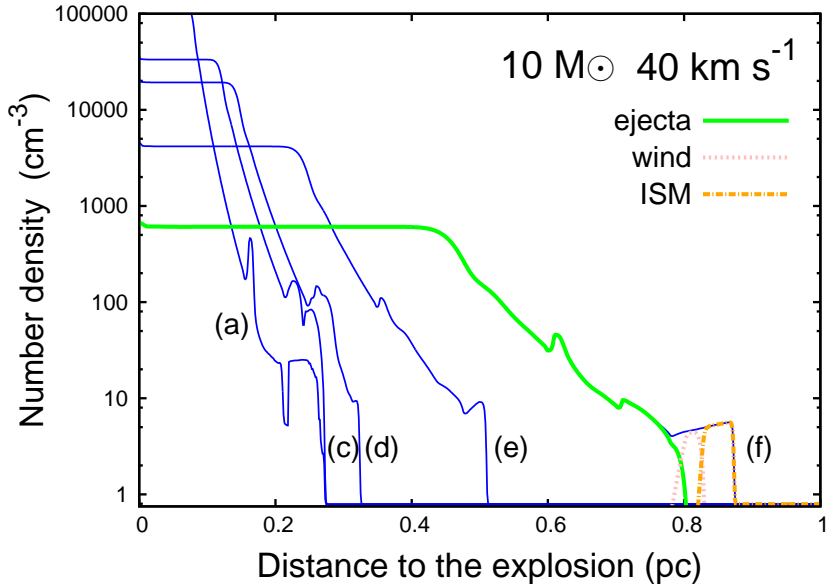
Figure 4.7: Cross-sections taken along the direction of motion of the progenitor through the number density field of the supernova blastwave interacting with $z \geq 0$ region of the bow shock produced by our initially $10\,M_\odot$ progenitor moving with velocity $40\,km\,s^{-1}$ (Fig. 4.6a-f). The respective proportion of the supernova ejecta (solid green), stellar wind (dotted red) and ISM material (dashed orange) are indicated for the curve (f).

The supernova remnants of our $40\,M_\odot$ progenitor are all strongly anisotropic, e.g. our model with velocity $v_\star = 70\,km\,s^{-1}$ has a dense shell of density $n \approx 10^2\,cm^{-3}$ along the direction $+\hat{z}$ and a cavity of density $n \approx 10^{-2}\,cm^{-3}$ in the opposite direction (Fig. 4.8c). On the basis of Table 4.6 and according to the above discussion, we find that the bow shocks of runaway stars that we simulate and which accumulate more than about $1.5\,M_\odot$ generate asymmetric supernova remnants. In the next section, we continue our study focusing on the asymmetric models only, i.e. generated either by our $20\,M_\odot$ progenitor moving with $v_\star = 20\,km\,s^{-1}$ or produced by our $40\,M_\odot$ star.

4.5 The old supernova remnant phase

In this section we detail the interaction between supernova ejecta and pre-shaped circumstellar medium once the expanding front has passed through the bow shock. We focus on our four models of supernova remnants whose solutions highly deviate from sphericity.

4.5.1 Physical characteristics of the remnants

Asymmetric structures...

We show the gas density fields in the old supernova remnant produced by our $20\,M_\odot$ progenitor moving with velocity $v_\star = 20\,km\,s^{-1}$ in Fig. 4.9. Figs 4.10, 4.11 and 4.12 are similar to our $40\,M_\odot$ progenitor moving with velocity $v_\star = 20, 40$ and $v_\star = 70\,km\,s^{-1}$, respectively. In each of these figures, the panel (a) corresponds to a time t_{ysnr} (our Table 4.4), the panel (b) shows the shock wave expanding into the wind cavity and the panel (c) shows the remnant at t_{osnr} when the simulation ends (our Table 4.5). The figures do not show the full computational domain. In Figs 4.9 to 4.12, the overplotted solid black line
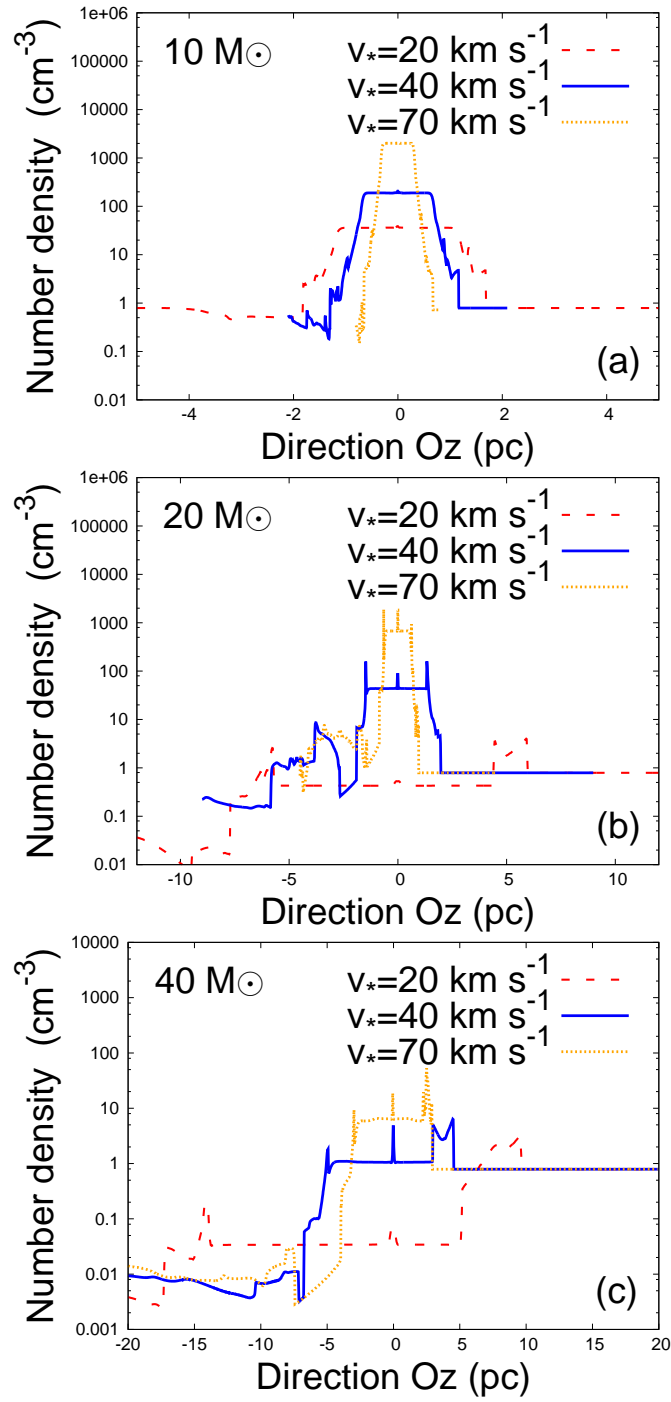
Figure 4.8: Density profiles (in cm^{-3}) of our supernova remnants taken along the direction of motion of our initially 10 (a), 20 (b) and $40\,M_\odot$ (c) progenitors at t_{ynsr}.

is the border between the wind and ISM gas where the value of the passive scalar $Q_1(r) = 1/2$, and the dashed black line is the discontinuity between the ejecta and the other materials where $Q_2(r) = 1/2$.

At a time t_{ysnr}, the shock wave is already asymmetric because its unusually dense surroundings (see our Table 4.6) strongly restrain it from expanding into the direction normal to the direction of motion of the progenitor (panels (a) of Figs 4.9 to 4.12). As an example, the forward shock in our model OSNR2020 at a time 2400 yr has reached about 5.8 pc and 6 pc along the $+\hat{R}$ and $+\hat{z}$ directions, respectively, whereas it expands to about -7.9 pc along the $-\hat{z}$ direction. This asymmetry of the shock wave is particularly pronounced in our simulation OSNR4020 whose pre-shaped circumstellar medium contains the most massive bow shock with a mass of $116\,M_\odot$ (Fig. 4.10ab).

At times larger than t_{ysnr}, the shock wave freely expands into the undisturbed ISM because it has entirely overtaken its circumstellar structure (Brighenti & D'Ercole, 1994), see Figs 4.10-4.12bc. It progressively recovers its sphericity, but this takes longer in our simulations with slowly moving progenitors because the mass in their bow shock is larger (Fig. 4.10c and 4.12c). The penetration of the shock wave through the wake of the bow shock results in its chanelling into the tubular cavity of unshocked stellar wind (Blandford et al., 1983). The constant cross-sectional area of the cavity continues to impose large temperature and pressure jumps at the post-shock region of the shock wave, which prevents it from decelerating and which collimates the ejecta as a tubular/jet-like extension to the spherical region of shocked ejecta (Cox, Gull & Green, 1991).

... of differential physical properties

Fig. 4.13 plots the spatio-temporal evolution of the shock front measured in our apsherical remnants along the $+\hat{z}$ and $-\hat{z}$ directions. The shock wave typically expands into the ISM at velocities of the order of a few hundred kilometers per seconds whereas it propagates inside the trail of the bow shock with a velocity of the order of a few thousands kilometers per seconds. E.g. at a time 4500 yr after the explosion, the model OSNR2020 has a shock wave velocity of 564 and 1578 km s^{-1} at 8.73 and 13.03 pc from the center of the explosion in the direction along and opposite of the progenitor's motion, respectively. The differential expansion of the shock wave is more important for our slowly moving progenitors which induce the strongest anisotropy in their circumstellar medium (Fig. 4.13a-b), whereas the ejecta velocity is larger for fast-moving progenitors (Fig. 4.13d).

Because the blastwave expand in non-uniform medium (Ferreira & de Jager, 2008), a wave created during the collision with the dense bow shock is reflected towards the center of the explosion and shocks back the unperturbed supernova ejecta (see Fig 4.9a-c). This mechanism generates a hot region of ejecta which progressively fills the entire cavity of the remnants, e.g. the shocked ejecta of our model OSNR2020 has $n \approx 3\,\mathrm{cm}^{-3}$ and $T \approx 10^6$ K (Fig. 4.9bc). Simultaneously, the collimated shock wave continues expanding downstream from the center of the explosion. It hits the tunnel's side, which postshock density increases up to about $30\,\mathrm{cm}^{-3}$ in model OSNR4020 and cools to less than 10^5 K. The shocked walls produce strong optical line emission (Cox, Gull & Green, 1991, see also Section 4.5.3).

A transmitted wave penetrates the shocked wind material in the bow shock (Brighenti & D'Ercole, 1994) while a wave is reflected towards the center of the tunnel. After the passage of the shock wave through the throttling that separates the tunnel from the bow shock, its cross-sectional area is locally constricted and accelerates the flow. It is about 1500 km s^{-1} at a time 4200 yr, about 2750 km s^{-1} at a time 4200 yr and decelerates down to 1450 km s^{-1} when the shock wave expands further in the tunnel at a time 12000 yr in our simulation OSNR2020 (Fig. 4.13). The same happens when the reflected waves collide at the center of the tunnel (Fig. 4.13a-b). At a time t_{ysnr} almost the whole interior of the remnant is shocked by the reflected shock wave, and these multiple reflections induce a strong mixing of ejecta, wind and ISM (see the overlapping of the lines where $Q_1(r) = Q_2(r) = 1/2$). The thin layer
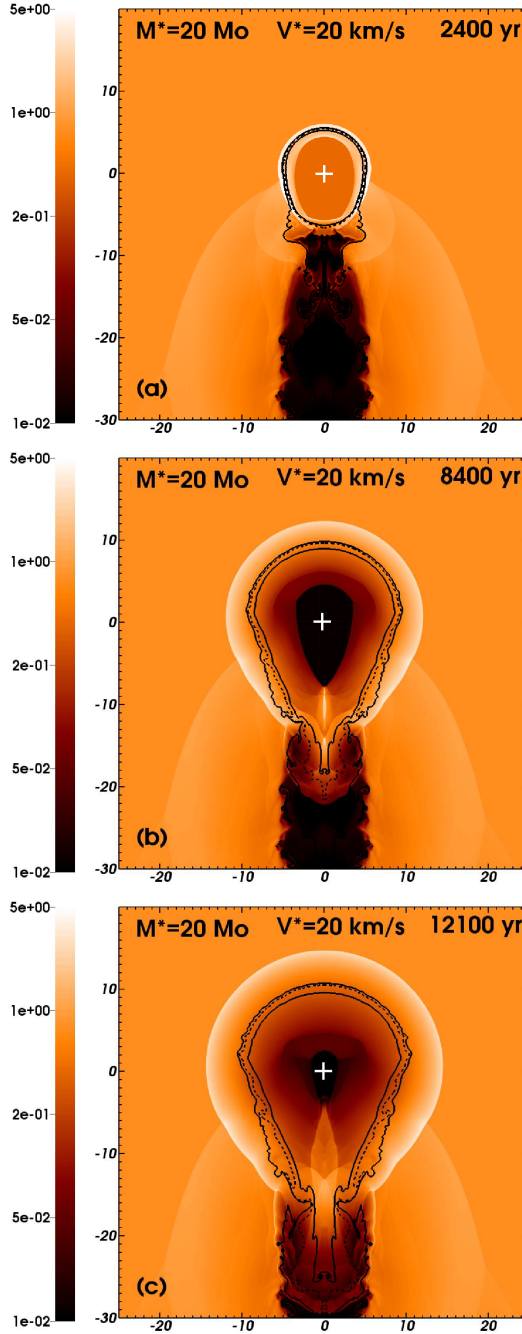
Figure 4.9: Time sequence of the evolution of the supernova remnant generated by our initially $20\,M_\odot$ progenitor moving with velocity $20\,km\,s^{-1}$. The figures are shown at a time t_{ysnr} (a), at an intermediate time (b) and at the end of the simulation, at a time t_{osnr} (c). The gas number density is shown with a density range from 10^{-2} to $5.0\,cm^{-3}$ on the logarithmic scale. Note that the color scale is reversed compare to Fig. 4.1 to 4.3. The cross marks the center of the explosion. The solid black contours trace the boundary between stellar wind material and either the supernova ejecta or ISM gas $Q_1(r) = 1/2$. The dotted black contour is the discontinuity between supernova ejecta and wind material $Q_2(r) = 1/2$. The nomenclature of the models follows our Table 4.5. The x-axis represents the radial direction and the y-axis the direction of stellar motion (in pc). Only part of the computational domain is shown in the figures.
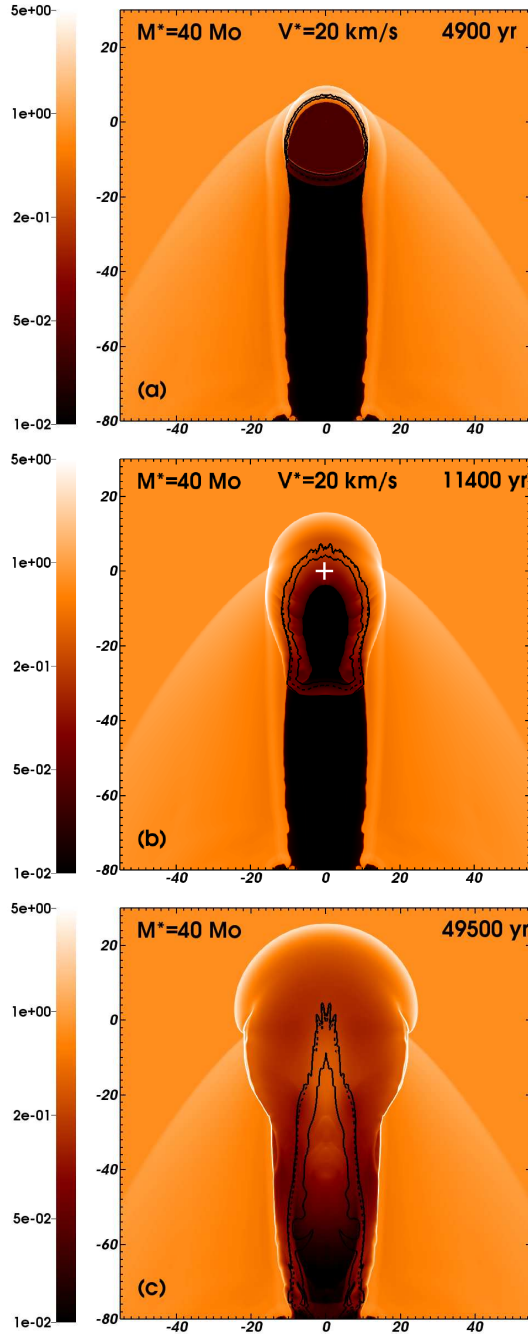
Figure 4.10: As Fig. 4.9, with our initially $40\,\mathrm{M}_\odot$ progenitor.

of stellar wind material upstream from the center of the explosion develops Rayleigh-Taylor-related instabilities (Kane, Drake & Remington, 1999), see Fig. 4.12c.

The stars end their lives as core-collapse supernovae and the explosion can produce a runaway neutron star (Lyne & Lorimer, 1994). Assuming a typical velocity of the compact object of about $400 \, \text{km s}^{-1}$ (Hobbs et al., 2005), one finds that it could not be further than about 4.84, 19.8, 5.6 and 4.2 pc from the center of the explosion in our simulations at t_{osnr} (Figs 4.9c, 4.10c, 4.11c and 4.12c). Consequently, we suggest that our remnants host a neutron star of mass $M_{\text{co}} \approx 2 \, \text{M}_\odot$ in the region close to the center of the explosion, i.e. out of the chimney-like extension of channelled ejecta.

4.5.2 Remnants luminosity

We plot the luminosities (in erg s^{-1}) of the aspherical supernova remmants as a function of time (in Myr) in Fig. 4.14. The bolometric luminosity by optically-thin radiation, L (red thin line with triangles), is estimated with the used cooling curve, integrating the energy emitted per unit time and per unit volume over the whole remnant. Similarly, we plot the contribution L_{ISM} from the hot ISM gas ($T > 10^7$ K, blue solid line) and from the warm ISM gas ($T \leq 10^7$ K, blue thin dashed lines) and the contribution L_{ej} from the ejecta (orange dotted line). The X-ray luminosity, L_{X}, is calculated for gas temperatures $10^5 \leq T \leq 1.58 \times 10^8$ K, with emission coefficients interpolated from tables generated with the XSPEC software (Arnaud, 1996) with solar metalicity and chemical abundances from Asplund et al. (2009) as in Mackey et al. (2014a).

The total luminosity L is first dominated by the hot ($T \geq 10^7$ K) gas emission from the shock wave before becoming dominated by emission from the warm ISM gas of temperature $T \leq 10^7$ K at a time about 8000 yr (see thick solid blue line in Fig. 4.14a-d) because during the post-shock temperature at the shock wave decreases during the adiabatic expansion of the blastwave. At larger times, the warm gas of temperature below 10^7 K emits more per unit time and per unit volume than the hot material because the cooling from the metals is stronger at $T \approx 10^6$ K than at $T \geq 10^7$ K (Fig.4a of Paper I), so L increases.

L increases as a function of time from t_{ysnr} up to the end of our simulation. The reflection of the shock wave towards the center of the explosion produces a growing hot, dense region that is upstream from the center of the explosion and augments the luminosity. The emission is influenced by the size of the bow shock at the pre-supernova phase which decreases with $v_\star$ and triggers the reflection of the shock wave (Paper I) and by the age of the remnant when the shock wave starts expanding through the ISM. L monotonically increases by less than one order of magnitude over a timescale of about 10^4 yr, e.g. in our model OSNR4070 $L \approx 1.2 \times 10^{36}$ erg s^{-1} at $t \approx 10^3$ yr and $L \approx 9.5 \times 10^{36}$ erg s^{-1} at a time 10^4 yr (Fig. 4.14d).

L_{ej} is smaller than L_{ISM} by about an order of magnitude at t_{ysnr}, e.g. just after the end of the shock wave-bow shock collision, $L \approx 8.0 \times 10^{35}$ and $L_{\text{ej}} \approx 3.0 \times 10^{35}$ erg s^{-1} in model OSNR4070 (Fig. 4.14d). It monotonically decreases with time as the shocked ejecta expands and its density decreases such that its emission finally become a negligible fraction of L (Fig. 4.14a-d). The contribution from the wind material is negligible compared to the bolometric luminosity (and so is not shown in Fig. 4.14) and it does not influence L at all.

The total X-ray emission, L_{X}, is calculated as the emission from photons at energies 0.1-50 keV. Not surprisingly, this is slightly smaller than the component of L_{ISM} from the gas with $T \leq 10^7$ K and follows the same trend as L (Fig. 4.14a-d). The soft X-ray emission, i.e. from photons in the 0.5-1.0 keV energy band, is fainter than L_{X} by less than an order of magnitude and has a similar behaviour as a function of time except for our older and larger supernova remnant OSNR4040 (Fig. 4.14b). The hard X-ray emission in the 2.0-5.0 keV energy band is fainter than L_{X} by about an order of magnitude at t_{ysnr}. It decreases as a function of time (Brighenti & D'Ercole, 1994) because the emission of very energetic X-
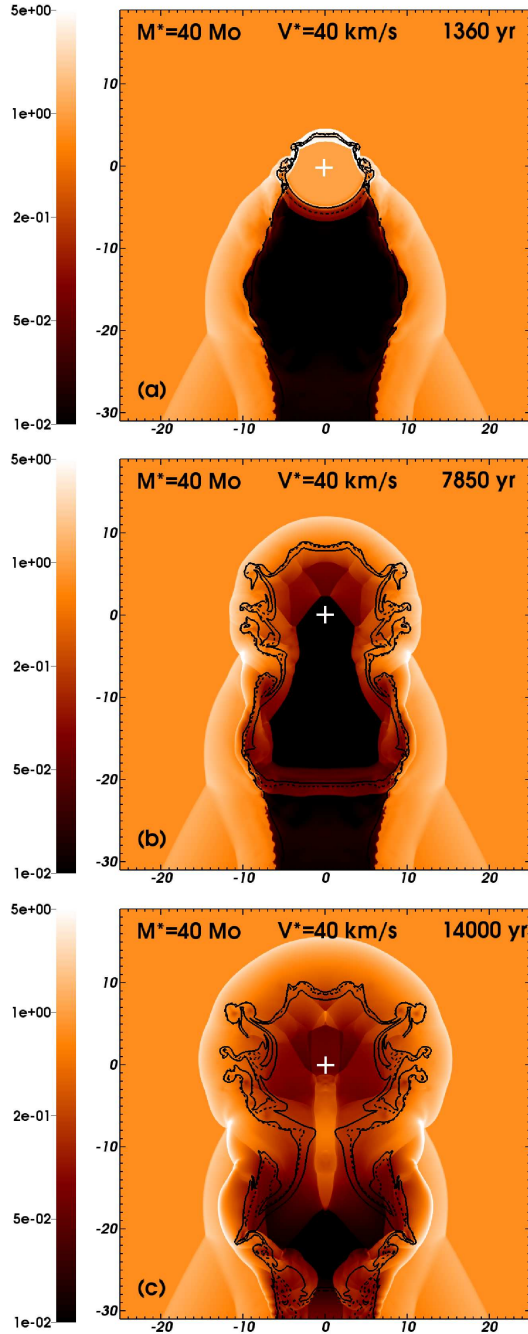
Figure 4.11: As Fig. 4.10, with space velocity $v_\star = 40 \, \mathrm{km \, s^{-1}}$.
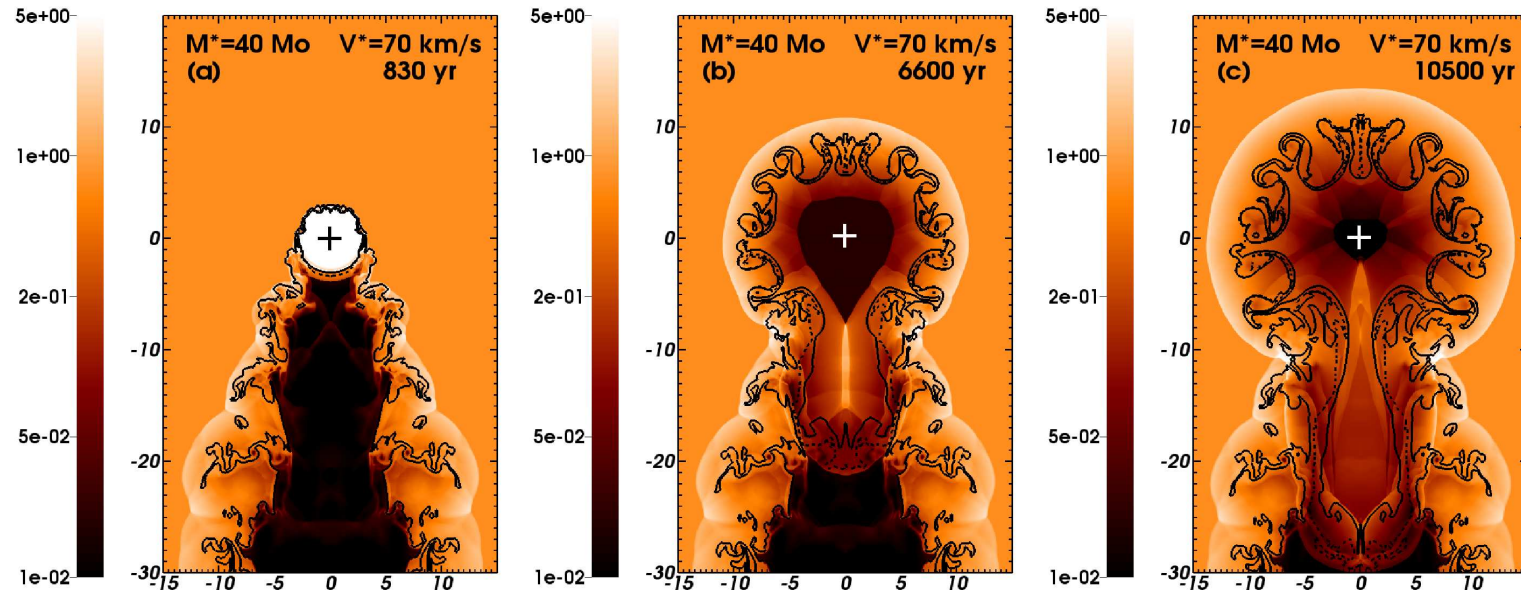
Figure 4.12: As Fig. 4.10, with space velocity $v_\star = 70\,\mathrm{km\,s^{-1}}$.
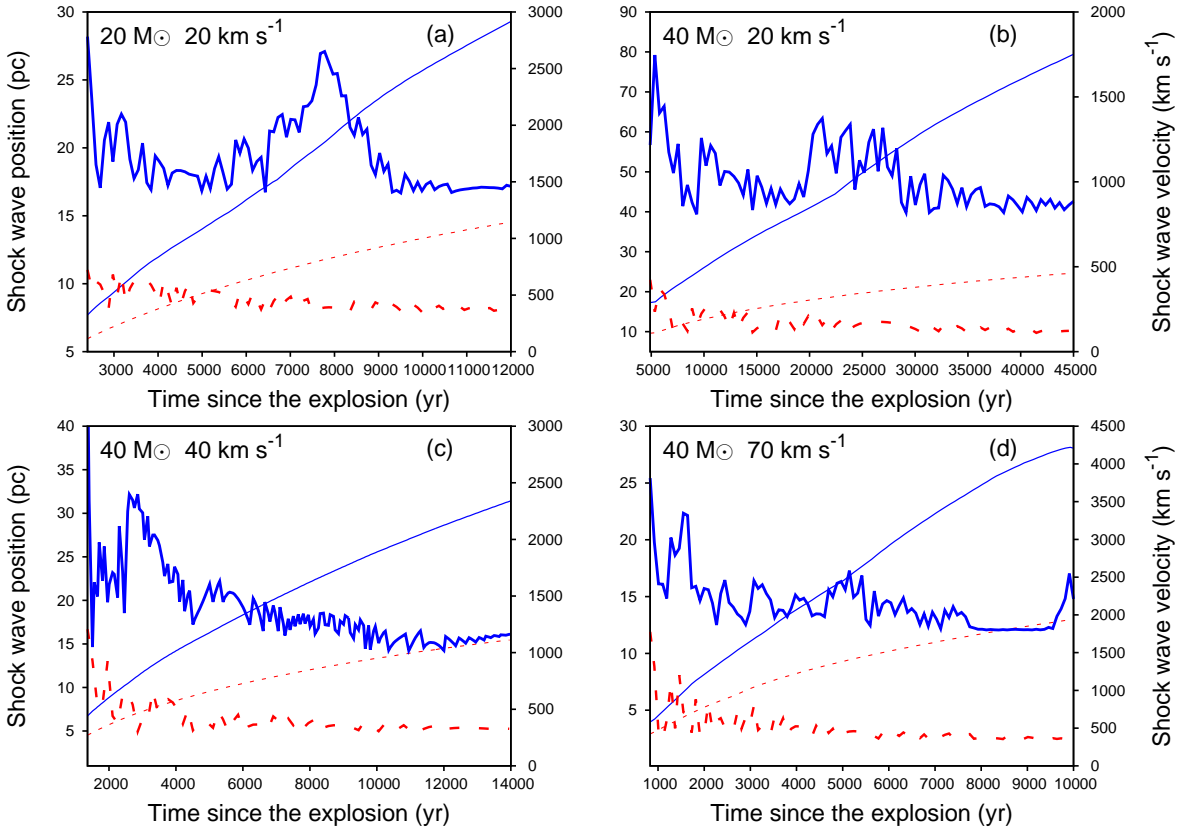
Figure 4.13: Time evolution of the shock waves of our aspherical supernova remnant models. The figure plots the shock wave position (thin lines, in pc) and velocity (thick lines, in km s^{-1}), upstream (solid blue lines, $+\hat{z}$ direction) and downstream (dashed red lines, $-\hat{z}$ direction) the center of the explosion, respectively. The figure represents the expansion from $t_{\rm ysnr}$ up to the end of the simulation at $t_{\rm osnr}$ (in yr) of the remnants generated by our initially $20\,{\rm M}_\odot$ progenitor moving with velocity $20\,{\rm km\,s^{-1}}$ (a), our initially $40\,{\rm M}_\odot$ progenitor moving with velocity 20 (b), 40 (c) and $70\,{\rm km\,s^{-1}}$ (d), respectively.
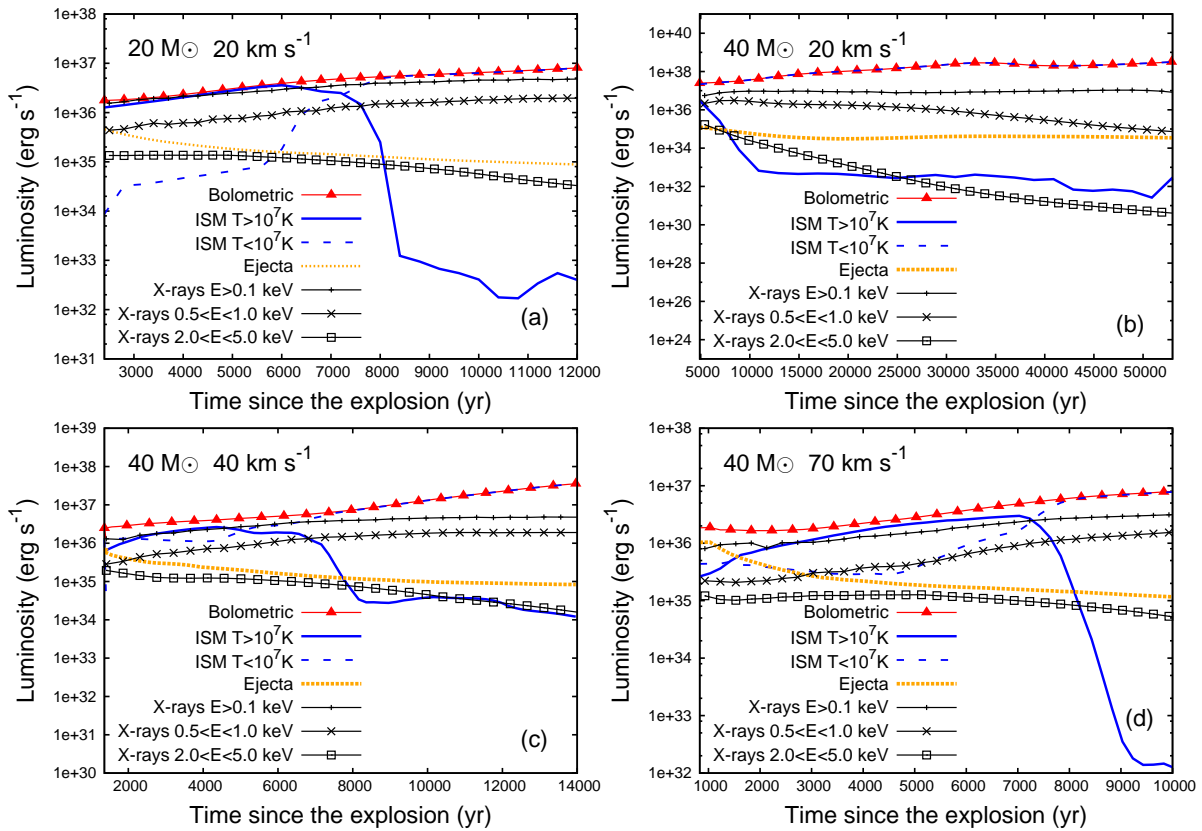
Figure 4.14: Lightcurves of our old apherical supernova remnants. We show the luminosities (in erg s^{-1}) during the time interval [t_{ysnr},t_{osnr}] (in Myr) of our aspherical supernova remnants generated by our initially 20 M$_\odot$ progenitor moving with velocity 20 km s^{-1} (a), our initially 40 M$_\odot$ progenitor moving with velocity 20 (b), 40 (c) and 70 km s^{-1} (d), respectively. The figures distinguish between the bolometric (total) luminosity from the gas (red thin line with triangles), the contribution from the hot ISM gas ($T > 10^7$ K, blue solid line), from the cold ISM gas ($T \leq 10^7$ K, blue thin dashed lines) and the contribution from the ejecta (orange dotted line). The black lines are the X-ray luminosity calculated at photons energies $E > 0.1$ keV (dashed line) and in the soft energy band 0.5-1.0 keV (crossed line) and and hard energy band 2.0-5.0 keV (squared line), respectively.

ray photons ceases as the remnant expands and cools. Consequently, our old remnants are more likely to be observed in the soft energy band of X-ray emission.

4.5.3 Emission maps

In Fig. 4.15 we show synthetic emission maps corresponding to the time t_{osnr} of the supernova remnants generated by our 20 $M_\odot$ progenitor moving with $v_\star = 20$ km s^{-1} (a,d) and by our 40 $M_\odot$ progenitor moving with $v_\star = 20$ (b,e) and 40 km s^{-1} (c,f), respectively. Fig. 4.16 is similar for our 40 $M_\odot$ progenitor moving with $v_\star = 70$ km s^{-1}. The left-hand side of each panel plots the Hα surface brightness (blue) whereas the right-hand side shows the [O III] λ 5007 surface brightness (green). The left-hand side of each bottom panel plots the hard X-ray surface brightness (red) and the right-hand side shows the soft X-ray surface brightness (grey). The spectral line emission coefficients are taken from the prescriptions by Osterbrock & Bochkarev (1989) and Dopita (1973) for Hα and [O III] λ 5007, respectively, with solar oxygen abundances (Lodders, 2003) and imposing a cut-off temperature at 10^6 K (cf. Cox, Gull & Green, 1991) when oxygen becomes further ionized (Sutherland & Dopita, 1993).

The region of maximum Hα surface brightness is located downstream from the center of the explosion. This happens because the Hα emissivity, $j_{\mathrm{H}\alpha} \propto T^{-0.9}$, is very faint in the region of hot shocked ejecta (Fig. 4.15a-c). The simulation with the slowly moving $40\,M_{\odot}$ progenitor has an emissivity peak along the walls of the wind cavity (Fig. 4.15b) because effective cooling of the gas makes the the post-shock region cool ($T \gtrsim 10^4$ K) and dense (up to $n \approx 50\,\mathrm{cm}^{-3}$). In the other simulations, the emission originates from the outer layers of the bow shocks because the walls of their less massive bow shocks allow a faster and deeper penetration of the shock wave into the shocked wind material (Fig. 4.16). Our predicted maximum Hα emission is above the diffuse emission sensitivity limit of the SuperCOS-MOS H-alpha Survey (SHS Parker et al., 2005) of 1.1–2.8×10^{-17} erg s^{-1} cm^{-2} arcsec^{-2}, e.g. our model OSNR4040 has a maximum emission larger than 9×10^{-16} erg s^{-1} cm^{-2} arcsec^{-2} (Fig. 4.15b), and could be compared with data from these surveys.

The [OIII] maximum surface brightness of our models originates from the dense ($n \approx 2$–$10\,\mathrm{cm}^{-3}$) and warm ($T \leq 10^6$ K) post-shock region behind the shock wave. It is located at the walls of the cavity and produces a ringed/tubular structure (Fig. 4.15a-c and 4.16a). It is generally not coincident with the projected Hα emission because the [OIII] emissivity has a different dependence on the temperature, i.e. $j_{[\mathrm{OIII}]} \propto e^{-1/T}/T^{1/2}$. However, the simulation OSNR4020 with a heavy bow shock have their [OIII] maximum surface brightness all along the walls of the wind tunnel and it is coincident with the region of maximum Hα emission, i.e. the behaviour of the emissivities with respect to the large compression of the gas in the walls ($\propto n^2$) overwhelms that of the gas temperature (Fig. 4.15b).

The X-ray emission originates from the hot gas with $10^5 \leq T \leq 10^8$ K, i.e. from near the shock wave expanding into the unperturbed ISM. The maximum surface brightness comes from the hot region of doubly shocked gas upstream from the center of the explosion, and from the post-shock region at the channelled shock wave (Figs 4.15d-f, 4.16b). The hard X-ray surface brightness is several orders of magnitude fainter than the projected soft X-ray emission, because the gas is not hot enough at t_{osnr} (Fig. 4.14). The emitting region in soft X-ray is peaked in the post-shock region at the shock wave whereas the hard X-ray come from a broader region of shocked gas which outer border is the shock wave (Fig. 4.15f). Note also the anti-correlation between the surface brightness in X-ray (hot region from near the forward shock) and in [OIII] (colder and denser walls) in our remnants generated by a fast-moving ($v_\star \geq 40\,\mathrm{km\,s}^{-1}$) progenitor (Fig. 4.15b,e;c,f).

4.6 Discussion

We here discuss our results in the light of precedent studies and pronounce on the best manner to observe aspherical supernova remnants generated by massive Galactic runaway stars. Finally, we examine our models in the context of recent observations.

4.6.1 Comparison with previous works

We tested that the code PLUTO (Mignone et al., 2007, 2012) reproduced the one-dimensional models of core-collapse supernovae interacting with their surroundings in Whalen et al. (2008) and van Veelen et al. (2009) using a uniform, spherically symmetric grid. Our numerical method (Paper I) is different from that in Whalen et al. (2008) because (i) they utilise a finite-difference scheme coupled to a network of chemical reactions following the non-equilibrium rates of the species composing the gas and (ii) their algorithm includes artificial viscosity (ZEUS code, see Stone & Norman, 1992).

We ran tests with their cooling curve (MacDonald & Bailey, 1981) and with a cooling curve for collisional ionization equilibrium medium (see details in section 2.4 of Paper I). We find no notable differences, mostly because they are similar in the high temperature regime ($T \geq 10^5$ K) that is relevant
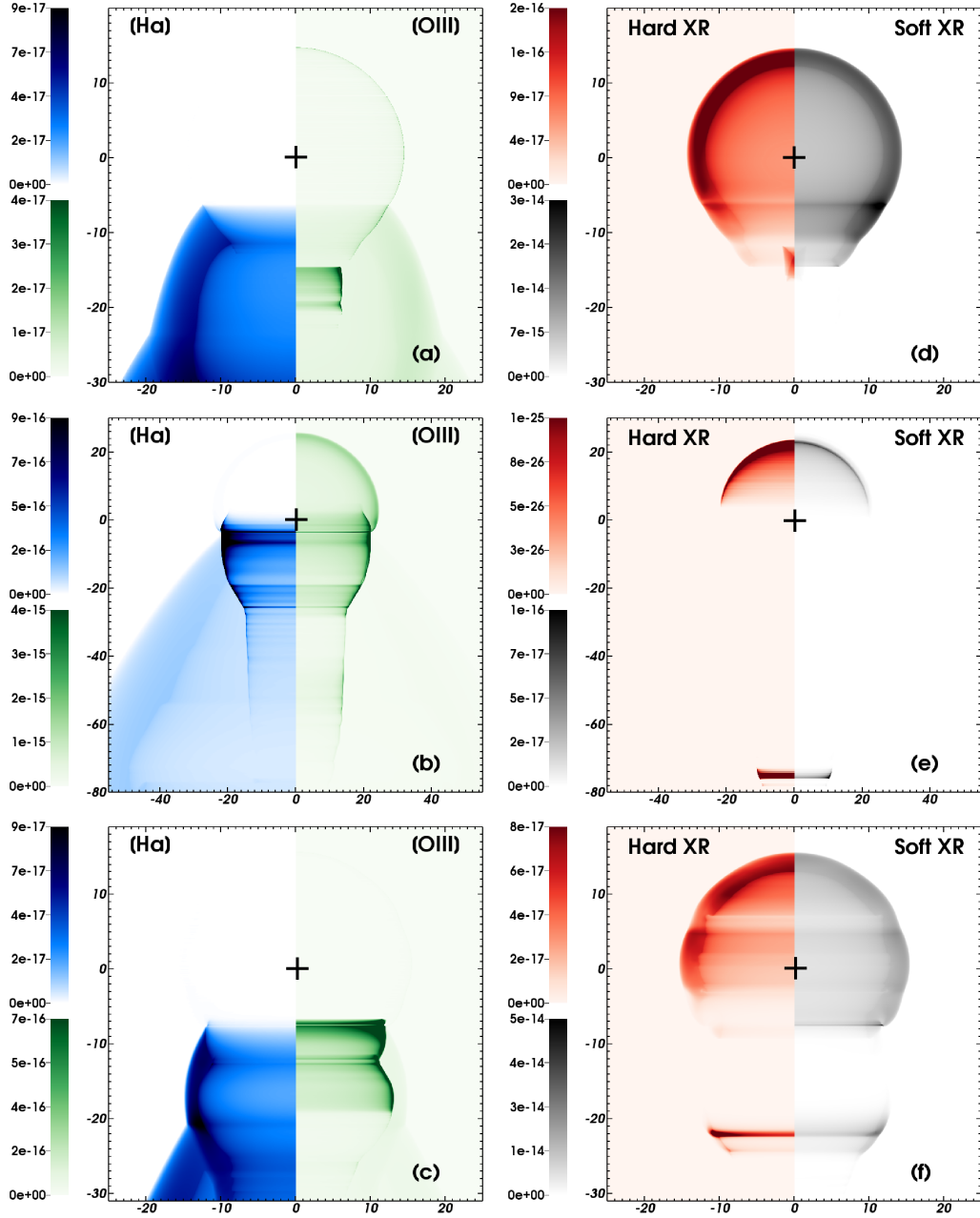
Figure 4.15: Synthetic emission maps of our models OSNR2020 at a time 12100 yr (a,d), OSNR4020 at time 49500 yr (b,e) and OSNR4040 at a time 14000 yr (c,f), plotted on the linear scale in units of erg s^{-1} cm^{-2} arcsec^{-2}. The left-hand part of the figures show the Hα surface brightness (blue) and the right-hand part the [O III] surface brightness (green), respectively. The black crosses mark the center of the explosion. The panels d-f show the projected X-ray emission maps in the hard (2.0-5.0 keV, left-hand part) and soft (0.5-1.0 keV, right-hand part) X-ray bands for the same models. The x-axis represents the radial direction and the y-axis the direction of stellar motion (in pc). Only part of the computational domain is shown in the figures.
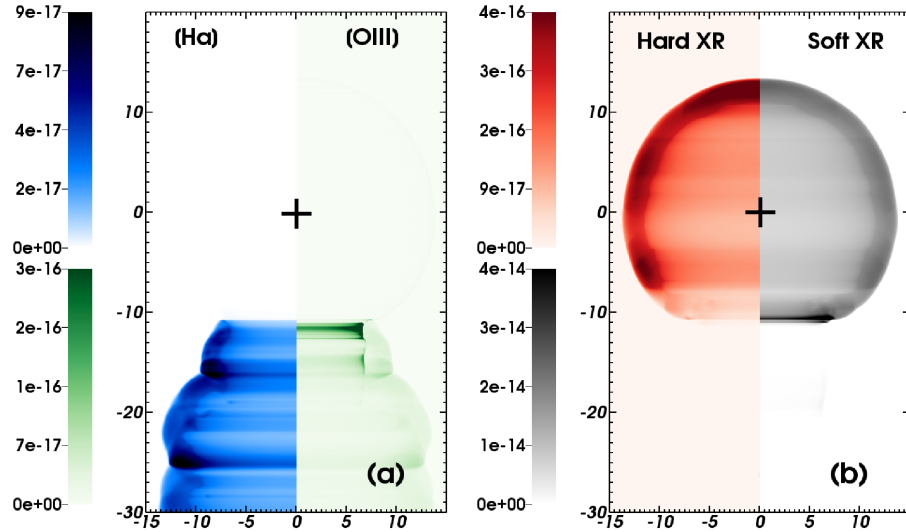
Figure 4.16: As Fig. 4.15, with an initially 40 M$_\odot$ progenitor moving with space velocity $v_\star = 70\,\mathrm{km\,s^{-1}}$. The H$\alpha$ and [O III] surface brightnesses are plotted in the left-hand panel, the projected hard and soft X-ray emissivity in the right-hand panel.

for the supernova-wind interaction (Fig. 4.5). We extend this method to two-dimensional, cylindrically symmetric tests of a supernova shock wave expanding into a homogeneous ISM to ensure that the sphericity of the shock wave is conserved throughout its expansion. We notice that the solution behaves well with respect to the symmetry axis Oz.

Models of an off-centered explosion in a wind-driven cavity are available in Rozyczka et al. (1993). Their model produces a parsec-scale jet-like feature as do our aspherical models (Figs 4.9c to 4.12c) but they neglect the progenitor's stellar evolution, assume a different microphysics, and correspond to a totally different point of the parameter space ($n = 10^6\,\mathrm{cm^{-3}}$). Our description of the supernova shock wave interacting with its pre-shaped bow shock is consistent with the works tailored to the Kepler's supernova remnant; see section 5.2 of Borkowski, Blondin & Sarazin (1992) but also Velázquez et al. (2006); Toledo-Roy et al. (2014).

The tunnel of unshocked wind that channels the shock wave, e.g. in our model OSNR4020 (Fig. 4.9a), is morphologically and structurally consistent with the model of the red supergiant progenitor of the Crab nebula in Cox, Gull & Green (1991), assuming a diluted ambient medium and a larger space velocity ($n = 0.25\,\mathrm{cm^{-3}}$, $v_\star = 69.5\,\mathrm{km\,s^{-1}}$). Notice that the simulations with fast-moving stars or post-main-sequence high-mass-loss events have a tunnel with clumpy walls (Fig. 4.9a and 4.12a) which do not prevent the tunneling of the shock, in contrast to the suggestion by Cox, Gull & Green (1991).

The growth and overall shape of our aspherical remnants are in accordance with Brighenti & D'Ercole (1994). Our model OSNR2020 is morphologically consistent with their model 1 ($v_\star = 17\,\mathrm{km\,s^{-1}}$, $n = 1\,\mathrm{cm^{-3}}$). They assumed a comparable mass loss ($\dot{M} = 10^{-5}\,\mathrm{M_\odot\,yr^{-1}}$) but a twice larger wind velocity ($v_\mathrm{w} = 20\,\mathrm{km\,s^{-1}}$) during the red supergiant phase which last about 7×10^5 yr. Identical remarks arise comparing their model 3 and our simulation OSNR4070 (Fig. 4.12a-c). Because our models include thermal conduction, the region of shocked wind in the bow shock from the main-sequence phase is larger and the tunnel in our simulation OSNR4020 narrower that in their model 4 and allows a more efficient channeling of the shock wave (Fig. 4.10a-c).

As a conclusion, for overlapping parameters our results agree well with previous models of supernova remnants produced by runaway progenitors. We extend the parameter space with a representative

sample of models tailored to the Galactic plane, whose progenitor's wind properties are taken from self-consistently pre-calculated stellar evolution models (Brott et al., 2011).

4.6.2 Comparison with observations

Comparing our simulations with observations is not a straightforward task. In spite of the fact that this paper explores a representative sample of Galactic, massive, runaway stars, our remnants can only develop asymmetries when the isotropic shock wave interacts with a dense bow shock, whereas also other mechanisms can induce asymmetries. They can originate from an intrinsically anisotropic explosion (Blondin, Lundqvist & Chevalier, 1996), the rotation of the progenitor, the magnetization of the ISM (Rozyczka & Tenorio-Tagle, 1995) or the presence of a neighbouring circumstellar structure (Ferreira & de Jager, 2008). Consequently, we hereby simply attempt to establish a qualitative discussion between our models and observations available in the literature.

Brighenti & D'Ercole (1994) and Eldridge, Langer & Tout (2011) already justified the relevance of studying runaway O stars in the understanding of supernova remnants and gamma-rays bursts. Particularly, they underline the difficulty of interpreting the shape of incomplete and/or inhomogeneous arc-like supernova remnants because the overdensities upstream from the center of the explosion can also be provoked by the interaction with a dense region (see, e.g. Orlando et al., 2008). The presence of OH maser emission originating from the shock front can discriminate between this scenario (Frail et al., 1996; Yusef-Zadeh et al., 2003), and led to the classification of about 20 Galactic arced remnants such as G31.9+0.0 or G189.1+3.0 as running into a dense cloud. Particularly, 3C391 which was believed to be the archetypal remnant from a moving progenitor (Brighenti & D'Ercole, 1994) is now associated with molecular line emission revealing an interaction with a dense medium (Gusdorf et al., 2014).

Exceptionally, the runaway nature of the progenitor of a supernova remnant moving to a dense region can be identified because of the imprint of its stellar winds. As the star goes through the cloud, its border is shaped as a function of its last mass-loss events. It creates a multiple-arced structure called Napoleon's hat which overhangs the remnant. Our model OSNR2020, which presents the remains of its main-sequence, red-supergiant phases and final increase of its mass loss (Fig. 4.9a), would produce a Napoleon's hat if it were be moving through the edge of a dense region. A famous example of this phenomenon is the remnant of SN1987a in the Large Magellanic Cloud (Wang, Dyson & Kahn, 1993).

The early development of our supernova remnants, i.e. when the shock wave interacts with the bow shock upstream from the center of the explosion (Fig. 4.10a) is consistent with the observation of one-sided supernova remnants such as G338.1+00.4. Its projected radio emission is noticeably brighter roundabout half of the structure (Whiteoak & Green, 1996). Nevertheless, this could be due to a density gradient of the ISM in which the star moves, as proposed in Aschenbach & Leahy (1999). One can also remark that the differential expansion of our models' shock waves (Fig. 4.13) is in accordance with the observations of RCW86: it has a shock wave asymmetrically interacting with a wind bubble (Broersen et al., 2014).

Previous studies identified the material composing the bilateral structures such as G296.5+10.0 as shocked pre-supernova wind (Manchester, 1987) and the presence of a neutron star in between the opposed arcs is reported in Zavlin, Pavlov & Trumper (1998). It is similar to our slowly moving model of an initially $40\,M_\odot$ at time 11400 yr after the explosion, when the shock wave hits the very dense walls of the wind tunnel (Fig. 4.10b). However, alternative explanations have been proposed for the fomation of bilateral remnants like G327.6+14.6 or G3.8-0.3. A strong axisymmetric background ISM magnetic field has also been suggested to be responsible for the bilateral character of some Galactic supernova remnants (Gaensler, 1998). It would indeed make their shape more elongated (Rozyczka & Tenorio-Tagle, 1995) and produce X-ray and/or radio synchrotron emission from the arcs (Velázquez et al., 2004;

Petruk et al., 2009; Schneiter et al., 2010).

Our Galactic, slowly moving, initially $20\,M_\odot$ progenitor produces supernova remnants whose outer region strongly emits in [O III]. The remnant generated by our slowly moving, initially $40\,M_\odot$ progenitor has an [O III] jet-like feature that has a Hα counterpart (Fig. 4.15) generated by ejecta channelled with velocity about $1000\,\mathrm{km\,s^{-1}}$ into the wind tunnel of the bow shock (Fig. 4.13b). Those tubular/jet-like features (Figs 4.15-4.16) evidently recall the chimney discovered in [OIII] in the Crab nebula (Blandford et al., 1983) and modeled in Cox, Gull & Green (1991). At higher $v_\star$, they become an [O III] tubular structure that is thinner and closer to the throttling separating the surroundings of the center of the explosion from the trail of the bow shock. Supernova happening in a wind cavity could form tunnels or barrel-like shapes, however, quite convincing demonstration, e.g. based on asymmetric explosions have been proposed (WB49, González-Casanova et al., 2014).

4.7 Conclusion

In this paper, we present a grid of hydrodynamical models of asymmetric supernova remnants generated by a representative sample of Galactic runaway massive stars whose circumstellar medium from the main-sequence and red supergiant phases is studied in Meyer et al. (2014b). We compute the bow shocks generated by our progenitors from near the pre-supernova phase and model the collision between the shock waves and the circumstellar medium which result in the generation of Galactic supernova remnants. The progenitors' initial masses range from 10 to $40\,M_\odot$ and they move with space velocities ranging from 20 to $70\,\mathrm{km\,s^{-1}}$. Our models include both optically-thin cooling and photoheating of the gas. Electronic thermal conduction is included in the calculations of the circumstellar medium and in the simulations of the supernova remnants.

We show that the bow shocks trapping at least $1.5\,M_\odot$ of ISM gas are likely to generate aspherical supernova remnants. They correspond to high mass and/or slowly moving stars (Brighenti & D'Ercole, 1994). At the ISM number density that we consider, they are produced either by our initially $20\,M_\odot$ star moving with space velocity of about $20\,\mathrm{km\,s^{-1}}$ or by our initially $40\,M_\odot$ runaway star. These mass-accumulating bow shocks generate a dense bulge of shocked ISM gas upstream from the direction of motion of the star whereas a cavity of low-density wind material forms in the opposite direction and extends as a tunnel of unshocked wind material into the trail of the bow shock.

After the supernova explosion, the shock wave expansion is strongly influenced by the anisotropy of its circumstellar medium. It collides with the overdense part of the bow shock whereas it expands at velocities of the order of $1000\,\mathrm{km\,s^{-1}}$ in the opposite direction, channelled by the pre-shaped tunnel of unshocked wind material (cf. observations of RCW86 in Vink, Kaastra & Bleeker, 1997). The mass of shocked ISM trapped in the bow shock decelerates the shock wave, which continues to penetrate the unperturbed ISM after the collision with velocity of the order of $100\,\mathrm{km\,s^{-1}}$.

As the shock wave evolves in a non-uniform media, it is partly reflected towards the center of the explosion (Ferreira & de Jager, 2008) after the collision with a dense bow shock. It induces mixing of supernova ejecta, stellar wind and ISM gas that is particularly important for fast-moving progenitors. This wave shocks the zone where is the center of the explosion, generating a growing region of hot gas that cools below $10^7\,\mathrm{K}$ because of the adiabatic expansion of the blastwave. Its luminosity increases, dominated by thermal Bremsstrahlung and soft X-ray emission originating from the shocked ISM that is upstream from the center of the explosion. The emission from the ejecta or from the progenitor's wind material does not contribute significantly to the remnants' total luminosity once the bow shock is overtaken by the shock wave.

Our Galactic aspherical supernova remnants have a [OIII] $\lambda\,5007$ surface brightness larger than their

projected Hα emission, i.e. the [OIII] is the most appropriate line to search for Galactic supernova remnants. Their [OIII] surface brightness is maximum in the post-shock region at the shock wave. It is concentrated along the walls of the tunnel of wind material. The region of maximum Hα emission is downstream from the direction of motion of the progenitor. It originates from the outer part of shocked ISM material in the trail of the progenitor's bow shock. In the case of our slowly moving initially $40\,M_\odot$ progenitor, it mainly comes from the region where the shock wave interacts with the walls of the tunnel, i.e. the ejecta forms an [O III] jet-like feature that has an Hα counterpart. Moreover, we find that our remnants are more likely to be observed in soft X-ray emission originating from near the shock wave than in hard X-ray emission coming from the post-shock region at the shock wave.

Supernova remnants generated by runaway progenitors provide a natural manner to generate structures highly deviating from sphericity. Particularly, our models of remnants generated by high-mass, slowly moving progenitors have morphologies consistent, e.g. with the bilateral character of observed barrel-like Galactic supernova remnants such as G296.5+10.0 or with the differential expansion of the ejecta such as in RCW86. However, other mechanisms are at work in the shaping of supernova remnants. Forthcoming work will investigate the effects of an ISM magnetic field on the evolution of our remnants, in order to quantitatively appreciate its consequences on the remnants dynamics and emission signatures.

Conclusion

In this thesis, we present the first grid of hydrodynamical simulations which aims at describing the circumstellar medium of a representative sample of massive runaway stars moving through the Galactic plane, and evolving from their main sequence phase to their final explosion as a core-collapse supernova. After the death of these stars, we model the expansion of the supernova blastwave in the pre-shaped circumstellar medium and focus on the description of their highly aspherical supernova remnants. We also explore how the external photoionization of bow shocks driven by cool stars can modify their appearance. Finally, by modelling the first optically-detected bow shock of a red supergiant star, we constrain the properties of IRC−10414.

Accomplished work

We first look at the formation and evolution of stellar wind bow shocks generated by evolving massive Galactic runaway stars exiled from their parent cluster (Meyer et al., 2014b). They form around the 10 to 25 per cent of the O stars that have a supersonic motion with respect to the ISM (Gies, 1987; Blaauw, 1993). They provide insight into the physics of the stellar winds and their interaction with their local ISM. These parsec-scale arcs of shocked stellar wind and swept-up ISM gas can be observed, e.g. around about 40 per cent of the runaway O stars (Huthoff & Kaper, 2002) and their morphology and brightness can constrain the stellar wind and local ISM properties. When these stars die, a supernova remnant develops inside the pre-shaped circumstellar medium and interacts with the bow shock before expanding into the unperturbed ISM, giving birth to nebulae called supernova remnants.

We run a grid of two-dimensional, cylindrically symmetric, hydrodynamical simulations of bow shocks around the most common massive runaway stars, i.e. stars of initial masses ranging from 10 to $40\,M_\odot$ moving with space velocities ranging from 20 to $70\,\mathrm{km\,s^{-1}}$. We explore the effects of their mass loss and space velocities on the bow shock size, stability and luminosity. The stellar wind properties are taken from stellar evolution models (Brott et al., 2011) and we follow their interaction with the ISM from the main sequence to the supernova phase. We continue by modelling the collision between the supernova shock waves and their surrounding bow shocks, because the shape of the arising remnants depends on the evolution history of the defunct star.

Our approach is different compared to previous examinations of the stellar wind bow shock problem. Particularly, all the models include cooling and heating by optically-thin gas radiation together with electronic thermal conduction (Cowie & McKee, 1977). The microphysics included in the models depends on the effective temperature of the runaway star. The cooling curve used during the

main sequence phase of our stars includes photoheating and [O II] and [O III] forbidden lines emission (Raga, Mellema & Lundqvist, 1997). The cooling curve utilised for their phase transition and the red supergiant phase takes into account the far UV background of the ISM. The equilibrium temperature of the medium is therefore dictated by the balance between heating and cooling instead of an arbitrary cut-off of the curve. The wind properties are taken from stellar evolution models which are state-of-the-art with respect to the main sequence of non-rotating massive star (Brott et al., 2011). The ISM properties are tailored to the Galactic plane, where are most of the observed runaway stars once they are exiled from their parent cluster (Huthoff & Kaper, 2002; Gvaramadze & Bomans, 2008). We explore the most probable range of initial masses and space velocities of the runaway stars (Eldridge, Langer & Tout, 2011). We use passive scalar tracers to follow the distribution of the wind and ISM into the bow shocks. Our investigation of the supernova remnant phase includes the same physics, except that we neglect thermal conduction during the early interaction between the blastwave and the stellar wind. This allows to avoid too severe restrictions on the timestep. Additionally, a third passive scalar is utilised to follow the advection of the ejecta. Our systematic exploration of the shape of supernova remnants generated by the most common massive Galactic runaway stars is original.

Our results are in accordance with previous works such as the ones presented in Brighenti & D'Ercole (1994) and in Comerón & Kaper (1998). We underline the importance of heat conduction to model the bow shocks around hot stars. We stress its effects on their morphology and structure, especially concerning the transport of ISM material from the outer part to the inner layer of these bow shocks. The heat transfer enlarges the bow shocks and considerably reduces the volume of shocked wind that shrinks. Their optical emission mainly originates from the shocked ISM material that gains the internal energy transfered from the reverse shock. We detail how their luminosities depend on the mass loss and space velocity of the star for both the main sequence and the red supergiant phases. We identify the initial masses and bulk velocity of the runaway progenitors producing the most aspherical Galactic supernova remnant and described their surface brightness and emission properties.

We finally focus on bow shocks generated by red supergiants, considering that both the stellar wind and the ISM are either fully ionized by an external field of photons or neutral (Meyer et al., 2014a). We investigate whether the smooth appearance of the bow shock nebula around the red supergiant IRC-10414 could be caused by the ionization of its stellar wind by an external source of radiation, e.g. the nearby Wolf-Rayet star WR114 or the star cluster NGC6611. We find that only some ionized models assuming a particular range of space velocities can simultaneously reproduces the overall shape and the brightness of this bow shock. Our study demonstrates that the ionization of its stellar wind results in its acceleration by about a factor of two, which reduces the shear at the contact discontinuity and makes the bow shock stable for a range of stellar space velocities and mass-loss rates.

Model limitations

First, our models evidently suffer from their two-dimensional nature. The development of instabilities in the wake of the bow shock models should be confronted and discussed in the light of three-dimensional models in order to figure out whether they are physical or artificially triggered, e.g. close to the symmetry axis in two-dimensional cylindrical coordinates. Secondly, our rather coarse resolution prevents us from carefully modelling the mixing of material inside the shocked layers, because the development of Rayleigh-Taylor instabilities partly depends on the adopted spatial resolution. Very high resolution simulations, e.g. using adaptive mesh refinement methods, could further study the flow inside stellar wind bow shocks.

Throughout this study, we have neglected the magnetization of the ISM. This is a crude assumption which reduces our work to a particular situation. However, the magnetohydrodynamical modelling of

bow shocks generated by hot stars, e.g. OB stars or blue supergiant, naturally brings the questions of (i) the anisotropy of thermal conduction and (ii) the electrical resistivity of the medium. Included in the Euler equations, these processes are parabolic terms whose numerical treatment is particularly fragile and which make the computations costly. Such models are far beyond the scope of these thesis, and would require considerable work on the numerical methods.

Finally, our models of photoionized structures around cool stars such as the red supergiant IRC−10414 have the weakness that consist in assuming that all the stellar wind is either neutral or totally photoionized. A careful modelling of the interface between neutral and ionized wind would request full radiation-hydrodynamical simulations such as in Mackey et al. (2014b).

Implication of the results: bow shocks

Our models of bow shocks generated by runaway main sequence and red supergiant stars moving through the Galactic plane show that (i) their luminosities are governed by their wind momentum, (ii) their luminosities monotonically scale with the volume of the bow shocks and (iii) they should be easiest to detect in the infrared. This is surprising because if slowly moving stars produce large bow shock as their stand-off distance $R(0) \propto v_\star^{-1}$ (Baranov, Krasnobaev & Kulikovskii, 1971; Wilkin, 1996), the weak compression of the gas does not induce extreme temperatures in the post-shock region at the forward shock that could cool and emit efficiently. As a consequence, barely supersonic massive Galactic runaway stars produce the brightest bow shocks. According to our grid of models and at the ISM density that we consider, the most easily detectable bow shocks from main sequence stars are those of high-mass stars of initially $40\,M_\odot$ moving with small space velocites, whereas those from red supergiant stars are produced by those of initially $20\,M_\odot$ moving with small space velocities.

We find that the principal coolants governing their total luminosities by optically-thin gas radiation are the optical forbidden lines [O II] and [O III]. This is consistent with previous observations of ζ Ophiuchi (see Gull & Sofia, 1979). This emission originates from the shocked ISM material. According to our study, forbidden emission lines are nevertheless fainter than the infrared emission. This is possible because the infrared luminosity is a fraction of the starlight absorbed by the dust grains in the bow shock and reemitted at longer wavelengths. However, our bow shock models can have Hα surface brightnesses above the detection threshold of the SuperCOSMOS H-alpha Survey (Parker et al., 2005), and should consequently be identifiable in the archives.

Our estimate of projected Hα emission and projected dust surface mass density allows us to discuss the respective origin of the Hα and infrared emission from Galactic bow shocks. The models with hot stars are brighter in Hα in the cold shocked ISM material near the contact discontinuity, where also their dust surface mass density, i.e. their infrared emission peaks. Our numerical simulations of circumstellar structures produced by red supergiants indicate that their large infrared emission peaks in the post-shock region at the reverse shock whereas very weak Hα emission originates from the post-shock region at the forward shock of the bow shock. This is an important point because its allows to link observables to a given layer of these generally parsec-sized structures. Because the gas is weakly ionized, their Hα emission is negligible compared to their luminosity by optically-thin radiation. As a consequence, this waveband is not the appropriate one to search for them. For all our models, the Hα surface brightness is maximum upstream from the star for small bulk velocities and is extended downstream from the star for larger space velocities.

Our best fit model of the bow shock of IRC−10414 shows that its space velocity and mass-loss rate can be constrain to about $50\,\mathrm{km\,s^{-1}}$ and about $10^{-6}\,\mathrm{M_\odot\,yr^{-1}}$, respectively. Under our assumptions, its local ISM number density is about $3.3\,\mathrm{cm^{-3}}$. This is an important result because the typical value of the mass-loss of a red supergiant star is still under debate, on both the theoretical and observational points

of view (Gvaramadze et al., 2014). We also point out that ionized models tailored to the bow shock of IRC −10414 have collisionally excited Hα+[N II] emission mostly originating from the shocked red supergiant wind, which explains the strong line emission from the wind material, enriched in nitrogen. This is consistent with the fact that we do not see many bow shocks around runaway red supergiant stars, and explains why this structure was optically discovered. Our work shows that the ionization of the stellar wind might be responsible for the smooth appearance of bow shocks generated by other red supergiants, or cool, e.g. asymptotic giant branch stars.

Implication of the results: supernova remnants

Our study shows that after the supernova explosion, only some of our bow shock models are able to prevent the shock wave from expanding spherically through the unperturbed ISM, producing asymmetric supernova remnants such as in Whiteoak & Green (1996); Reach et al. (2006); Pannuti et al. (2014). The bow shocks that accumulate more than about $1.5 \, M_\odot$ throughout their evolution are likely to generate strongly aspherical remnants. This applies to the bow shocks produced by our slowly moving, initially $20 \, M_\odot$ star and to our $40 \, M_\odot$ progenitors.

These dense bow shocks induce a differential expansion of the shock wave through the circumstellar medium. It is decelerated during the collision with the bow shock upstream from the center of the explosion and then continues expanding into the ISM with velocitiy of the order of $100 \, \mathrm{km \, s^{-1}}$. In the opposite direction, it is channeled at velocities of the order of $1000 \, \mathrm{km \, s^{-1}}$ into the pre-shaped cavity of unshocked wind material (see observations of RCW86 in Vink, Kaastra & Bleeker, 1997). This mechanisms produces jet-like structures similar to the one observed in the Crab nebula (Blandford et al., 1983) and investigated in Cox, Gull & Green (1991). The [O III] surface brightness of our asymmetric remnants is maximum in the post-shock region at the expanding shock wave upstream from the center of the explosion. In the opposite direction, it peaks at the walls of the pre-shaped wind tunnel into which the shock wave is channeled.

The asymmetric supernova remnant produced by our slowly moving, initially $20 \, M_\odot$ progenitor has a drop-like shape whose outer layer emits in [O III]. When the shock wave interacts with the bow shock of our slowly moving, initially $40 \, M_\odot$ progenitor, the remnant has a morphology consistent with the bilateral character of barrel-like supernova remnants such as G296.5+10.0 (Manchester, 1987) and shows an [O III] tubular/jet-like feature that has a Hα counterpart generated by ejecta channeled into the bow shock with velocity about $1000 \, \mathrm{km \, s^{-1}}$. The region of maximum Hα and [O III] is not coincident in remnants induced by faster progenitors. Moreover, the region of the shock wave interacting with the walls of the cavity becomes an [O III] ring-like structure that is thinner and closer to the throttling separating the region of freely-expanding shock wave from the pre-shaped bow shock. For these fast progenitors, the shock wave is channeled at velocities up to about $5000 \, \mathrm{km \, s^{-1}}$ thought the bow shock. This is an important information because the distance to Galactic remnants is more difficult to estimate than the motion of a portion of their structure.

Additionally, we describe how the collision between the blastwave and the dense circumstellar medium produces a reverberation of the supernova shock wave towards the center of the explosion. This creates a hot-phased region upstream from the center of the explosion, which produces x-rays emission by thermal Bremsstrahlung dominating the remnant lightcurve up to about several millenniums after the supernova. It induces mixing of supernova ejecta, stellar wind and ISM gas that is important upstream from the center of the explosion. Our larger asymmetric remnants have an important [O III] surface brightness because the shock wave produces an efficient cooling when it interact with the dense walls. Consequently, the remnants induced by slowly moving, high-mass progenitors are the easiest to observed. Our remnants are likely to be observed in soft X-ray emission originating from near the shock

wave than in hard X-ray emission coming from the post-shock region at the shock wave. Finally, we find that these remnants are easier to observe in [O III] emission lines than in Hα or in [N II].

Relevance of this study and future works

This work is important for the fields of astronomy which deal with the cycle of matter in galaxies. Knowing the properties of massive stars such as their mass loss allows to constrain stellar evolution, which in its turn depends on the physics of stellar interiors. Being able to recognize stellar wind bow shocks, e.g. in the neighbourhood of stellar cluster, and identifying the properties of their driving star is of prime interest, e.g. in the study of the cluster's history. Moreover, a connection with star formation studies could be envisaged. Indeed, large stellar wind bow shocks produced by high-mass, slowly moving massive runaways stars create dense, low temperature and metal-rich regions in their wake that could trigger the formation of stars. Next works on the circumstellar medium of runaway massive stars could investigate the effects of a non-axisymmetric ISM magnetic field on the structure of their stellar wind bow shocks. It will update our estimates of the bow shocks surface brightnesses and provide finer predictions regarding their detectability, e.g. at Hα. This would require sophisticated three-dimensional, non-ideal, magnetohydrodynamical simulations such as the ones carried out by the community modelling the heliosphere.

Appendix

6.1 Tests of stellar wind-ISM interactions with the code PLUTO

6.1.1 Modelling the circumstellar medium of an OB star at rest

Figure 6.1 reports a series of hydrodynamic models of the circumstellar medium around an OB star at rest. The initial ISM parameters are its number density $n = 1.0\,\mathrm{cm}^{-3}$ and its temperature $T = 10^4$ K. The main stellar wind parameter is its mechanical luminosity,

$$L_{\mathrm{w}} = \frac{1}{2}\frac{dM_{\star}}{dt}v_{\mathrm{w}}^2 = 1.27 \times 10^{36}\ \mathrm{erg\ s}^{-1}, \qquad (6.1)$$

where $dM_{\star}/dt = 10^{-6}\,\mathrm{M}_{\odot}\,\mathrm{yr}^{-1}$ is the star mass loss, $v_{\mathrm{w}} = 2000\,\mathrm{km\,s}^{-1}$ is the radial wind velocity and $T_{\star} = 3.5 \times 10^4$ K is the effective temperature. Panel (a) of Fig. 6.1 is an adiabatic simulation. It describes the four characteristic regions forming when a stellar wind-ISM interaction occurs, which are, from the star to the unperturbed medium: the free-expanding wind, the shocked wind region called the hot bubble, the dense region of shocked ISM usually called the shell and finally the unperturbed ISM. The contact discontinuity located at about 30 pc from the star separates wind and ISM materials. It is located between the reverse shock at about 5 pc and the forward shock at about 40 pc from the star. Panel (b) of Fig. 6.1 shows a model with similar initial conditions, but including optically-thin radiative cooling for fully ionized gas (see description of our cooling module in Chapter 2). This model illustrates the narrow, thin, and cold shell of shocked ISM gas which develops at the edge of the bubble and shrinks to about 27 pc along the radial direction. Panel (c) of Fig. 6.1 plots a simulation taking into account heat conduction (Cowie & McKee, 1977). It highlights the heat transfers happening at the reverse shock and at the contact discontinuity (Weaver et al., 1977). This is generated by the temperature differences (i) inside the bubble itself and (ii) between the hot bubble and the shell through the contact discontinuity. Panel (d) of Fig. 6.1 represents a model including both cooling and heat conduction. This realistic bubble contains both the effects of the cooling, i.e. a dense shell, but also smoothed density and temperature profiles in the post-shock regions at both the reverse and at the forward shocks.
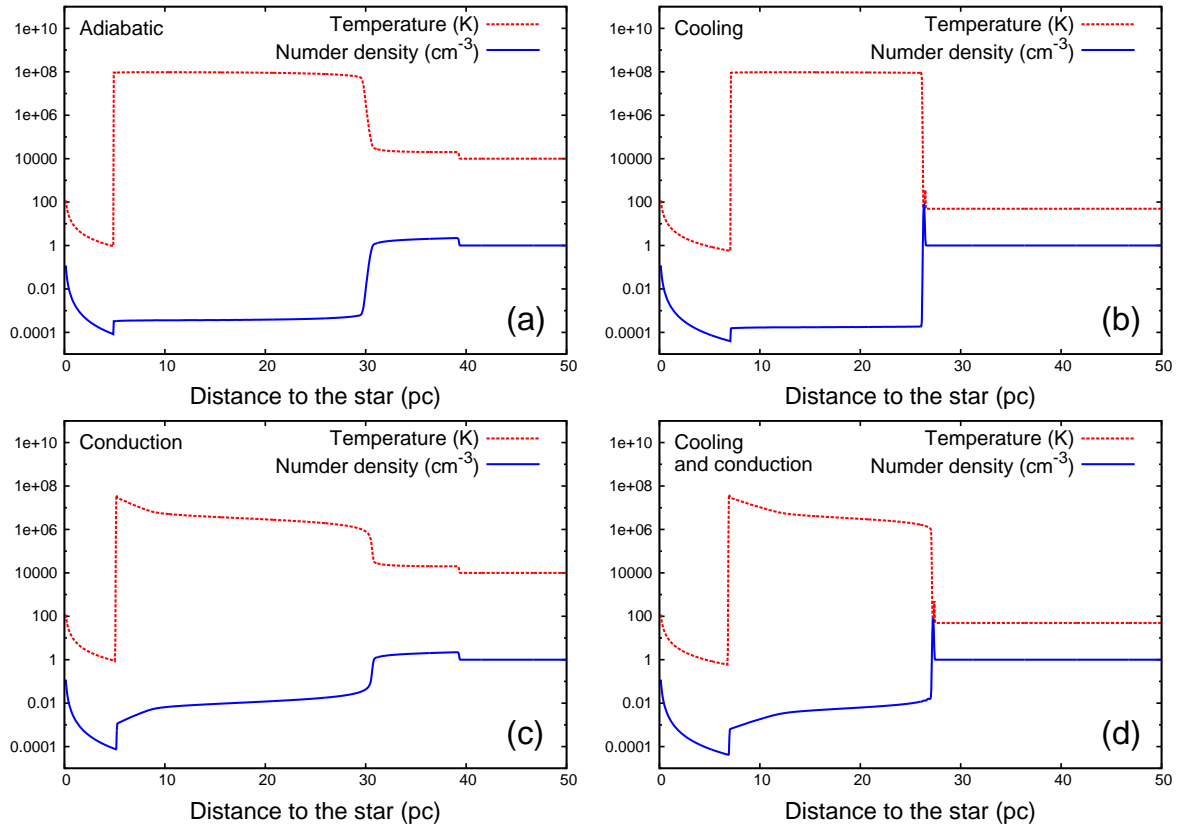
Figure 6.1: Effects of the included physics on the structure of a wind bubble produced by an OB star in an ISM of number density $n = 1\,\mathrm{cm}^{-3}$. Panel (a) shows an adiabatic model, panel (b) is a model including optically-thin radiative cooling and heating, panel (c) shows a model with heat conduction and panel (d) plots a model with both gas cooling and heating by optically-thin radiation plus heat conduction. All models have the same initial conditions, i.e. only the included physics is different. The x-axis represents the distance to the star (in pc) and the y-axis the gas nucleon number density (blue solid line, in cm^{-3}) and temperature (red dashed line, in K). Only part of the computational domain is shown in the figure.

6.1.2 Effects of the included physics on a bow shock model around a moving OB star

The translational motion of a massive star changes the spherically symmetric shape of its circumstellar medium into a bow shock. The four different regions of a typical wind bubble (see previous paragraph) adopt an egg-shaped structure (van Buren, 1993) whose characteristic quantity is the so-called stand-off distance $R(0)$, see in Baranov, Krasnobaev & Kulikovskii (1971). It represents the distance between the star and the layer of the bow shock where the wind and ISM momenta balance each other. Figure 6.2 shows the gas number density fields of a series of (non-ideal) hydrodynamical models of the main-sequence of our initially $10\,M_\odot$ star which wind properties were modelled without rotation and assuming Galactic metalicity (Brott et al., 2011). The star is moving with velocity $v_\star = 40\,\mathrm{km\,s^{-1}}$ through the Galactic plane, i.e. the ambient hydrogen number density is about $0.57\,\mathrm{cm^{-3}}$ (Wolfire et al., 2003). Figures are displayed as a function of the included physics, i.e. photoheating plus losses by optically-thin radiative cooling (our Chap. 2) and/or heat transfers by electronic conduction (Spitzer, 1962; Cowie & McKee, 1977). The dashed line traces the material discontinuity and the right part of the figures shows the ISM streamlines.

Panel (a) of Fig. 6.2 plots an adiabatic model which has a material discontinuity coinciding with the contact discontinuity. This discontinuity separates the dense and cold ($T \leq 10^5\,\mathrm{K}$) shocked ISM from the diluted and hot ($T \geq 10^5 - 10^6\,\mathrm{K}$) shocked wind material. This model has been successfully scaled with the code PLUTO on the Supercomputer JUROPA at Forschungzentrum Jülich (see Fig. 6.3). Panel (b) of Fig. 6.2 shows a model including losses by optically-thin radiative cooling. The properties of the shocked wind and the position of the material discontinuity are unchanged with respect to the model shown in panel (a). However, the hot layer of shocked ISM gas is cold and becomes denser. As a consequence, the volume of the shocked ISM material decreases together with the volume of the bow shock. Panel (c) of Fig. 6.2 plots the density field of a model taking into account electronic heat conduction. It illustrates (i) the transfer of internal energy from the hot to the cold shocked ISM gas and (ii) the effects of thermal conduction on the bow shock volume. Finally, panel (d) of Fig. 6.2 shows a model including both radiative cooling and thermal conduction. It has both an enlarged bow shock volume and the flow of ISM material almost reaching the reverse shock because of thermal transfers on the one hand; a denser and reduced volume of shocked ISM gas compared to the model without cooling (c) on the other hand. This demonstrates the importance of both cooling and conduction to properly simulate circumstellar structures around moving hot stars. Further investigations concerning the volume-dependence of the bow shock luminosities are detailed in Chapter 2.

6.2 Producing emission maps and dust column density

The simulations are post-processed in order to obtain projected Hα emission maps and ISM dust projected mass. The gas T is calculated according to Eq. (2.5). For every cell of the computational domain and for a given quantity $\xi(T)$ of units $[\xi]$ representing either rate of emission (in $\mathrm{erg\,s^{-1}\,cm^{-3}}$) or a density (in $\mathrm{g\,cm^{-3}}$) we calculate its projection $\mathcal{P}_\xi$. The integral of ξ is performed inside the bow shock along a path perpendicular to the plane (O, R, z), excluding the unperturbed ISM. Taking into account the projection factor, it is,

$$\mathcal{P}_\xi(R, z) = 2 \int_{R'=R}^{R'=R_{max}} \xi(R', z) \frac{R'\, dR'}{\sqrt{R'^2 - R^2}}\, [\xi]\, \mathrm{cm}. \qquad (6.2)$$

For hot, photoionized medium we use the Hα emissivity rate interpolated from the Table 4.4 available
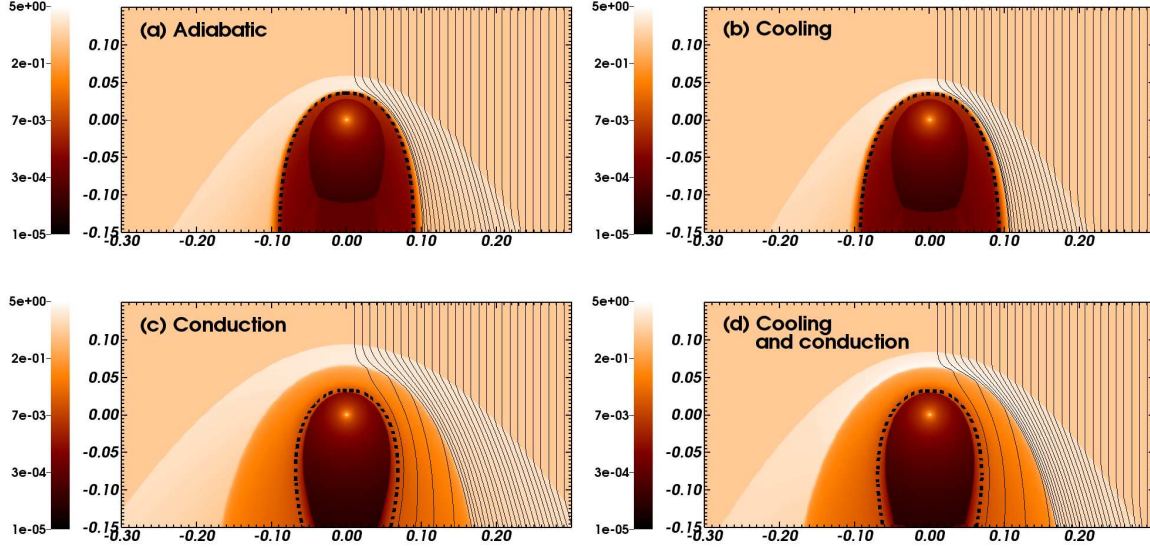
Figure 6.2: Series of hydrodynamical models showing the effects of the included physics on the bow shock produced by an initially $10\,M_\odot$ main-sequence star moving with $v_\star = 40\,\mathrm{km\,s^{-1}}$ through the Galactic plane. Panel (a) shows an adiabatic model, panel (b) is a model including optically-thin radiative cooling and heating, panel (c) represents a model with heat conduction and panel (d) shows a model with both gas cooling by optically-thin radiation plus heat conduction. The gas number density is shown with a density range from 10^{-5} to $5.0\,\mathrm{cm^{-3}}$. The solid black contour traces the boundary between wind and ISM material. The right part of each figure also shows ISM flow streamlines. It highlights the penetration of ISM material into the layer of the bow shocks. All models have the same initial conditions. The x-axis represents the radial direction and the y-axis the direction of stellar motion (in pc). Only part of the computational domain is shown in the figures.
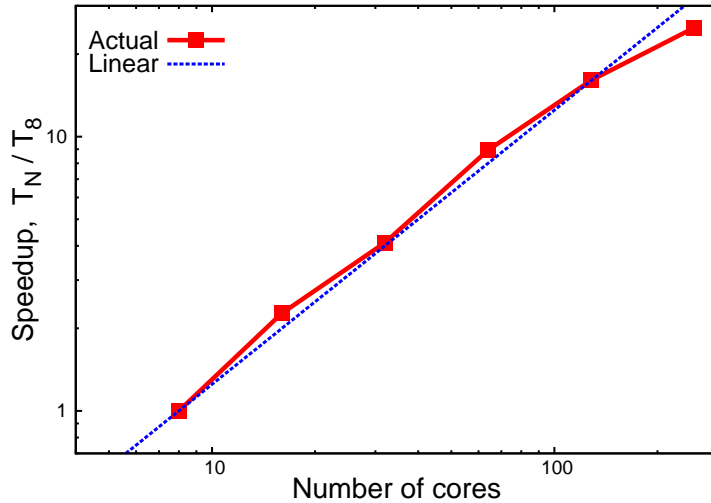
Figure 6.3: Speedup obtained with the PLUTO code (Mignone et al., 2007, 2012) on the supercomputer JUROPA in Jülich, shown as a function of the number of cores used (N), normalised to 8 cores. The test problem is the adiabatic model of a bow shock generated by a hot star similar as the model shown in panel (a) of Fig. 6.2 but run with a grid of 256×512 cells.

in Osterbrock & Bochkarev (1989), which is,

$$\xi(T) \approx 1.21 \times 10^{-22} T^{-0.9} n_e n_p \text{ erg s}^{-1} \text{ cm}^{-3} \text{ sr}^{-1}, \tag{6.3}$$

where n_e and n_p are the number of electrons and protons per unit volume, respectively. For cool, CIE medium we employ a similar formalism, taking into account the fact that only the ions emit, i.e. the emission is proportional to $n_e n_i$ with n_i the number of ions per unit volume. The emission rate is,

$$\xi(T) \approx 1.21 \times 10^{-22} T^{-0.9} n_i n_e \text{ erg s}^{-1} \text{ cm}^{-3} \text{ sr}^{-1}. \tag{6.4}$$

The ISM projected dust mass is calculated integrating the number density. For a dust-to-gas ratio $X_{d/g}$ and for the total gas number density n, its expression is,

$$\xi(T) = n X_{d/g} \mu m_p \text{ g cm}^{-3}. \tag{6.5}$$

We use a dust-to-gas ratio $X_{d/g} = 1/200$ by mass for the ISM in our simulations (Neilson et al., 2010; Neilson, Cantiello & Langer, 2011) and for the red supergiant winds (Lamers & Cassinelli, 1999). The calculation of the dust density for bow shocks around hot stars also requires us to exclude from the integral in Eq. 6.2 the region which are only made of wind material, i.e. which do not contain any dust.

6.3 Estimating of the infrared emission of the bow shocks

Learning from previous studies on the behaviour of dust in stellar bow shock (van Marle et al., 2011a; Decin et al., 2012; Decin, 2012), the infrared emission of a model is estimated as a part of the starlight absorbed by the dust grains and reemitted at longer wavelengths, plus the gas collisional heating of the dust particles.

We assumed that the shocked ISM material into the outer layer of the bow shock is filled with spherical grains of radius $a = 4.5$ nm (van Marle et al., 2011a) in a proportion of $X_{d/g} = 1/200$ by mass (Neilson et al., 2010; Neilson, Cantiello & Langer, 2011). The interstellar grains are assumed to be made of silicates whose density is $\rho_g = 3.3$ g cm^{-3} (Draine & Lee, 1984). The dust in the red supergiant wind is treated as in Mackey et al. (2012), but considering grains of radius $a = 5.0$ nm only. Such an approach is in accordance with interpretation of $24 \, \mu m$ infrared emission suggesting that small-sized dust grains are not destroyed in ionized regions in the vicinity of young massive stars (Pavlyuchenkov, Kirsanova & Wiebe, 2013). We assume that no dust crosses the material discontinuity, i.e. the shocked wind is dust-free in bow shocks around main sequence stars.

The flux from the starlight $L_\star$ is intercepted at a distance d from the star by the dust, which geometrical cross section is $\sigma_d = \pi a^2$ cm^2. A part of the flux from the star is absorbed by the dust to be instantaneously re-radiated as,

$$\Gamma_\star^{\text{dust}} = \frac{L_\star}{4\pi d^2} n_d \sigma_d (1 - A) \text{ erg s}^{-1} \text{ cm}^{-3}, \tag{6.6}$$

where $A = 1/2$ is the dust grain albedo (van Buren & McCray, 1988). This assumes that the dust is not decoupled from the gas, which is realistic for ionized bow shocks, whereas it may not be true in bow shocks around cool stars (van Marle et al., 2011a). This would influence both our estimation of n_d and $\Gamma_\star^{\text{dust}}$.

Besides, we estimate the dust collisional heating rate $\Gamma_{\text{coll}}^{\text{dust}}(T)$. On the one hand, the collisional heating

for a photoionized medium is computed following Ostriker & Silk (1973),

$$\Gamma^{\text{dust}}_{\text{coll,photo}}(T) = \frac{2^{5/2}}{\sqrt{\pi m_p}} f Q n n_d \sigma_d \left(k_B T\right)^{3/2} \text{ erg s}^{-1} \text{ cm}^{-3}, \qquad (6.7)$$

where n_d is the dust number density, m_p is the mass of the proton and $Q \simeq 1$ is a correction due to the electrical properties of the grains. On the other hand, it is calculated for the CIE medium following Hollenbach & McKee (1979), with,

$$\Gamma^{\text{dust}}_{\text{coll,CIE}}(T) = 2k_B n n_d \sigma_d f v_p \times (T - T_d) \text{ erg s}^{-1} \text{ cm}^{-3}, \qquad (6.8)$$

where k_B is the Boltzman constant, $v_p = \sqrt{k_B T / m_p}$ is the proton thermal velocity, $f \approx 10$ is a parameter representing the effects of the species other than the protons and T_d is the dust temperature,

$$T_d = 2.3 \left(\frac{f n_d}{a(\mu m)} \left(\frac{T}{10^4 \text{ K}} \right)^{3/2} \right)^{1/5} \text{ K.} \qquad (6.9)$$

In Eq. 6.9, $a(\mu m)$ is the dust radius expressed in μm.

This method to calculate the infrared emission from a stellar wind bow shock is rather simple. It assumes that the starlight is reemitted by the smallest possible grains and therefore constitute an upper limit of the corresponding luminosity. For all models it was found that radiative heating is dominant over collisional heating for all regions within the bow shock.

6.4 Modelling supernova-ISM interaction with the code PLUTO

Figure 6.4 shows a test model of a supernova explosion releasing $10\,M_\odot$ of ejecta and 10^{51} erg into the ISM. The method to setup the blastwave is taken from Whalen et al. (2008) and van Veelen et al. (2009). Fig. 6.4a shows an adiabatic model, and Fig. 6.4b shows a model based on the same initial conditions but including losses through optically-thin radiative cooling. A boundary effect happens as a results of the explicit scheme treating the cooling, and creates an artificial jet developing vertically along the symmetry axis Oz. However, this does not affect the overall solutions. The forward shock expands spherically and its radius grows similarly for both models during the same time interval. A distortion of the reverse shock of the blastwave develops. This is an usual behaviour with grid codes and its tends to shape it as an octagone. In both models, instabilities characteristic of the Richtmyer-Meshkov instability develops in the post shock region at the reverse shock. This particular kind of Rayleigh-Taylor instability appears at the interface between two gas of different densities, when one of them is brutally accelerated in the direction normal to the interface (Kane, Drake & Remington, 1999).
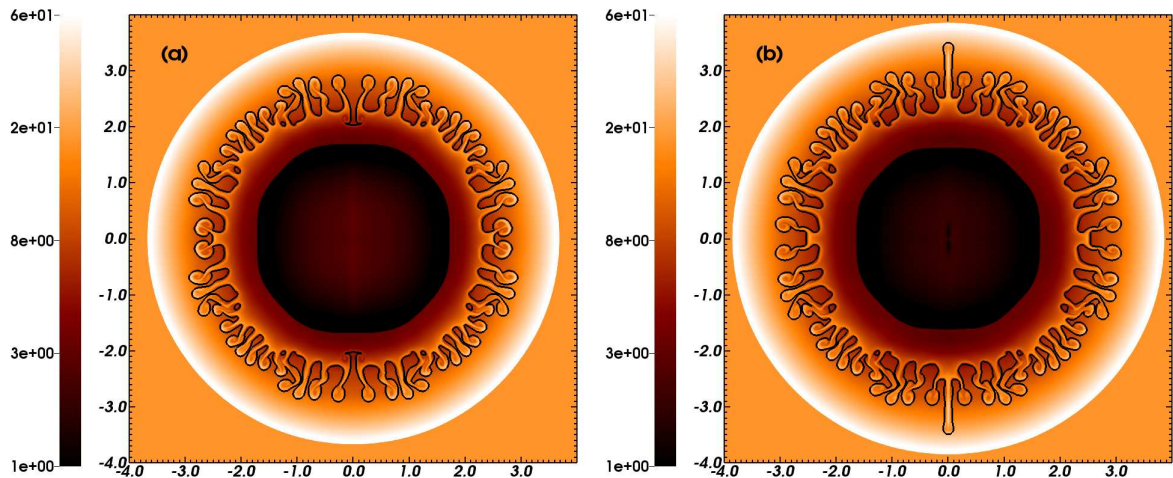
Figure 6.4: Remnants generated by a core-collapse supernova releasing $10\,\mathrm{M}_\odot$ and 10^{51} erg into an homogeneous medium of number density $10.0\,\mathrm{cm}^{-3}$. Panel (a) shows an adiabatic model about $10^{-2}\,\mathrm{Myr}$ after the supernova, panel (b) is the evolution of the same supernova remnant, including optically-thin radiative cooling and heating. Panel (c) plots the same test run but with thermal conduction only, and panel (d) shows the test with heat conduction and cooling by optically-thin gas radiation. The solid black contour traces the boundary between wind and ISM material. The *x*-axis represents the radial direction and the *y*-axis the direction of the progenitor's motion (in pc). Only part of the computational domain is shown in the figures.

Bibliography

Abdo A. A., Ackermann M., Ajello M., 2010, ApJ, 722, 1303

Alexiades V., Amiez G., Gremaud P.-A., 1996, Communication in Numerical Methods in Engineering, 12, 31

Arnaud K. A., 1996, in Astronomical Society of the Pacific Conference Series, Vol. 101, Astronomical Data Analysis Software and Systems V, Jacoby G. H., Barnes J., eds., p. 17

Arthur S. J., Hoare M. G., 2006, ApJS, 165, 283

Aschenbach B., Leahy D. A., 1999, A&A, 341, 602

Asplund M., Grevesse N., Sauval A. J., Scott P., 2009, ARA&A, 47, 481

Baade W., 1938, ApJ, 88, 285

Badenes C., Maoz D., Draine B. T., 2010, MNRAS, 407, 1301

Baranov V. B., Krasnobaev K. V., Kulikovskii A. G., 1971, Soviet Physics Doklady, 15, 791

Bedogni R., D'Ercole A., 1988, A&A, 190, 320

Benaglia P., Romero G. E., Martí J., Peri C. S., Araudo A. T., 2010, A&A, 517, L10

Blaauw A., 1993, in Astronomical Society of the Pacific Conference Series, Vol. 35, Massive Stars: Their Lives in the Interstellar Medium, Cassinelli J. P., Churchwell E. B., eds., p. 207

Blandford R. D., Kennel C. F., McKee C. F., Ostriker J. P., 1983, Nature, 301, 586

Blondin J. M., Koerwer J. F., 1998, New Ast., 3, 571

Blondin J. M., Lundqvist P., Chevalier R. A., 1996, ApJ, 472, 257

Borkowski K. J., Blondin J. M., Sarazin C. L., 1992, ApJ, 400, 222

Brighenti F., D'Ercole A., 1994, MNRAS, 270, 65

Brighenti F., D'Ercole A., 1995a, MNRAS, 277, 53

Brighenti F., D'Ercole A., 1995b, MNRAS, 273, 443

Broersen S., Chiotellis A., Vink J., Bamba A., 2014, MNRAS, 441, 3040

Brott I. et al., 2011, A&A, 530, A115

Bucciantini N., Blondin J. M., Del Zanna L., Amato E., 2003, A&A, 405, 617

Cao Y., Terebey S., Prince T. A., Beichman C. A., 1997, ApJS, 111, 387

Chevalier R. A., 1982, ApJ, 258, 790

Chevalier R. A., Liang E. P., 1989, ApJ, 344, 332

Chiotellis A., Schure K. M., Vink J., 2012, A&A, 537, A139

Chita S. M., 2011, PhD thesis, Utrecht University, Netherland

Chita S. M., Langer N., van Marle A. J., García-Segura G., Heger A., 2008, A&A, 488, L37

Ciotti L., D'Ercole A., 1989, A&A, 215, 347

Comerón F., Kaper L., 1998, A&A, 338, 273

Cowie L. L., McKee C. F., 1977, ApJ, 211, 135

Cox C. I., Gull S. F., Green D. A., 1991, MNRAS, 250, 750

Cox N. L. J., Kerschbaum F., van Marle A.-J., Decin L., Ladjal D., Mayer, 2012a, A&A, 537, A35

Cox N. L. J., Kerschbaum F., van Marle A.-J., Decin L., Ladjal D., Mayer A., 2012b, A&A, 537, A35

Dalcanton J. J., 2009, Nature, 457, 41

de Jager C., Nieuwenhuijzen H., van der Hucht K. A., 1988, A&AS, 72, 259

Decin L. et al., 2012, A&A, 548, A113

Decin L., 2012, Advances in Space Research, 50, 843

Dgani R., van Buren D., Noriega-Crespo A., 1996a, ApJ, 461, 927

Dgani R., van Buren D., Noriega-Crespo A., 1996b, ApJ, 461, 372

Diaz-Miller R. I., Franco J., Shore S. N., 1998, ApJ, 501, 192

Dopita M. A., 1973, A&A, 29, 387

Draine B. T., Lee H. M., 1984, ApJ, 285, 89

Dwarkadas V. V., 2005, ApJ, 630, 892

Dwarkadas V. V., 2007, ApJ, 667, 226

Eldridge J. J., Genet F., Daigne F., Mochkovitch R., 2006, MNRAS, 367, 186

Eldridge J. J., Langer N., Tout C. A., 2011, MNRAS, 414, 3501

Ferreira S. E. S., de Jager O. C., 2008, A&A, 478, 17

Filippenko A. V., 1997, ARA&A, 35, 309

Frail D. A., Goss W. M., Reynoso E. M., Giacani E. B., Green A. J., Otrupcek R., 1996, AJ, 111, 1651

Fraley G. S., 1968, Ap&SS, 2, 96

Frew D. J., Bojicic I. S., Parker Q. A., Pierce M. J., Gunawardhana M. L. P., Reid W. A., 2013, ArXiv e-prints

Freyer T., Hensler G., Yorke H. W., 2003, ApJ, 594, 888

Freyer T., Hensler G., Yorke H. W., 2006, ApJ, 638, 262

Gaensler B. M., 1998, ApJ, 493, 781

Gaensler B. M., 1999, PhD thesis, University of Sydney

Garcia-Segura G., Langer N., Mac Low M.-M., 1996, A&A, 316, 133

Garcia-Segura G., Mac Low M.-M., 1995a, ApJ, 455, 145

Garcia-Segura G., Mac Low M.-M., 1995b, ApJ, 455, 160

Garcia-Segura G., Mac Low M.-M., Langer N., 1996, A&A, 305, 229

Gehrz R. D., Becklin E. E., de Pater I., Lester D. F., Roellig T. L., Woodward C. E., 2009, Advances in Space Research, 44, 413

Gies D. R., 1987, ApJS, 64, 545

Goldsmith D. W., Habing H. J., Field G. B., 1969, ApJ, 158, 173

González-Casanova D. F., De Colle F., Ramirez-Ruiz E., Lopez L. A., 2014, ApJ, 781, L26

Green D. A., 2009, VizieR Online Data Catalog, 7253, 0

Green D. A., Stephenson F. R., 2003, in Lecture Notes in Physics, Berlin Springer Verlag, Vol. 598, Supernovae and Gamma-Ray Bursters, Weiler K., ed., pp. 7–19

Gull T. R., Sofia S., 1979, ApJ, 230, 782

Gusdorf A., Güsten R., Anderl S., Hezareh T., Wiesemeyer H., 2014, in IAU Symposium, Vol. 296, IAU Symposium, Ray A., McCray R. A., eds., pp. 178–182

Gvaramadze V. V., Bomans D. J., 2008, A&A, 490, 1071

Gvaramadze V. V., Gualandris A., 2011, MNRAS, 410, 304

Gvaramadze V. V., Gualandris A., Portegies Zwart S., 2009, MNRAS, 396, 570

Gvaramadze V. V., Kniazev A. Y., Kroupa P., Oh S., 2011a, A&A, 535, A29

Gvaramadze V. V., Kroupa P., Pflamm-Altenburg J., 2010a, A&A, 519, A33

Gvaramadze V. V., Kroupa P., Pflamm-Altenburg J., 2010b, A&A, 519, A33

Gvaramadze V. V., Langer N., Mackey J., 2012, MNRAS, 427, L50

Gvaramadze V. V., Menten K. M., Kniazev A. Y., Langer N., Mackey J., Kraus A., Meyer D. M.-A., Kaminski T., 2013, ArXiv e-prints

Gvaramadze V. V., Menten K. M., Kniazev A. Y., Langer N., Mackey J., Kraus A., Meyer D. M.-A., Kamiński T., 2014, MNRAS, 437, 843

Gvaramadze V. V., Röser S., Scholz R.-D., Schilbach E., 2011b, A&A, 529, A14

Heger A., 2012, in Astrophysics and Space Science Library, Vol. 384, Astrophysics and Space Science Library, Davidson K., Humphreys R. M., eds., p. 299

Heger A., Fryer C. L., Woosley S. E., Langer N., Hartmann D. H., 2003, ApJ, 591, 288

Heger A., Langer N., Woosley S. E., 2000, ApJ, 528, 368

Henney W. J., Arthur S. J., de Colle F., Mellema G., 2009, MNRAS, 398, 157

Hobbs G., Lorimer D. R., Lyne A. G., Kramer M., 2005, MNRAS, 360, 974

Hollenbach D., McKee C. F., 1979, ApJS, 41, 555

Hollenbach D., McKee C. F., 1989, ApJ, 342, 306

Hummer D. G., 1994, MNRAS, 268, 109

Huthoff F., Kaper L., 2002, A&A, 383, 999

Indebetouw R. et al., 2005, ApJ, 619, 931

James P. A., Anderson J. P., 2006, A&A, 453, 57

Janka H.-T., Langanke K., Marek A., Martínez-Pinedo G., Müller B., 2007, Phys. Rep., 442, 38

Jorissen A. et al., 2011, A&A, 532, A135

Kane J., Drake R. P., Remington B. A., 1999, ApJ, 511, 335

Kaper L., van Loon J. T., Augusteijn T., Goudfrooij P., Patat F., Waters L. B. F. M., Zijlstra A. A., 1997, ApJ, 475, L37

Kippenhahn R., Weigert A., 1994, Stellar Structure and Evolution

Kobulnicky H. A., Gilbert I. J., Kiminki D. C., 2010, ApJ, 710, 549

Kothes R., Fedotov K., Foster T. J., Uyanıker B., 2006, A&A, 457, 1081

Kroupa P., 2001, MNRAS, 322, 231

Kwak K., Henley D. B., Shelton R. L., 2011, ApJ, 739, 30

Lamers H. J. G. L. M., Cassinelli J. P., 1999, Introduction to Stellar Winds

Langer N., 1991, A&A, 252, 669

Langer N., 2012, ARA&A, 50, 107

Langer N., García-Segura G., Mac Low M.-M., 1999, ApJ, 520, L49

Le Bertre T., Matthews L. D., Gérard E., Libert Y., 2012, MNRAS, 422, 3433

Lequeux J., 2002, Le milieu interstellaire, edp sciences edn. CNRS Editions

Lodders K., 2003, ApJ, 591, 1220

López-Santiago J. et al., 2012, ApJ, 757, L6

Lozinskaya T. A., 1997, Ap&SS, 252, 199

Lyne A. G., Lorimer D. R., 1994, Nature, 369, 127

Mac Low M.-M., van Buren D., Wood D. O. S., Churchwell E., 1991, ApJ, 369, 395

MacDonald J., Bailey M. E., 1981, MNRAS, 197, 995

Mackey J., Gvaramadze V. V., Mohamed S., Langer N., 2014a, ArXiv e-prints

Mackey J., Langer N., Gvaramadze V. V., 2013, MNRAS

Mackey J., Mohamed S., Gvaramadze V. V., Kotak R., Langer N., Meyer D. M.-A., Moriya T. J., Neilson H. R., 2014b, Nature, 512, 282

Mackey J., Mohamed S., Neilson H. R., Langer N., Meyer D. M.-A., 2012, ApJ, 751, L10

Maeda T. et al., 2008, PASJ, 60, 1057

Maeder A., 2009, Physics, Formation and Evolution of Rotating Stars

Manchester R. N., 1987, A&A, 171, 205

Markevitch M., Gonzalez A. H., David L., Vikhlinin A., Murray S., Forman W., Jones C., Tucker W., 2002, ApJ, 567, L27

Mathis J. S., Rumpl W., Nordsieck K. H., 1977, ApJ, 217, 425

McKee C. F., Ostriker E. C., 2007, ARA&A, 45, 565

McKee C. F., Ostriker J. P., 1977, ApJ, 218, 148

Meyer D. M.-A., Gvaramadze V. V., Langer N., Mackey J., Boumis P., Mohamed S., 2014a, MNRAS, 439, L41

Meyer D. M.-A., Mackey J., Langer N., Gvaramadze V. V., Mignone A., Izzard R. G., Kaper L., 2014b, MNRAS, 444, 2754

Mignone A., 2014, Journal of Computational Physics, 270, 784

Mignone A., Bodo G., Massaglia S., Matsakos T., Tesileanu O., Zanni C., Ferrari A., 2007, ApJS, 170, 228

Mignone A., Zanni C., Tzeferacos P., van Straalen B., Colella P., Bodo G., 2012, ApJS, 198, 7

Mohamed S., Mackey J., Langer N., 2012, A&A, 541, A1

Morris M., Jura M., 1983, ApJ, 267, 179

Neilson H. R., Cantiello M., Langer N., 2011, A&A, 529, L9

Neilson H. R., Ngeow C.-C., Kanbur S. M., Lester J. B., 2010, ApJ, 716, 1136

Nomoto K., 1984, ApJ, 277, 791

Nomoto K., 1987, ApJ, 322, 206

Noriega-Crespo A., van Buren D., Cao Y., Dgani R., 1997, AJ, 114, 837

Oort J. H., Spitzer, Jr. L., 1955, ApJ, 121, 6

Orlando S., Bocchino F., Miceli M., Petruk O., Pumo M. L., 2012, ApJ, 749, 156

Orlando S., Bocchino F., Reale F., Peres G., Pagano P., 2008, ApJ, 678, 274

Osterbrock D. E., Bochkarev N. G., 1989, Soviet Ast., 33, 694

Ostriker J., Silk J., 1973, ApJ, 184, L113

Pannuti T. G., Rho J., Heinke C. O., Moffitt W. P., 2014, AJ, 147, 55

Parker Q. A., Phillipps S., Pierce M. J., Hartley M., Hambly N. C., Read M. A., MacGillivray, 2005, MNRAS, 362, 689

Pavlyuchenkov Y. N., Kirsanova M. S., Wiebe D. S., 2013, Astronomy Reports, 57, 573

Pérez-Rendón B., García-Segura G., Langer N., 2009, A&A, 506, 1249

Peri C. S., Benaglia P., Brookes D. P., Stevens I. R., Isequilla N. L., 2012, A&A, 538, A108

Petruk O. et al., 2009, MNRAS, 393, 1034

Pilbratt G. L. et al., 2010, A&A, 518, L1

Raga A. C., 1986, ApJ, 300, 745

Raga A. C., Mellema G., Lundqvist P., 1997, ApJS, 109, 517

Raga A. C., Noriega-Crespo A., Cantó J., Steffen W., van Buren D., Mellema G., Lundqvist P., 1997, Rev. Mex. Ast., 33, 73

Reach W. T. et al., 2006, AJ, 131, 1479

Rigon L. et al., 2003, MNRAS, 340, 191

Rozyczka M., Tenorio-Tagle G., 1995, MNRAS, 274, 1157

Rozyczka M., Tenorio-Tagle G., Franco J., Bodenheimer P., 1993, MNRAS, 261, 674

Russell C. T., 1985, Washington DC American Geophysical Union Geophysical Monograph Series, 35, 109

Sahai R., Claussen M., Morris M., Ainsworth R., 2009, in Bulletin of the American Astronomical Society, Vol. 41, American Astronomical Society Meeting Abstracts #213, p. 485.06

Salpeter E. E., 1955, ApJ, 121, 161

Santos-Lleo M., Schartel N., Tananbaum H., Tucker W., Weisskopf M. C., 2009, Nature, 462, 997

Schaller G., Schaerer D., Meynet G., Maeder A., 1992, A&AS, 96, 269

Schlegel E. M., 1990, MNRAS, 244, 269

Schneiter E. M., Velázquez P. F., Reynoso E. M., de Colle F., 2010, MNRAS, 408, 430

Schure K. M., Bell A. R., 2013, MNRAS, 435, 1174

Seok J. Y., Koo B.-C., Onaka T., 2013, ApJ, 779, 134

Smith M. D., Rosen A., 2003, MNRAS, 339, 133

Spitzer L., 1962, Physics of Fully Ionized Gases

Stevens I. R., Blondin J. M., Pollock A. M. T., 1992, ApJ, 386, 265

Stone J. M., Norman M. L., 1992, ApJS, 80, 753

Suess S. T., 1990, Reviews of Geophysics, 28, 97

Sutherland R. S., Dopita M. A., 1993, ApJS, 88, 253

Teşileanu O., Mignone A., Massaglia S., 2008, A&A, 488, 429

Tenorio-Tagle G., Bodenheimer P., Franco J., Rozyczka M., 1990, MNRAS, 244, 563

Tenorio-Tagle G., Rozyczka M., Franco J., Bodenheimer P., 1991, MNRAS, 251, 318

Tenorio-Tagle G., Rozyczka M., Yorke H. W., 1985, A&A, 148, 52

Toledo-Roy J. C., Esquivel A., Velázquez P. F., Reynoso E. M., 2014, MNRAS, 442, 229

Truelove J. K., McKee C. F., 1999, ApJS, 120, 299

Ueta T. et al., 2008, PASJ, 60, 407

van Buren D., 1993, in Astronomical Society of the Pacific Conference Series, Vol. 35, Massive Stars: Their Lives in the Interstellar Medium, Cassinelli J. P., Churchwell E. B., eds., p. 315

van Buren D., McCray R., 1988, ApJ, 329, L93

van Buren D., Noriega-Crespo A., Dgani R., 1995, AJ, 110, 2914

van Marle A. J., 2006, PhD thesis, Utrecht University

van Marle A. J., Decin L., Meliani Z., 2014, A&A, 561, A152

van Marle A. J., Keppens R., 2010, ArXiv e-prints

van Marle A. J., Langer N., Achterberg A., García-Segura G., 2006, A&A, 460, 105

van Marle A. J., Langer N., García-Segura G., 2005, A&A, 444, 837

van Marle A. J., Langer N., García-Segura G., 2007, A&A, 469, 941

van Marle A. J., Langer N., Yoon S.-C., García-Segura G., 2008, A&A, 478, 769

van Marle A. J., Meliani Z., Keppens R., Decin L., 2011a, ApJ, 734, L26

van Marle A. J., Meliani Z., Keppens R., Decin L., 2011b, ApJ, 734, L26

van Marle A. J., Smith N., Owocki S. P., van Veelen B., 2010, MNRAS, 407, 2305

van Veelen B., 2010, PhD thesis, Utrecht University, Netherland

van Veelen B., Langer N., Vink J., García-Segura G., van Marle A. J., 2009, A&A, 503, 495

Velázquez P. F., Martinell J. J., Raga A. C., Giacani E. B., 2004, ApJ, 601, 885

Velázquez P. F., Vigh C. D., Reynoso E. M., Gómez D. O., Schneiter E. M., 2006, ApJ, 649, 779

Vidotto A. A., Jardine M., Helling C., 2011, MNRAS, 411, L46

Vieser W., Hensler G., 2007, A&A, 472, 141

Vigh C. D., Velázquez P. F., Gómez D. O., Reynoso E. M., Esquivel A., Matias Schneiter E., 2011, ApJ, 727, 32

Villaver E., Manchado A., García-Segura G., 2012, ApJ, 748, 94

Vink J., 2012, A&A Rev., 20, 49

Vink J., Kaastra J. S., Bleeker J. A. M., 1996, A&A, 307, L41

Vink J., Kaastra J. S., Bleeker J. A. M., 1997, A&A, 328, 628

Vink J. S., 2006, in Astronomical Society of the Pacific Conference Series, Vol. 353, Stellar Evolution at Low Metallicity: Mass Loss, Explosions, Cosmology, Lamers H. J. G. L. M., Langer N., Nugis T., Annuk K., eds., p. 113

Vink J. S., de Koter A., Lamers H. J. G. L. M., 2000, A&A, 362, 295

Vink J. S., de Koter A., Lamers H. J. G. L. M., 2001, A&A, 369, 574

Vishniac E. T., 1994, ApJ, 428, 186

Wampler E. J., Wang L., Baade D., Banse K., D'Odorico S., Gouiffes C., Tarenghi M., 1990, ApJ, 362, L13

Wang L., Dyson J. E., Kahn F. D., 1993, MNRAS, 261, 391

Wang L., Wampler E. J., 1992, A&A, 262, L9

Wareing C. J., Zijlstra A. A., O'Brien T. J., 2007a, MNRAS, 382, 1233

Wareing C. J., Zijlstra A. A., O'Brien T. J., 2007b, ApJ, 660, L129

Weaver R., McCray R., Castor J., Shapiro P., Moore R., 1977, ApJ, 218, 377

Werner M. W. et al., 2004, ApJS, 154, 1

Whalen D., van Veelen B., O'Shea B. W., Norman M. L., 2008, ApJ, 682, 49

Whiteoak J. B. Z., Green A. J., 1996, A&AS, 118, 329

Wiersma R. P. C., Schaye J., Smith B. D., 2009, MNRAS, 393, 99

Wilkin F. P., 1996, ApJ, 459, L31

Wolfire M. G., McKee C. F., Hollenbach D., Tielens A. G. G. M., 2003, ApJ, 587, 278

Woltjer L., 1972, ARA&A, 10, 129

Woosley S. E., Heger A., Weaver T. A., 2002, Reviews of Modern Physics, 74, 1015

Wright E. L. et al., 2010, AJ, 140, 1868

Yoon S.-C., Langer N., 2005, A&A, 443, 643

Yusef-Zadeh F., Wardle M., Rho J., Sakano M., 2003, ApJ, 585, 319

Zavlin V. E., Pavlov G. G., Trumper J., 1998, A&A, 331, 821

List of Figures

134

List of Tables